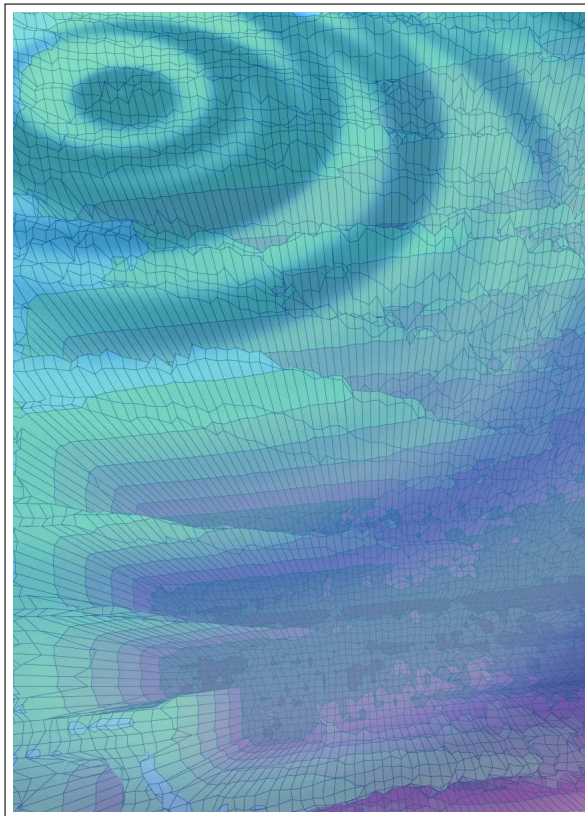# Plasma Polymer Gradients

Developing A Tool For The Screening Of
Biological Responses To Surfaces

Ph.D. Thesis

DI Mischa Zelzer

University of Nottingham

April 2009

Sonnet - To Science

Science! true daughter of Old Time thou art!
   Who alterest all things with thy peering eyes.
Why preyest thou thus upon the poet's heart,
   Vulture whose wings are dull realities?
How should he love thee? or how deem thee wise,
   Who wouldst not leave him in his wandering
To seek for treasure in the jewelled skies,
   Albeit he soared with an undaunted wing?
Hast thou not dragged Diana from her car?
   And driven the Hamadryad from the wood
To seek a shelter in some happier star?
   Hast thou not torn the Naiad from her flood,
The Elfin from the green grass, and from me
The summer dream beneath the tamarind tree?

Edgar Allan Poe

Abstract

Controlling the interaction of cells with a material surface is of major interest in the field of biomedical material science. Plasma polymers are an attractive way to modify the surface chemistry of a material because this technique is versatile and can be applied to a wide range of different surfaces. The aim of the present work is to prepare a new chemical gradient tool using plasma polymerisation and assess its ability to provoke position dependent cell-surface interactions. A novel diffusion based approach is used to develop gradients from hydrophobic hexane (ppHex) to more hydrophilic allylamine (ppAAm) plasma polymers. The surface of the gradient and that of uniform control samples is characterised using WCA, XPS, ToF-SIMS and AFM. This data shows that the most distinct gradient was found in the wettability profile which can be controlled by changing the size of the opening through which diffusion of depositing species from the plasma occurs.

The mechanism of the gradient formation is studied with channels of well defined cross sections. The deposition rate obtained on these samples shows a sharp drop off in the amount of ppHex deposited from the plasma starting 2 mm in advance of the opening. An estimation of the sheath dimensions indicates that this corresponds to the sheath thickness. It is suggested that plasma deposition through small openings such as pores depends on the relative dimensions of the sheath and the pore cross section. Inside the channels, oligomer formation is observed in the gas phase, presumably following a nucleophilic addition reaction mechanism.

To study the stability of these plasma polymer surfaces in physiological conditions, surface analysis is also carried out on samples exposed to aqueous solutions. Some changes in the topography of the plasma polymer films are found. Most notably, uniform samples of ppHex deposited on top of ppAAm show the formation of blisters that are not observed on other samples. It is argued that these blisters are the result of water penetrating through the top ppHex layer and interacting with the more hydrophilic ppAAm or glass substrate.

3T3 fibroblasts cultured on the gradients show a gradual increase in cell density. This cell density gradient can be related linearly to the wettability gradient on the surface with non-linear relationships being observed with other surface parameters such as the ppHex thickness. The cell number on uniform ppAAm is much greater than on the ppAAm side of the gradient. Data from experiments with non-proliferating 3T3 fibroblasts indicates that the differences between the gradient and uniform ppAAm as well as the cell density increase along the gradient have their origin in a different number of cells adhered to the surface within the first 24 hours of cell culture.

The adsorption of albumin and fibronectin on the plasma polymers demonstrate that displacement of the former by the latter takes place on the surface when adsorbed competitively. However, this displacement does not occur in different extents along the gradient surface, suggesting that protein displacement can not explain the increase in cell density towards the ppAAm end of the gradient.

Acknowledgements

The time I spent working on this thesis was a very fruitful life experience for me. On the way I met many people who I am indebted to for support during the course of my work.

I am very grateful to Dr. Morgan Alexander for his guidance and continued support for this work. I very much appreciate all the discussions we had and his help in data interpretation. He was always available as a supervisor while still allowing me the freedom to pursue my own line of work.

I am much indebted to my wife Ruby Majani; you were surely the most precious thing I came away with from my PhD. Your constant support and understanding helped me on more occasions than I can remember, and were the reason why I would always come out with solutions during any difficulties I had. Also, your knowledge in biology conveniently filled several gaps in my understanding of cell processes.

My thanks also go to my colleagues who carried out some of the measurements presented in this thesis. Dr. David Scurr put much effort into acquiring and processing the ToF-SIMS data. Dr. Badr Abdullah performed the mass spectrometry measurements of plasma species penetrating through glass tubes at the University of Liverpool. I am also grateful to Ruby Majani (again) for the sample preparation for SEM and the SEM image acquisition.

Many conclusions are the result of long discussions with other scientists. For these I want to especially thank Dr. Felicity Rose for her valuable contributions to the cell culture studies. Prof. James Bradley's knowledge on plasma polymer physics was very helpful in the study of plasma diffusion and his efforts on the development of the physical models are greatly appreciated.

Also very valuable to me were the efforts of many colleagues to introduce me to new instruments and techniques. First of all, I am very grateful to Dr. Nikolaj Gadegaard for kindly hosting me at the University of Glasgow where he taught me how to prepare the POP moulds. I thank Dr. Catalin Fotea for teaching me how to operate the plasma reactor and Dr. Chafika Dehili and Dr. Daniel Howard for the introduction to cell culture techniques. Emily Smith was an invaluable help for all XPS analysis I performed. I am very grateful for her helpful nature and the patience with which she taught me the use of the X-ray spectrometer. Prof. Xinyong Chen was extremely forthcoming whenever I needed help in the acquisition of AFM images. Finally, I would also like to thank Dr. Andrew Urquhart for all his support during the pico-litre WCA measurements and Dr. Victoria Wright for showing me how to use the fluorescence slide scanner.

More special thanks go to Dr. Michael Taylor for all the serious and not so serious discussions we had. I also appreciate your help and advice on many random occasions.

I also want to express my thanks to Paul Cooling, Ashley Buckler-Brown and Christy Grainger-Boultby who were invaluable to keep the laboratories running and to Richard Johnson, Susanne Finn, Julia Crouch and Maureen Day for all their help in administrative work.

Publications

Zelzer M, Majani R, Bradley JW, Rose FRAJ, Davies MC, Alexander MR. *Investigation of cell-surface interactions using chemical gradients formed from plasma polymers.* Biomaterials **2008**, 29 (2), 172-184.

Voronin SA, Bradley JW, Fotea C, Zelzer M, Alexander MR. *Characterization of thin-film deposition in a pulsed acrylic acid polymerizing discharge.* Journal of Vacuum Science & Technology A **2007**, 25 (4), 1093-1097.

Taylor M, Urquhart AJ, Zelzer M, Davies MC, Alexander MR. *Picoliter water contact angle measurement on polymers.* Langmuir **2007**, 23 (13), 6875-6878.

Voronin SA, Zelzer M, Fotea C, Alexander MR, Bradley JW. J. Phys. Chem. B *Pulsed and continuous wave acrylic acid radio frequency plasma deposits: Plasma and surface chemistry.* **2007**, 111 (13), 3419-3429.

Contents

Appendices

List of Tables

List of Figures

List of Schemes

Chapter 1

Introduction

1.1　Scientific Background

In modern healthcare the treatment of damaged or diseased tissue is a major field of interest. Maintenance, regeneration and replacement of tissue or organs are costly and suffer from a severe shortage of donors or are limited due to the restricted functionality of implants. In response, over the last two decades, tissue engineering has emerged as a major field of research which aims to provide new ways to prepare cost-effective and functional substitutes for damaged tissue [1, 2].

One approach to the engineering of new tissue uses preformed substrates or scaffolds that allow control over cell growth, proliferation and function of the cells and thus the final shape and function of the tissue. For the successful application of materials as scaffolds or as medical implants it is imperative that the surface of these materials supports controlled cell attachment and growth.

The cell response to materials has been shown to depend both on the surface chemistry and the topography of the material [3–5]. However, the surface of a material with bulk properties suitable for a specific application may not necessarily promote cell adhesion and growth. Consequently, considerable efforts have been made to modify the surface of materials approved for medical application [6, 7] to control adhesion and proliferation of cells by a precise spatial distribution of adhesion promoting properties [2]. For example, surface modification of a porous poly(D,L-lactic acid) 3D scaffold with thin plasma polymer films has been used to achieve a more homogeneous distribution of cells in the interior of the scaffold [8].

In order to provoke a desired biological response to the material surface, it is important to identify surface properties and coating materials that can be used to control the adhesion and proliferation of cells on a variety of different substrates. Testing of the cell response on a multitude of samples with varying surface properties can be a daunting and time consuming task; therefore, high throughput screening methods such as arrays [9, 10] or gradient surfaces [7, 11, 12] have been developed that offer the possibility of evaluating the biological response in a time and cost effective manner.

Plasma polymerisation is a very attractive surface modification technique, because it allows the deposition of films with various chemical properties independent of the surface chemistry of the substrate [13]. In the past, most plasma polymer deposits have been described as smooth films able to retain the topography of the substrate [14]. Because of this, plasma polymers are promising materials to study the relation between surface chemistry and the cell response on a flat substrate without the need to consider topographical effects of the surface.

Plasma polymer gradients on flat surfaces have potential as valuable tools to investigate cell-surface interactions. The use of plasma polymers to spatially control cell adhesion has been reported in several publications [15–19]. Whittle *et al.* first reported the preparation of a chemical gradient using plasma polymerisation in 2003 [20]. In this work, gradients with an acrylic acid plasma polymer on one end and either an allylamine or a 1,7-octadiene plasma polymer on the other were obtained. Barry *et al.* used the gradual deposition of plasma polymers in small pores to create a hydrophobic periphery with a more hydrophilic core in the interior of a porous scaffold [8]. This process was thought to be controlled by the diffusion of depositing species from the plasma through the pores, thus creating a thickness gradient of the deposited plasma polymer from the edge to the center of the scaffold.

The number of studies on the biological application of plasma polymers increases steadily and much data is available on the surface characterization of these materials. The ageing of plasma polymer films under ambient conditions has been extensively studied by Gengenbach *et al.* [21–25]. However, studies on the effect of a physiological environment on plasma polymer deposits are limited. Generally, some swelling of nitrogen based plasma polymer films was observed in water [26, 27, 27–30], but the oxidation process was shown to be similar in water and in air [31]. Only recently the effect of solvents on plasma polymers was considered by Vasilev *et al.* who reported the formation of pores on an *n*-heptylamine plasma polymer after immersion in water [32].

1.2   Aim of the Thesis

The overall aim of this work is the development of a suitable method to prepare surface chemical gradients from allylamine and hexane as tool for screening applications in biological studies. In addition, the biological response to these gradients will be investigated with the intention to determine if a gradual response occurs on the surface and, should this be the case, to identify the surface properties responsible for the gradual cell response and show how this information is conveyed by the protein layer to the adhered cells. The thematic separation of these two objectives was accounted for by presenting this work in two parts; PART I presents the method development and surface analysis of plasma polymer gradients and PART II relates the biological response to these surfaces.

In order to obtain plasma polymer gradients with properties ideal for application as a screening tool for cell adhesion behavior, several preparation techniques – including the one already introduced by Whittle *et al.* – will be tested. The optimal surface should provide a gradient in the concentration of nitrogen functionalities accompanied by a gradient in wettability over a millimeter to centimeter

length scale. When using 3T3 fibroblasts, it has been shown that for optimal cell adhesion on one side and non cell adhesive properties on the other, the wettability would need to be very to moderately hydrophilic on one end and hydrophobic on the other [8]. Thus, a large water contact angle range is desirable to increase the variety of surface chemistries tested in the cell-adhesion experiments.

These gradients and the cell-surface interactions that can be readily investigated on flat substrates are also suitable models for the surfaces obtained by plasma polymerisation in the interior of porous scaffolds. To understand the mechanisms involved in the penetration of depositing plasma species through small openings, in particular pore like structures, the formation of gradients in model pores will be investigated with the aim to develop a deposition mechanism and to quantify the diffusion properties of the plasma.

Another part of this work will address the lack of work on the behavior of plasma polymers in physiological conditions. The prepared gradients and uniform plasma polymer samples will be exposed to various aqueous environments to estimate how the presence of cell culture media may affect the material.

The biological part of this work will establish if the gradient properties of the samples can be translated into a gradual cell response. The cell response will subsequently be linked to the surface analysis data to identify any connections between the cell behavior and the surface properties. Attention will also be paid to the comparison of cell-surface relationships with data from samples before and after exposure to phosphate buffered saline (PBS). Even though the plasma polymer gradients prepared by Whittle *et al.* were used before to study the adsorption of immunoglobulin G [33] and to bind heparin with a gradually increasing density [34], no published data is yet available on the adhesion of cells to this kind of gradient surfaces.

For gradient approaches that are applied as rapid screening methods to assess a cell response, it is important to validate the results in comparison to uniform sample formats. It was found that literature dealing with gradient surfaces for biological applications often do not specifically emphasize the comparison with uniform samples. In these cases it is not possible to comment on the validity of the results obtained on gradients when they are intended as models for uniform samples. Therefore, the present study will also focus on the question whether or not cells behave differently on the gradient compared to a uniform sample.

To provide a more in depth understanding of the observed cell response, the interaction of a cell adhesive protein (fibronectin) and a non cell adhesive protein (albumin) with the surface will be explored. It has previously been postulated that cell attachment on the plasma polymers is determined by the adsorption and displacement of serum proteins (Vroman effect) which in turn can be controlled by the surface chemistry [8]. This claim will be investigated in more detail in this work.

Part I

Plasma Polymer Gradients

Chapter 2

Scientific Background

2.1 Plasma Polymerisation

2.1.1 Plasma Fundamentals

2.1.1.1 The Plasma State

Before going into any detail about the processes involved in plasma polymerisation, it is necessary to obtain a basic understanding of the plasma state and its main properties.

Plasmas consist of ionised gases; in more detail, the plasma state describes a collection of charged particles that can move around freely in random directions. Overall the plasma is electrically neutral [35]. Because the ionised state of a plasma is obtained by feeding sufficient energy into a gas, continuing the classification of state transitions from solid to liquid to gas, the plasma state is also commonly referred to as the 4th state of matter [36].

A common way to classify a plasma can be made according to its temperature. *Hot plasmas* are characterised by very high electron and molecule temperatures (4000 K up to 20000 K) and are close to complete ionisation (100%). Therefore they are also called *near-equilibrium plasmas*. Examples of hot plasmas are the combusting gases of stars or electrical arcs. In *cold plasmas*, where the temperature is significantly lower (several hundred Kelvin down to room temperature), the degree of ionisation of the heavy particles in the gas is reduced (10^{-4}% - 10%). The electrons and heavy ions are not in thermal equilibrium because the energy loss of heavy ions due to collision becomes significant. Such plasmas ar also referred to as *non-equilibrium plasmas*. Examples for cold plasmas are low pressure direct current (DC) discharges in plasma flames and neon light tubes [36]. In this cold plasma, the electrons are able to dissociate gas molecules through a *collision cascade*. In this process, free electrons (which are always present in a gas though their concentrations are low) are accelerated by the high potential between the electrodes. Collision of an electron with a molecule can cause another electron to be ejected, ionising the molecule in the process. These collisions become more frequent as the number of ejected electrons increases and provide the reactive radicals and ions necessary for the deposition of thin films [37].

The pressure of the gas in which the plasma is sustained can also be used to categorize it. If the plasma is operated at reduced pressure, that is, if the sustaining gas flows through a previously evacuated chamber, it is referred to as a *low pressure plasma*. Due to the higher instrumental effort in creating such kind of plasmas, large scale industrial applications try to move away from vacuum systems to plasmas operated at ambient conditions, so called *atmospheric pressure plasmas* [36].

2.1.1.2 Glow Discharge Plasmas

Plasmas are created artificially by ionisation of a gas with a high energy source. Because plasmas lose energy to their surroundings through collisions and radiation, they have to be sustained by a constant supply of energy. Electrical energy is the easiest and therefore the most common way to artificially create and sustain a plasma [36].

Glow discharges are widely used to initiate the plasma state. They are generated in a low pressure system (10^{-2} - 10^2 Torr) between two conductive electrodes. Various plasma reactor systems have been used [35, 38, 39]. The main operational differences between the reactors are the type and position of the electrodes, the way and mode the power is supplied, the shape of the reactor and the positioning of the sample inside it [36].

The type of the electrodes determines how the glow discharge is created. If positioned inside the reactor, the electrodes are usually parallel plates and produce a *capacitively coupled plasma*. When coils are used as electrodes, they are typically external and the resulting plasma is called an *inductively coupled plasma* [38].

Similarly, the plasma can be defined by the power that is supplied. Both DC and AC power supplies have been used. The most commonly used frequencies for AC plasmas are 13.56 MHz (radio frequency, RF) and 2.45 GHz (microwave frequency) [39]. In addition, the power supply can be pulsed. In such *pulsed plasmas*, the *on* and *off time* of the pulses provide an additional parameter to optimise the surface treatment. In contrast, if the power supply remains constant throughout the whole process, the plasma is operated in *continuous wave* (CW) mode [38].

The shape of the reactor has a significant influence on the distribution, homogeneity and general properties of the plasma created. *Bell shaped reactors* and *tubular reactors* are widely used [38]. In both cases the sample can be positioned in between or – in the case of planar electrodes – on top of the electrodes, inside the actual plasma glow area. Alternatively, the sample can be placed before or after the plasma glow area with respect to the flow direction of the sustaining gas. If the sample is closer to the gas inlet, the treatment is performed *upstream* of the plasma, whereas a *downstream* treatment is carried out when the sample is closer to the gas outlet [40].

2.1.1.3 Reactions in the Glow Discharge Plasma

In glow discharge plasmas, the high voltage applied to the electrodes (10^2 - 10^3 V) creates an electric field in which free electrons are accelerated. The applied voltage – and hence the strength of the electric field – determines how much kinetic energy will be transferred to the electrons. This, in turn, influences the kind of interactions the electrons undergo upon collision with the other species
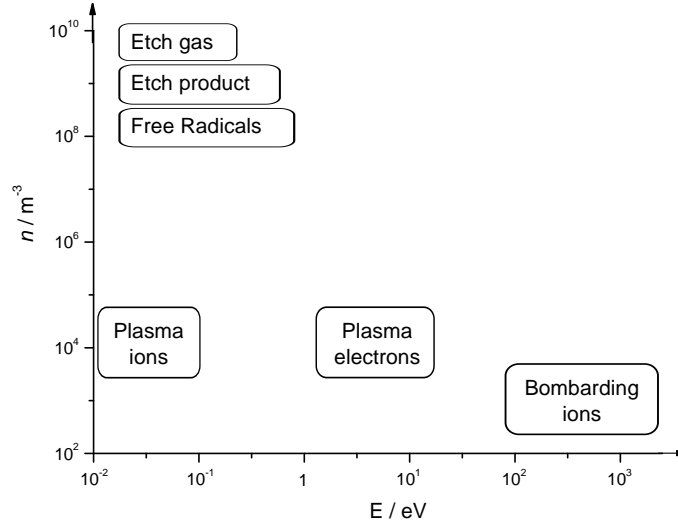
Figure 2.1: Typical particle densities (n) and energies (E) for various species in a low pressure capacitive RF discharge (adapted from [35]).

present in the gas. At low kinetic energies, elastic collisions prevail and merely the direction of the electron movement is changed while most of the electrons' kinetic energy is conserved. However, if the change in direction coincides with the orientation of the electric field, the electrons gain kinetic energy. If higher voltages are applied, inelastic collisions become more predominant and energy will be transferred to the gas molecules as well. [36].

The energy transferred from the electrons can cause several state changes in the gas molecules. Possible transitions are ionisation, fragmentation, recombination, creation of radicals and excitation of the molecules [41]. These processes result in the creation of a variety of different species (charged and neutral) and eventually lead to the ignition of a glow discharge [36]. In the plasma the inelastic collision events become more complex, making the collisions between electrons-ions, electrons-neutrals, electrons-radicals, ions-neutrals, neutrals-neutrals, ions-radicals and radicals-radicals likely possibilities [39]. Typical particle densities and energy distributions of various plasma species are shown in FIGURE 2.1. Overall, the number of positively and negatively charged species are balanced so that the plasma as a whole is electrically neutral.

Excited molecules can lose their energy by non-radiative or radiative processes. Upon collision with other species, the excitation energy can be passed on to a second molecule non-radiatively either as kinetic energy or by exciting the second molecule. If the energy is lost radiatively, that is, the excited electrons in the molecule drop back to their ground state, the excitation energy is emitted as photons both in the UV and visible region of the electromagnetic spectrum. This creates the distinct glow that characterises a glow discharge plasma [39].

2.1.1.4 The Plasma Sheath

A plasma in contact with a surface (electrodes, reactor walls, substrate surfaces, *etc.*) results in the formation of a sheath, a non-neutral potential region between the plasma and the surface. This *plasma sheath* is the consequence of an electron loss to the surface from the plasma area that is in close vicinity to that surface [35, 41].

In the bulk plasma, a long distance away from the surface, the electron density (n_e) equals the ion density (n_i) and the net charge is zero (FIGURE 2.2). However, because the mobility of the free electrons (the most important negative charge carriers) is much higher than the mobility of the heavy ions, electrons are lost to the surface, decreasing the electron density in front of the substrate and charging the surface negatively relative to the plasma potential. Thus, a positively charged sheath is formed where $n_i \gg n_e$. The net charge density in the sheath becomes positive, creating a potential profile that is positive within the plasma and falls sharply towards the surface. This drop in potential acts as a barrier for electrons, confining them in the plasma, while at the same time positively charged ions are accelerated through the sheath towards the surface [35, 41].
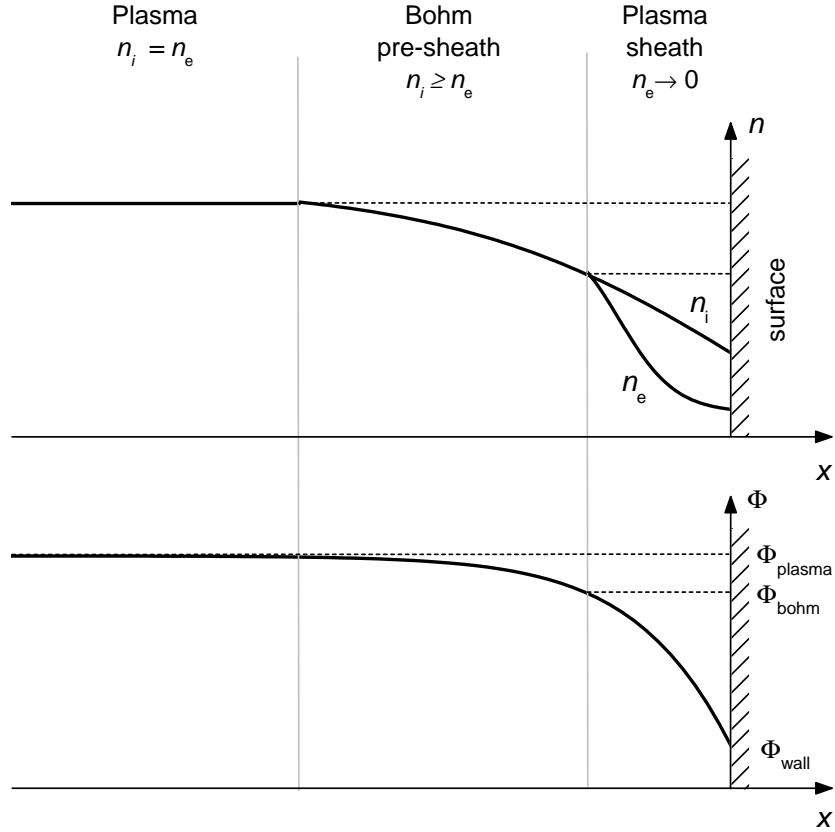
Figure 2.2: Characteristic particle density (n) and potential (Φ) distribution in the sheath formed between the plasma and a surface (adapted from [35] and [41]).

In order for the ion flux from the plasma to the sheath region to be maintained, another electric field, the *Bohm pre-sheath*, has to be introduced. This Bohm pre-sheath is typically much wider than the plasma sheath. In it, the quasi-neutrality of the plasma is only slightly disturbed ($n_i \gtrsim n_e$). However, it accelerates the ions towards the plasma sheath to a velocity known as the *Bohm velocity* (u_B). Thus, in a collisionless sheath of a DC discharge, when the velocity of the ions is u_i, the plasma (having $u_i < u_B$) joins the sheath (having $u_i \geq u_B$) exactly at $u_i = u_B$ [35].

In an RF discharge, the oscillation frequency ω of the electrons is much higher than that of the ions ($\omega_i < \omega_{ex} \ll \omega_e$ where ω_{ex} is the RF frequency). This means, that ions take much longer – several RF cycles – to move through the plasma sheath while electrons react instantaneously to the change in the electric field [41]. Thus, the current flux through the sheath is mostly due to the movement of electrons [35].

2.1.2   Plasma Polymer Deposition

2.1.2.1   Definition of a Plasma Polymer

The materials described as plasma polymers are distinctly different from conventional polymers. Conventional polymers generally have a well defined structure composed of repeating units that corresponds to the monomer used for its synthesis (SCHEME 2.1). The term *plasma polymer* describes a coating or film obtained from the activation and recombination of organic precursors (*monomers*) within an electric discharge. In such a *depositing plasma*, volatile organic molecules are used to sustain the plasma, in contrast to *etching plasmas* that are usually sustained by non polymerisable (O_2) or noble (Ar) gases [38].

During plasma polymerisation, the plasma activates and/or fragments the organic precursor, thus creating reactive species – generally radicals – that can recombine both in the plasma and
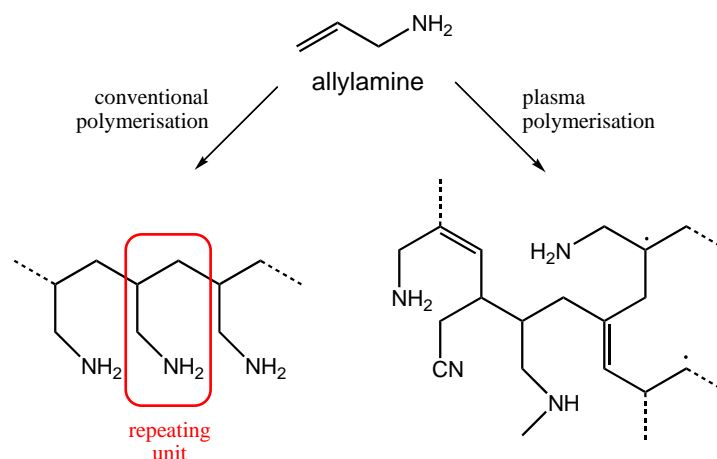
SCHEME 2.1: Schematic illustration of the polymers obtained from allylamine upon conventional and plasma polymerisation. Note the absence of a repeating unit and the presence of trapped radicals in the plasma polymer.

on a substrate surface; thus, a highly crosslinked, randomly structured deposit is formed on the substrate (SCHEME 2.1). During plasma polymerisation, partial loss of functional groups may occur. Additionally, the plasma polymer contains a large number of trapped radicals [42]. Hence, the material obtained from plasma polymerisation is very different than that obtained by conventional polymerisation of the same monomer [39].

Attempts have been made to produce plasma polymers with chemistries similar to conventional polymers. Generally, the high power input for the formation of the plasma and its UV radiation cause the monomers to crosslink randomly and lose some of their functional groups [43]. It has been shown that more defined plasma polymers with high functional group retention can be obtained by depositing at low power, positioning the sample downstream and using pulsed plasma polymerisation [43–45]. Employing one or more of these conditions for the plasma polymerisation of monomers that contain polymerisable groups such as alkenes or alkynes allows the plasma to be used as an initiator in a radical polymerisation rather than inducing random fragmentation of the monomers. In this way, well defined plasma polymers with high functional group retention were obtained from allylamine, allyl alcohol and acrylic acid [43].

In addition to the structural differences, the elemental composition of plasma polymers also deviates from that of conventional polymers prepared from the same monomer. For example, while the elemental composition of conventionally polymerised polyethylene (C_2H_4) is equal to that of the monomer (C_2H_4) – neglecting small differences induced by the endgroups – the hydrogen concentration of plasma polymerised ethylene is lower ($C_2H_{2.6}O_{0.4}$). At the same time some oxygen has been incorporated in the plasma polymer. However, even though both polymers have different elemental compositions, their physical properties are similar [39].

Due to its underlying mechanism of forming deposits on a substrate placed in the plasma reactor, plasma polymerisation is generally a surface coating technique. As such, it provides the means to change the surface chemistry of a substrate without altering the bulk properties of the material.

Several surface modification techniques are commonly used to alter the chemistry of a substrate; for example self assembled monolayers (SAMs), silanisations, chemical vapor deposition (CVD), physical vapour deposition (PVD), corona discharges, spin coating of polymer films and polymer grafts. All these methods have one or more limitations that can be overcome with plasma polymerisation. The main advantages of plasma polymerisation are that

- a wide variety of monomers and thus a variety of different surfaces chemistries are available,

- the deposition can occur at relatively low (ambient) temperatures,

- it is applicable to any solid material,

- no solvent is required,

- the surfaces of complex 3D objects can be coated,

- the inside coating of porous substrates is possible,

- the substrate remains mostly unchanged while only a thin film is deposited on top of the material,

- the deposited film has a very low surface roughness and follows the topography of the substrate surface and

- no initiator or solvent is needed [14, 40, 46].

The disadvantages are that

- generally low pressure systems have to be used,

- the reaction mechanisms are very complex, hence

- the chemistry of the formed deposits is not very predictable and therefore

- the process is influenced by a series of parameters that have to be thoroughly controlled (see SECTION 2.1.2.2).

One of the main advantages of plasma polymerisation is the wide variety of organic precursors or monomers that can be used, resulting in a variety of different chemistries that can be translated from the monomer onto the substrate surface. Since plasma polymerisation proceeds mainly by creating radical species in organic molecules by applying an electric discharge (see SECTION 2.1.2.3), any volatile organic compound can be plasma polymerised. Thus, plasma polymerisation is not limited to molecules with polymerisable groups such as double bonds, and even alkanes can be readily activated and crosslinked [38].

2.1.2.2   Deposition Parameters

The properties of the deposited plasma polymer and the deposition rate largely depend on the settings of the operational parameters. Aside from the monomer used, the parameters that can be controlled are [38, 39]

- the size, shape and geometry of the reactor,

- working pressure,

- base pressure,

- discharge power,

- monomer flow rate,

- substrate temperature,

- position of the substrate in the reactor,

- proximity of the sample to RF coupling objects,

- deposition time and/or film thickness,

- discharge current supply (AC or DC),

- AC current frequency,

- discharge mode (continuous wave or pulsed plasma) and

- on/off times for pulsed plasma systems.

For a specific deposition reactor, many of these parameters are fixed; the parameters that are commonly varied in one system to optimize the deposition rate and plasma polymer properties are deposition time or film thickness, working pressure, discharge power and monomer flow rate [38].

The choice of deposition parameters strongly influences the properties of the plasma polymer. FIGURE 2.3 shows how the physical state of plasma polymerised ethylene depends on pressure and discharge power. When working in an *energy deficient region* (low RF power), active species are consumed faster than they are generated and at a low monomer pressure, stable films are obtained. At high monomer pressure, however, there is not enough energy to sustain the plasma and the discharge becomes unstable. In the *energy sufficient region* (high RF power) where enough energy is provided to ensure that the generation of active species outweighs their consumption, films or powders are obtained if the monomer pressure is kept low. If both a high monomer pressure and high power are used, the plasma polymers begin to degrade (see SECTION 2.1.2.3) and form tacky films or oils [39].
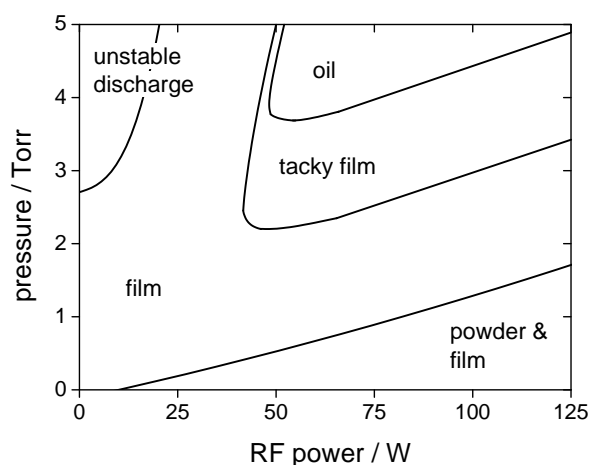
Figure 2.3: Influence of pressure and RF power on the physical appearance of plasma polymerised ethylene (adapted from [39]).

2.1.2.3 Polymerisation Mechanism

Plasma polymerisation is a very complex process that has not yet been understood to its full extent. In SECTION 2.1.1.3 the creation of ions and radicals from the monomer has been described. To describe the plasma polymerisation process, the various interactions of these species with each other, the surroundings and the sample have to be considered.

The high concentration of radicals compared to that of charged species in the plasma and the presence of radicals in the deposited polymers led to the conclusion that plasma polymerisation mainly follows a radical mechanism [42, 47, 48]. Denaro *et al.* showed that plasma polymerised styrene contains a large number of radicals which was proportional to the weight of the deposited plasma polymer [47]. In 1976, Yasuda demonstrated that exposure of a polyethylene coated glass rod to a N_2-plasma induces radical species not only on the polymer surface but also in the glass substrate underneath [42]. Further experiments suggested that the UV radiation in the plasma is the main source for the formation of radicals in the material. Yasuda also showed that gases such N_2 and O_2 that are rather inactive in conventional polymerisation procedures can be incorporated into the plasma polymer if present in the plasma [49]. Indeed, plasma polymerisation is not limited to monomers containing polymerisable groups such as alkenes, but due to fragmentation and ionisation of the monomer it also allows the polymerisation of alkanes and other non conventionally polymerisable molecules [39].

The radicals are mainly formed via two types of reaction; hydrogen abstraction or scission of C-C-bonds. This leads to the creation of activated species that can contain more than one radical. Similar to conventional radical polymerisation, Yasuda proposed various recombination and propagation mechanisms for the radical species that lead to the formation of oligomers and longer chains both in the plasma and on the substrate surface (SCHEME 2.2) [13]. Yasuda described this as a *rapid step growth polymerisation* (RSGP) *mechanism*.

Upon activation in the plasma the monomer can form either mono- (M·) or diradicals (·M·). Both species then have the possibility to react with other inactivated monomer molecules (M_i), which would preserve the radical state (*propagation*) and yield another active radical as product.

Alternatively, the monomer radicals can combine with other mono- (M_j·) or diradicals (·M_k·). If the monoradical M· reacts with a diradical, one radical is preserved; thus, another monoradical is created that can react further with any of the other species. However, if M· combines with another monoradical, both radicals are consumed in the reaction. The resulting inactive oligomer can only take part in the reaction again if it interacts with another radical or gets reactivated by the plasma (Cycle I in SCHEME 2.2).

The diradicals obtained by plasma activation equally retain their radicals upon reaction with another diradical (Cycle II). In contrast to monoradicals, however, diradicals do not become inactive upon reaction with another monoradical because only one of its two radicals is needed for the combination step. The resulting monoradical can then be fed back into Cycle I.

The active species created in the plasma subsequently form films on the exposed surfaces – either by physical deposition and/or by reacting with active sites on the surface. Thus, many different

species contribute to the material deposition, forming the highly crosslinked random structure typical for a plasma polymer.

Besides the formation of radicals, the plasma also induces fragmentation in the monomers [39]. The properties of the deposited plasma polymer not only depends on the type of monomer that is used, but also on the way the molecules are fragmented. The degree of fragmentation and what kind of fragments are formed varies with the operational parameters and the type of monomer that is used. It has been demonstrated that in a plasma sustained by toluene more fragments are formed when a higher discharge power is used [50]. In general, higher power induces a higher degree of fragmentation and creates a larger number of radicals, thus leading to a higher degree of crosslinking within the plasma polymer.

The dependance of the deposition rate on discharge power and flow rate can be expressed using the W/FM parameter that has been introduced by Yasuda (FIGURE 2.4) [13]. It takes the discharge power (W in J/s), the flowrate (F in mol/s) and the molecular mass of the monomer (M in kg/mol) into account to calculate an apparent input energy for a specific amount of monomer introduced into the plasma.

The W/FM parameter is considered to be proportional to the amount of activated species present in the plasma. At a low W/FM value an increase in power will result in an increase in the polymer deposition rate (*monomer sufficient region*). If the power is increased further the

Cycle I

Cycle II
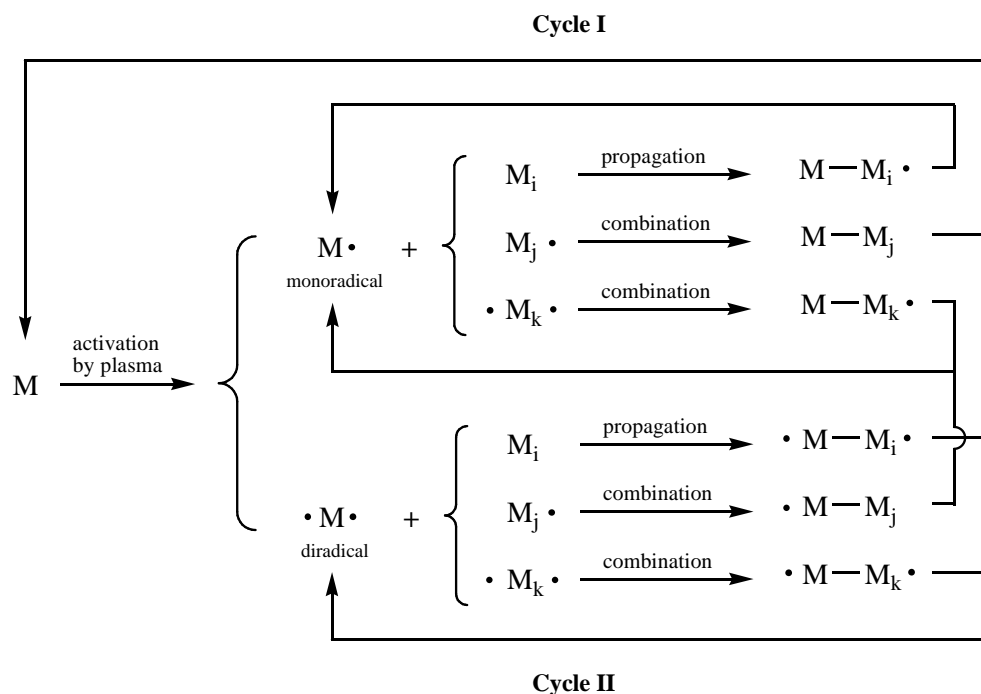
SCHEME 2.2: Plasma polymerisation mechanism on the basis of a rapid step growth polymerisation (RSGP) suggested by Yasuda (adapted from [13]).
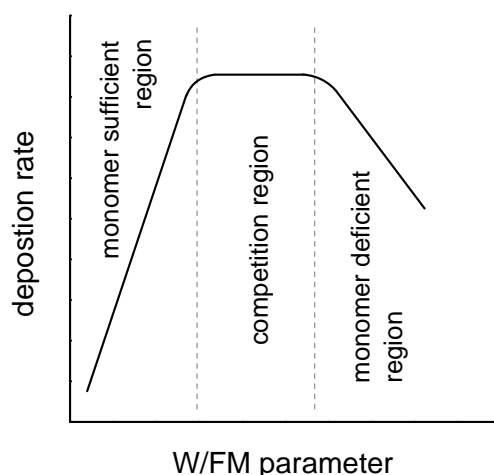
Figure 2.4: Dependance of the plasma polymer depo-
sition rate on the W/FM parameter [39].

deposition rate enters the *competition region* and levels off. At even higher powers the deposition
rate drops again; this is referred to as the *monomer deficient region*. A similar dependance of the
deposition rate is observed when the flow rate is changed.

The chemistry of the plasma polymers obtained from these three regions can be distinctly dif-
ferent. In the monomer sufficient region the power input per monomer unit is low. The monomer
is subject to a lower amount of fragmentation and the plasma polymer retains more of the original
functional groups of the monomer. In contrast, the monomer suffers high degrees of fragmentation
and a considerate loss of functional groups in the monomer deficient region [39].

After deposition, the polymer is constantly exposed to the reactive species and the high vacuum
UV irradiation in the plasma. Similar to an etching plasma, this causes the material to degrade,
rendering it different from the newly deposited polymer. These processes were summarised in
Yasuda's *competitive ablation and polymerisation* (CAP) mechanism [13].

The CAP mechanism describes the competitive nature of depositing and etching mechanisms
in a plasma sustained by an organic precursor (FIGURE 2.5). In a depositing plasma, the polymer
deposition rate will increase when the discharge power is increased. In contrast, a higher discharge
power in an etching plasma will result in a decrease in the plasma polymer deposition rate while
the etching rate is increased.

Besides the discharge power, the monomer flow rate also changes the depositing and/or etching
nature of the plasma. FIGURE 2.6 shows that a high flowrate of tetrafluoroethylene results in a
depositing plasma (deposition rate increases with increasing discharge power) whereas at a low
flow rate the tetrafluoroethylene plasma becomes an etching plasma (deposition rate decreases with
increasing discharge power) [39].
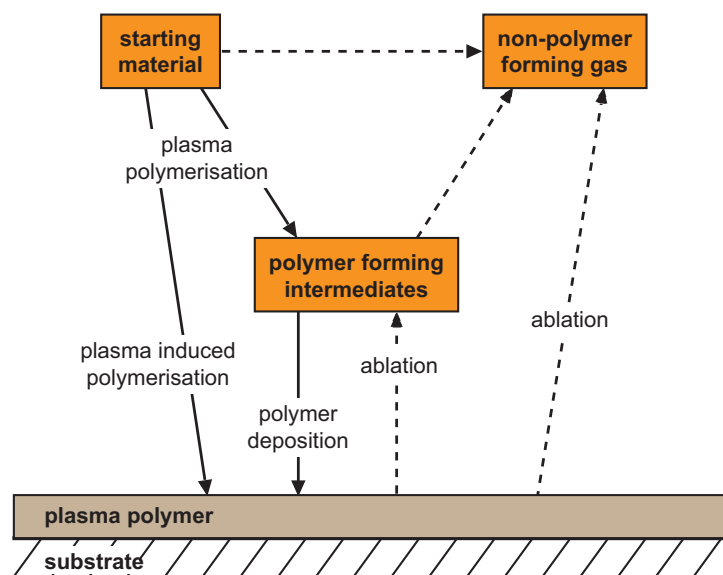
Figure 2.5: Competitive ablation and polymerisation (CAP) mechanism (adapted from [13]).
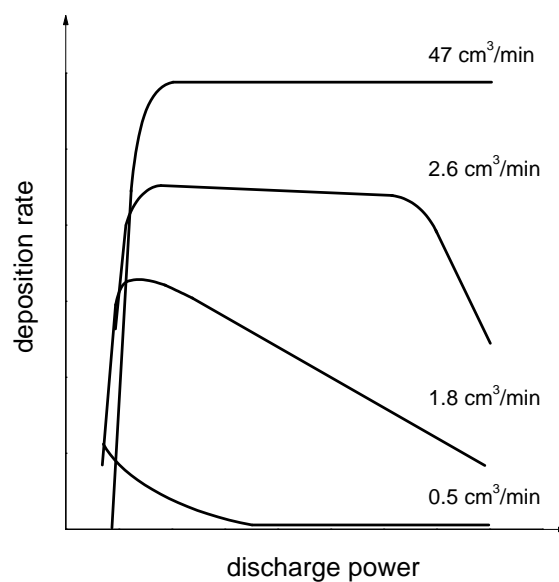
Figure 2.6: Qualitative illustration of the relationship between deposition rate, discharge power and flow rate in a tetrafluoroethylene plasma (adapted from [39]).

The dependance of the deposition rate on monomer flow rate and discharge power lead to the conclusion that both deposition and ablation occur simultaneously. Plasma polymerisation is a balance between deposition and ablation that can be shifted by changing the process parameters.

2.1.2.4 Interaction of the Plasma with the Substrate Material

Due to interactions of the plasma with the substrate the plasma polymerisation process is generally not constant over time. Pure metal substrates have high surface free energies, causing them to have layers of strongly adsorbed gases on the surface. These gases can not be removed by simple evacuation of the chamber. Hence, in the initial period after ignition of the plasma, the adsorbed gases will be etched off the surface, mix with the monomer to form a first layer of plasma polymer that is different from the subsequently deposited material [45].

In the case of polymers or glass, the surface free energy is lower so that gases are only weakly adsorbed and can mostly be removed during evacuation of the reactor. However, polymer substrates readily interact with the plasma themselves, causing molecule fragments from the substrate to merge with the plasma which in turn alters the first layer of the coating (Figure 2.7) [45].

In addition to the incorporation of unwanted molecules into the plasma polymer, the deposited material is also exposed to vacuum ultraviolet (VUV) radiation generated by the plasma. The VUV photons penetrate deeper into the material and are adsorbed with a much higher efficiency than near-UV radiation, thus largely accelerating the effect UV radiation has on polymers (see Section 2.1.3). As a result, freshly deposited plasma polymer is different from the underlying material that has been altered because of a longer exposure to VUV radiation [51].

Due to these two processes – incorporation of foreign molecules and alteration of deposited plasma polymer material by VUV radiation – the resulting coating is not uniform throughout its depth. Between the substrate and the fresh top coating there is an interphase layer that contains functionalities foreign to the bulk plasma polymer. In addition, the deeper part of the plasma polymer coating is constituted of material that has been altered by VUV radiation, rendering it different from the top layer of plasma polymer [45].
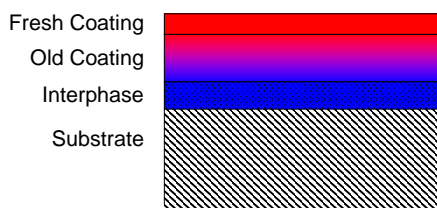
Figure 2.7: Composition of a plasma polymer coating. The coating consists of an interphase layer into which foreign material from the substrate has been incorporated, and a layer of plasma material that has been altered due to VUV irradiation and a layer of freshly deposited plasma polymer.

2.1.3 Stability and Degradation of Plasma Polymers

2.1.3.1 General Degradation Mechanisms

Knowledge of the stability of polymers is crucial to evaluate their performance for the intended application [52]. Not only can the degradation of polymers alter the physical properties (topography, stiffness, *etc.*) of the material, it can also induce changes in the surface chemistry.

The investigation of the mechanisms involved in the degradation of plasma polymers is difficult because of their heterogenous nature. The random structure of a plasma polymer makes the establishment of general mechanistic degradation pathways for these materials a considerable challenge. The basic chemical processes, however, are the same as in conventional polymers. Therefore, degradation mechanisms for conventional polymers will be introduced first, followed by a discussion of their relevance to plasma polymers and a review of the work published on plasma polymer degradation so far.

In general, four different ways of degradation are distinguished [45]:

- thermal degradation,

- oxidation,

- photodegradation and

- hydrolysis.

The mechanisms involved in the first three degradation processes often proceed through radicals that are created in the polymer chain. Depending on the type of polymer, and in particular the mobility of the polymer chains, recombination of the radicals and consequently crosslinking of the polymer chains can be a competing pathway to the weight loss usually observed upon degradation.

Thermal degradation often involves the abstraction of hydrogen atoms from the carbon backbone resulting in the formation of radicals (SCHEME 2.3). This process is even more favored in branched polymers, where the created radical is stabilised by a tertiary carbon. The result is a bond scission between two carbons that leads to the formation of a double bond and another radical. If the polymer – such as polyethylene oxide – contains oxygen in its backbone, thermal degradation can lead to the formation of carbonyl-groups (SCHEME 2.4) [45].
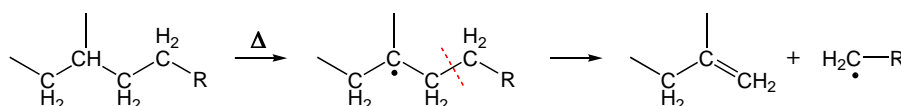
SCHEME 2.3: Hydrogen abstraction and subsequent bond scission induced by thermal degradation.
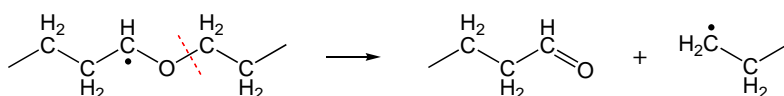
SCHEME 2.4: Thermal degradation of polyethylene oxide.

The *oxidation* of a polymer usually requires the presence of radicals in the material. New radicals can be created thermally, by irradiation or upon exposure to chemicals. In its ground state, the oxygen molecule is paramagnetic; therefore, it has to be considered as a diradical. Thus, oxygen reacts rapidly with radicals present in the polymer material to form peroxy-radicals which can subsequently be transformed into hydroperoxides by hydrogen abstraction (SCHEME 2.5). In the presence of UV radiation or metal catalysts, hydroperoxides readily decompose into two separate radicalic species (SCHEME 2.6). A competing reaction is the abstraction of the hydrogen from the hydroperoxide by other radicalic species. In the polymer, the decomposition of the hydroperoxides leads to bond scission as well as the formation of alcohols and carbonyl groups [45].
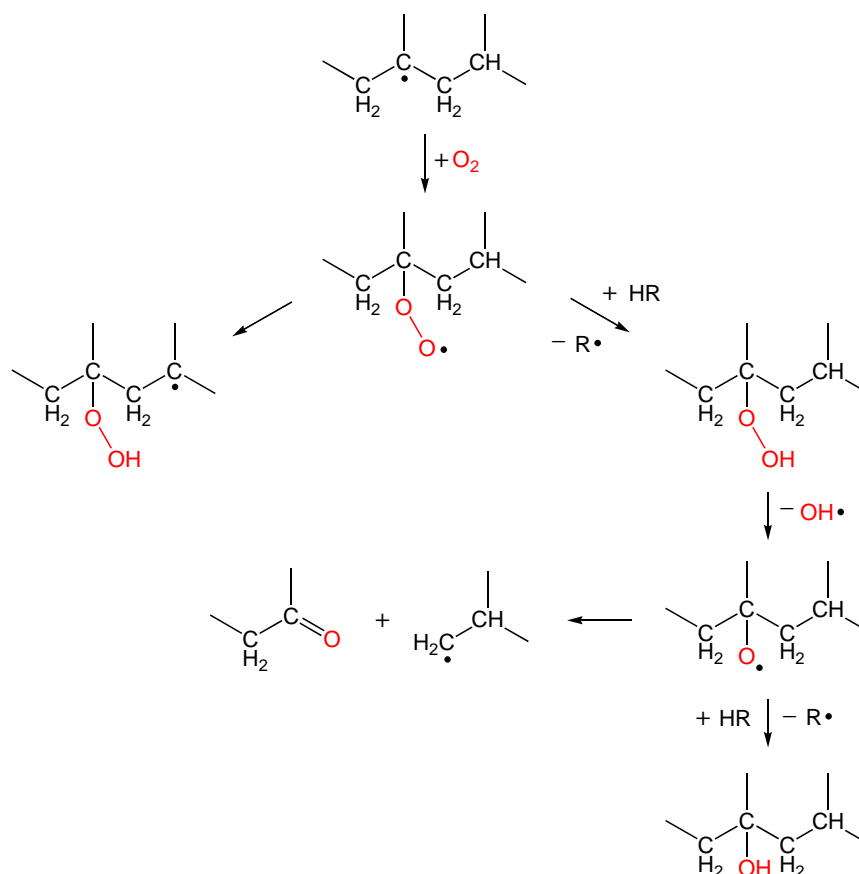
SCHEME 2.5: Mechanism for the oxidative degradation of polymers.

$$ROOH \longrightarrow RO\bullet + \bullet OH$$

$$ROOH + R'O\bullet \longrightarrow ROO\bullet + R'OH$$

$$ROOH + HO\bullet \longrightarrow ROO\bullet + H_2O$$
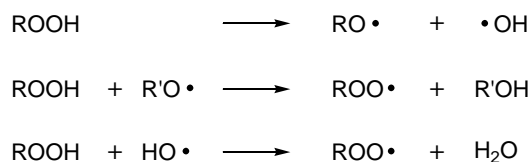
SCHEME 2.6: Reactions of peroxides formed in polymer backbones.

Photodegradation is caused by exposure of the polymer to light. Since pure hydrocarbon molecules and molecules containing single oxygen and nitrogen bonds and isolated double bonds generally absorb light below 200 nm, their photodegradation is negligible. Most photodegradation processes are based on carbonyl groups which absorb in the near UV and visible region of the electromagnetic spectrum. The two basic reactions for the scission of the bond between the carbonyl-carbon and the α-carbon are described by the Norrish reactions. In the *Norrish Type 1 reaction*, the C–$C(=O)$ bond is broken directly upon irradiation (SCHEME 2.7). For the *Norrish Type 2 reaction*, a hydrogen atom is transferred from the γ-carbon to the carbonyl oxygen, creating two radicals in the molecule (SCHEME 2.8). Subsequently, the bond between the α- and β-carbons breaks, leading to the recombination of the radicals and the formation of two double bonds. The Norrish Type reactions also occur in other carbonyl containing functional groups such as esters and amides [53].

When the polymer is in repeated contact with an aqueous environment, *hydrolysis* of functional groups can become a major degradation pathway. This includes both the conversion of functional groups and the subsequent fragmentation of the material by hydrolytic bond scissions. For the present work, the main focus lies on the hydrolytic degradation of nitrogen based functional groups, including amines, imines, nitriles and amides [53].
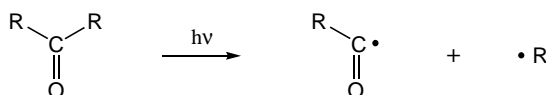
SCHEME 2.7: Norrish Type 1 photodegradation.
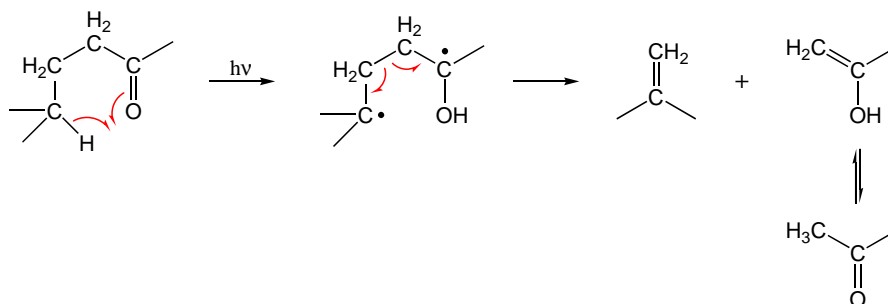
SCHEME 2.8: Norrish Type 2 photodegradation.

Amines do not hydrolyse as such, but they can be readily converted into other functional groups by oxidation (e.g. amides). If there is a double bond between the α- and the β-carbon, the enamine rapidly converts to an imine (Scheme 2.9).
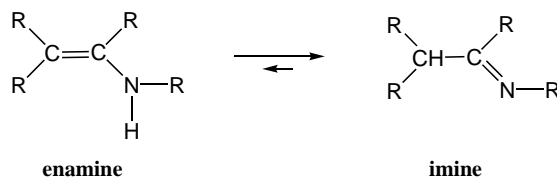
enamine   **imine**

Scheme 2.9: Enamine - imine tautomerisation.

Imines readily hydrolyse – consequently, the C–N bond is broken, resulting in the formation of an amine and a carbonyl functionality (Scheme 2.10).
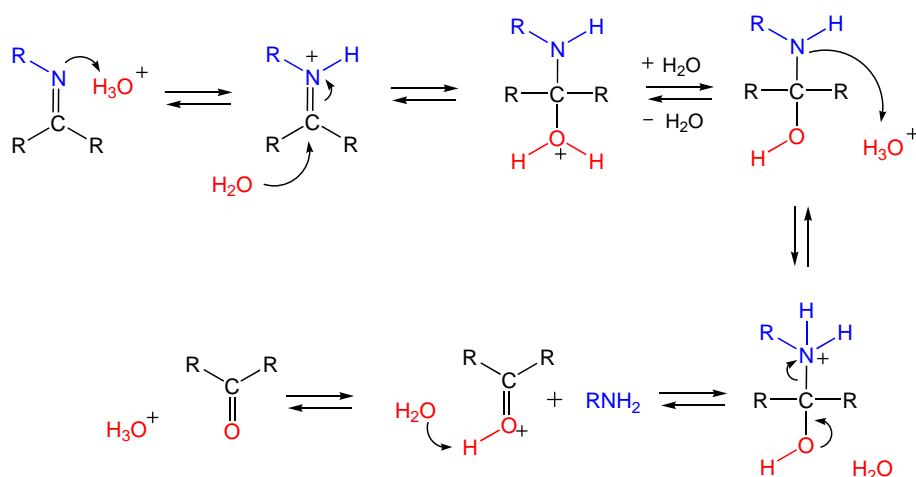
Scheme 2.10: Hydrolytic degradation of imines.

Hydrolysis of nitriles result in the formation of amides and subsequently carboxylic acid functionalities. This, however, has little relevance for the present work because it requires acidic catalysts and elevated temperatures.

Amides are more readily hydrolysed in the presence of either an acid or a base (Scheme 2.11). In this case, the reaction again leads to the scission of the C–N bond, forming a carboxylic acid and an amine functionality.
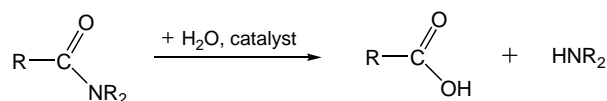
Scheme 2.11: Hydrolytic degradation of amides.

2.1.3.2 Plasma Polymer Degradation

Plasma polymer degradation follows the same basic pathways that have been described above. They inherently contain a large number of trapped radicals (see Section 2.1.2.3) that are easily stabilised by the large number of tertiary carbon atoms available. Due to the high degree of crosslinking in plasma polymers, the polymer chains are generally stiff. This restricts their movement and makes it difficult for the radicals to recombine [38].

Upon exposure to air, the trapped radicals in the plasma polymer can react with oxygen and water vapor. The uptake of oxygen containing species leads to a gradual incorporation of oxygen that makes the material more hydrophilic. Bond rupture and recombination of radicals also leads to a partial rearrangement of the polymer chains. The nature of the plasma polymer, the deposition parameters and thus the amount of trapped radicals determine how fast and to what degree the material ages or degrades [45].

The work presented in this thesis is based on plasma polymer films obtained from allylamine (ppAAm) and n-hexane (ppHex). Thus, the degradation behaviour of alkyl- and amine-containing plasma polymers are of particular importance and the focus of this section will be on reviewing the available literature to date on these plasma polymers.

Degradation can induce changes in both surface topography and surface chemistry. When studying the aging of 1,3-diaminopropane and n-heptylamine plasma polymers and an ammonia plasma modified perfluorinated ethylene-propylene copolymer in air, no significant changes in the surface topography were observed [52, 54]. In these studies, it was concluded that surface analysis data on these plasma polymers only reflects changes in the surface chemistry and topographical effects were excluded.

It is frequently reported that plasma polymers contain oxygen even if oxygen-free monomers are used and oxygen and water contaminations were kept to a minimum [16, 21, 22, 55, 56]. Gengenbach *et al.* used plasma polymers from n-hexane [21], n-heptylamine [23], methyl-methacrylate [57], ethylenediamine [22] and diaminopropane [25] to demonstrate that oxygen-uptake after deposition occurs almost instantaneously upon exposure to air and can be linked to a reaction of the material with either O_2 or water from the environment. Whittle *et al.* performed a similar study on allylamine, allyl alcohol, acrylic acid and octa-1,7-diene plasma polymers [56]. By comparing their results with previously published studies, however, it was evident that some of their data differed significantly from previously published material even though similar deposition conditions were used. The authors concluded that the ageing characteristics also depend on the plasma reactor [56]. Finally, it was shown that plasma polymer degradation can be reduced when the exposure to high energy particles is minimised, for example by using pulsed plasmas or by placing the sample in a downstream position [25, 58].

Hydrocarbon Plasma Polymers

In plasma polymerised hexane (ppHex), oxygen incorporation proceeds in three stages at different rates [21]. Immediately after exposure to air, the oxygen content determined with XPS increases

rapidly within the first 4 hours. It then reaches a second stage where the oxygen incorporation is slower. After 21 days, the oxidation decreases even more and proceeds at a constant rate over 7 months. Gengenbach and coworkers also found that oxidation in the bulk proceeded slower than on the surface of the plasma polymer. Notably, the oxidation started without the lag phase usually observed for conventional polymers. This was attributed to the fact that plasma polymers already contain a large number of radicals that are not present in conventional polymers.

Over the whole time period studied, the surface of the hexane plasma polymer remained smooth and stayed intact. C−C bond scission events such as the Norrish Type reactions – and thus the loss of the physical integrity of the material – are usually associated with higher oxidation states. Compared to polyolefines, ppHex did show a lower amount of carbonyl- and carboxyl-groups, whereas more C–O groups were observed. This suggests that there is less C–C bond fragmentation in plasma polymers, resulting in an increased retention of the physical integrity of the material [21].

Amine Containing Plasma Polymers

In a similar study of plasma polymerised *n*-heptylamine (ppHepA), Gengenbach *et al.* also observed aging of the material in three stages [23]. XPS analysis showed that the oxygen content increased rapidly within the first few days, after which the oxygen incorporation slowed down over a period of 4-6 weeks. In a third stage, the oxygen uptake became even slower but did not level off within the observed time frame. The total incorporation of oxygen was larger than 20% of the elemental composition. The same behaviour was observed by Whittle *et al.* and Malkov *et al.* with ppAAm that showed a sharp oxygen uptake within the first 30 days after deposition [56, 59].

In both the ppAAm and ppHepA the nitrogen content only decreased slightly over time with a major decrease occurring within the first few days after deposition [23, 56]. After several years of storage, the total loss of nitrogen in ppHepA was approximately 20% [23], while the nitrogen content in ppAAm was reported to decrease by 13% over 11 months [59].

To explain this loss of nitrogen, three different mechanisms were proposed [22]:

- oxidative chain scission that removes nitrogen rich volatile fragments,

- the presence of imine groups in the plasma polymer; these are easily hydrolysed upon exposure to water vapor, forming carbonyl groups in the polymer while liberating NH_3 from the material and

- rearrangement of the surface due to unfavorable interfacial tensions that lead to the migration of the polar nitrogen groups towards the interior of the material.

Due to their high degree of cross-linking, plasma polymers are often thought to have a limited capability to undergo surface rearrangements [52]. Gengenbach *et al.* used FTIR spectroscopy to show that the change in nitrogen content was not limited to the surface of ppHepA but equally affected the bulk of the material [23]. This, however, stands in contrast with data from angle resolved XPS experiments by Malkov *et al.* They reported that the loss of nitrogen was most

significant at a take-off angle of 80° for allylamine and hexylamine plasma polymers (ppHexA) and therefore more significant on the surface than in the bulk (take-off angles of 45° and 10°) [59].

The transformation of functional groups has experimentally been studied by XPS spectroscopy. Using the change of the C 1s signal and its fitted components and comparing the data from ppHepA and ppHex, Gengenbach *et al.* concluded that the evolution of the spectra is very similar. Thus, it was assumed that both plasma polymers age via similar oxidation reactions that are mostly unaffected by the nitrogen present in ppHepA. However, in the case of ppHepA, most of the oxygen was incorporated near the nitrogen-based functional groups in the material. Consequently, at the end of the second aging stage, about 66% of the nitrogen containing groups were oxidised [23]. Monitoring the relative positions of the C 1s and N 1s signals in the XPS spectra, it could be shown that a shift in the binding energy of the N 1s peak from 399.37 eV to 399.56 eV occurred in both ppAAm and ppHepA. This indicated a loss in the number of amine- (399.0 eV) and imine-functionalities (399.1 eV) while the amount of amide-groups (399.9 eV) increased [23, 56]. Malkov *et al.* suggested that an exchange of nitrogen by atmospheric oxygen on the material surface is the most likely mechanism for the degradation of ppAAm and ppHexA [59].

Fally *et al.* studied the oxygen uptake of *n*-heptylamine and 1,3-diaminopropane plasma polymers with angle resolved XPS spectroscopy [60]. They showed that the O/C ratio was higher at 75° than at 0° immediately after deposition, but that the situation was reversed after the first few days. In an extensive review, Siow *et al.* concluded that functional group conversion, surface rearrangement and the loss of volatile fragments are likely to compete with each other and collectively contribute to the aging behaviour of plasma polymers [52]. It was therefore recommended to use plasma polymer samples within a few days after preparation to avoid the additional complications of dynamic surfaces [61].

2.1.3.3 Effect of Aqueous Environments on Plasma Polymers

For the use of plasma polymers in biological applications, the effect of water on the polymer films is of particular importance. Various plasma polymers such as ppAAm [46, 62] and ppAAc (plasma polymerised acrylic acid) [63, 64] have been used in biological studies (see also SECTION 6.3.1). In general, plasma polymers immersed in a solvent can be subject to several processes, including

- delamination of the film,

- extraction of small molecules and oligomers into the solvent,

- swelling of the film and

- reaction of functional groups with the solvent.

Despite this, only a small number of publications are available that focus on the chemical and physical changes induced in plasma polymers by the aqueous environment. To date, no studies could be found that investigate the effect of water on ppHex or similar alkane-based plasma polymers; thus, only data for amine containing plasma polymers will be reviewed.

In 1989 Krishnamurthy *et al.* reported that allylamine deposited from a plasma at 30 - 100 W and 500 mTorr for 10 - 30 min were not soluble in acetone, chloroform, toluene or water [65]. When immersed in water, though, a neutron reflectivity study showed that ppAAm deposited at 20 W, 20 Pa in CW mode was penetrated by the solvent ($\sim$ 3 vol-%) and swelled by 15% [30]. A heptylamine plasma polymer (ppHepA), which was also investigated by the same group, contained $\sim$ 5 vol-% water and swelled by 1%. The swelling characteristics of other plasma polymers have also been reported [26, 27, 29].

Zhang *et al.* showed that the degree of swelling strongly depends on the deposition parameters [26]. Using surface plasmon resonance (SPR) it was demonstrated that ppAAm deposited at 20 W does not swell considerably while a ppAAm film deposited at 5 W showed a large degree of swelling. It was concluded that ppAAm deposited at low powers contains a large number of oligomers that are not covalently bound to the rest of the film. Consequently, these oligomers can be extracted by a suitable solvent, decreasing the overall thickness of the plasma polymer film [28].

When studying the topography of ppAAm (5 W, CW), Förch *et al.* found that the 'cauliflower' structure they observed in air for their ppAAm deposit did not change when immersing the film in PBS [28]. However, the rms roughness increased from 0.85 nm in air to 1.26 nm in PBS. This was attributed to the swelling of the plasma polymer film in water.

Recently, Vasilev *et al.* also reported the formation of pores of several nanometers in diameter on ppHepA after the plasma polymer has been immersed in water for 24h [32]. They found that the dimension of the pores depended on the deposition conditions with larger pores being formed when the film was deposited at lower powers. Based on the identification of small monomer-like moieties in the aqueous phase after immersion of the sample, it was argued that pores are formed due to the extraction of low molecular weight fragments from the plasma polymer by the water. This leads to the formation of voids in the material which in turn causes stress on the polymer chains due to shrinkage. This can not be compensated by mere rearrangement of the polymer chains but leads to ruptures in the film causing the experimentally observed porosity.

Both ppAAm and ppHex contained labile protons (24% and 9% for ppAAm and ppHepA, respectively) which could be exchanged with the aqueous solvent. These protons were attributed to reactive nitrogen- or oxygen-containing functional groups, suggesting that ppAAm is more reactive than ppHepA [30].

Tarasova *et al.* studied the change in surface chemistry of ppAAm and ppHepA (20 W, 20 Pa, CW) upon immersion in water for up to 24 hours on dried samples with XPS [31]. They found that the results were comparable to those obtained when these plasma polymers were degraded in air (see SECTION 2.1.3.2), undergoing rapid oxidation in both cases. Over time, a conversion of amine and imine groups to amides together with an increase of C−O and C=O groups was observed.

The charge of the surface is also of interest since it is significantly affected by parameters such as the *pH* of the environment. Using modified AFM tips, Schönherr *et al.* were able to map amine groups on ppAAm at different *pH* values with a spatial resolution below 50 nm, showing that the distribution of functional groups was not uniform [66]. Muir *et al.* measured the zeta potential of a ppAAm and ppHepA over time. The surface of ppHepA is initially positively charged, but became

negative after 30 min when $pH > 4.7$ [30]. The zeta potential became constant after 60 min. The ppAAm aged faster with an aging rate that increased when the pH is raised. At $pH > 8.4$ the ppAAm was negatively charged immediately after immersion in the solution. This was attributed to the hydrolytic degradation of the nitrogen functionalities (see SECTION 2.1.3.1) that caused a loss of species with higher pK_a (more positively charged amines) and an increase of functional groups with a lower pK_a (more negatively charged carboxylic acids). The same was reported by Tarasova *et al.* who used a colloid probe AFM to demonstrate that the density of positive surface charges decreases over time while the negative charge density increases on both ppAAm and ppHepA [31].

Even though the studies presented here were prepared under similar conditions, it has been shown in other plasma polymer systems that the interaction of the plasma polymer also depends on the deposition parameters [28]. Therefore, optimizing these parameters can be useful to reduce the changes induced in the plasma polymers by the aqueous environment. Additionally, pretreatment for cleaning or activation of the substrate has been used to prevent delamination of the polymer film [28].

2.2   Surface Analysis

2.2.1   Requirements for Surface Analysis

The surface of a material is generally not well defined and the part of the material considered as its surface depends on the application and analysis techniques employed to investigate it [67]. An analysis technique is generally considered *surface sensitive* when it is able to selectively provide information about properties of the uppermost layer of a material. The type of information can either be chemical (elemental composition, presence of functional groups, *etc.*) or physical (topography, *etc.*).

The *analysis depth* of chemical surface analysis depends on the technique; while some techniques probe the surface with a depth of as little as 1 nm, other methods require a minimal layer thickness of several hundreds of nanometers [67].

2.2.2   Surface Analysis of Plasma Polymers

Plasma polymers can be analysed with the same surface analysis techniques employed to characterise conventional organic thin films. Data interpretation, however, may prove more challenging due to the complex and random nature of plasma polymer films. Some of the most common techniques are listed below; for a more exhaustive description, the reader is referred to the literature [67, 68]:

- Water contact angle (WCA)

- X-ray photoelectron spectroscopy (XPS)

- Time of flight secondary ion mass spectrometry (ToF-SIMS)

- Attenuated total internal reflection (ATIR) infrared spectroscopy

- Ellipsometry

- Neutron reflection (NR)

- Scanning electron microscopy (SEM)

- Atomic Force Microscopy (AFM)

While the analysis depth of WCA and ToF-SIMS is very similar ($\sim$ 1 nm), XPS probes a depth of about 10 nm of the surface. ATIR requires films that are at least several tens of nanometers thick to provide sufficient absorption of the infrared radiation. Neutron reflection and ellipsometry allow the identification of several layers in multilayer films. AFM and SEM can both be used to characterise the topography of the material. When analysing polymer samples, AFM has the advantage of being able to image non conductive surfaces and can be employed in liquid environments [67]. Below, the main surface analytical techniques used in this work are introduced.

2.2.3 Surface Sensitive Analytical Techniques

2.2.3.1 Water Contact Angle

In any given material the individual atoms or molecules are exposed to attractive and repulsive forces from their surrounding. In the bulk of the material, attraction between the same molecules predominates and is equal in all directions. At the material surface, however, the attractive forces of the molecules from the bulk stand in equilibrium with forces acting from the adjacent material (air, water, *etc.*). This increases the intermolecular distance at the surface, putting it into a state of tension that is described as *surface tension* [67].

The surface tension is an interfacial phenomenon between two materials and therefore depends on the properties of both substances. If a liquid such as water is placed on a solid material, the surface tension at the interfaces will cause the liquid to form a drop shape with a defined contact angle θ (FIGURE 2.8) that is sensitive to the chemical composition of the surface. This water contact angle (WCA) is a result of an equilibrium between surface tensions at the solid-liquid (γ_{sl}), liquid-gas (γ_{lg}) and solid-gas (γ_{sg}) interface that is described by the Young equation:

$$\gamma_{sg} = \gamma_{sl} + \gamma_{lg} \cdot cos\theta \tag{2.1}$$

A low WCA is attributed to a hydrophilic surface (surfaces with polar groups such as alcohols), while hydrophobic surfaces (apolar surfaces such as hydrocarbon materials) have higher WCAs [39].

There are several ways to perform WCA measurements. *Static WCA* or *sessile drop* measurements are obtained when a stationary droplet is at an equilibrium on the surface. When acquiring *dynamic WCA* measurements, the contact angle is determined at the balance of the interfacial driving force and the viscous retarding force of a moving front. This can be done either with *advancing* or *receding* WCAs and is rate-dependent.
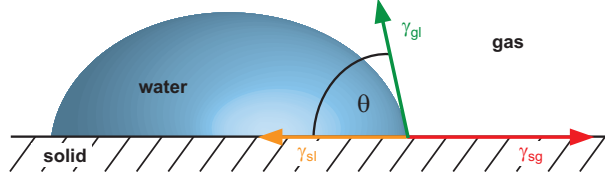
Figure 2.8: Forces acting on a water drop resting on a surface.

Because the WCA depends on the chemistry of the very top layer of the material it is extremely surface sensitive ($\sim$ 1 nm). This was shown in a study by Bain and Whitesides with ω-mercapto-ethers in which they experimentally obtained a depth sensitivity of 0.33 - 1 nm for WCA measurements [69]. Therefore, WCA measurements are very susceptible to contaminations. However, they can also be influenced by other material properties such as deformation of soft samples that can lead to large errors due to changes in the solid-gas component (γ_{sg}) [67].

The effects of surface roughness on the WCA have been described by Wenzel [70] and Cassie and Baxter [71]. Wenzel showed that, when the water drop is in complete contact with the rough surface (FIGURE 2.9), the contact angle can be related to a factor r that describes the ratio of the actual surface area to the projected surface area (EQUATION 2.2) [70, 72].

$$cos\theta_W = rcos\theta \tag{2.2}$$

A correction for the WCA of a drop that rests on an inhomogeneous surface has been derived by Cassie and Baxter (EQUATION 2.3) [71]:

$$cos\theta_{CB} = \sum_i^n \varphi_i cos\theta_i \tag{2.3}$$

In this case, the contribution of the surface tensions γ_i at the interface of the liquid for each different surface region (n to i) is taken into consideration. φ is the contribution of each area i to the total surface area covered by the liquid. In the case of a water droplet resting on top of surface topographical features with air trapped between the liquid and the surface (FIGURE 2.9), $n = 2$ and EQUATION 2.3 rearranges to

$$cos\theta_{CB} = \varphi(cos\theta + 1) - 1 \tag{2.4}$$

where φ becomes the fraction of the material surface that is in contact with the liquid.
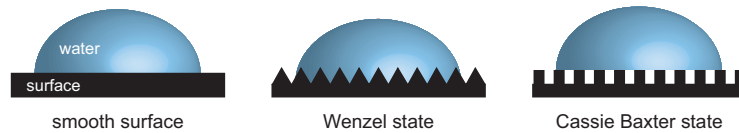
Figure 2.9: Schematic of the Wenzel and Cassie Baxter state.

2.2.3.2   X-ray Photoelectron Spectroscopy

A sample irradiated with a monochromated X-ray source emits *photoelectrons* from the core shell of the surface atoms. To be able to stimulate the emission of a photoelectron, the energy of the X-rays ($h\nu$) has to be greater than the *binding energy* (E_B) – the energy difference between the ground state and the Fermi level – of the electron. In addition, to separate the photoelectron from the bulk material, a small and constant amount of energy is needed, which is referred to as *work function* (ϕ). The remaining X-ray energy is transferred to the photoelectron as *kinetic energy* (E_K) and can be measured (FIGURE 2.10). Thus, the binding energy of the photoelectron can be calculated according to

$$E_B = h\nu - E_K - \phi \tag{2.5}$$

Photoelectron emission occurs in all atoms in which core shell electrons have a binding energy that is lower than the X-ray energy. Since the binding energy is characteristic for each element, qualitative and quantitative analysis of the surface is possible. This technique is known as *X-ray photoelectron spectroscopy* (XPS) [73].

The mean free path of photoelectrons is relatively short. Thus, only photoelectrons emitted from the first 10 nm of the material are able to leave the sample and reach the detector, making XPS a surface sensitive technique [68].

The binding energy not only depends on the nature of the element, but also on the chemical environment of the atom. While more electronegative binding partners increase the binding energy, more electropositive elements cause E_B to decrease. This effect results in a *chemical shift* of the peak in the spectra that is characteristic for the elements bound to the atom in question. Thus, XPS can not only be used to confirm the presence of a certain element on the surface, but it can also be employed to gain information about its chemical state [74].
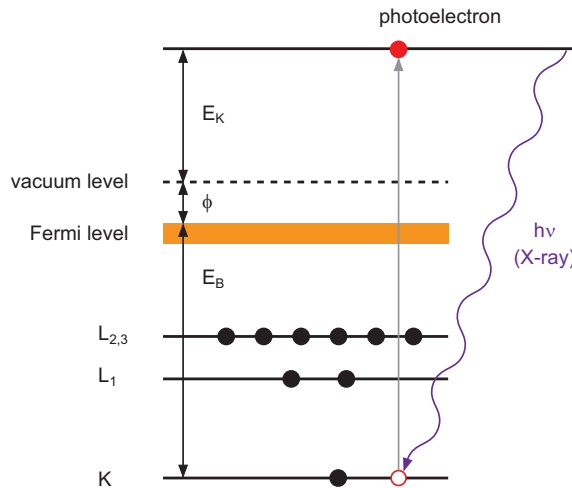
Figure 2.10: Schematic of the photoelectron emission in XPS.

2.2.3.3 Atomic Force Microscopy

Atomic force microscopy (AFM) is an imaging technique that can be used to acquire information about the surface topography of a sample. The technique is based on the interaction of the sample surface with a sharp tip on a cantilever which is mounted on a scanner head. In an ideal situation the edge of the tip consist of only a single atom. When the tip is approached to the surface it encounters a repulsive force due to the overlap of the electron shells of the atoms on the tip and the surface. Consequently, the cantilever is deflected, which can be detected using a laser that is reflected from the back of the cantilever towards a split photodiode (FIGURE 2.11) [67].

To image the sample surface, the tip is moved across the surface by a piezoelectric scanner. During the scanning in *contact mode*, the scanner head is held at a constant height. Changes in topography cause the cantilever to approach or retract from the surface and are monitored by the reflection of the laser. When the AFM is operated in *tapping mode*, the cantilever is oscillated at its resonance frequency while being moved across the surface. In this case, height differences on the surface change the amplitude of the cantilever oscillation, which again can be transformed into a height information [75].
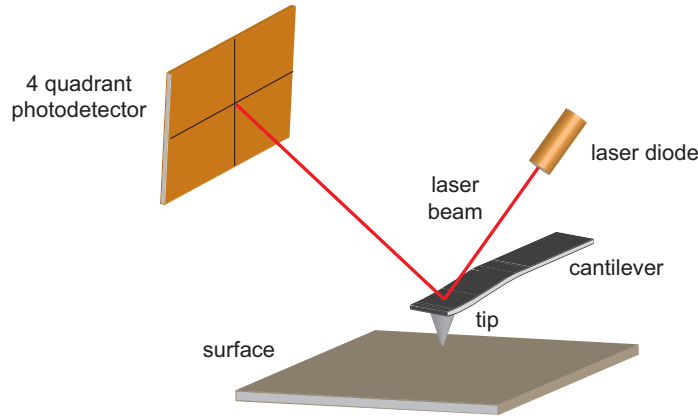
Figure 2.11: Schematic of the components in an AFM.

2.2.3.4 Time of Flight Secondary Ion Mass Spectrometry

A beam of *primary ions* which is accelerated to a surface causes a series of collisions that eventually lead to the emission of a variety of species from the surface, including electrons, photons, neutral species and positively and negatively charged *secondary ions*. This is called the *sputtering effect* (FIGURE 2.12). Secondary ion mass spectrometry (SIMS) uses this effect to obtain information about the composition of the surface by analysing the fragments sputtered from the surface with a mass spectrometer [76]. In *static SIMS*, the ion dose of the primary beam is kept low ($< 10^{13}$ ions cm^{-2}) in order to minimize the damage to the surface, whereas the higher dose of the ion beam used in *dynamic SIMS* causes erosion of the surface [77].
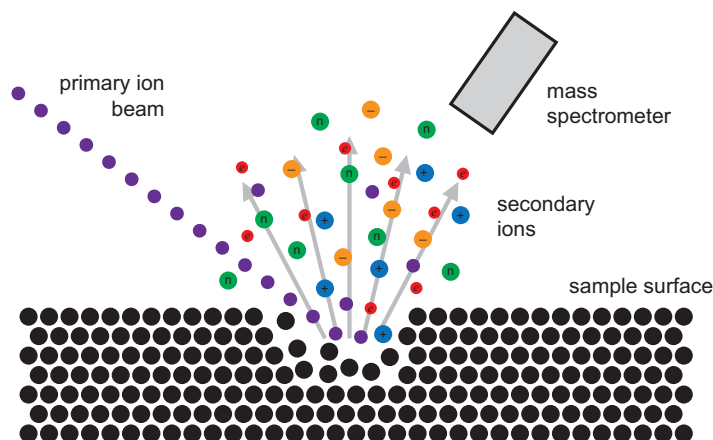
Figure 2.12: Schematic of the sputtering effect.

In *time of flight secondary ion mass spectrometry* (ToF-SIMS), sputtered ions of one polarity are accelerated to a given potential. Before reaching the detector the fragments drift through a field-free path. Since all ions have the same kinetic energy at the beginning of the path, the time it takes them to travel a fixed distance only depends on their mass. Lighter ions reach the detector earlier than heavier fragments and can therefore be separated from each other. The main advantage of this method is that all ions of a given charge can be analysed at the same time [76].

2.3 Gradient Surfaces

2.3.1 Surface Gradient Attributes

Gradient surfaces are surfaces that display a change in at least one physicochemical property either over distance or over time. This class of materials has attracted attention from a variety of different disciplines, each with their individual requirements. As a result, various surface gradient systems have been developed. In a recent review, Genzer and Bhat classified gradient surfaces according to their type, directionality, time dependency, dimensionality and functionality (TABLE 2.1) [12]. In the present study, static chemical gradients were prepared from plasma polymers both in a linear and radial manner.

2.3.2 Preparation of Soft Matter Based Gradient Surfaces

Over the past decades, a large number of techniques were proposed to prepare gradient surfaces of different types, directions and dimensions. An extensive overview of the techniques used to date has been given by Genzer and Bhat [12] and Morgenthaler *et al.* [11]. Here, the focus will lie on surface gradients based on soft materials, in particular on chemical gradients, as this will be the main topic of the work presented.

Table 2.1: Classification of surface gradients as proposed by Genzer and Bath [12].

Classification	Attribute
Type	Chemical Physical
Direction	Linear Radial Orthogonal
Time Dependency	Static Dynamic
Dimensionality	1D 2D 3D
Functionality	Driving a Phenomenon Recording a Phenomenon Screening a Property

Table 2.2: Classification of gradient preparation techniques according to the underlying physical principle [11].

Principle	Precursor	Substrate
Diffusion	Silanes, alkanethiols, polymers	Si, PDMS, Au
Printing	Silanes, alkanethiols, biomolecules	Si, Au
Desorption	Alkanethiols, polymers	Au
Advancing solution	Silane, alkanethiols, biomolecules, organic monomers	Si, Au, glass, PVC, PDMS
Irradiation	Silane, organic monomers, polyatomic ions or directly on the substrate	Si, glass, PDMS, polymers
Temperature	Polymers	functionalised Si
Irradiation and replacement	Alkanethiols	Au
Physically controlled polymerisation	Organic monomers	any

The techniques that have been explored so far for the preparation of chemical surface gradients are classified according to their underlying principle in TABLE 2.2. They are generally based on self assembled monolayers (SAMs) or polymer coatings [11]. TABLE 2.3 gives a schematic overview of each of the individual techniques that are shortly introduced below. However, many of the listed techniques are restricted to specific precursors or substrates, or both. The use of each individual approach will depend on its limitations towards the intended application (e.g. stability, solubility, reactivity, swelling etc.).

2.3.2.1 Diffusion

In diffusion controlled systems, the concentration of the precursor along the surface of the gradient is governed by its diffusion characteristics. Diffusion can take place in the *gas phase* (e.g. silanes on silicon [78] or palladium on cellulose acetate [6]), in *liquid* (e.g. diffusion of silanes through a solvent [79]) and through a *solid matrix* (e.g. diffusion of alkanethiols through a polysaccharide matrix [80]).

2.3.2.2 Printing

Gradients can be printed onto a surface by using a stamp that has previously been soaked with the precursor material. The amount of precursor that is transferred from the stamp to the surface depends on the quantity of precursor available and is thus proportional to the thickness of the stamp (*contact printing*) [81]. Alternatively, the precursor can be transferred onto the surface via *inkjet printing* [82].
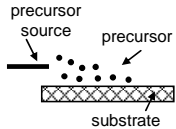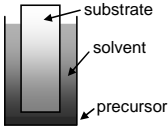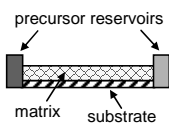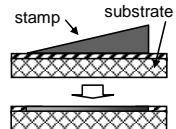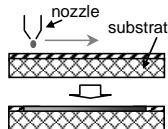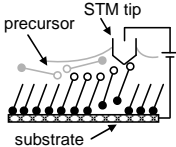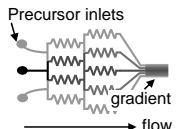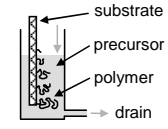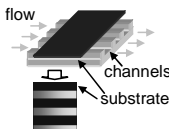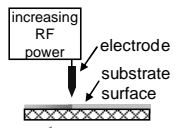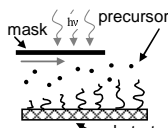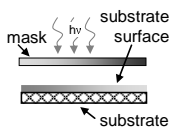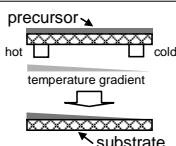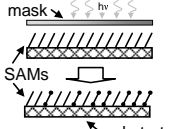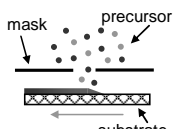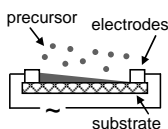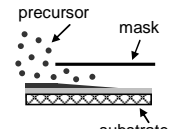
2.3.2.3 Desorption

Electrochemical methods can be applied to gradually desorb alkanethiols from a gold substrate. In the presence of a second alkanethiol, the first alkanethiol will be displaced, resulting in the formation of a SAM gradient [83, 84].

2.3.2.4 Advancing Solution

Gradient surfaces can also be obtained by gradually changing the properties of a liquid environment which contains the precursor used for the formation of the gradient. For example, a *concentration gradient* in a liquid matrix can be formed by repeated mixing and splitting different flows in a microfluidic system. When the flow from all channels is recombined, the resulting flow shows a gradual transition between the properties of each neighboring channel [85]. Gradients in polymer chain length were obtained by controlling the *reaction time* along the sample. When the monomer containing solution is drained continuously, longer reaction times are achieved at the bottom part of the sample, thus allowing the formation of longer polymer chains [86]. This technique was also employed to obtain orthogonal gradients made from block-polymers [87]. Finally, a gradual adsorption of proteins on a PDMS substrate was achieved by *depletion* of the protein solution.

Table 2.3: Techniques used to prepare soft matter surface gradients (adapted from [11]).

Principle	Limiting Factor		
	Vapour phase	**Solvent**	**Through a matrix**
Diffusion			
	Contact	**Inkjet**	
Printing			
	By potential		
Desorption			
	Concentration Gradient	**Reaction time**	**Depletion**
Advancing solution			
	Intensity	**Exposure time**	**Masking**
Irradiation			
	Temperature Gradient		
Temperature			
	Masking and exposure time		
Irradiation and replacement			
	Plasma polymerisation	**Electropolymerisation**	**Plasma diffusion**[a]
Physically controlled polymerisation			

[a] This new technique was not included in reference [11] and will be introduced in CHAPTER 3.

While flowing through microchannels, the protein concentration in the solution gradually decreases, resulting in a decreased adsorption of proteins onto the substrate further down the channels [88, 89].

2.3.2.5 Irradiation

Irradiation is a common way to modify surfaces with random reactive or polar groups. By changing the *intensity of the irradiation* along the substrate, a gradual modification of the surface can be achieved [90]. These surfaces could then either be used directly, or as templates to prepare gradients from a second material, for example a polymer surface with a gradually changing graft density [91]. Different *exposure times* along the sample can be used to prepare gradients in polymer chain lengths. In this case, the reaction time of monomers is varied locally, resulting in gradually increasing polymer lengths [92]. Varying exposure times have also been used to control the number of active sites, which were then used to link biomolecules to the substrate surface in gradually changing densities [93, 94]. The intensity of the irradiation has also been controlled by *masking the surface* with a variable density filter [95, 96].

2.3.2.6 Temperature

A gradient in temperature along the substrate has been used to control the conditions for grafting polymers onto the surface. Thus, gradually changing grafting densities were obtained [97]. These gradients have subsequently been used as a base for the immobilisation of biomolecules in a gradual manner [98, 99].

2.3.2.7 Irradiation and Replacement

By irradiation through a mask, SAMs have been degraded along the surface in a gradual manner such that the density of degraded thiol links increased from one side of the sample to the other. Molecules with cleaved thiol links are subsequently displaced by different alkanethiols, which results in a gradient of alkanethiols on the surface [100, 101].

2.3.2.8 Physically Controlled Polymerisation

Gradients can also be obtained if the depositing species is physically controlled at the surface. In the case of plasma polymerisation, the composition of the depositing material can be changed while the sample is moved under a small opening through which the sample is incrementally exposed, resulting in the formation of *co*-polymer gradient [20]. When using electropolymerisation, a potential gradient can be used to control the polymerisation rate on the surface, yielding a gradient in thickness of the deposited polymer [102]. To present a complete overview, the new technique to prepare gradients from plasma polymers presented in this work is also shown in TABLE 2.3. This technique can be classed either as physically controlled or as diffusion based, since a physical mask is used to control the diffusion of plasma species under the mask [103].

2.3.3   Surfaces Analysis of Gradients

In addition to the requirements introduced in SECTION 2.2 surface analytical techniques employed for the characterisation of gradient surfaces are also required to have a spatial resolution on length scales that are small compared to the gradient transition. The present work deals with gradients of several millimeters in length. Thus, the previously introduced surface analysis techniques will be briefly discussed with respect to their ability to analyse features in the submillimeter scale.

2.3.3.1   Water Contact Angle

The drop size generally employed for WCA is in the μL range, which produces drops of several millimeter in diameter on the surface, depending on its hydrophilicity [104]. Moreover, it has been shown that water drops can move on a surface with a wettability gradient towards the more hydrophilic end [105]. Therefore, conventional WCA measurements are not suitable for the analysis of gradients on the millimeter scale.

However, other techniques from the ones that were already introduced are available to measure the wettability of gradients. In the *capillary rise method* the water is allowed to rise between two adjacent plates. If gradients are prepared on the inner surface of these plates, the change in wettability can be measured by the height to which the water rises at each point (Figure 2.13).
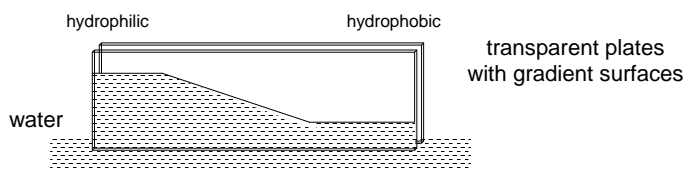
Figure 2.13: Capillary rise method to measure the wettability of gradient surfaces.
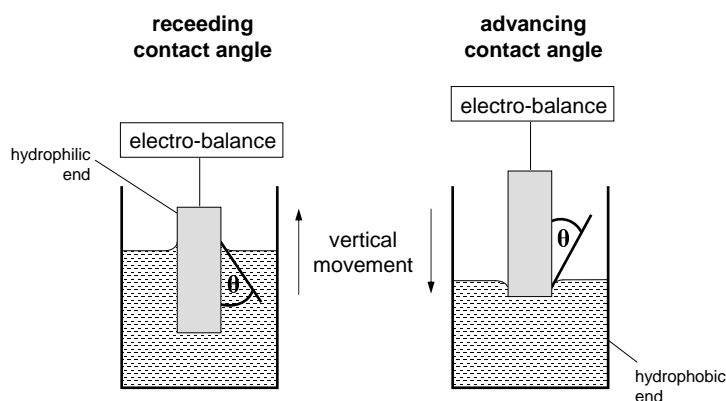
Figure 2.14: Wilhelmy plate method to measure the wettability of gradient surfaces.
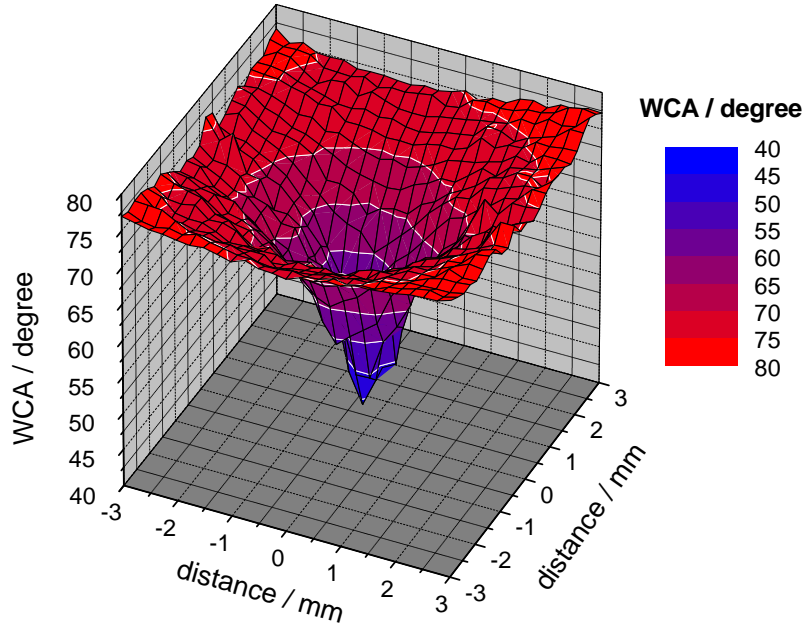
Figure 2.15: WCA map of a radial gradient of ppHex on ppAAm measured with pico-litre sized droplets. Measurements were taken in 0.25 mm intervals.

A disadvantage of this method is that it requires two similar gradients prepared on transparent substrates [6].

The *Wilhelmy plate method* uses an electro-balance to measure the force needed to retract or immerse a gradient surface from/into a liquid as a function of time and immersion depth (Figure 2.14). Both advancing and receding contact angles can be measured with this technique. Its disadvantage is that the surface tension of the test liquid has to be known accurately and it must be ensured that it is not affected by surfactants desorbed from the sample [6, 67].

To overcome the limitations of the previously mentioned methods and increase the spatial resolution of water contact angle measurements, a new technique has emerged within the last 3 years, that is based on the use of pico-litre sized water droplets for WCA analysis. The drop size is controlled by a piezo-doser, providing drop volumes in the order of magnitude of 100 pL that have a drop base diameter of about 70 μm at a contact angle of 90°. An automated stage allows precise positioning of the drops on the surface on the micrometer scale.

This method is at its early stages, but its concept is promising for the WCA analysis of samples with submillimeter resolution. However, a major question in WCA analysis is how the drop size affects the measured contact angle [67]. A number of studies have been published on this subject that come to different conclusions [106–108]. While with larger drops, the gravity pulling the water towards the surface can change the contact angle, drops that are too small may show pinning effects during evaporation. To validate the pico-litre based WCA analysis technique, a study was

performed to compare it with results obtained from conventional sessile drop WCA analysis [109]. No significant differences were found between the two methods. In addition, it was shown that with pico-litre sized droplets submillimeter resolution can be obtained by mapping the wettability of a radial gradient with a transition length of approximately 3 mm (FIGURE 2.15).

2.3.3.2 X-ray Photoelectron Spectroscopy

Conventional XPS has a very poor spatial resolution, exciting and collecting from a sample area with millimeter dimensions. The spatial resolution can be improved by one of two methods. The area on the sample that is excited can be minimised by stimulating X-rays emission with a focused electron beam and then focusing the X-rays on the surface through a monochromator. Alternatively, only a small field of view can be selected for analysis via a transfer lens. Thus, even though a large surface area is excited by the X-rays, photoelectrons are only collected and analysed from the selected area. With this *small spot XPS analysis*, the resolution can be improved down to 15 μm. In addition, *imaging XPS* is becoming more advanced and can make use of the higher resolution to obtain a chemical map of the sample surface [67, 68, 73].

2.3.3.3 Atomic Force Microscopy

Atomic force microscopy is an imaging technique based on force interactions on the atomic level. Thus, it has an inherently high lateral resolution which can be as low as 0.01 nm [75]. Its routine field of view, however is limited at the upper end to several tens of micrometers, which makes it impossible to observe topographical features on the millimeter scale.

2.3.3.4 Time of Flight Secondary Ion Mass Spectrometry

The spatial resolution of ToF-SIMS generally depends on the size of the primary ion beam. Electron impact sources can be focused to a diameter of 4 - 10 μm. Duoplasmatrons give beam diameters down to 0.5 μm while even smaller beam diameters of 200 to 20 nm can be achieved with liquid metal ion sources [74, 76]. Surface imaging can be performed in two different modes. In *scanning mode*, the ion beam is scanned across the sample and each point is measured individually. In this case, the spatial resolution only depends on the size of the ion beam. In *direct imaging mode* the whole area of interest is irradiated and ions from the whole area are detected simultaneously. Here, the resolution does not depend on the primary ion beam, but is limited by the energy distribution of the secondary ions and, in the routine analysis of polymers, on the ion yield of the sample. Thus, a lateral resolution of about 1 μm can be achieved [74].

Chapter 3

Preparation & Characterisation

3.1 Development of Gradient Deposition Techniques

3.1.1 Properties Required of the Gradient Surface

For the present work, a gradient in wettability was required that supports cell attachment and proliferation at one end but loses its cell adhesive properties gradually when moving to the opposite end of the sample. Additionally, the length scale of the gradient has to be in a region where characterisation of the surface is possible at good spatial resolution such that the surface properties at a given position can be related to the measured biological response but still small enough to allow rapid chemical and biological analysis of the whole sample. Since the cell dimensions are in the micrometer range, the gradient transition should be discrete at the micrometer scale, such that all cells experience similar conditions on all sides at any position. Thus, gradients with transition lengths of several millimeters up to a centimeter are desirable, that show a WCA range of about 100° to 40°.

It has been shown previously that rather hydrophilic materials containing amine-functionalities such as plasma polymerised allylamine (ppAAm) stimulate neuronal [62, 110] and fibroblast [111, 112] cell adhesion while hydrophobic hydrocarbon based surfaces such as plasma polymerised hexane (ppHex) prevent hamster ovary [16] and fibroblast [113] cell attachment and proliferation. Moreover, ppHex has been shown to be non-cytotoxic to animal and human fibroblasts [113]. Therefore, the preparation of plasma polymer gradients deposited from allylamine and hexane will be explored.

3.1.2 Methods for the Deposition of Gradients from Plasma Polymers

When developing methods to prepare surface chemical gradients from a plasma one has to take into account several characteristics of the system at hand (see Section 2.1). The diffuse and complex nature of the plasma does not allow for an accurate spatial control of the concentration of depositing species at the sample surface. In addition, plasma deposition occurs over the entire surface area of any object placed inside the plasma region, including the interior of porous substrates [46]. Hence, to
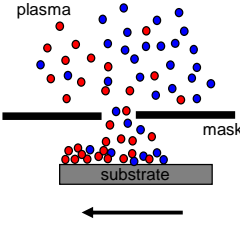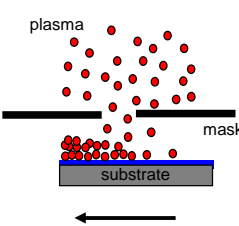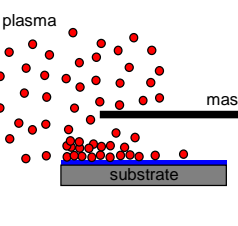
obtain a plasma polymer coating with gradually changing properties, parts of the substrate surface have to be masked during the deposition to obtain different deposition parameters for different positions along the sample that ultimately result in the formation of a chemical gradient.

Three different approaches for the gradient deposition can be envisioned (TABLE 3.1):

(i) The sample surface is gradually exposed to the plasma through a mask with an aperture moving at a constant speed while at the same time the composition of the plasma is changed in a gradual manner.

(ii) The sample surface is gradually exposed to the plasma through a mask with an aperture moving at an increasing/decreasing speed while the composition of the plasma is kept constant.

(iii) The sample surface is covered by a fixed mask which is slightly raised from the sample such that diffusion of depositing species can occur under the mask.

While the deposit prepared in method (i) ideally forms a coating of uniform thickness with a chemical composition gradient, method (ii) and (iii) result in the formation of a coating with a gradually changing thickness. The chemical gradients on these samples are a result of the thinning of the top plasma polymer layer that allows the chemistry of the substrate to 'leak through'. The chemical gradient therefore depends on the choice of chemistries of the top (plasma polymer) and bottom layers (substrate). In the experiments below, the desired effect is achieved by coating the substrate with one plasma polymer before the deposition of the second in a gradual manner. Thus,

Table 3.1: Approaches for the preparation of chemical gradients from plasma polymers.

	Co-polymer gradient	Exposure Time Gradient	Diffusion Gradient
Schematic			
Process variable	Plasma composition	Exposure time	Penetration depth
Sample speed	constant	increasing	static
Substrate pre-coated	no	yes	yes
Gas composition	2 monomers changing ratio	1 monomer constant	1 monomer constant
Surface gradient in	composition	thickness	thickness

strictly speaking both method (ii) and (iii) are thickness gradients, but the terms *exposure time gradient* and *diffusion gradient* are used to avoid any ambiguity in this work.

Whittle *et al* were the first to report the preparation of plasma polymer gradients in 2003, using method (i) [20]. During plasma deposition, the initially fully exposed sample was gradually moved into a box such that the sample was progressively shielded from the plasma. During this process, the monomer composition was changed gradually from allylamine to acrylic acid, yielding a plasma *co*-polymer based gradient. The masking technique was later further developed such that multiple samples can be prepared simultaneously [33].

3.1.3   Evaluation of Gradient Deposition Techniques

First attempts to prepare gradients from ppHex to ppAAm were based on methods (i) and (ii), using a similar deposition apparatus as that developed by Whittle *et al* (FIGURE 3.1). It consists of a sample compartment (bottom) with six rows that can hold 5 circular glass coverslips each. The sample compartment can be moved gradually forward and backward during the deposition. A metal mask with six slot like openings (one above each sample row) is screwed on top of the sample compartment such that exposure to the plasma only occurs through the slot openings. The width of the openings in the mask was 1.5 mm, while the samples were separated from the mask by a distance of approximately 0.2 mm. The gradient tray was positioned in the protruding section of the plasma chamber (FIGURE 3.2). Since the plasma is mainly located between the two electrodes, the general setup shown in FIGURE E.1 in APPENDIX E had to be modified for this experiment such that the working electrode is placed on the third arm of the chamber, diverting the plasma over the sample tray (FIGURE 3.2).

Co-polymer gradients were prepared in the same manner as reported by Whittle *et al*. The monomer composition was changed incrementally from either hexane to allylamine or vice versa,
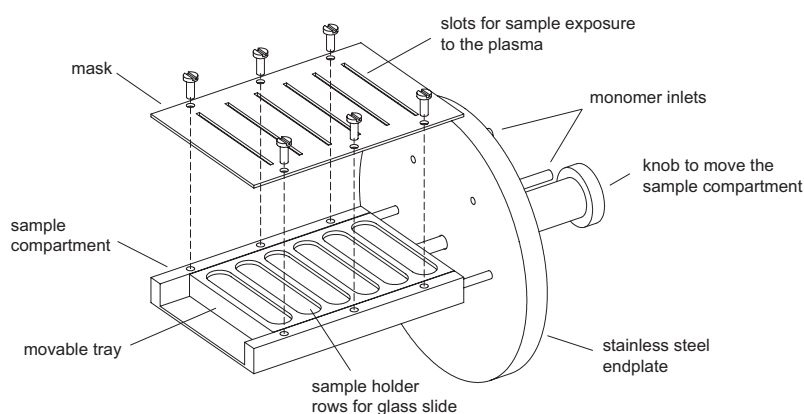
Figure 3.1: Schematic of the gradient tray deposition apparatus used in the preparation of plasma *co*-polymer and exposure time gradients.
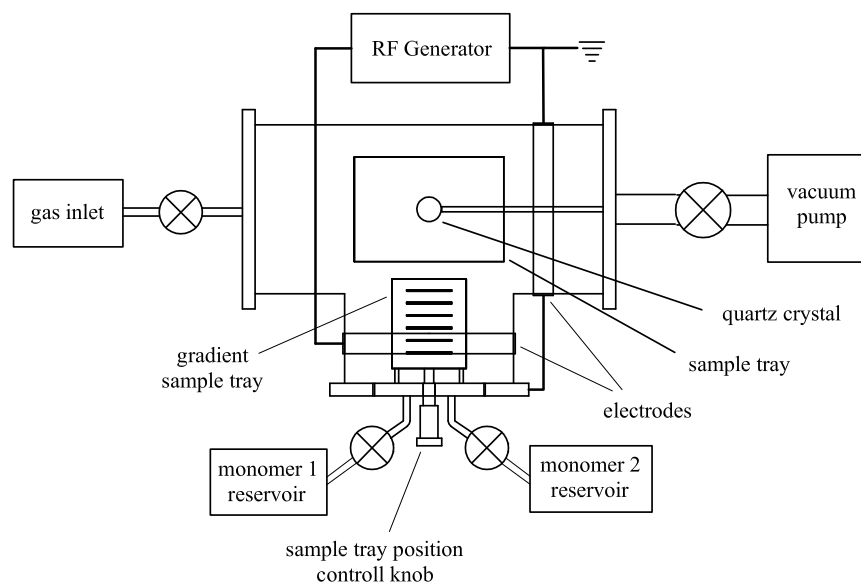
Figure 3.2: Schematic of the plasma deposition chamber for use with the gradient tray.

maintaining a total working pressure of 300 mTorr in the chamber. The samples were moved under the opening incrementally, using different time intervals in different experiments to optimise the transition length and obtain endpoints whose composition is as close as possible to the uniform plasma polymer. The wettability of the gradients was screened with conventional WCA analysis. The results of the most successful approach are shown in FIGURE 3.3 (left), where the sample was moved in 0.5 mm increments every 90 s while the monomer composition was changed in steps from 100% hexane to 100% allylamine. A gradient transition was achieved over 12 mm with a range in WCA of approximately 20°. The WCA on both ends was about 10° lower than on the uniform samples. When the gas composition was changed from 100% allylamine to 100% hexane, the WCA of uniform ppHex was achieved on the hydrophobic side but the other end of the gradient was less hydrophilic than uniform ppAAm. Therefore, diffusion of the depositing species under the mask seems to play a major role on the results obtained with this method. Thus, the formation of deposits on masked areas of the sample due to diffusion caused the surface chemistry of the first monomer to be suppressed by that of the second.

To prepare *exposure time gradients*, method (ii) was used in which the exposure time along the sample was changed incrementally. ppHex was deposited at either increasing (0.25 s/mm) or decreasing (-0.4 s/mm) exposure times on a ppAAm coated sample (FIGURE 3.3, right). Even though the WCA range was improved compared to the *co*-polymer gradients, the gradient transition was very small and only covered 2 - 4 mm.

The *diffusion gradient* method was subsequently developed in an attempt to take advantage of the high penetration depth of depositing species from the plasma under a mask. The ppAAm coated sample was masked with another coverslip that was separated from the surface by a spacer.

Thus, the active species were allowed to diffuse underneath the mask and form a deposit on the sample. The resulting gradient showed a promising WCA profile that had a range of more than 25° and its length scale stretched over 10 mm (FIGURE 3.4), matching the requirements specified before. Diffusion based gradients were therefore further characterised and used in the biological response studies carried out in PART II of this thesis.
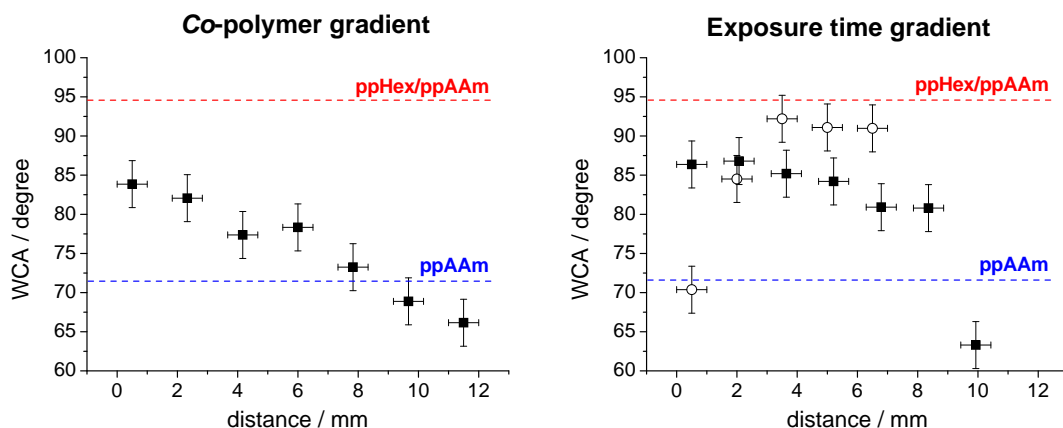
Figure 3.3: Screening WCA-measurements on gradient samples prepared by the *co*-polymer and exposure time method. The graphs show representative data that consists of single measurements along the surfaces using conventional WCA analysis. Exposure time gradients were prepared with either decreasing ■ or increasing ○ exposure times. The error bars are estimated experimental errors. Dashed lines represent the WCA of uniform ppHex deposited on top of ppAAm (ppHex/ppAAm) (red) and uniform ppAAm (blue).
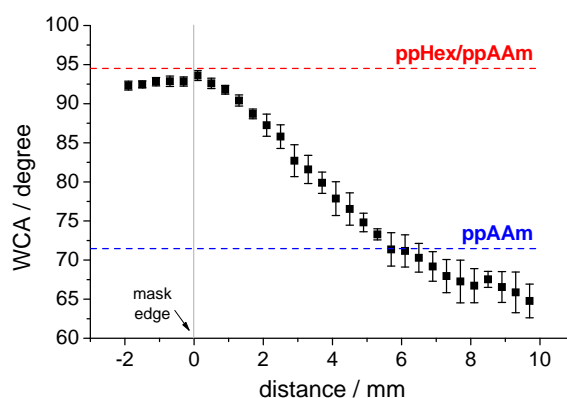
Figure 3.4: WCA profile for the gradient prepared with the diffusion approach. Error bars represent the standard deviation. Dashed lines represent the WCA of uniform ppHex deposited on top of ppAAm (ppHex/ppAAm) (red) and uniform ppAAm (blue).

3.2 Reproducibility of the Coating Procedure

To make a valid comparison between the data obtained from different plasma polymer samples, it is important to ensure that the deposition process is reproducible. Variations in the composition and properties of the plasma polymer coating can either occur due to different deposition parameters (such as temperature, cleanliness of the monomers and the reactor etc.) from one batch to another or depend on the position of the sample in the plasma reactor. The dependance of plasma polymer deposition and specifically the deposition rate on the sample position in the reactor has been pointed out in the literature [39, 114]. While differences between batches are made obvious by comparing data from repeated experiments, variations from samples at different positions inside the reactor have to be investigated in a separate experiment.

To investigate the position dependance of the deposition of ppHex and ppAAm in the plasma reactor used in this work, glass coverslips were positioned in a 5 x 10 matrix on the sample tray as shown in FIGURE 3.5 a; after deposition, water contact angle analysis was employed to asses
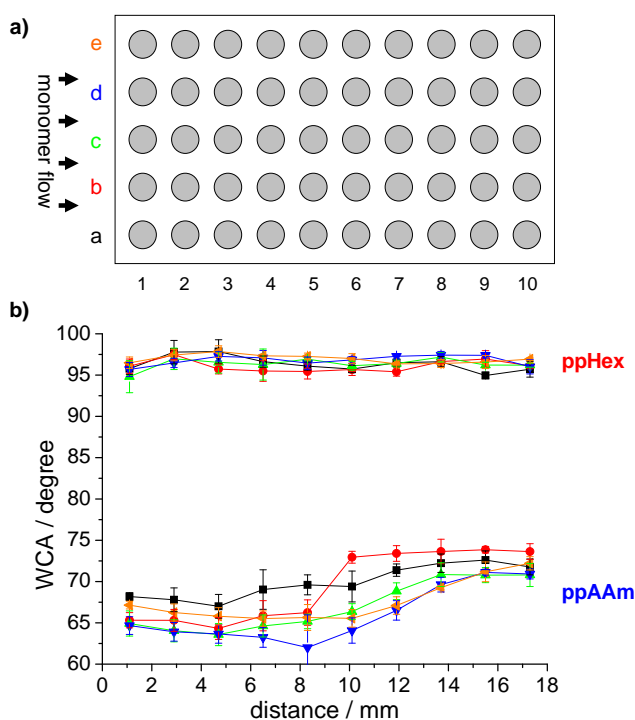
Figure 3.5: Overview of the homogeneity of allylamine and hexane plasma deposition on the sample tray using WCA measurements. (a) Schematic showing a top view of the sample arrangement on the sample tray, ensuring that all samples were situated in between the two electrodes. The monomer gas flows from left to right. (b) WCA of ppHex (top) and ppAAm (bottom) deposits on the samples. The data is an average of 3 measurements on each sample; error bars represent the standard deviation.

the variation of the plasma polymer deposition on the sample tray area. FIGURE 3.5 b shows the change in WCA for ppHex and ppAAm deposits along the flow direction of the monomer obtained at 300 mTorr and 20 W deposited to a thickness of 50 nm on the quartz crystal. While the WCA on the ppHex samples is similar over the whole sample tray area, the ppAAm samples become more hydrophobic the further their position is moved away from the monomer inlet.

In a similar experiment based on three different sample positions in the reactor, Kelly *et al.* reported that the retention of carboxylic acid groups on a plasma polymer deposited from acrylic acid depends on the position of the sample in the reactor [115]. They hypothesized that this could be attributed to the fragmentation of the monomer that increases with the residence of the molecule in the plasma machine.

The observations in FIGURE 3.5 could be related to a similar effect. The allylamine molecules entering the plasma will be activated and subject to increasing fragmentation the further they travel downstream. In addition, it is also plausible that the reactivity of the various monomer fragments in the plasma could contribute to the decreasing hydrophilicity on the ppAAm samples downstream. Since heteroatoms such as the nitrogen in allylamine cause asymmetric electron distributions in the molecule, they are more easily activated and C−N bonds are more easily ruptured than pure hydrocarbon based molecules. Thus, a large amount of activated nitrogen containing fragments is available upstream in the reactor. The fragments are quickly consumed due to reactions with the sample and the wall, so that their amount decreases and less nitrogen containing fragments are available for deposition in the downstream positions. However, a detailed study and explanation of this effect is beyond the scope of this thesis and it is sufficient to note that all ppAAm deposits were prepared in the upstream position on the sample tray to obtain reproducible allylamine plasma polymers with the desired wettability.

3.3 Characterisation of Diffusion Gradients

3.3.1 Linear Diffusion Gradients

3.3.1.1 Sample Format

Since the work in PART II of this thesis is based on (linear) diffusion gradients, a detailed analysis of the surface is required in order to find relationships between the surface properties and the biological response. The preparation of these gradient surfaces is based on the diffusion gradient method introduced in SECTION 3.1.3 and described in detail in APPENDIX E.

The substrate consists of a glass slide that has been uniformly coated with ppAAm. After masking the samples, active species from a hexane plasma diffuse under the mask and form a ppHex layer that gradually decreases in thickness and forms a wettability gradient. Two sample formats will be described in this chapter. The first type is a *steep gradient* with a very short gradient transition, that is achieved by bringing a mask in direct contact with the substrate. The second sample is a *shallow gradient*, that is prepared by separating the mask 0.04 mm from the surface (FIGURE 3.6). The data is compared to uniform samples; as ppAAm control, allylamine was
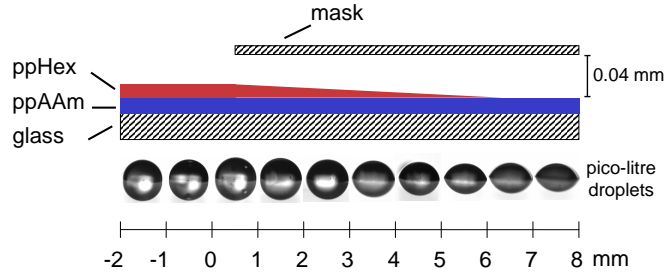
Figure 3.6: Schematic of the linear diffusion gradient. A mask is used to shield the ppAAm coated substrate from the hexane plasma, such that active species have to diffuse under the mask to form a ppHex layer with a gradually decreasing thickness. This produces a wettability gradient as demonstrated with the water droplets placed on the surface.

deposited directly onto clean glass substrates, while ppHex controls were prepared by depositing hexane on top of a ppAAm layer; this sample format will subsequently be labeled ppHex/ppAAm.

3.3.1.2 Wettability

The WCAs measured on these samples are shown in FIGURE 3.7. On the unmasked area (at $x < 0$), where deposition of ppHex could proceed freely, the WCA of both gradient samples is approximately $93°$. The hydrophobic end thus corresponds well to a uniform ppHex/ppAAm sample $(94.5° \pm 0.7°)$. The change in wettability occurred over a distance of 1.5 and 8 mm for the steep and shallow gradient, respectively. This proves that the formation of wettability gradients from surfaces comprised of hydrophobic ppHex to more hydrophilic ppAAm has been achieved. The length of the gradient transition can be controlled by changing the distance between the sample and the mask which will be explored in more detail in a later experiment (CHAPTER 4). Both wettability gradients start at the mask edge $(x = 0)$ and proceed under the masked area (positive x-values). At the more hydrophilic ppAAm side of the samples, WCAs of approximately $60°$ and $66°$ were reached for the steep and shallow gradient, respectively. This is considerably lower than the WCA of uniform ppAAm $(71.5° \pm 0.3°)$ and most apparent on the steep gradient.

The WCAs measured on the uniform samples is in the same range as those reported in literature [16, 112]. The different values of the ppAAm end of the gradient compared to uniform ppAAm is assumed to be related to the incorporation of oxygen-functionalities on the gradient sample which will be explored with XPS data below. Since the ppAAm pre-coating of the gradient sample was prepared under the same conditions as the uniform samples, the change in the surface on the ppAAm side of the gradient must have occurred during or after the gradual deposition of the hexane plasma polymer. For example, non-depositing species could have diffused under the mask, activating the uncoated ppAAm end of the gradient by introducing radicals, rendering it prone to oxidation once exposed to air. In addition, alterations of the deposits by UV irradiation from the plasma is possible.
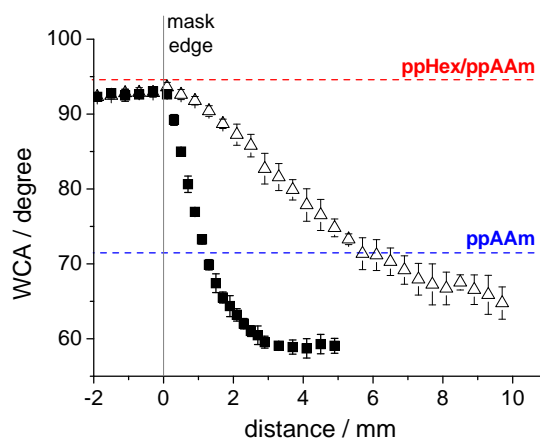
Figure 3.7: Water contact angles on the steep ■ and shallow △ gradients measured with pico-litre sized droplets. The dashed lines show the WCA of uniform ppHex/ppAAm and ppAAm. Error bars represent the standard deviation between 15 measurements from three gradients.

3.3.1.3 Quantification of the Surface Chemistry

Chemical information of the samples was obtained by XPS analysis. Spectra were taken along the gradient transition in lines perpendicular to the edge of the mask in 0.25 mm increments (FIGURE 3.8). Oxygen, nitrogen and carbon but no silicon were detected. The oxygen level was < 2.5 at% and < 10 at% for the steep and shallow gradient, respectively. The presence of oxygen in plasma polymers obtained from oxygen free monomers was reported previously [21, 55]. Gengenbach *et al.* showed that this is related to post-oxidation after the deposition and therefore increases over time [21]. This effect will be explored in more detail in CHAPTER 5 with respect to its implications for biological applications. For the present analysis, samples were analysed within 3 days of deposition to keep the effects of post-oxidation to a minimum.

The functional group composition was determined by fitting curves to the C 1s core level signals (FIGURE 3.9). The assignment of the individual peaks was carried out according to previously published data [31, 56, 60, 116], restricting the full width half maximum of all components to that of the C−C/C−H component at 284.8 eV and fixing the positions of the other components to 285.8 eV (C−N), 286.3 eV (C=N/C−O), 287.9 eV (C(=O)N/C=O) and 288.9 eV (C(=O)O). TABLE 3.2 shows the elemental and functional group composition of uniform samples, the extreme ends of the gradients and the position on the gradient that has a WCA comparable to that of uniform ppAAm. Amides were found on uniform ppAAm (5% of carbon) and the gradients (1 -11% of carbon) and higher amounts of imide and/or alcohol and ester functionalities (2 - 36% of carbon) were detected. No significant differences in functional composition between the uniform ppAAm, the positions on the gradients with a corresponding WCA and the ppAAm end of the gradient were observed that
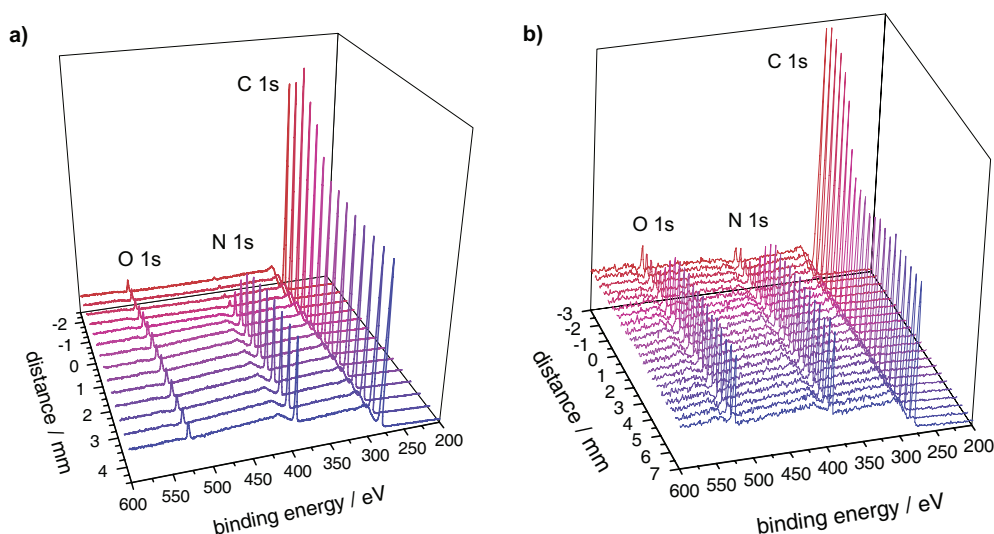
Figure 3.8: Evolution of the XPS spectra along the steep (a) and shallow (b) diffusion gradients (ppHex side: back, red; ppAAm side: front, blue). Every second scan is shown (0.5 mm increments).
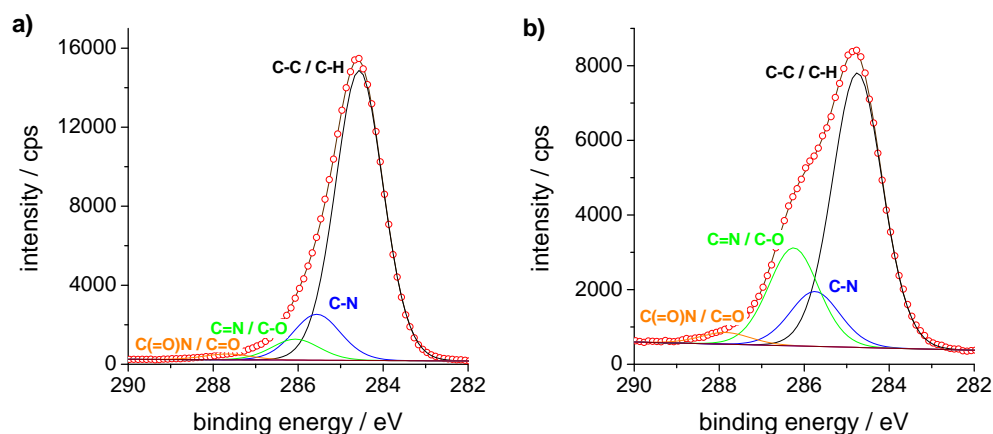
Figure 3.9: Curve fits of C 1s peaks to determine the functional group composition. Shown are typical spectra for the ppHex side (a) and the ppAAm side (b) of the gradients. Measured spectrum: red circles, envelope of curve fits: brown line.

would provide an explanation for the lower WCA on the ppAAm end of the gradient samples. The differences detected by the WCA measurements therefore seem to have their origin in the top layer of the material to which this XPS experiment was not sensitive.

When comparing the amount of nitrogen obtained from the elemental composition with that of the relative amount of nitrogen containing functional groups on uniform ppAAm, there seems to be a discrepancy between the results. While the former suggests that 18% of the carbon atoms on the

Table 3.2: Elemental composition and relative amount of functional groups on the uniform ppHex/ppAAm and ppAAm and the gradient surfaces in atomic %.

	ppHex/	ppAAm	Steep gradient [a]			Shallow gradient [a]		
	ppAAm		-2 mm	1.25 mm	4.5 mm	-3 mm	6 mm	7 mm
Elemental composition								
[C]	98	76	98	82	80	94	73	75
[N]	-	18	0.6	15	18	2.7	17	16
[O]	1.9	5.7	1.6	2.4	2.0	3.2	10	9.3
Functional groups [b]								
C−C/C−H	94	60	91	67	63	87	53	52
C−N *(1.0)*	2.7	2.5	5.7	4.1	13	-	-	-
C=N/C−O *(1.5)*	2.2	32	2.7	25	22	9.3	35	36
C(=O)N/C=O *(3.1)*	0.9	5.4	1.0	3.4	2.5	3.3	11	11
C(=O)O *(4.1)*	-	0.3	-	-	-	0.6	0.8	1.7

[a] The extreme ends of the gradient (left and right columns for ppHex and ppAAm, respectively) and the position with a WCA corresponding to uniform ppAAm (middle column) are shown.
[b] The functional group composition was determined from the C 1s signal (R = H or CH_X). The numbers in parentheses indicate chemical shifts in eV.

surface are bound to a nitrogen atom, the fitted peak attributed to C=N/C−O indicates that – even after considering a contribution from oxygen groups of 5.7% – about 26% of the carbon atoms bear nitrogen functionalities. This apparent contradiction can be explained with the presence of nitriles on the surface. It has been shown before, that C≡N groups in amine containing plasma polymers do not only affect the binding energy of the carbon immediately next to the nitrogen atom, but also shift the α-carbon (**C**−C≡N) next to the nitrile group [117]. This effect also explains the high percentage of C=N/C−O groups, which in reality seem to contain substantial amounts of other nitrogen based functionalities, amongst which nitriles are expected to be the most important.

The elemental N/C concentration ratio calculated from the spectra is plotted in FIGURE 3.10. The majority of the change in the N/C ratio (0 to 0.22) occurred over approximately 2 mm for the steep gradient compared to approximately 5 mm for the shallow gradient, confirming that the shallow gradient stretches over a longer distance.

In the case of the steep gradient, diffusion of ppHex depositing species under the mask (to the right of the x-axis origin) was restricted to approximately 1.5 mm. This indicates that depositing species can, to a small extent, diffuse even under a mask that is in close contact with the substrate. The penetration of depositing and etching plasmas through small pores (up to 10 nm in diameter) has been observed before [118]. In contrast to the steep gradient, the transition of the N/C ratio on the shallow gradient extended to both sides of the sample/mask interface (FIGURE 3.10 b).

The thickness of the ppHex layer deposited on top of ppAAm can be estimated from XPS data. The calculations are based on the attenuation of the nitrogen signal when photoelectrons from the
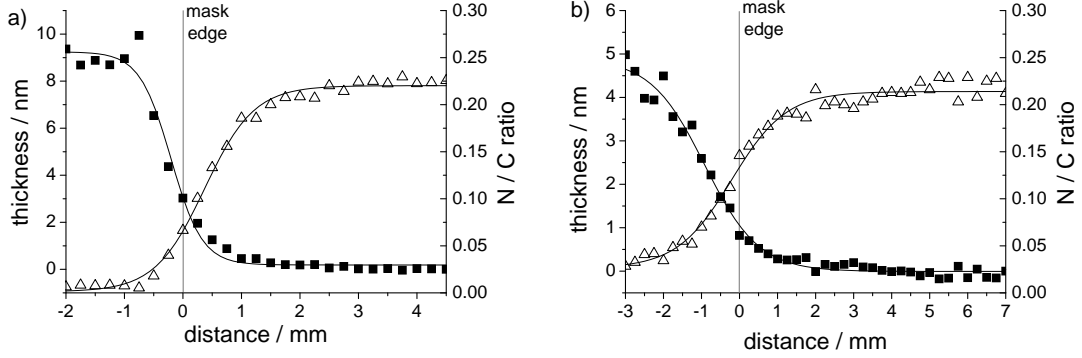
Figure 3.10: N/C ratio △ and thickness profile of the ppHex layer ■ calculated from the XPS data for the steep (a) and shallow (b) gradients (ppHex side: left; ppAAm side: right).

N 1s shell in the buried ppAAm layer travel through the ppHex layer. Based on the *Lambert Beer equation*, the thickness t of the ppHex layer at each position can be calculated according to [119]:

$$t = -\lambda ln\frac{I}{I_0} \tag{3.1}$$

where λ is the inelastic mean free path of the N 1s photoelectrons originating from the buried ppAAm layer, I_0 the N 1s photoelectron intensity of the plain ppAAm underlayer and I the measured intensity of the N 1s photoelectrons. The inelastic mean free path of the N 1s photoelectrons was calculated with the *Tanuma, Powell and Penn formula* (IMFP-TPP2M) [120]. For this calculation it was assumed that the overlayer consisted of carbon only and that the N 1s photoelectrons have an energy of 1080 eV, which results in a value of $\lambda = 2.8$ nm. This approach has been proven to be accurate for a film thickness of up to 10 nm [121].

The thickness of the ppHex overlayer for both the steep and shallow gradients is shown in FIGURE 3.10. On both samples the thickness approached zero towards the ppAAm end of the sample which had been covered by the mask. The ppHex thickness of the unmasked side of the sample was 10 nm and 5 nm on the steep and the shallow gradients, respectively. On the shallow gradient the ppHex thickness decreased in advance of the edge of the raised mask.

At this point, it shall suffice to assume that the transition under the masked area is a result of a diffusion controlled mechanism and the depletion of depositing species. However, the change of the N/C ratio and thickness in front of the mask cannot be explained by this mechanism. CHAPTER 4 will provide a more detailed investigation in the mechanisms involved in the penetration of plasma species through small openings and the subsequent deposition of a plasma polymer film inside pores or channels.

By combining the WCA measurements with the results from the XPS analysis, a relation between the surface chemistry and the wettability of the surface can be established (FIGURE 3.11). An increase in the WCA with the ppHex thickness was observed up to a value of about 0.4 nm.
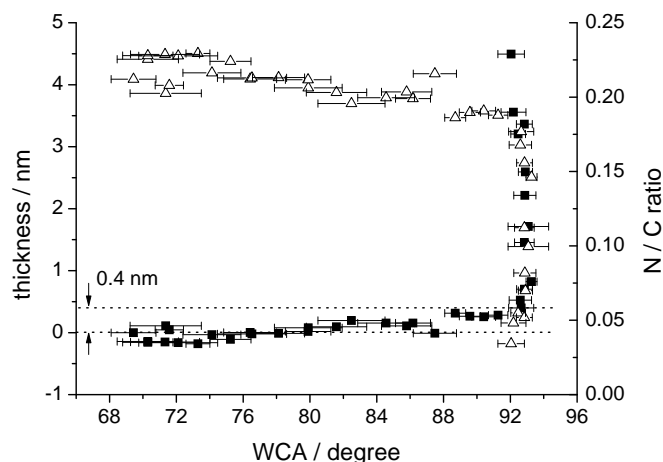
Figure 3.11: Thickness of the ppHex layer ■ and N/C ratio △ as a function of the WCA (ppAAm side: left; ppHex side: right). Error bars show the standard deviation ($n = 15$) for the WCA. The standard deviation for the thickness and N/C ratio was calculated from the experimental error of the XPS measurement and is smaller than the symbols. The main change in WCA occurs within a thickness of 0.4 nm.

For thicker ppHex layers, the WCA was constant and corresponded to the WCA of a uniform ppHex/ppAAm coating. This suggests that the depth sensitivity of the WCA measurements is about 0.4 nm. The variation in WCA along the gradients was therefore achieved by a change of the ppHex thickness from 0 to 0.4 nm. This estimate of the depth sensitivity of the WCA measurement in this system is in good agreement with a study performed by Bain and Whitesides. A closely packed ω-mercapto-ether SAM was prepared where an ether-oxygen atom was 'buried' under alkane chains of different length. In this experiment, the depth sensitivity of contact angle measurements was estimated to be 0.33 - 1 nm [69]. However, since the length scale of the ppHex thickness estimated here corresponds to the dimensions of only a few atoms, it is likely that the ppHex layer forms a patchy film when moving along the gradient and the thickness estimate only represents an average apparent thickness of the ppHex layer.

3.3.1.4 Surface Topography

The topography of the shallow plasma polymer gradient and the uniform samples was investigated by atomic force microscopy (AFM). No features were observed when the samples were imaged in air (FIGURE 3.12). The rms roughness was low and constant along the gradient (0.35 to 0.38 nm, TABLE 3.3). The roughness on the uniform samples (rms of 0.27 ± 0.03 nm and 0.59 ± 0.05 nm for ppHex/ppAAm and ppAAm, respectively) was in the same range as that of the gradient.
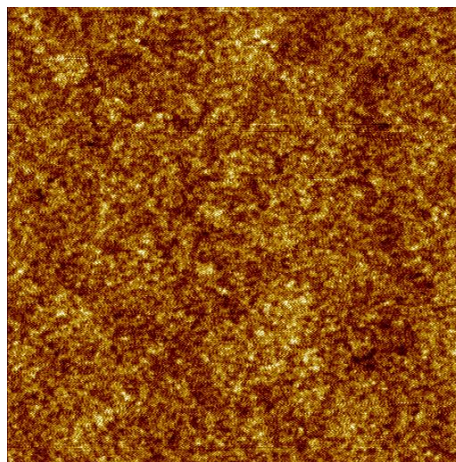
Figure 3.12: Representative AFM micro-graph (10 x 10 μm, z-range: 2.7 nm) of the shallow plasma polymer gradient.

Table 3.3: Route mean square roughness (rms) and average roughness (r_a) of the shallow gradient as a function of distance d (ppHex side: top; ppAAm side: bottom).

d / mm	rms / nm	r_a / nm
-2	0.37	0.29
0	0.36	0.27
2	0.37	0.30
4	0.35	0.28
6	0.38	0.30
8	0.38	0.30

3.3.1.5   Homogeneity of the Surface Chemistry

To investigate the uniformity of the gradient samples, the shallow gradient was imaged with time of flight secondary ion mass spectrometry (ToF-SIMS). The images in FIGURE 3.13 show the surface distribution of positively and negatively charged fragments that were detected. The ppHex side of the gradient is visible in the images of the CH groups as intense white bands to the left; the intensity of the CH fragments then gradually decreases towards the ppAAm side on the right. A reverse trend is observed on the images of nitrogen containing fragments. These results underline the previous data in confirming the formation of a surface chemical gradient.

Besides CH and N containing fragments, oxygen containing ions, Na, Cl, F and Si ions were detected. The Si fragments were attributed to PDMS contamination; the uniform distribution of PDMS over the whole sample suggests that it is not contributing to the gradient attributes of the sample. Oxygen is attributed to post-oxidation as has been noted previously. Its decreased intensity on the ppHex side indicates that oxidation is more important on areas of the sample where the
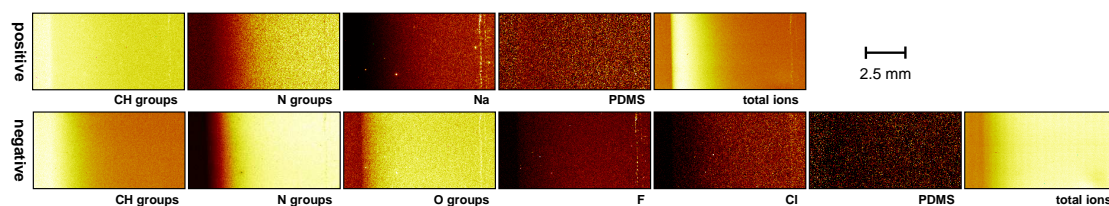
Figure 3.13: Positive and negative ToF-SIMS images of the shallow diffusion gradient. Hydrocarbon, nitrogen and oxygen containing fragments have been combined to give images of CH-groups, N-groups and O-groups, respectively. Silicon containing fragments were detected which were typical for PDMS. Image size: 9.3 x 4.65 mm. The data in all images has been normalized to the total ion count. ppHex side: left; ppAAm side: right.

ppAAm layer is not covered by ppHex. Na, Cl and F ions are not detected on the ppHex side, but show a gradual increase towards the ppAAm side, suggesting that they are linked to the ppAAm layer, as well. Therefore, the presence of these ions is assumed to be related to reactions of the nitrogen groups with contaminants from air after deposition due to the activation of the ppAAm layer during the ppHex deposition. This would also explain the decrease in WCA on the ppAAm side of the gradient compared to the uniform ppAAm samples.

It is also important to point out that the distribution of all fragments is uniform in the direction perpendicular to the gradient. This shows that a change in surface chemistry occurs linearly in one single direction on the sample.

The current chapter only deals with the analysis of freshly deposited plasma polymer gradients. For the biological studies presented in PART II of this thesis, the surface properties in an aqueous environment will also be of relevance. A more detailed study of surface changes under aqueous conditions – in particular the surface topography of plasma polymer gradients and uniform plasma polymer samples – can be found in CHAPTER 5.

3.4   Summary

Hexane and allylamine have been identified from data in the literature as suitable precursors for plasma polymers used in *in vitro* cell culture. To prepare linear gradients from the plasma polymers, three methods have been explored that were classified as

- *Co*-polymer gradients

- Exposure time gradients and

- Diffusion gradients

The method of *co*-polymer gradients was previously reported as the first technique that has been used to prepare plasma polymer gradients. In the present system, though, it showed a limited

range in WCA, while the exposure time gradient method was limited in its transition length. Both methods seemed to be affected by the ability of depositing species from the plasma to penetrate through very small gaps. This property was turned into an advantage by intentionally allowing the plasma to penetrate underneath a fixed mask placed at a set distance from the sample surface. This diffusion based method yielded gradients with a broader range in WCA over distances of several millimeters that can also be readily adjusted.

The surface of a steep and shallow diffusion gradient where ppHex was deposited as a gradient on top of uniform ppAAm was extensively characterised with WCA, XPS, AFM and ToF-SIMS. WCA, XPS and ToF-SIMS confirmed the formation of a surface chemical gradient. The gradient transition was most pronounced in the WCA profile where it stretched over 8 mm from 93° to 66° on the shallow diffusion gradient. Comparison with control samples demonstrated that the extreme ends of the gradient are mostly similar to uniform samples, with the exception of the WCA, which is lower on the ppAAm side of the gradient than on uniform ppAAm. The thickness of the ppHex layer on top of ppAAm could be estimated using calculations based on the XPS measurements. In addition, a comparison of the thickness profile of the gradient with the WCA allowed an estimate of the depth sensitivity of the WCA measurements, which was found to be ~ 0.4 nm. AFM images acquired along the length of the gradient demonstrated that the deposit showed no features and was very smooth.

The uniformity of ppHex and ppAAm deposit formation in the plasma reactor was investigated to ensure that comparison between samples is valid. ToF-SIMS imaging showed that the gradients are laterally uniform.

Chapter 4

Plasma Diffusion

4.1 Gradient Formation in Channels

4.1.1 Plasma Polymerisation in Small Channels and Pores

The diffusion based preparation of gradient surfaces from plasma polymers is a new concept that has not been exploited before. In order to gain good control of the process, it is essential to understand the underlying mechanism of diffusion and polymerisation of plasma species through small openings.

The analysis of processes inside the plasma is challenging, not only because of the complex nature of the plasma, but also because of the plasma sheath that forms at material surfaces in the plasma, including sensors and probes designed to analyse the plasma. Since the properties of the plasma sheath are different from the bulk plasma, one may assume that polymerisation in the bulk gas phase is substantially different from polymerisation in the gas phase of the sheath and at the surface of the sample. The general plasma polymerisation mechanism is still not well established, but it is known to be dependent on the deposition parameters and the chemical composition of the monomer. Initial studies demonstrated the importance of neutral species for the plasma polymerisation process [13], while later on evidence for the contribution of positive [122] and recently also negative ions has been reported. Even though the ability of plasma species to penetrate through small pores has been noted before [8, 118], the polymerisation mechanism within these pores remains subject to speculations.

In this paragraph, a sample format will be used that allows a more systematic study of the penetration of plasma species from a hexane plasma through geometrically well defined model structures. Channels with square cross sections of various sizes will be used to simulate pores. This will allow the establishment of a correlation between the channel cross section and the transition length of the gradient.

4.1.2 Experimental Design

Pore like channel structures with different cross sections were prepared by pressing a glass slide against a mask which contained five preformed channels that were open at the bottom and on one end. The glass slide was precoated with ppAAm (FIGURE 4.1 a). The mask was placed on top of the ppAAm coated glass slide (FIGURE 4.1 b) to form channels with cross sections of 0.25, 0.5, 1, 2 and 5 mm. The masked sample was subsequently exposed to a hexane plasma (FIGURE 4.1 c) which resulted in the formation of five ppHex gradients of different length on top of the ppAAm coated glass slide (FIGURE 4.1 d).
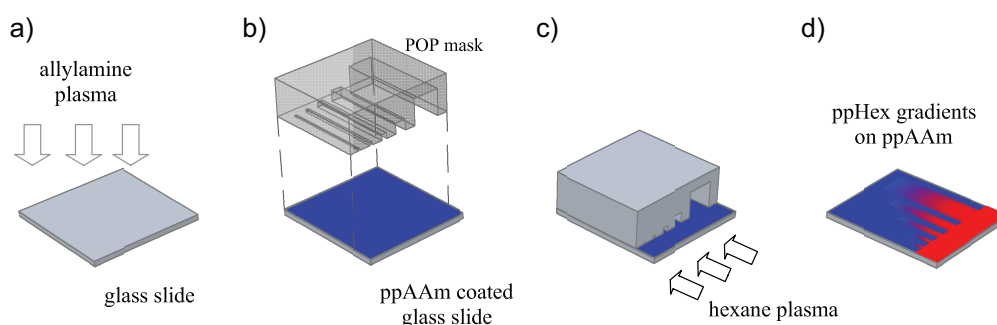
Figure 4.1: Schematic of the experimental setup to study the plasma deposition through diffusion down pores. ppAAm (blue) is deposited uniformly on a glass substrate (a). The POP mould is placed on top of the ppAAm coated sample (b) which is subsequently exposed to a hexane plasma (c) resulting in the formation of ppHex gradients (red) of different length (d).

4.1.3 Gradient Characterization

4.1.3.1 Surface Wettability

The wettability of the surface was analysed with water contact angle (WCA) measurements using pico-litre water droplets. By taking single measurements in 0.25 mm increments over the whole sample a WCA map of the surface was obtained (FIGURE 4.2 a). The WCA map shows the presence of five wettability gradients of different length that were formed in the area inside the channels. The wettability decrease from hydrophobic ppHex (red, left) to more hydrophilic ppAAm (blue, right) down the channels is steepest on the 0.25 mm wide area. Areas that were in direct contact with the mask mostly maintained the lower WCA of ppAAm ($\sim 66°$), although some loss of pattern fidelity was observed for the larger channels. This was attributed to diffusion of depositing species in between the mask and the substrate.

FIGURE 4.2 b shows WCA line profiles for all five gradients that were obtained by averaging the WCA data from each channel. The drop off in WCA is steepest in the smallest channel (transition over a length of 6 mm) and decreases at a slower rate for the wider channels. For the three larger channels the WCA drop off rate is very similar. At the closed end of the channel the WCA

of ppAAm is only attained on the smallest (0.25 mm) gradient which illustrates the penetrative nature of active species from the hexane plasma.

The change in WCA for each gradient expressed as the slope of the WCA profile was plotted as a function of the channel size in FIGURE 4.2 c. From this graph it can be seen that the WCA change
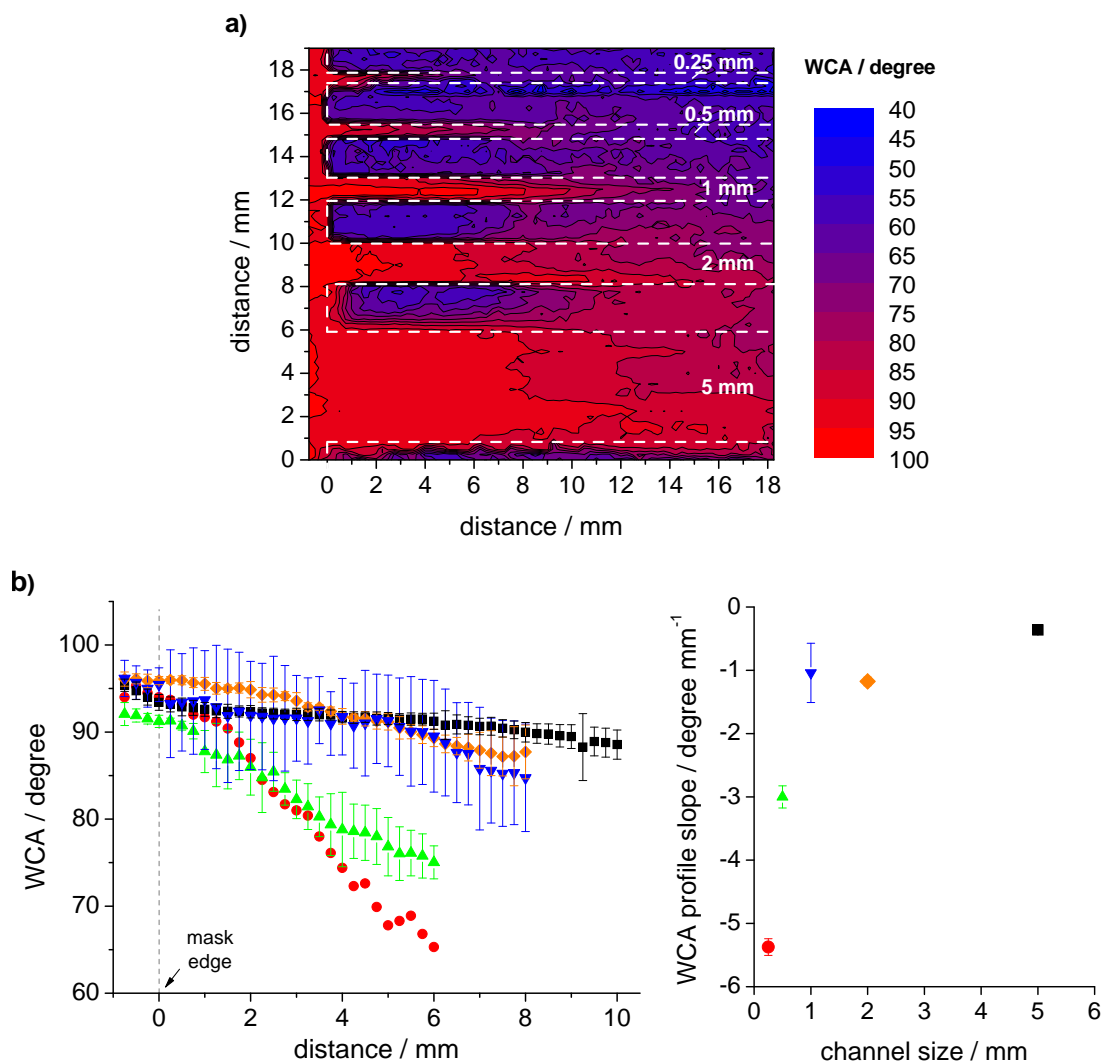
Figure 4.2: WCA map and WCA profiles of the gradients formed by plasma diffusion through small openings. a) Mapping data was acquired in 0.25 mm increments. The opening of the channels was on the left while the monomer flowed from left to right. The white dashed lines outline the channels and indicate the contact area of the mask with the surface. b) WCA profile of the 0.25 (●), 0.5 (▲), 1 (▼), 2 (♦) and 5 mm (■) channels averaged from the WCA-map data ($n = 1, 3, 5, 8$ and 22, respectively). c) Slope of the WCA profile of the gradient from a linear regression of the data at $x > 0$ plotted against the channel size. Error bars represent standard deviations.

was steepest in the smallest channels but quickly decreases when the channel size became larger. The WCA change was similar for the two larger channels and appeared to level off for channels larger than 5 mm.

4.1.3.2 Visualization of the Surface Chemical Gradients

ToF-SIMS analysis of positively charged fragments was used to obtain images of the spatial distribution of surface chemistries on the sample. In the ToF-SIMS spectra, hydrocarbon (C^-, CH^-, C_2^-, CH_2^-, C_2H^-), nitrogen (NH^-, CN^-, CHN^-), oxygen (O^-, OH^-) and low intensities of fluorine and silicon ions (not present in the displayed range) were identified (FIGURE 4.3). These fragments were grouped together and are shown as images of the surface chemistry distribution in FIGURE 4.4. The result is similar to what has already been reported in SECTION 3.3.1.5, showing an increase in N and a decrease in CH groups from the ppHex (left) to the ppAAm side (right) on all five gradient. In addition, the images show that the length of the gradient transition becomes larger as the cross-section of the channels increases.

The hydrocarbon and nitrogen ions are good indicators for the ppHex and ppAAm coated areas, respectively. A compilation of both groups shown in FIGURE 4.4 F demonstrates that the intensity of the CH-groups increases gradually down the channels (from left to right), suggesting that, as the top ppHex layer gets thinner, the surface gets richer in nitrogen functionalities from the buried ppAAm layer.

Signals from oxygen containing fragments were attributed to nonspecific post-oxidation of the plasma polymers [21, 25] and were therefore not useful in discriminating between the ppAAm and ppHex coated areas (FIGURE 4.4 A). Si was attributed to PDMS contamination. This was most likely transferred to the sample by the POP mask, despite the efforts to exclude such contaminations
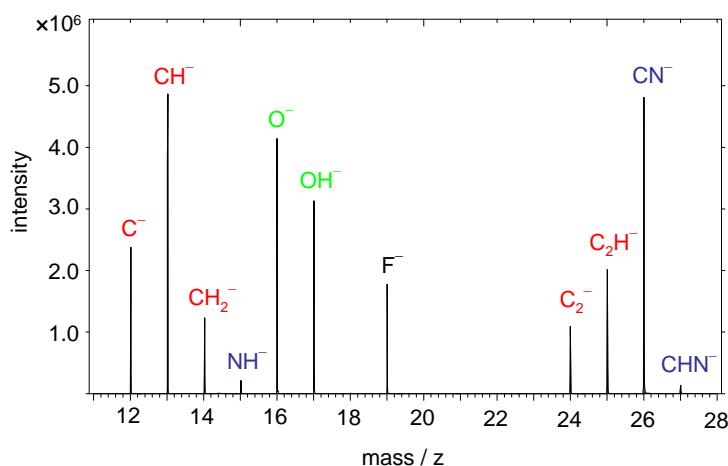
Figure 4.3: Representative ToF-SIMS spectrum from the gradients formed inside the channels. The peaks used for the images of oxygen, nitrogen and hydrocarbon groups in FIGURE 4.4 are labeled in green, blue and red, respectively.
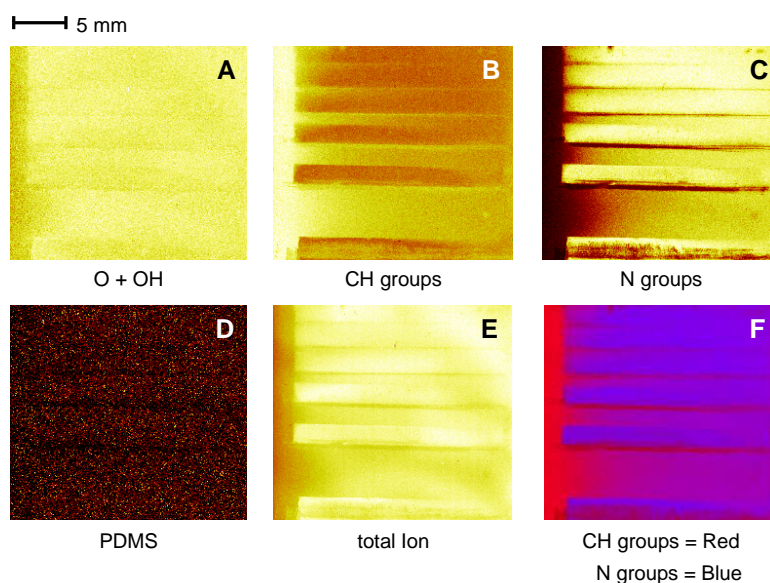
Figure 4.4: ToF-SIMS images of gradients formed by plasma diffusion through small openings. The open side of the channels faced towards the left, with the gradients proceeding from left (ppHex) to right (ppAAm). The cross section of the channels increases from top (0.25 mm) to bottom (5 mm). Negatively charged fragments containing oxygen (A), nitrogen (B) and purely hydrocarbon (C) were grouped together. Silicon containing fragments were attributed to PDMS (D). All data was normalized to the total ion intensity. The distribution of N (blue) and CH groups (red) relative to each other is shown in image (F).

during the fabrication of the mould. However, the PDMS distribution is mostly uniform on the sample (FIGURE 4.4 D), so that it can be assumed that its influence on the spatial distribution of the other groups is negligible.

When the WCA map is compared qualitatively to the image obtained from ToF-SIMS, it can be seen that a decreasing wettability corresponds to areas with an increasing amount of apolar CH groups, while the presence of polar nitrogen functionalities relate to an increase in wettability. These complementary results confirm that the wettability gradient is linked to the gradient of surface chemistry.

4.1.3.3 Quantification of the Surface Chemistry on the Gradients

The chemical composition of the sample was analysed with small area XPS in lines along the gradients and in front of the mask. FIGURE 4.5 shows typical spectra of the binding energy regions of interest from all five gradients at 2 mm intervals starting at the beginning of the channel ($x = 0$ mm). Carbon, oxygen and nitrogen but no silicon were detected on the surface. The oxygen content was low and constant (< 4 at%); in accordance with previous interpretations it was attributed to postoxidation. The fact that no Si was detected (the sensitivity of ToF-SIMS is much higher than that of XPS) confirms that the level of PDMS contamination is low.
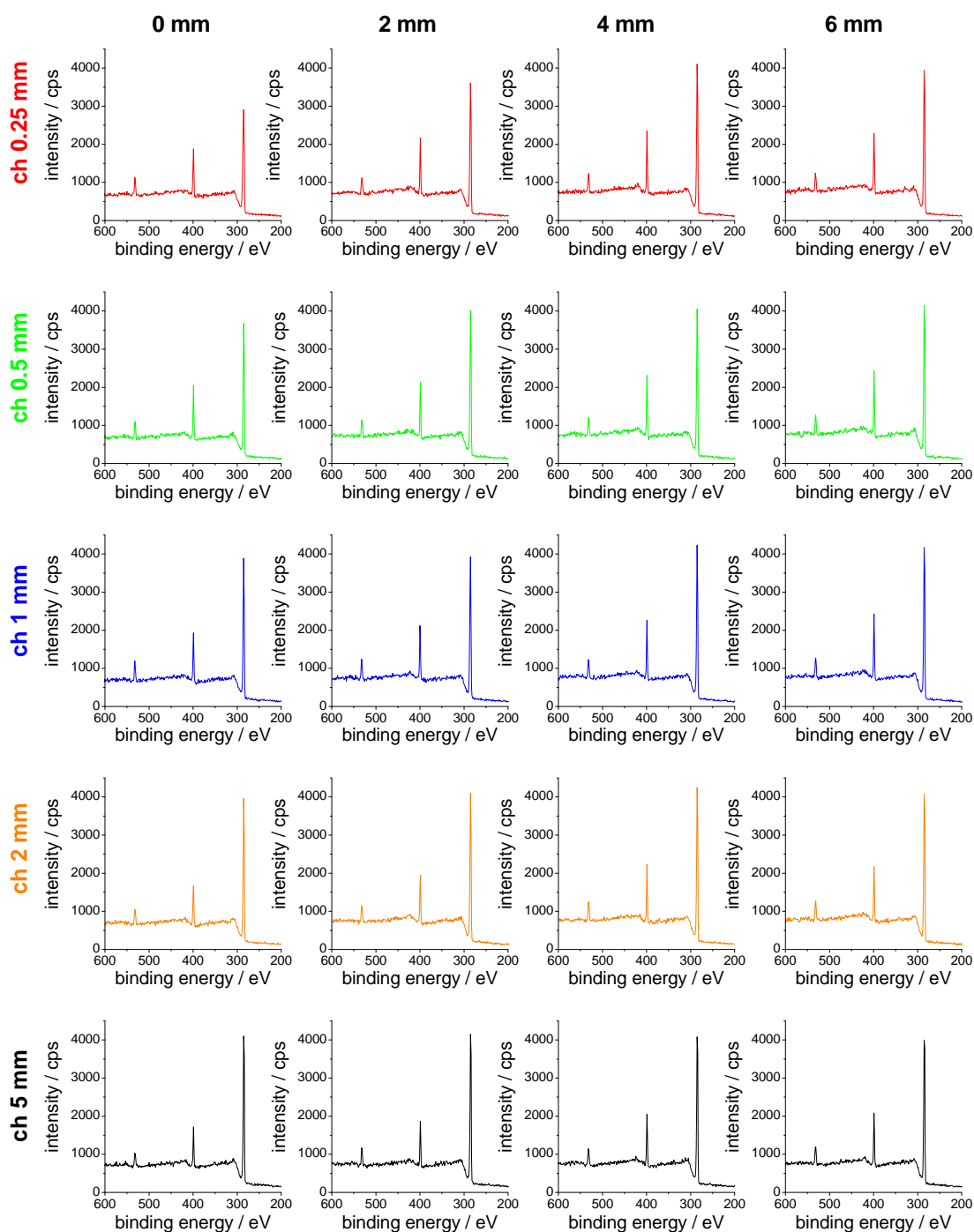
Figure 4.5: XPS spectra of selected positions on the gradients formed underneath the channels. The gradient transition starts at $x = 0$ (ppHex side: left; ppAAm side: right). For better display, the binding energy region has been reduced to 200 - 600 eV, where C (284 eV), N (399 eV) and O (532 eV) were detected.
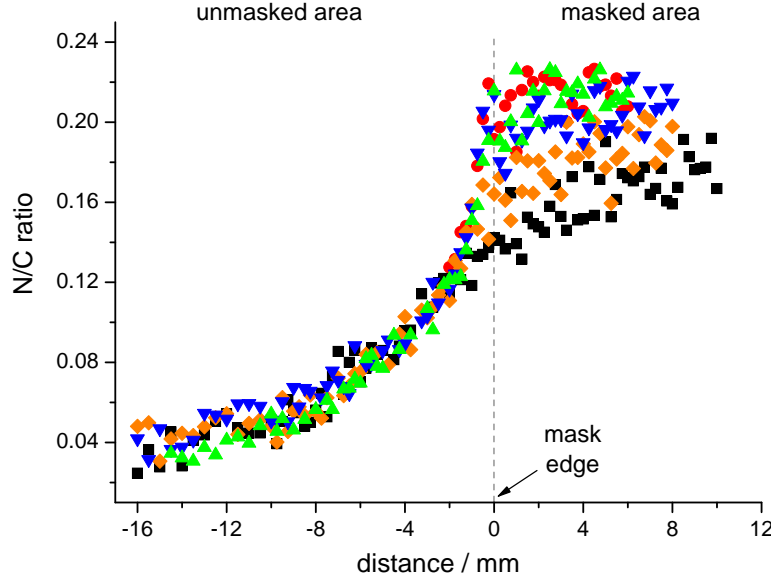
Figure 4.6: N/C ratio of the gradients formed inside the channels as determined by XPS. ● 0.25 mm, ▲ 0.5 mm, ▼ 1 mm, ◆ 2 mm, ■ 5 mm. ppHex side: left; ppAAm side: right.

On all gradients a slight increase in the relative amount of nitrogen could be observed along the gradient which is most visible on the 0.25 mm gradient. The carbon intensity is very similar in all spectra except for the 0.25 mm gradient, where it increases along the channel. This variation in the C 1s signal intensity could be explained with misalignments of the X-ray beam on the sample due to the small dimensions of the gradient and is reflected in the larger variation of the XPS data of the 0.25 mm channel compared to the data from the other channels.

A good indicator of the progress of the gradient transition is the N/C-ratio plotted in FIGURE 4.6. In the masked area ($x > 0$ mm), the gradient transition from ppHex to ppAAm is reflected by an increase in the N/C ratio that is moderate and proceeds over a long distance (several millimeters) on the 5 mm gradient. The further the cross section of the channels is reduced, the shorter and steeper the N/C ratio profile becomes before leveling off.

Besides displaying data from the area covered by the mask FIGURE 4.6 also shows the area in front of the mask at ($x < 0$ mm). Here the most interesting feature is that the N/C ratio profile continuous to drop for a long time when moving away from the mask instead of leveling off immediately in front of the mask as would be expected from a uniform ppHex coating on an unmasked sample. The N/C ratio first drops sharply for about 2 mm and then continuous to drop at a decreasing rate over a distance of about 14 mm in front of the mask before it starts to approach a constant level.

While the N/C ratio profile in the masked area where diffusion is supposed to take place does not come as a surprise, the long and significant drop off phase in front of the mask was unexpected.

There is no physical obstruction in this area that would cause a change in the profile. Moreover, the flow rate of the monomer is relatively low, so that inhomogeneities in the concentration of active species over such a large distance seems unlikely. In the following section, these results will be further discussed by developing theoretical models to explain the measured effects in front of the mask.

4.2 Physical Description of Plasma Diffusion in Channels

4.2.1 Deposition Rates on the Sample Surface

To further understand the processes involved in the ppHex deposition inside the channels and in front of the mask, the deposition rate of the ppHex deposit for each line profile is compared and set in relation to the channel size. In SECTION 3.3.1.3 it was shown that the gradient of ppHex formed by the diffusion of plasma species through small openings is actually a gradient of decreasing thickness that can described on the basis of XPS data.

The thickness for each line profile was calculated as described in SECTION 3.3.1.3. It was then converted into a nominal deposition rate based on the total time during which the ppHex was deposited on the sample. A graph showing the ppHex deposition rate as function of the distance along all five channels is shown in FIGURE 4.7 a. Three different zones were identified in the deposition rate profiles. Most notably, a change in the deposition rate started more than 16 mm in advance of the mask. In this area (*zone I*) the ppHex deposition rate decreases gradually up to 2 mm in front of the opening of the channels regardless of their cross section. This is followed by a more drastic change in deposition rate immediately before the opening where the steepness of the deposition rate decrease depends on the channel dimensions (*zone II*).

The deposition rate inside the channel (*zone III*) was modeled to a logarithmic decay (inset in 4.7 a):

$$r = r_0 e^{-kx} \tag{4.1}$$

with r = deposition rate, r_0 = initial deposition rate, x = distance and $k \cong 0.5$ mm^{-1}). A linear regression is placed through the dataset of each channel, showing that the slope (k) is similar for all five gradients and demonstrating that the total decrease in deposition rate of ppHex decreased at similar rates in each channel. The different gradient transition lengths in the channels is caused by different initial deposition rates r_0 at the beginning of each gradient.

To investigate the possibility that the decrease in deposition rate in *zone I* is the result of flow effects in the plasma, a control experiment was carried out with a ppAAm coated sample that was in contact with a plain POP object (FIGURE 4.8). This control sample was placed at the same position as the gradient sample in the bulk plasma; the analysed surface, however, faced away from the monomer inlet. XPS spectra were taken along a horizontal and a vertical line on the control sample. The deposition rate profile in advance of and underneath the object was similar to the
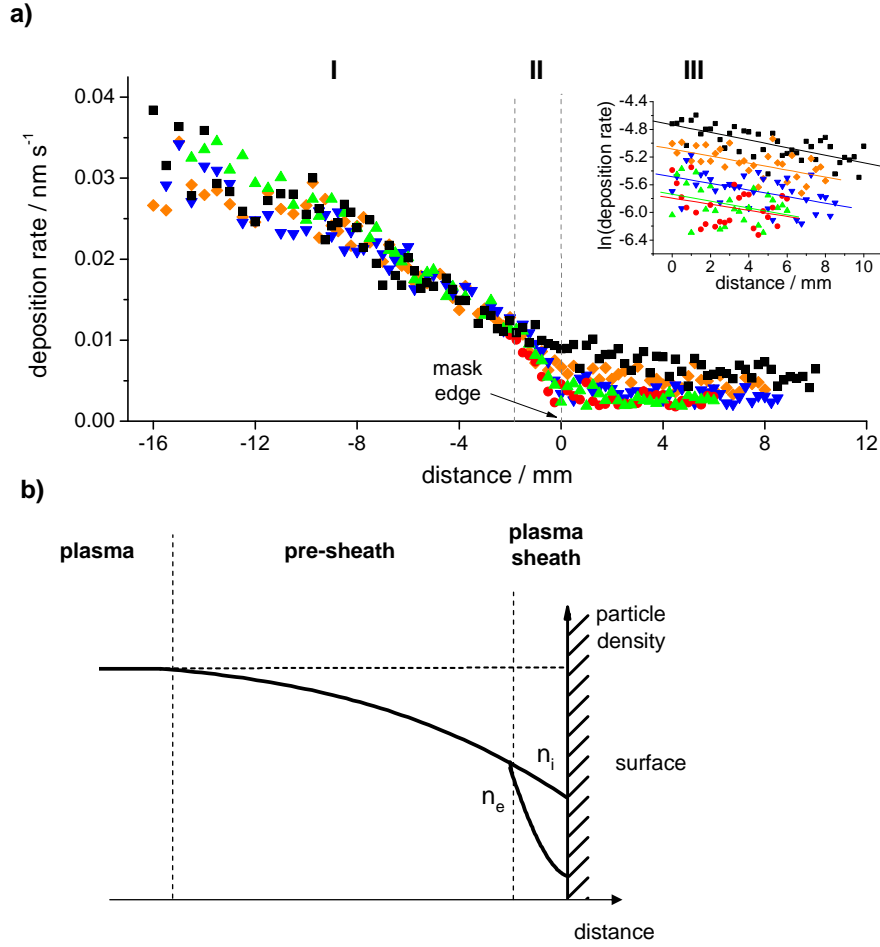
Figure 4.7: Deposition rate profile of the ppHex layer for the gradients in the 0.25 (●), 0.5 (▲), 1 (▼), 2 (♦) and 5 mm (■) channels calculated from the XPS data (a). The obtained deposition rate profile decreases already in front of the mask, dropping sharply within the last 2 mm. This profile corresponds to the change of electron (n_e) and ion (n_i) densities in the plasma sheath (b, adapted from [35]). The inset in (a) shows the natural logarithm of the deposition rate inside the channels.

one measured on the two smallest channels (FIGURE 4.9). Therefore, the flow of plasma species in advance and over the mask can not explain the deposition rate profile in *zone I*. Another possible explanation could be based on the effect of a non-equilibrium plasma area or *plasma sheath* which is the result of an electrical response at the surface of any object located within the plasma.

In a first step to support the hypothesis that the plasma sheath reduces the deposition rate in front of the mask, the experimental deposition rate profile was compared with qualitative descriptions of ion and electron densities (n_i and n_e) in the plasma from the literature (FIGURE 4.7 b) [35]. The deposition rate profile is similar to the density distribution of ions and electrons in
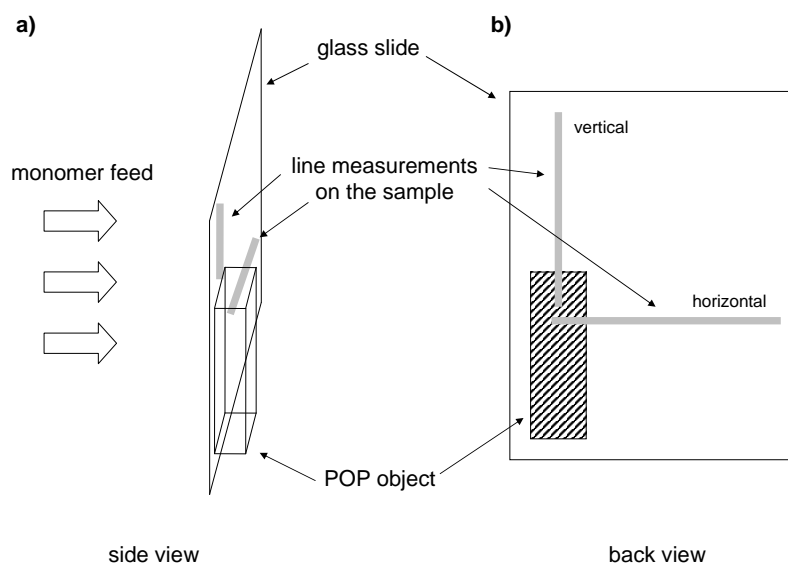
Figure 4.8: Experimental setup to study flow effects on the deposition rate in front of an object. The ppAAm coated sample carrying a POP object on its surface was placed in the plasma reactor such that the coated side faced away from the hexane feed (a). XPS measurements were taken along two perpendicular lines in advance and across the area masked by the object (b).
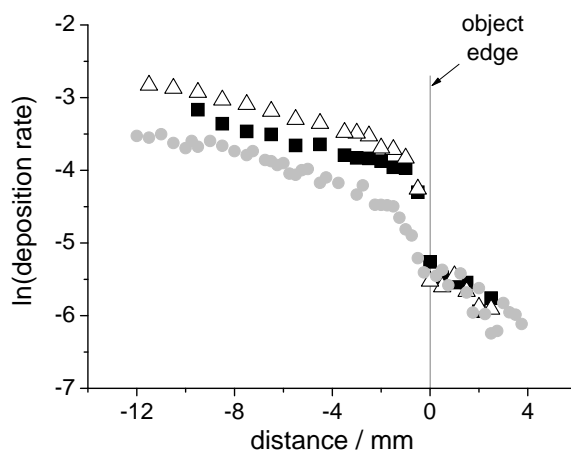
Figure 4.9: Natural logarithm of the deposition rate from a hexane plasma on the control sample calculated from XPS measurements. The profile of the 0.5mm gradient is also shown for comparison. Positive x-values correspond to the masked area while negative x-values relate to the area in advance of the object. △ vertical, ■ horizontal, ● 0.5 mm gradient.

the (positively charged) plasma sheath area present at the surface of an electrically floating object within the plasma. In the present case of a surface masked by another object, two perpendicular surfaces are created and thus the present observations relate to a sheath created at the surface of the object lying in the plane perpendicular to the analyzed surface.

For both the ppHex deposition rate and the ion density in the sheath the profile drops in two stages; first at a moderate slope over a longer distance which is followed by a more rapid drop in the close vicinity of the surface. These two regions in the particle density distribution are referred to as the pre-sheath and plasma sheath, respectively and match with *zone I* and *II* of the deposition rate profile. It is therefore proposed that this experiment shows the effect of a plasma sheath on the deposition rate of a plasma polymer on the surface.

4.2.2   Theoretical Plasma Sheath Dimensions

In order to quantitatively investigate the hypothesis that the electron depletion in the sheath correlates with the deposition rate, the thickness of the plasma sheath in the system will be estimated in this section and compared to the experimental data.

The sheath thickness s can be expresses as a function of the Debye length (λ_{De}) [35]:

$$s = \lambda_{De} \left(\frac{eV_s}{kT_e} \right)^{3/4} \tag{4.2}$$

where V_s is the sheath potential (the potential difference between the surface and the sheath edge) and T_e the electron temperature, k the Boltzmann constant and e the electron charge. Although it was not possible to measure V_s in the present system, V_s is usually large compared to kT_e/e. For an electrically floating sheath containing ions with a mean ion mass m_i and an electron mass m_e, V_s can be calculated according to

$$V_s = \frac{kT_e}{2e} Ln \left(\frac{m_i}{2\pi m_e} \right) \tag{4.3}$$

Thus, if $m_i = 1.43 \cdot 10^{-22}$ g (MW_{Hexane}/N_A) and the electron temperature is estimated to be $kT_e/e = 2 - 3$ V ($2 \cdot 11,600$ K to $3 \cdot 11,600$ K) then V_s is about 10 to 15 V. The sheath thickness can therefore be assumed to be 5 to 15 Debye lengths.

When the electron density is assumed to be $n_e = 1 - 5 \cdot 10^{15}$ m^{-3} [123], the Debye length can be calculated according to [39]:

$$\lambda_{De} = \left(\frac{\epsilon_0 kT_e}{e^2 n_e} \right)^{1/2} \tag{4.4}$$

where ϵ_0 is the permittivity of free space. Thus, the Debye length is between 0.15 mm $< \lambda_{De} <$ 0.41 mm. The estimated sheath thickness is therefore in the range of 0.7 mm $< s <$ 6 mm, which is comparable to the length scale of *zone II* in Figure 4.7 a, that describes the rapid drop of the ppHex deposition rate in front of the mask. Further, we can assume that *zone I* in the ppHex deposition rate profile relates to the pre-sheath, which can stretch over several centimeters in length.

The size of the pre-sheath is harder to estimate, because it is determined by a number of physical mechanisms such as ionization, mean-free path, collisional mean-free path and the geometry of the object.

The similar length scales of the experimental drop in deposition rate and the theoretical sheath thickness supports the hypothesis that the drop in deposition rate in advance of the mask is a result of the plasma sheath on the surface which is responsible for a gradually changing composition of the plasma along the surface towards the mask.

It can be concluded that the deposition rate of ppHex within small channels depends on the plasma sheath and its thickness at the channel opening, a factor directly influenced by the cross section of the opening. In particular, the relative dimensions of the sheath and the opening will determine whether the plasma is excluded from the channel or not. In the present case of a sheath of approximately 2 mm thickness, all but the 5 mm channel are completely enclosed by the plasma sheath. The formation of the sheath causes negative species – mainly electrons – to be repelled, while positive ions are accelerated from the plasma to surface potential. Neutrals should be unaffected by the sheath if their mean free path for a collision with ions is larger than its thickness. In the case of channels with different cross sections, negatively charged depositing species therefore have to travel through an increasingly efficient sheath barrier as the opening of the channel gets smaller. This reduces the concentration of active species both at the sample surface just in front and underneath the mask since electrons are responsible for the formation of all reactive plasma species from the monomer molecules in the collision cascade. In pores of sufficiently small dimensions (i. e. the 0.25 and 0.5 mm openings in this experiment) negative plasma species are almost completely excluded as has been experimentally proven in SECTION 4.3.

4.2.3 Plasma Diffusion Model

Significant ppHex deposition is seen inside the channels in *zone III*. This is attributed to downstream plasma deposition caused by species that are able to diffuse down the channels. In a system where the dimension of the channel cross section is smaller than the mean free path of the molecules, one would assume that the *Knudsen diffusion* model is able to describe the system [124, 125]. In this model, the depositing species diffuse down the channels and frequently collide with the wall where deposits will be formed. In this model the unknown sticking coefficient is assumed to be close to 1 for this system, i.e. all molecules that collide with the wall remain at the surface and are thus taken out of the gas phase. If the cross section of the channel decreases the collision frequency with the wall increases for a given mean free path. The ratio between the surface area of the wall and the volume of the gas phase increases as the cross section decreases and hence depositing species would be lost to the wall more rapidly in smaller channels, causing the drop off rate of the ppHex deposition rate to increase. To establish if this model is applicable to the present system, the mean free path λ of the neutral species in the plasma as calculated according to:

$$\lambda = \frac{1}{\sigma n_0} \tag{4.5}$$

where σ is the cross section of collision and n_0 the neutral particle density. For an operating pressure of 300 mTorr (40 Pa), $n_0 = 10^{22}$ m^{-3}; with $\sigma = 5 \cdot 10^{-20}$ m^2 for hexane, $\lambda = 2$ mm. Thus, all but the 5 mm channel would meet the requirements needed for the Knudsen model to be applicable and should show different drop off rates in the ppHex deposition rate for the four smaller channels. According to this model, the natural logarithm of the ppHex deposition rate was plotted against the distance inside the channels (inset in FIGURE 4.7 a), showing that the deposition rate decreases in all five channels at approximately the same rate. Thus, even though the present system meets the length scale requirements, fitting the deposition rate profile to a Knudsen diffusion model did not provide a satisfactory description of this experiment. Deviations from the assumed value for the sticking coefficient or errors in the estimation of the mean free path – for example because positively charged species are involved in the deposition process – could account for the difference.

The deposition mechanism inside pores and on the surface of an unmasked sample could be very different. In the literature, a radical based mechanism has often been proposed for plasma polymerisation [13]. Here, it was shown that in small pores negatively charged fragments do not contribute to the deposition mechanism. On the unmasked area of the sample, two different mechanisms are proposed to explain the decrease in ppHex deposition rate. Both are based on the assumption that the properties of the plasma, in particular its density immediately above the surface are directly related to the rate of deposition on the substrate. This is only possible if the collisional mean free path of the species involved is smaller than the scale over which the plasma density varies, such that only particles in the close vicinity to the surface are likely to collide and react with it; this has already been shown to be the case above.
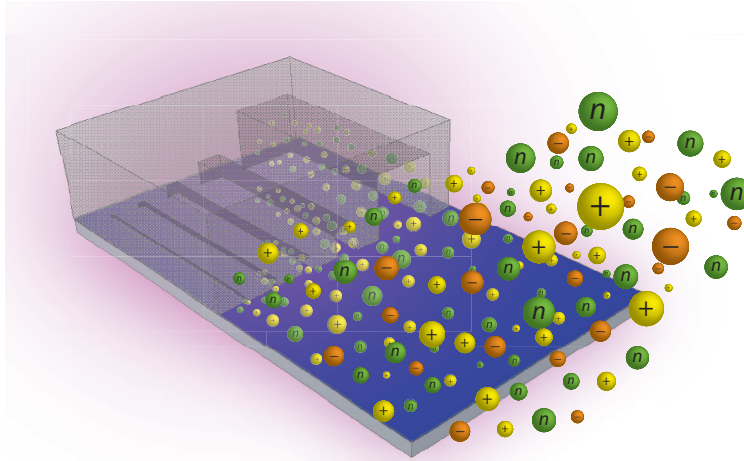
Figure 4.10: Schematic of the model proposed for the formation of deposits in small channels from a hexane plasma. The plasma consists of neutrals (green), positively (yellow) and negatively charged species (orange). Negatively charged species are prevented from entering the channels by the plasma sheath.

One possible deposition mechanism could depend on the presence of electrons that are required to form reactive species upon collision with gas molecules. Since the electron density decreases towards the object, (typically by a factor of two in the bulk and then to zero quickly in the boundary sheath) this could account for the parallel decrease in ppHex deposition rate. Alternatively, the deposition rate could depend on the presence of positively charged fragments, (that is, the positive species are responsible for the formation of the film) the density of which, in the absence of any negative ions, equals the electron density in the pre-sheath up to the sheath edge and hence also decreases. Only in the sheath will the ion density exceed the very rapidly falling electron density. It is not possible to conclude from this study whether it is the spatial distribution of radical or ion density directly mapped on to the substrate which gives rise the observed variation in deposition rate with distance, however the results do suggest a very strong correlation between plasma density and film thickness.

Based on the data present in this chapter, it is proposed that the deposition rate and thus the thickness of the deposited ppHex layer is controlled by the plasma sheath. The sheath acts as a filter that excludes negatively charged species, in particular electrons. The decreasing concentration of electrons in front of the mask consequently results in a reduced generation of active plasma species needed for deposition of the plasma polymer on the surface.

For the penetration of plasma species through small openings, the relative dimensions of the plasma sheath and the channel cross section is important. If the sheath thickness is larger than half the cross section, negatively charged species are effectively excluded from the channels. Based on the calculations carried out in SECTION 4.2.2 this would be the case for all but the 5 mm channel in this experiment.

For the deposition mechanism inside the channels, a model is therefore proposed in which only neutral and positively charged species are able to penetrate and react inside the channels (FIGURE 4.10). The concentration of both neutral and positively charged species decreased over length scales similar to the gradient transition.

4.3   Penetration of Plasma Species Through Tubes

4.3.1   Identification of Penetrating Species

To complete the study of the penetration properties of plasma species through small channels, this section will focus on identifying the nature of the active species able to penetrate through small openings. This could provide a better understanding of the mechanisms involved in the plasma polymer formation inside the channels. Mass spectrometry was used with the aim to identify neutral, positively and negatively charged species that are able to penetrate from the hexane plasma through a tube with a square cross section of 0.5 x 0.5 mm. Both neutral and positively charged species were detected at the end of a tube of a length of 2 mm (FIGURE 4.11) but no negatively charged fragments were observed. This suggests that negative fragments are not able to penetrate into the tube and therefore do not contribute to the formation of the deposit inside the channel.
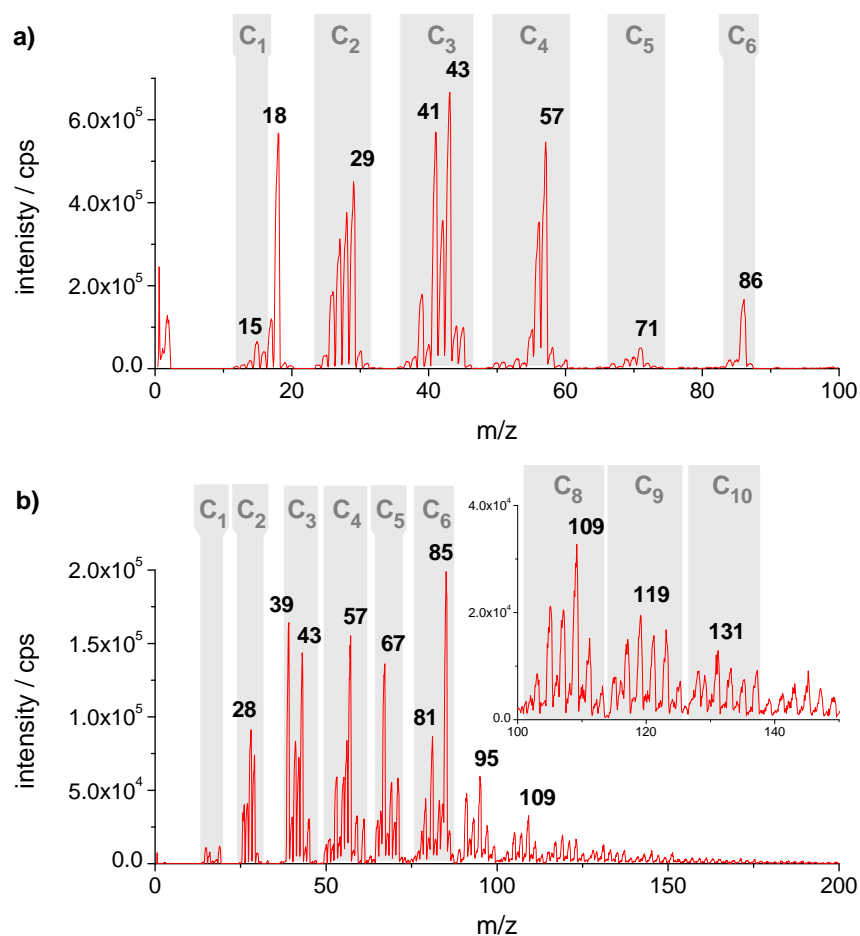
Figure 4.11: Mass spectra of neutral (a) and positive fragments (b) penetrating from the hexane plasma through 2 mm long tubes. The inset in (b) shows a magnified area of the higher molecular mass section of the positively charged fragments. The data were acquired by Dr. Badr Abdullah at the University of Liverpool.

TABLE 4.1 shows the main neutral and positively charged fragments observed in the mass spectra in FIGURE 4.11. It should be noted that for many m/z-values several structures are possible; the structures shown are the most stable products obtained after fragmentation. The m/z value of 18 in the spectrum for neutral species was attributed to H_2O but is not shown in TABLE 4.1 because it is not a fragmentation product of hexane.

In the spectrum for neutral species, evidence for fragments with one to five carbon atoms (C_1 to C_5) was found, although the C_1 and C_5 species were present at much lower intensities than the C_2, C_3 and C_4 fragments. SCHEME 4.1 shows how these last three species can be formed from n-hexane by homolytic bond scission at the 2,3- and 3,4-position. Other species are formed from these fragments by hydrogen abstraction as shown in SCHEME 4.2. The formation of these molecules through cleavage of the monomer after hydrogen abstraction seems unlikely because of

Table 4.1: Structures assigned to major peaks in the mass spectra of fragments penetrating from a hexane plasma through a 2 mm long tube.[a]

Neutrals			Positive ions		
m/z	Fragment	Structure [b]	m/z	Fragment	Structure [b]
15	CH_3	$^+CH_3$	28	$C_2H_4^{\cdot+}$	$H_2\overset{\cdot}{C}-\overset{+}{C}H_2$
27	$C_2H_3^+$	$HC\overset{}{=}CH_2$ (+)	39	$C_3H_3^+$	$HC=CH$ with $\overset{+}{C}H$ bridge
28	$C_2H_4^{\cdot+}$	$H_2\overset{\cdot}{C}-\overset{+}{C}H_2$	41	$C_3H_5^+$	$H_2C=\overset{H}{C}-\overset{+}{C}H_2$
29	$C_2H_5^+$	$H_2\overset{+}{C}-CH_3$	43	$C_3H_7^+$	$H_3C-\overset{H}{\overset{+}{C}}-CH_3$
41	$C_3H_5^+$	$H_2C=\overset{H}{C}-\overset{+}{C}H_2$	57	$C_4H_9^+$	$H_3C-\overset{H_2}{C}-\overset{+}{\underset{H}{C}}-CH_3$
42	$C_3H_6^{\cdot+}$	$H_3C-\overset{H}{\overset{\cdot}{C}}-\overset{+}{C}H_2$	67	$C_5H_7^+$	$H_2C=\overset{H}{C}-\overset{H}{C}=\overset{+}{C}H_2$
43	$C_3H_7^+$	$H_3C-\overset{H}{\overset{+}{C}}-CH_3$	69	$C_5H_9^+$	$H_3C-\overset{H}{C}=\overset{H}{C}-\overset{+}{\underset{H}{C}}-CH_3$
56	$C_4H_8^{\cdot+}$	$H_3C-\overset{H}{\overset{\cdot}{C}}-\overset{+}{\underset{H}{C}}-CH_3$	71	$C_5H_{11}^+$	$H_3C-\overset{H_2}{C}-\overset{+}{\underset{H}{C}}-\overset{H_2}{C}-CH_3$
57	$C_4H_9^+$	$H_3C-\overset{H_2}{C}-\overset{+}{\underset{H}{C}}-CH_3$	81	$C_6H_9^+$	$H_2C=\overset{H}{C}-\overset{H}{C}=\overset{H}{C}-\overset{+}{C}H-CH_3$
71	$C_5H_{11}^+$	$H_3C-\overset{H_2}{C}-\overset{+}{\underset{H}{C}}-\overset{H_2}{C}-CH_3$	**85**	$\mathbf{C_6H_{13}^+}$ [c]	$H_3C-\overset{H_2}{C}-\overset{H}{\underset{H_2}{C}}-\overset{+}{\underset{H_2}{C}}-CH_3$
86	$\mathbf{C_6H_{14}^{\cdot+}}$ [c]	$H_3C-\overset{H_2}{C}-\overset{H_2}{\underset{H_2}{C}}-\overset{H_2}{\underset{H_2}{C}}-CH_3$ (radical cation)	91	$C_7H_7^+$	tropylium ring (HC, CH, ^+CH)
			95	$C_7H_{11}^+$	$H_3C-\overset{H}{C}=\overset{H}{C}-\overset{H}{C}=\overset{H}{C}-\overset{+}{C}H-CH_3$
			109	$C_8H_{13}^+$	$H_3C-\overset{H}{C}=\overset{H}{C}-\overset{H}{C}=\overset{H}{C}-\overset{+}{\underset{H_2}{C}}-CH_3$
			119	$C_9H_{11}^+$	tropylium ring with $CH-\overset{+}{C}-CH_2$ / CH_3 substituent

[a] The m/z value of 18 in FIGURE 4.11 a was assigned to H_2O but is not listed in the table because it is not part of the fragmentation of the monomer.
[b] Only one possible mesomeric structure is shown for each fragment.
[c] Monomer.
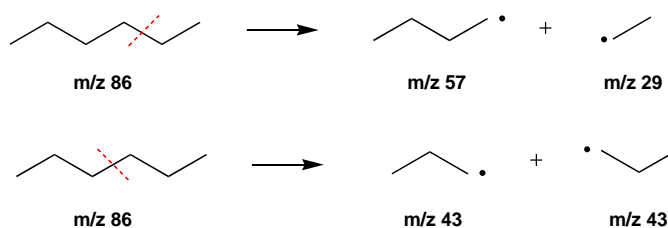
Scheme 4.1: Proposed fragmentation of *n*-hexane in the plasma based on the mass spectrum of neutral species. The m/z values of major fragments are shown in bold.
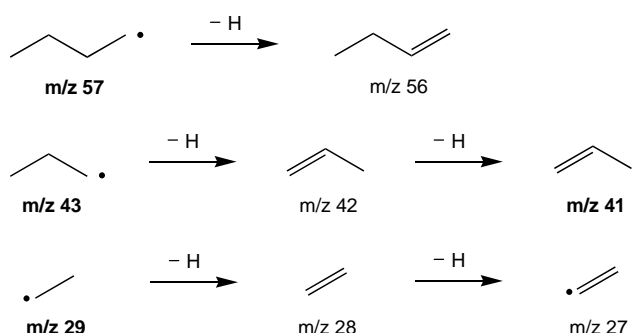
Scheme 4.2: Hydrogen abstraction from main neutral fragments. The m/z values of major fragments are shown in bold.

the low intensities of peaks just below m/z = 86. Equally, bond scission of *n*-hexane at the 1,2-position is not a dominant mechanism because the intensities of the expected products (m/z = 15 and 71) are very low. This can be attributed to the low stability of radicals on single carbon molecules [53]. Thus, the reactions shown in SCHEME 4.1 and 4.2 can account for the formation of all the major neutral fragments present in the tube.

The mass spectrum for positively charged species showed more peaks than the spectrum for neutrals and displays m/z values higher than that of the monomer (m/z = 85). Consequently, positively charged fragments from the hexane plasma were not only subject to stronger fragmentation but also participated in recombination reactions that yield higher molecular mass products. Strong peaks were observed for fragments containing two to five carbon atoms (C_2 to C_5). Similar to uncharged hexane, bond scission at the 2,3- and 3,4-positions of the hexane cation (SCHEME 4.3) and subsequent hydrogen abstraction (SCHEME 4.4) can explain the formation of C_2, C_3 and C_4 fragments. The presence of C_5-fragments in the spectrum for positive species stands in contrast to the result for neutral species above. A cleavage of the hexane cation at the 1,2-position still seems unlikely because of the low intensities of the possible products. It is therefore proposed that the molecule at m/z = 67 is the result of the fragmentation of a cation with a higher molecular mass as described in SCHEME 4.5. The formation of these molecules will be discussed in SECTION 4.3.2.
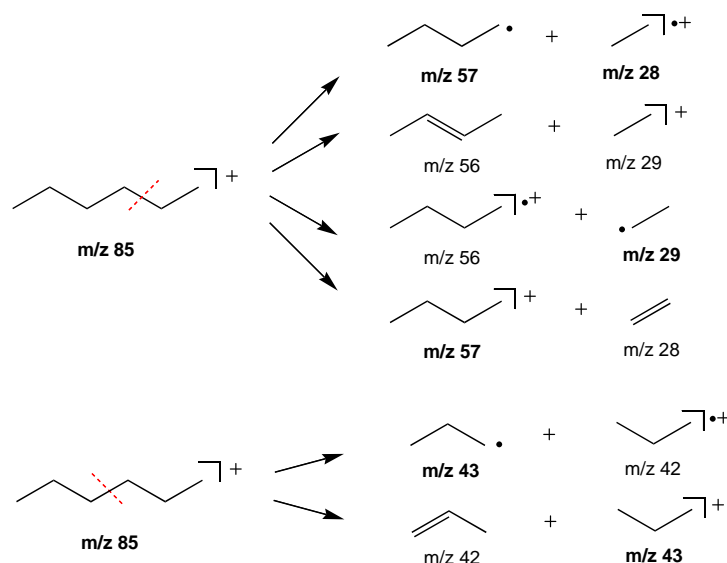
Scheme 4.3: Proposed fragmentation of n-hexane in the plasma based on the mass spectrum of positive species. The m/z values of major fragments are shown in bold.
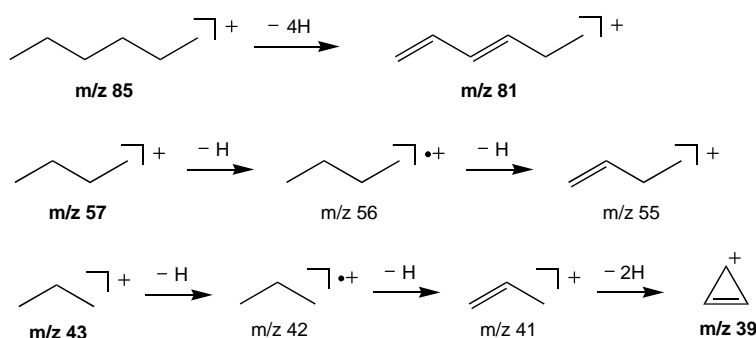
Scheme 4.4: Hydrogen abstraction from main positive fragments. The m/z values of major fragments are shown in bold.

The intensity of neutral species inside the tube was significantly higher than that of positively charged molecules, suggesting that the plasma was operated in a monomer sufficient region (see SECTION 2.1.2.3). When considering the fragmentation reactions discussed above, it can be noted that in the fragmentation of each carbocation one positive and one neutral molecule is formed. Thus, while the bond scission in neutral molecules only yields uncharged products, the fragmentation of positive species contributes to the formation of neutrals and consequently to the higher intensity of neutral species.
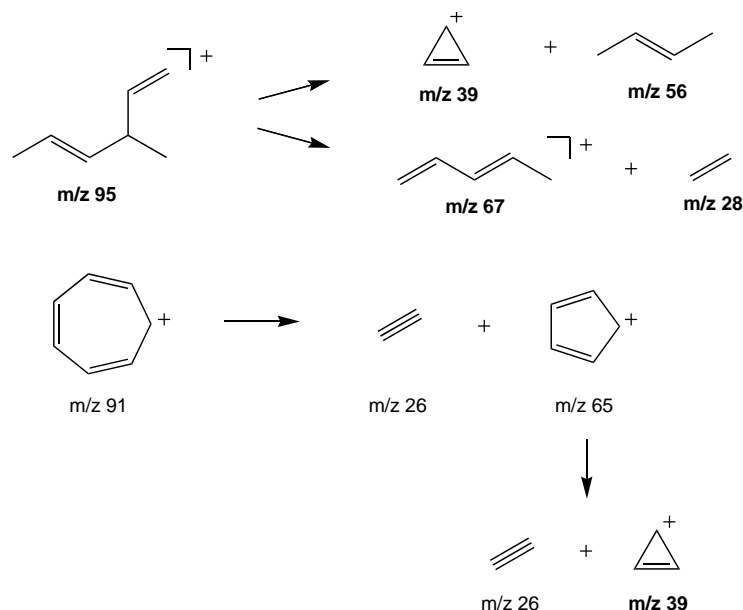
Scheme 4.5: Proposed formation of fragments from higher molecular mass species in the positive mass spectrum. The m/z values of major fragments are shown in bold.

4.3.2 Polymerisation Mechanisms in the Gas Phase

The presence of higher molecular mass fragments in the mass spectrum of positive ions highlights the likelihood of neutral-positive plasma phase reactions. In this section, possible pathways for the formation of positively charged fragments with molecular masses larger than the monomer will be explored.

Most major peaks at m/z values higher than 85 – notably at m/z = 91, 119 and 131 – have at least four double bond equivalents (see TABLE 4.1) and are therefore likely to have an aromatic structure. The formation of aromatic compounds has been noted before in SIMS analysis of aliphatic polymers [126, 127] and in ToF-SIMS analysis of polymers from plasma polymerised ethylene [128], allyl alcohol [129] and allylamine [130]. The present observation of aromatic compounds in the plasma indicates that these fragments are already formed in the gas phase and may then be deposited onto the surface.

Most notable is the presence of a fragment at m/z = 91, which corresponds to the mass of the tropylium cation, $C_7H_7^+$ [77]. This peak has also been found in the literature in ToF-SIMS spectra of plasma polymer films [128–130] and in mass spectra of an acrylic acid plasma [131] although the formation pathway of this molecule has not been discussed. SCHEME 4.6 shows two possible mechanisms through which tropylium may be formed from fragments in the hexane plasma. Following the generally accepted formation of tropylium through structural rearrangement of a toluene cation [77], it is proposed that both pathways initially proceed via the formation of a substituted benzene ring. This can be accomplished either by nucleophilic addition of a neutral
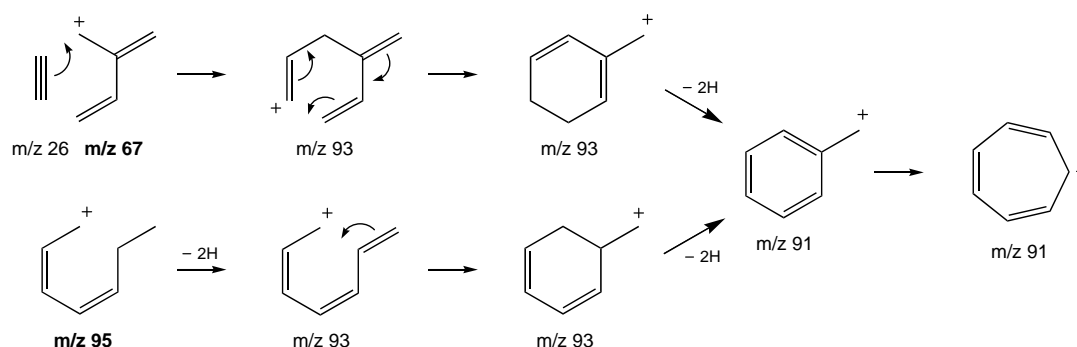
Scheme 4.6: Proposed mechanism for the formation of the tropylium cation ($C_7H_7^+$; m/z = 91) in the hexane plasma. The m/z values of major fragments are shown in bold.

fragment to a cation or by ring closure in a positively charged C_7 fragment. Both reactions have to be followed by the abstraction of hydrogen to form the aromatic structure. Due to its aromatic character, tropylium is relatively stable; it may, however, fragment into lower molecular species as shown before in SCHEME 4.5 [77]. The formation of tropylium is also important to explain the presence of other higher molecular mass fragments as will become evident below.

While the formation of $C_7H_7^+$ was best explained by a nucleophilic reaction mechanism, for the formation of most other higher molecular mass fragments radical mechanisms have to be considered, as well. Since no masses higher than the monomer (m/z = 86) were observed in the spectrum of neutral species, it is evident that cations are necessary for the formation of new molecules. Further, assuming that especially the first larger molecules (C_7 to C_{10}) are formed by recombination of two fragments only, all reactions can be simplified to the combination of a neutral and a positively charged fragment.

From TABLE 4.1 it can be seen that in the spectrum for positive species almost no radicals – with the exception of $C_2H_4^{\cdot+}$ – can be found among the major peaks. in contrast, many stable neutral fragments contained unpaired electrons. SCHEMES 4.7, 4.8 and 4.9 summarize possible reaction pathways for the formation of molecules with m/z values of 95, 109 and 119, respectively. When using the structures in TABLE 4.1 for these reactions and considering the possible reaction products, it has to be kept in mind that especially in the high energy environment of the plasma structural rearrangements of both products and reactants are likely and that in the schemes shown here merely some of the more stable reactants and the most likely products have been chosen. It should also be noted that in plasma the existence of diradicals is possible (see SECTION 2.1.2.3), a factor that has not been taken into account here.

Given the large number of fragments identified in the spectra, several combinations of fragments are thinkable that may lead to molecules with m/z values of 95, 109 and 119. While it can be argued that lower intensities indicate molecules with higher reactivities that are depleted faster, fragments with higher intensities and therefore higher concentrations in the gas phase have a higher collision frequency with other molecules which increases the probability of recombination reactions taking

Addition Reactions
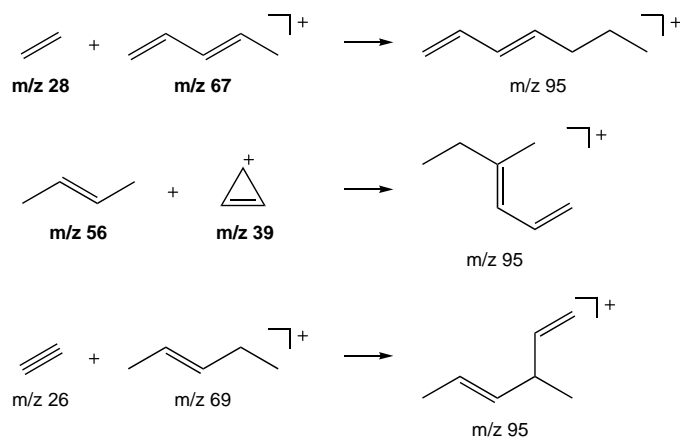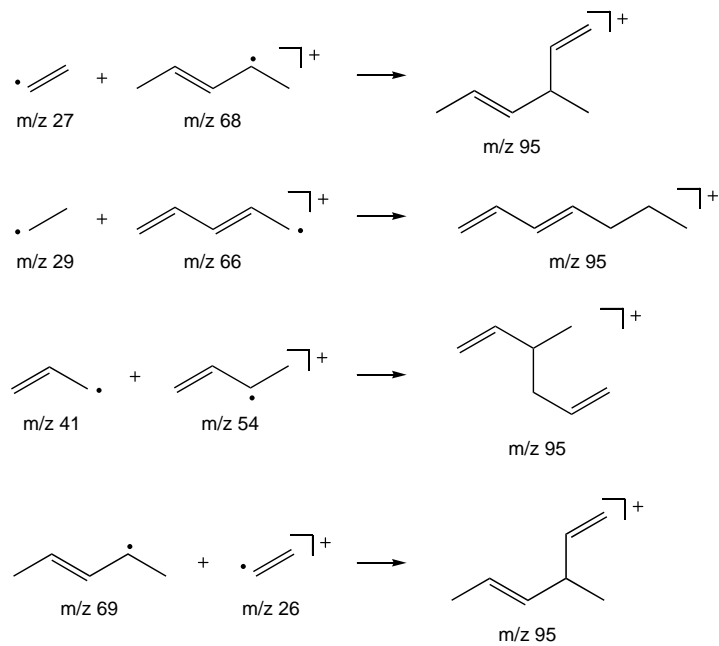
Radical Reactions

Scheme 4.7: Reactions of plasma species resulting in the formation of fragments with m/z = 95. The m/z values of major fragments are shown in bold.

Addition Reactions
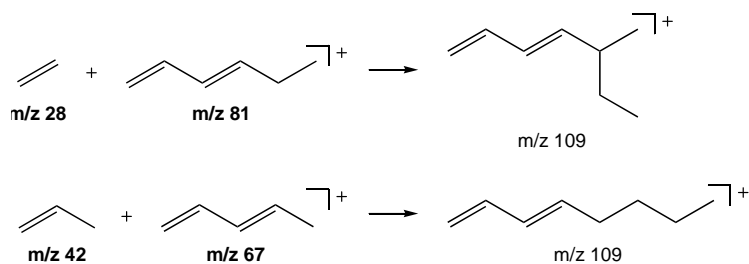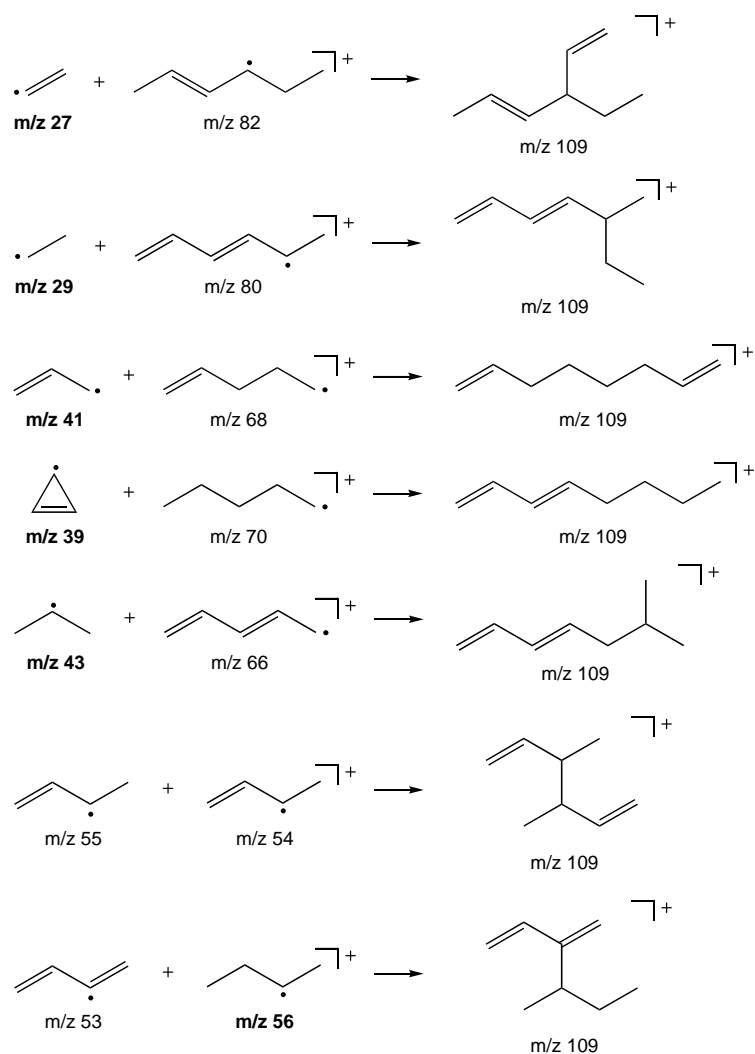
Radical Reactions

Scheme 4.8: Reactions of plasma species resulting in the formation of fragments with m/z = 109. The m/z values of major fragments are shown in bold.

Addition Reactions

m/z 28   m/z 91   m/z 119

Radical Reactions

m/z 27

m/z 92   m/z 119

m/z 41

m/z 78   m/z 119
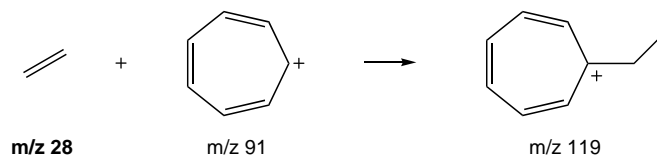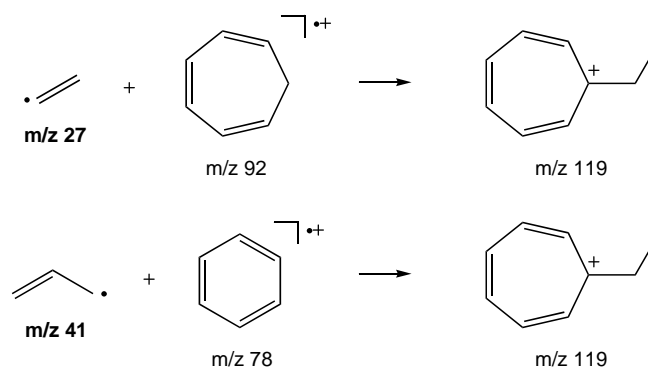
Scheme 4.9: Reactions of plasma species resulting in the formation of fragments with m/z = 119. The m/z values of major fragments are shown in bold.

place. Since it is not possible to determine the relative importance of high and medium or low intensity fragments in the formation of higher molecular mass fragments with the present data, all possible pathways that include at least one fragment of medium intensity are considered in SCHEMES 4.7 to 4.9.

When comparing the fragments taking part in radical reaction mechanisms to those undergoing nucleophilic addition, it becomes evident that the former always requires the combination of fragments with strong and weak intensities, while for the latter the reactions mainly proceed via two molecules with higher concentrations. The products shown in the reactions for m/z = 95 and 109 are often branched hydrocarbon structures, highlighting the random structure of the final plasma polymer. The formation of the molecule at m/z = 119 is best described as a combination of small neutral fragments with the tropylium cation (SCHEME 4.9). Even though reaction mechanisms have only been shown for the most intense higher molecular mass species in the positive spectrum, the other fragments with higher or lower mass generally differ by an m/z value of 2 and can be derived either by hydrogen abstraction from the product or by reaction of fragments containing fewer double bond equivalents. It is also notable that no combination of a radical and a non-radical fragment fit the stoichiometric requirements needed to form any of the products in question. This suggests that in the present case only the recombination of radicals needs to be considered, while the addition of radicals to double bonds is less likely, reducing the probability of radical chain propagations.

Recombination of positive and neutral species to form higher molecular mass products in the plasma can occur via many different combinations. The common element identified here, though, is that only the nucleophilic addition of double bond containing neutrals to positive fragments is supported by high concentrations (high peak intensities) of the reacting molecules. Combinations of two radical species can not be excluded but seems less likely due to the low concentration of at least one of the fragments required in all reactions. A predominantly neutral and cation driven plasma polymerisation has been suggested before for a CF_4 plasma [132]. It is therefore proposed that in the present hexane plasma, the formation of larger molecules in the tubes and possibly also in the bulk plasma proceeds via nucleophilic addition of double bonds to the positive species.

4.3.3 Penetration Depth

The mass spectrometric analysis of plasma species penetrating through small openings was carried out with tubes of different length (0, 2, 4, 6, 8 and 12mm) to determine how far the fragments are able to penetrate into the channels. Again, no negative fragments were detected at the end of the tubes regardless of their length. The intensities of the major fragments for neutral and positively charged species identified in TABLE 4.1 are plotted against the tube length in FIGURE 4.12. The intensity of all major species decreases with the tube length, presumably because an increasing number of fragments is lost to the walls the longer they remain in the channel. No fragments were found at the end of tubes that were equal or longer then 12 mm and 8 mm for neutrals and positive ions, respectively.

As has been pointed out in the previous section, not only relatively stable neutral species but also high molecular mass positive ions are observed to be transmitted through the tubes. The stability over such large downstream distances and times is consistent with the previous observation of long lifetimes for large positive ions in the afterglow portion of pulsed plasmas reported by Swindells *et*
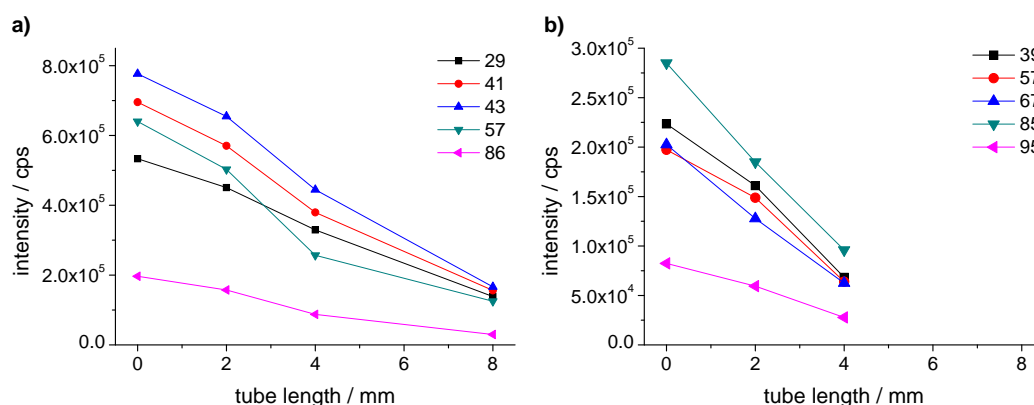
Figure 4.12: Intensity of the main neutral (a) and positively charged fragments (b) penetrating through tubes of different length. The legends show the m/z value of the corresponding dataset.

al. [133]. Both neutrals and positive ions could therefore contribute to the formation of deposits on the surface. From the current data it is not possible to conclude if only one or both species are required for the formation of a ppHex film in the channels.

4.4 Summary

Knowledge of the mechanisms involved in the formation of diffusion gradients is not only interesting from a theoretical point of view but also essential to obtain good control of the process. In this chapter, two model systems were developed with the aim to combine surface analytical techniques and plasma analysis to establish a deposition model for plasma polymerisation in small channels.

Surface chemical gradients were formed by hexane diffusion down channels with various cross sections. The gradients were characterised with WCA, ToF-SIMS and XPS analysis. WCA and ToF-SIMS measurements allowed the acquisition of a wettability and surface chemistry map, respectively, that showed the length characteristics of the gradients. Data from XPS analysis was converted into deposition rate profiles that showed that changes in the deposition rate occur not only inside the channels but also several millimeters in front of the mask. The changes in front of the mask were independent on the channel size except for a 2 mm wide area just before the openings where a steeper decrease was observed for smaller cross section. It was shown that the length scales correspond to the thickness of the plasma sheath that was calculated for this system.

A separate experiment allowed the identification of plasma species that are able to penetrate through a small opening using plasma mass spectrometry. While neutral and positively charged species are able to penetrate into the channel, negatively charged species are excluded. This was again attributed to the plasma sheath which shields the opening to the channel. Both neutrals and positively charged species were able to penetrate several millimeters down the channel. In addition, higher molecular mass products were observed in the mass spectra for positive fragments, providing evidence that polymerisation based on a mechanism including positive plasma species takes place in the gas phase. Based on the structures assigned to the fragments found in the mass spectra, it was suggested that a nucleophilic addition of double bond containing neutrals to positively charged species is the most likely reaction mechanism for the formation of these higher molecular mass cations.

Chapter 5

Stability and Degradation in Aqueous Environments

5.1 Uniform Plasma Polymers

5.1.1 Instrumental Challenges and Experimental Design

A main incentive for this work is the application of plasma polymer gradients in biological studies. It is therefore not sufficient to describe the surface properties of these gradients in ambient conditions under air. Some of the surface analysis techniques employed in CHAPTER 2.1 to characterise the gradients are carried out under high vacuum and are thus far removed from the environment the sample will be exposed to in any of the biological work presented in PART II where the plasma polymers will be immersed cell culture media (Dulbeccos modified Eagle's media, DMEM) and phosphate buffered saline (PBS).

This chapter will explore the surface properties of plasma polymer gradients in an aqueous environment to identify any changes in the surface properties. These differences will become of major importance in SECTION 7.3 and 8.2 where the relationship between the biological response (cell density and protein adsorption) and the surface properties will be investigated.

Most analysis techniques that have a spatial resolution suitable for the surface analysis of the present gradient format cannot be carried out in liquid. WCA, XPS and ToF-SIMS analysis were therefore carried out on samples that were exposed to PBS in a standard cell culture incubator (37℃, 5% CO_2) and dried prior to analysis. AFM was the only technique that allowed direct analysis of the surface in an aqueous environment.

For the development of gradient surfaces as rapid screening tools as an alternative to the use of large numbers of uniform samples, it is important to have control samples with uniform properties to asses the transferability of results from the gradient to a uniform sample format. The plasma polymer gradients developed in this work are not only a new preparation method, they also present

a surface design in which one plasma polymer layer is deposited on top of another. Even though layered plasma polymers have been prepared before [110], so far it is not known if the layered formation of plasma deposits is equivalent to the plasma polymers deposited on separate samples in a single step.

Before presenting the results for the gradients, the first part of this chapter will therefore focus on the analysis of the effect of PBS exposure on the surface of uniform plasma polymers of allylamine (ppAAm), hexane (ppHex) and ppHex deposited on top of ppAAm (ppHex/ppAAm) to match the surface design of the ppHex side of the gradients. To study the time dependance of any changes that might take place, exposure to PBS for these uniform samples is carried out for different times (0h, 1h, 3h, 6h, 12h, 1d, 2d, 3d, 4d) up to four days, at which point the gradual cell response reported in SECTION 7.1 starts to turn into a uniform distribution at the ppAAm end because the cells become confluent.

5.1.2 Time Dependent Changes

5.1.2.1 Wettability

The WCA of the plasma polymers is one of the most relevant surface properties in the assessment of biological responses. Cell attachment has often been explained in terms of surface wettability (see SECTION 6.1.3) and in CHAPTER 7 and 8 its importance in the current study will be highlighted.

The change in surface wettability of all three uniform plasma polymers over time is presented in FIGURE 5.1. For both ppAAm and ppHex a decrease of the WCA was observed that mainly occurs within the first 6h but stays mostly constant during the following 4 days. In both cases the final difference in WCA to the unexposed sample was approximately $5°$. In contrast, the WCA on the ppHex/ppAAm sample dropped sharply ($\sim 3°$) within the first hour but then continued to drop over 3 days until it was $9°$ below the value of the unexposed sample. Consequently, the WCA range between the two extremes relevant for the gradient samples (ppAAm and ppHex/ppAAm) narrowed slightly from $29°$ to $23°$.

It should also be emphasized that the profiles of the ppHex and ppHex/ppAAm samples are distinctly different from each other. This concerns mainly two important points: (i) the drop in wettability is almost immediate on ppHex/ppAAm whereas ppHex retains its initial hydrophobicity for about 6h and (ii) after the first day the changes seem to have terminated on ppHex while a drop in WCA on ppHex/ppAAm can still be seen for several days after immersion in PBS.

The change in surface chemistry on ppAAm surfaces immersed in ethanol and water has previously been studied with XPS by Tarasova *et al.* [31]. In SECTION 2.1.3.3 it was explained that the changes seen in this study were claimed to be similar to the oxidative degradation of ppAAm in air and is therefore assumed to be due to oxidation of the surface in water. Even though this explanation would seem valid for the increase in hydrophilicity of ppAAm and ppHex surfaces – this assumption will be explored with XPS data presented later on in this section – it is not sufficient to describe the differences between ppHex and ppHex/ppAAm, which seems to be related to the layered structure of a ppHex surface deposited on a hydrophilic ppAAm film. Four separate effects
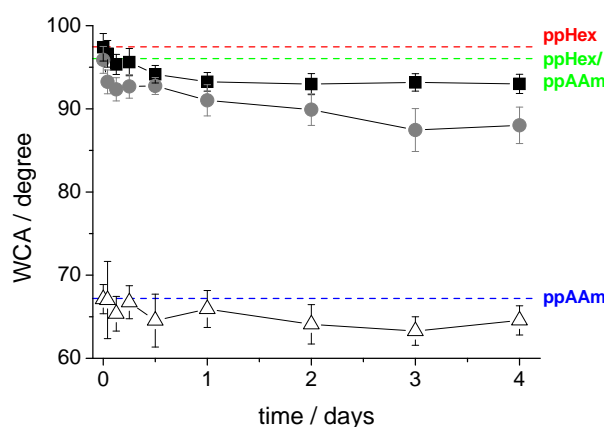
Figure 5.1: Change of the WCA on ppAAm ($\triangle$), ppHex ($\blacksquare$) and ppHex/ppAAm ($\bullet$) after different exposure times to PBS. The WCA of the unexposed plasma polymers is shown as dashed lines (ppHex: top; ppHex/ppAAm: middle; ppAAm: bottom). The data is an average of at least 22 measurements obtained from a total of six samples prepared in two separate experiments.

could provide plausible explanations for the lower WCA of ppHex/ppAAm:

(i) the ppHex film is partly removed from the underlying ppAAm, exposing small areas of higher hydrophilicity,

(ii) additional to the oxidation of ppHex, oxidation of ppAAm occurs at a slower rate through the overlaying ppHex film and is detected by the WCA analysis,

(iii) reorientation of the polymer chains occurs over time, moving some of the more hydrophilic nitrogen-based functionalities to the surface of the sample,

(iv) topographical changes occur that affect the WCA measurement.

If removal of ppHex occurs as explained in (i), it can be assumed that it has to occur on a length scale that is much smaller than the average size of the water drops used for WCA analysis (that are in the micrometer range); if this would not be the case, the error between measurements on the samples would be expected to be considerably higher. This can be further investigated by imaging the surface chemistry which is explored later in SECTION 5.1.3.2. Possible topographical changes will be studied in SECTION 5.1.3.1. Below, XPS analysis is used to investigate possibilities (ii) and (iii) further.

5.1.2.2   Surface Chemistry

XPS analysis allowed the detection of chemical changes on the surface at each time point. Similar to the unexposed samples, carbon and oxygen but no significant amount of silicon (< 0.5 at%)

were detected on all three plasma polymers. The oxygen content was lower on ppHex/ppAAm (< 5 at%) than on ppAAm and ppHex (< 20 at%). Nitrogen was detected on ppAAm (12 - 15 at%) and, in small amounts, on ppHex/ppAAm ($< 1.5\%$). Therefore, all polar functional groups are based on either oxygen or nitrogen and the change of functional group density on the surface relative to the hydrophobic hydrocarbon backbone of the plasma polymer can be approximated by the N/C and O/C ratios. These ratios are plotted in FIGURE 5.2 as a function of the exposure time to PBS. On ppHex/ppAAm, the N/C ratio increases slightly within the first 6h but then stays constant and close to the initial value over the whole period monitored. In contrast, on ppAAm the N/C ratio drops sharply to about 83% of the initial value within the first hour and levels off after 1 day. Therefore, some nitrogen functionalities were lost upon immersion of the sample in PBS. This is likely due to the dissolution of nitrogen containing low molecular weight fragments from the deposit. However, the drop of about 17% in the N/C ratio is not consistent with the 4% drop of the WCA in FIGURE 5.1 which would suggest an increase in the relative amount of polar functional groups.

The trend in the O/C ratio on ppAAm (FIGURE 5.2 b) is opposite to that of the N/C ratio. Here, a large increase in the O/C ratio (38%) is observed immediately after immersion in PBS and could account for the decrease in wettability observed in FIGURE 5.1. This is qualitatively consistent with the results obtained by Tarasova *et al.* who reported a rapid increase in the oxygen content on ppAAm within the first 2 hours of exposure to water [31]. It was suggested that the accelerated oxidation compared to oxidation in air is due to the rapid reaction of water with the radicals trapped in the plasma polymer (see SECTION 2.1.3.2).

The O/C ratio on ppHex/ppAAm increased at a constant rate to up to 2.5 times the initial value on day 4 but did not level off at this point. Again, this trend is similar to what was observed on the WCA profile and could therefore explain the constant decrease in WCA on ppHex/ppAAm
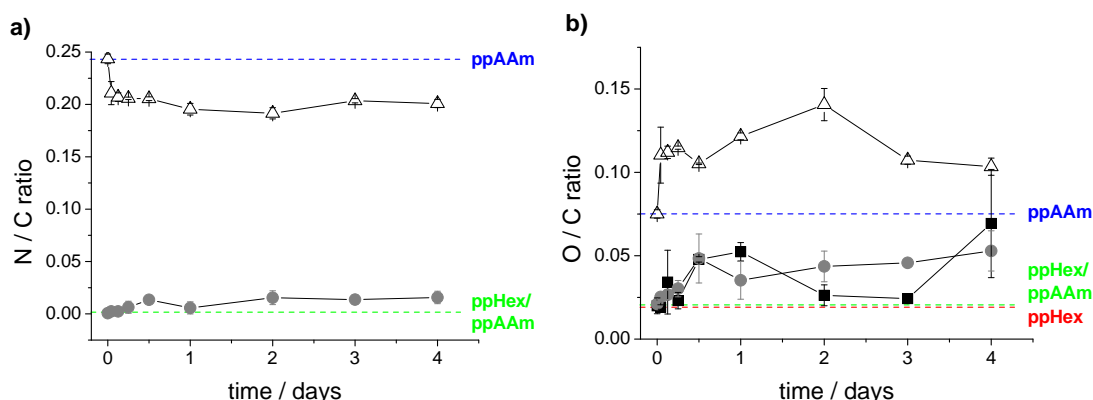
Figure 5.2: Evolution of the N/C (a) and O/C (b) ratios from the elemental composition (at%) with exposure time to PBS determined by XPS analysis on ppAAm ($\triangle$), ppHex ($\blacksquare$) and ppHex/ppAAm ($\bullet$). The WCA of the unexposed plasma polymers is shown as dashed lines. The data represents an average of 3 measurements.

upon exposure to PBS. However, although more scattered than on the ppHex/ppAAm surface, the O/C ratio on ppHex follows a similar trend as on ppHex/ppAAm but still has a higher WCA. Therefore, even though the elemental composition from XPS analysis indicates that changes in surface chemistry can explain some of the trends observed in the wettability profiles (keeping in mind that the analysis depth of these two techniques is different, giving room for variations in the profiles between them; see SECTION 2.2), it does not provide a satisfactory explanation of the WCA-differences on ppHex/ppAAm and ppHex.

To determine how the functional group density changes with exposure time to PBS and how they relate to the change in oxygen and nitrogen concentrations, curve fits of high resolution C 1s XPS spectra were carried out. The same parameters as in SECTION 3.3.1.3 were used with the exception of the addition of a separate component for C=O at 287.5 eV which was necessary to obtain good fits after exposure of the samples to PBS. FIGURES 5.3 a-c show typical curve fits for ppAAm, ppHex and ppHex/ppAAm after 1h of exposure. On ppAAm hydrocarbon (C−C and C−H) and amine (C−N) signals as well components attributed to the oxidation of these two groups – alcohols (C−O) and/or imines (C=N), carbonyl groups (C=O), amides (C(=O)N) and carboxylic acids (C(=O)O) – were detected. These groups are also observed on ppHex/ppAAm, but at lower intensities. The oxidation of amines to amides on plasma polymers due to storage in air has been reported before [23]. For ppHex, no nitrogen containing groups were fitted because no nitrogen was observed in the wide scan. It therefore only shows hydrocarbons, alcohols, carbonyl groups and – in traces – carboxylic acids. The presence of oxygen containing functional groups of higher oxidation states on all plasma polymers in significant quantities follows the previously postulated oxidative effect of the aqueous environment. The change of the relative intensities of these functional groups is shown in FIGURES 5.3 d-f. On all plasma polymers, the C(=O)O, C(=O)N and C=N/C−O signals are constant and therefore do not seem to be affected by the exposure to PBS. The amount of C−N is also mostly constant on ppAAm and ppHex/ppAAm, although the latter shows some larger variations. Interestingly, the relative amount of C−N is higher on ppHex/ppAAm than on ppAAm, but the C=N/C−O, C(=O)N and especially the C=O concentration is much lower. Considering the analysis depth of XPS (about 10 nm) and the approximate thickness of the ppHex layer on top of ppAAm on the ppHex/ppAAm sample (about 5 nm, see SECTION 3.3.1.3), it can be assumed that the XPS analysis actually analyses both the ppHex and the ppAAm layer, thus accounting for the presence of the nitrogen functionalities in ppHex/ppAAm. But while the ppAAm sample is fully exposed to the aqueous environment, the ppAAm layer in ppHex/ppAAm is protected by the top ppHex layer (quantitatively expressed in a higher percentage of C−C/C−H groups on ppHex/ppAAm). Oxidation of the allylamine plasma polymer therefore occurs either slower or to a lesser extent on ppHex/ppAAm than on ppAAm, resulting in a significantly lower amount of oxidation products (C=N/C−O, C(=O)N, C=O) and a higher retention of C−N groups in the layer analysed by XPS. These results support model (ii) in SECTION 5.1.2.1, attributing the difference in WCA between ppHex and ppHex/ppAAm to oxidation effects of the underlying ppAAm layer in ppHex/ppAAm.
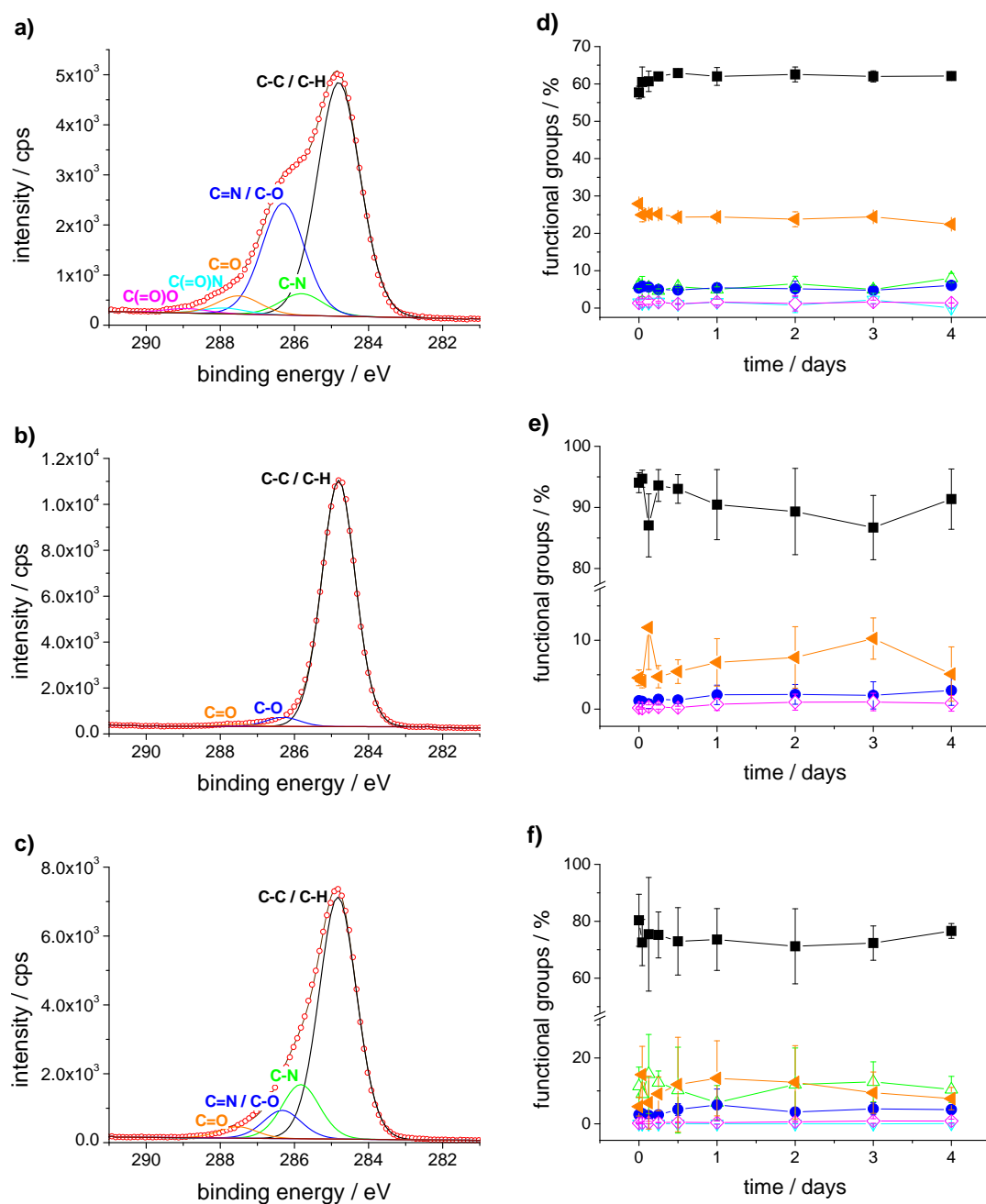
Figure 5.3: Typical curve fits of the C 1s signals of ppAAm (a), ppHex (b) and ppHex/ppAAm (c) for samples that were exposed to PBS for 1h. The evolution of the chemical composition of the plasma polymers exposed to PBS for different times is shown in d, e, f for ppAAm, ppHex and ppHex/ppAAm, respectively. The data is an average of 3 measurements. ■ C−C/C−H (284.8 eV), △ C−N (285.8 eV), ● C=N/C−O (286.3 eV), ◀ C=O (287.5 eV), ▽ C(=O)N (287.9 eV), ◇ C(=O)O (288.9 eV), measured spectrum: red circles, envelope of curve fits: brown line.

On all three plasma polymers, significant changes in the chemical composition over time only occur for the C−C/C−H and C=O groups. On ppHex and ppHex/ppAAm, the relative amount of hydrocarbon reduced within the first 6h due to an increase of the C=O group. But while the relative intensity of both groups leveled off on ppHex/ppAAm after half a day, on ppHex the relative amount kept changing at a slow rate over 3 days. Therefore, on both samples the increasing O/C ratio over time can be mainly attributed to the slow oxidation of the carbon backbone to carbonyl containing moieties. In addition, ppHex/ppAAm has a higher C=O content than ppHex, presumably due to the presence of the ppAAm bottom layer that seems to be more susceptible to oxidative processes than the ppHex. It is possible, that the oxidation of ppAAm underneath the ppHex coating could occur because of defects in the top ppHex layer that allows oxidising species to reach the underlying ppAAm layer. This will be considered in more detail in SECTION 5.1.3. From the present data, it can be concluded that the change in WCA on ppHex/ppAAm and ppHex can therefore be partly attributed to the formation of carbonyl groups on both samples.

Although on ppAAm the C−N percentage was slightly lower than on ppHex/ppAAm, the amount of C=O groups was significantly higher than on the ppHex and ppHex/ppAAm polymers, presumably contributing to the higher level of oxygen and the lower WCA of ppAAm. The increased formation of carboxyl groups on ppAAm compared to the other two plasma polymers was probably facilitated by the hydrolytic degradation of imines which in turn are easily obtained by enamine tautomerisation (see SCHEME 2.9 and 2.10 in SECTION 2.1.3.1). Interestingly, the trend in the evolution of the concentration of C−C/C−H and C=O groups was opposite on ppAAm compared to the two other sample formats. Within the first 6h, the hydrocarbon amount increased upon exposure to PBS whereas the number of C=O groups decreased. In both cases, the functional group density remained constant after the initial change. Apparently, some C=O groups were lost during exposure to PBS, and could therefore not contribute to the increased O/C ratio or the decrease in WCA. This could be explained by the extraction of polar fragments with low molecular weights from ppAAm to the aqueous environment. The strong presence of carboxyl groups further assists the fragmentation of the material by photodegradation via Norrish Type I and II reactions (see SCHEME 2.7 and 2.8 in SECTION 2.1.3.1), resulting in the formation of smaller, polar moieties that are more soluble in water. These results are contradictory to the increase in the O/C ratio observed in FIGURE 5.2 that would suggest a reduced amount of C−C/C−H and more oxygen based functionalities. Since only C, O and N were found on the sample, and no NO_x groups were observed in the N 1s high resolution spectra, the additional oxygen detected in the wide scan can not be chemically bound to either the carbon or the nitrogen atoms. However, in PBS (buffered at *pH* 7.2), the basic amine functionalities (the typical pK_a of amines is ~ 10 [134]) are protonated, and therefore positively charged. Upon rinsing of the sample with water after the degradation, the inorganic anions are displaced by hydroxy ions (OH^-), which are not covalently bound to the polymer but will still be detected in the wide scan XPS spectra.

In conclusion, the XPS results have demonstrated that the formation of oxygen containing functional groups rather than an increased number of nitrogen functionalities is responsible for the

wettability increase of all plasma polymers after exposure to PBS. Even though some caution has to be used in the comparison of WCA and XPS data due to their different analysis depths, it is proposed that the more significant decrease in WCA on ppHex/ppAAm compared to ppHex is caused by stronger oxidation of the surface (model (ii) in SECTION 5.1.2.1) rather than a reorientation of the polymer chains.

The increased amount of oxygen observed on ppAAm was attributed to the formation of hydroxy-salts with amines because no increase in oxygen containing functional groups was observed in the C 1s curve fits. The large increase in the O/C ratio is not reflected in the small decrease in WCA of ppAAm upon exposure to PBS. This is presumably because the control sample at $t = 0$ which was not previously exposed to PBS also experiences the effect of an aqueous environment once the water drop is placed on the surfaces. Consequently, the surface of the control sample will be conditioned in a way similar to the degraded samples, resulting in the formation of the same ionic compounds on the ppAAm samples that yield similar water contact angles.

At this point, the reader should keep in mind that all measurements in this section were carried out on dried samples. Although this was necessary to perform the analysis required, the results still might not reflect the condition of the surface *in situ* due to drying effects or interactions of the sample with air after treatment (for example, reordering of chains upon transfer of the sample from the hydrophilic aqueous environment to hydrophobic air).

5.1.3 Surface Imaging

5.1.3.1 Surface Topography

Even though it has been established before that the surfaces of ppAAm and ppHex/ppAAm are very smooth after deposition (SECTION 3.3.1.4), the topography of the plasma polymers could be subject to changes in an aqueous environment. This can be studied directly in liquid with atomic force microscopy (AFM).

In a first step, AFM micrographs of ppAAm, ppHex and ppHex/ppAAm taken directly in PBS were compared with those obtained from the unexposed dry samples (first and third row in FIGURE 5.4). While no significant changes were seen on ppAAm, on ppHex the formation of small holes of $\sim 0.1\ \mu$m in diameter was observed. To establish if these holes could be attributed to the underlying glass substrate that might have been exposed during imaging the sample, AFM images of oxygen etched glass were taken as well. These control measurements showed that no holes are present on the glass neither in air nor in PBS. The features observed on ppHex are therefore a created in the plasma polymer upon exposure to PBS.

Very drastic changes were observed on the ppAAm/ppHex surface when immersed in PBS. In contrast to the flat topography of the freshly deposited material, the surface appeared blistered, displaying islands of several tens of nanometers in height with diameters between 0.4 and 0.8 μm. To investigate if these islands are features created by the effect of the liquid on the plasma polymer or salt crystals deposited from the buffer, the surface needed to be imaged in pure water as well. Considering the conditions to which the plasma polymers will be subjected in the studies presented
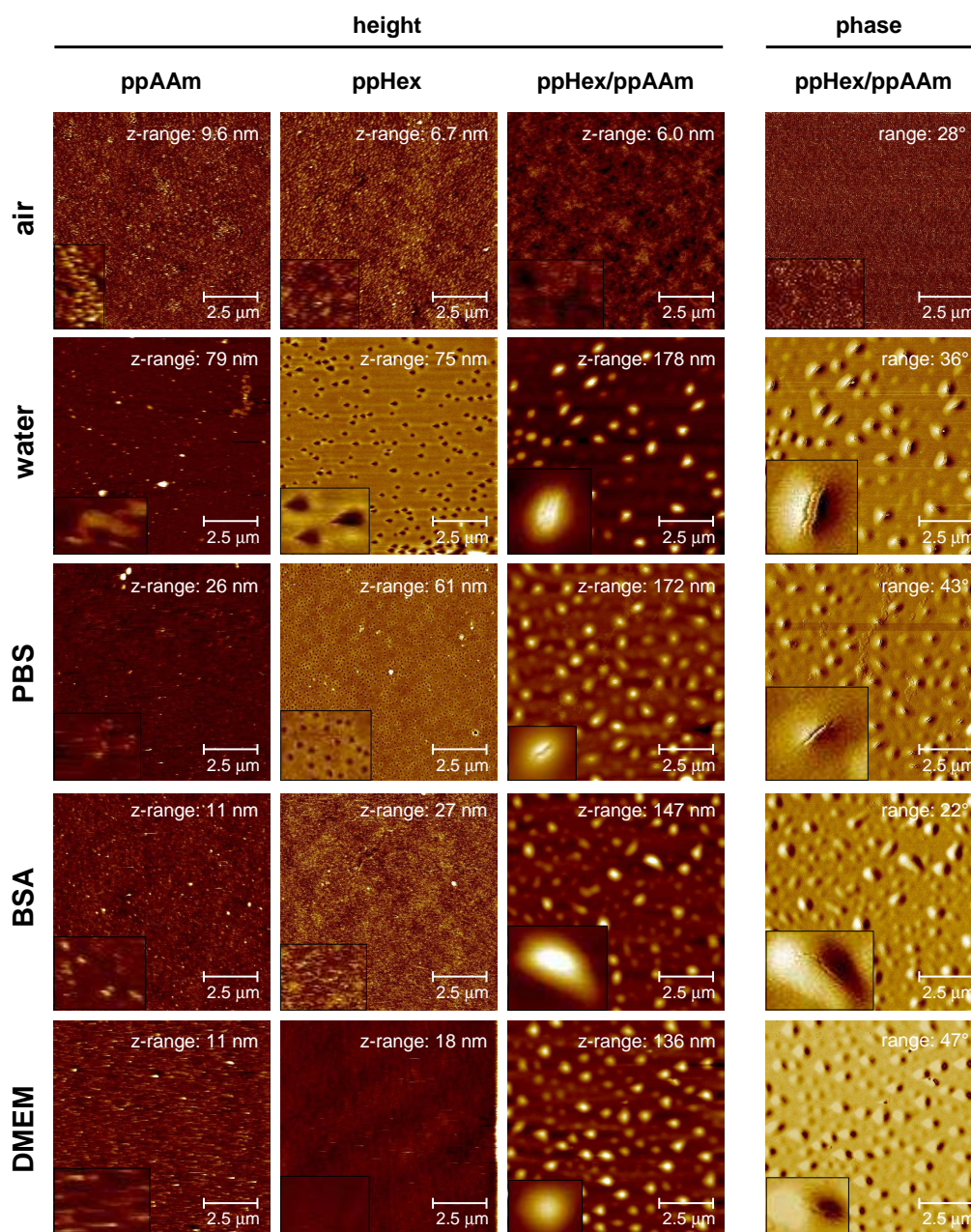
Figure 5.4: AFM micrographs (10 x 10 μm) of ppAAm, ppHex/ppAAm and ppHex plasma polymers obtained in air, deionised water, phosphate buffered saline (PBS), bovine serum albumin (BSA) and cell culture media (Dulbeccos Modified Eagle's Media, DMEM, supplemented with 10% fetal calf serum) taken within two hours after exposure. The right row shows the phase images of the ppHex/ppAAm surface. The insets in these micrographs are 4x magnifications of the features in the images.
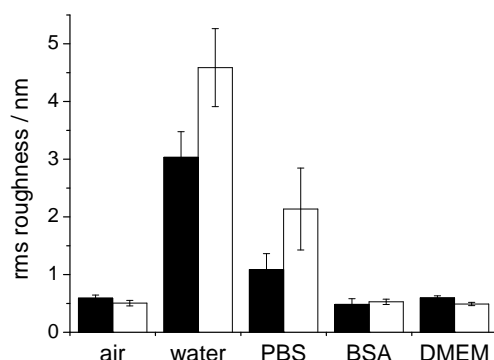
Figure 5.5: Route mean square (rms) roughness of ppAAm (■) and ppHex (□) in various environments calculated from AFM micrographs (10 x 10 μm). The data is an average of at least three measurements; error bars represent the standard deviation.

in PART II of this work, all three samples were also imaged in a 4 mg/ml solution of bovine serum albumin (BSA) and in tissue culture media (Dulbeccos modified Eagle's media). Representative AFM micrographs of these experiments are shown in FIGURE 5.4. All analysis was done within the first two hours after exposure to the liquid to ensure a similar timescale to that required for the first cells to attach to the surface in the biological studies (see CHAPTER 7).

The images taken on ppAAm show little differences in the topography between the five environments. The rms roughness determined from these micrographs is plotted in FIGURE 5.5. Most notably, the rms roughness increased from 0.6 nm in air to 3.0 nm in pure water. While the rms roughness in PBS (1.1 nm) was double the value in air, the rms roughness measured in BSA and DMEM was close to that of the unexposed sample.

A similar pattern was observed for the rms roughness of ppHex in these environments (FIGURE 5.5). The micrographs of ppHex taken in protein containing solutions (BSA and DMEM) showed no features and had an rms roughness which was again similar to that of the unexposed sample (0.5 nm). As in PBS, exposure of ppHex to pure water resulted in the formation of pores in the plasma polymer that were even slightly larger than those observed in PBS (0.3 to 0.4 μm in diameter). The coverage increased slightly from 7% in PBS to 9% in water. Thus, the rms roughness is larger in water (4.6 nm) than in PBS (2.1 nm).

The results for the rms roughness and the AFM micrographs for ppAAm and ppHex show that the exposure of these plasma polymers to aqueous environments induces changes that are most significant in pure water, followed by PBS. In both cases the rms roughness in BSA and DMEM does not change significantly. This suggests that the solubility of extracted oligomers from the plasma polymer is reduced due to the presence of other dissolved molecules in the water.

On ppHex/ppAAm, the islands observed in PBS were also present in all other aqueous environments. The coverage of the surface by these features was between 15% and 17% and thus similar
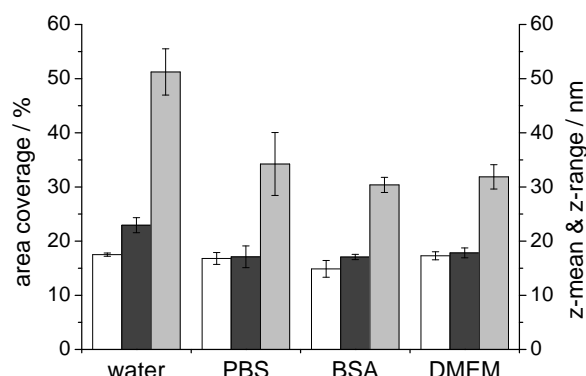
Figure 5.6: Percent area coverage (□), z-mean (■) and z-range (▨) of the features observed on ppHex/ppAAm in different aqueous environments determined from AFM micrographs (10 x 10 μm). The data is an average of at least three measurements; error bars represent the standard deviation.

for all four liquids (FIGURE 5.6). The mean difference between the highest and lowest point of the features (z-mean) is slightly above 17 nm for all liquids but pure water, which has a higher z-mean of 23 nm. Similarly, the z-range is highest in water (51 nm) but lower in PBS (34 nm), BSA (30 nm) and DMEM (32 nm). Thus, a stabilizing effect is observed again in protein containing solutions and PBS that reduce the z-range of the features compared to water.

Previously, other studies have reported a swelling of ppAAm upon exposure to water [26, 30]. Even though the ppAAm prepared here did not have the same cauliflower structure reported by Förch *et al.* [28], the change in the rms roughness from 0.8 nm in air to 1.3 nm in PBS is consistent with the present results (0.6 to 1.1 nm). In these studies, the increase in roughness was attributed to a swelling of the plasma polymer. The pores observed on ppHex in water and PBS have not previously been reported. Previously, the formation of pores in an *n*-heptylamine plasma polymer (ppHepA) after exposure to water was observed by Vasilev *et al.* [32]. Even though these results were not obtained *in situ* but on samples that have been dried after exposure to water, their relevance and similarities to the results presented here merits some consideration. In contrast to these results, the amine containing plasma polymer used in this work (ppAAm) did not have any pores nor develop any other features in any of the solutions tested. The pores observed in this work on ppHex – although similar in dimension to those reported by Vasilev *et al.* – had a significantly different topography. While the pores in ppHex were holes of regular circular shape in the material, the pores on some of the ppHepA samples have an irregular shape and seem to be surrounded by an elevated border. Nevertheless, it is reasonable to assume that pore formation in ppHex and ppHepA follows the same principle for both plasma polymers; small fragments are extracted from the polymer into the solution, causing stress in the polymer structure and eventually resulting in the formation of holes in the surface of the film.
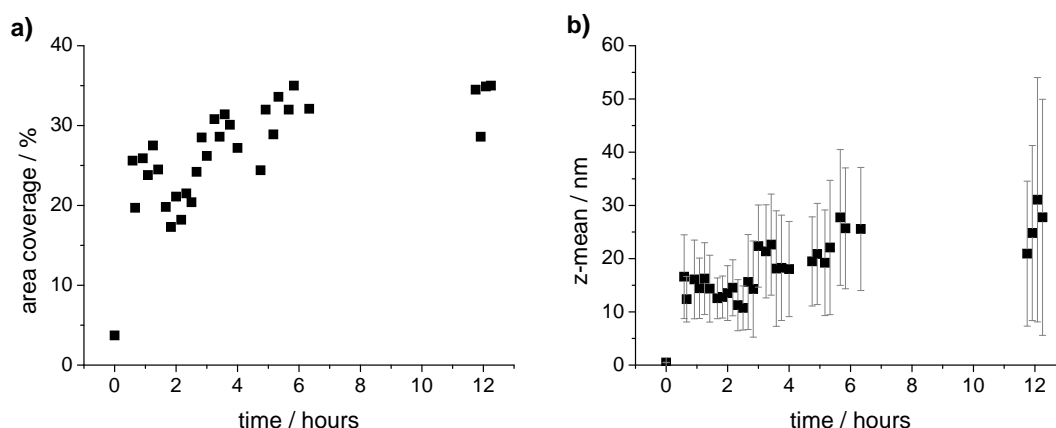
Figure 5.7: Time dependent evolution of the area coverage and z-mean of the features observed on ppHex/ppAAm measured with AFM in PBS at room temperature. Image size: 10 x 10 μm. Error bars represent standard deviations for each image.

The formation of blistered areas on ppHex/ppAAm can explained either by (i) segregation of material to form local clusters on the surface or (ii) a local penetration of the liquid through the polymer film, causing local swelling in the underlying ppAAm. Magnification of the features, especially in the phase images presented in FIGURE 5.4, reveal additional information about the blisters on ppHex/ppAAm formed in liquid. On the top of the blisters, fractures can be observed (insets in FIGURE 5.4) that suggest that the polymer film has actually been cracked open at this point. This indicates that liquid penetrates through the top ppHex layer rather than the islands being caused by segregation of material at the surface. A further attempt to underline this conclusion will be made in SECTION 5.1.3.2 below, where ToF-SIMS images of the surface chemistry will be presented.

To determine if long term changes in the surface topography occur over time, the three sample formats were imaged in PBS over a period of 12h. While the changes in topography on ppAAm and ppHex occurred within the time needed to acquire the first measurement (about 15 min), no additional changes were observed within the following twelve hours. In contrast, the area coverage of the features on ppHex/ppAAm increased over the first six hours from 20% to 30% (FIGURE 5.7 a). Over the following 6h the coverage did not change significantly. A similar trend is shown in FIGURE 5.7 b for the z-mean. The fact that the initial change is also immediate for ppHex/ppAAm (within the time it takes for the first measurement) and that it is not too steep within the first two hours confirms the validity of the previous presentation of average data over this period. However, the trends observed are only valid for the initial stage of transformation and might be different for other points in time.

5.1.3.2 Surface Chemistry

The formation of distinct topographical features on ppHex/ppAAm samples raises the question whether the surface is chemically uniform in an aqueous environment. This is also important to validate the point measurements taken in XPS and WCA analysis because chemical heterogeneities could mean that the analysed points are not necessarily representative of the whole surface.

In a first step to analyse the limits of data acquired from dried ppHex/ppAAm samples, in particular the effect of the drying procedure on the surface topography, samples dried according to the same procedure used in SECTION 5.1.2 were imaged with AFM. FIGURE 5.8 shows the results for ppHex/ppAAm samples that have been exposed to PBS for 1, 3, 6 and 12h. The distinct height of the islands observed directly in PBS (z-range of 34 nm) was reduced drastically to z-ranges below 10 nm. The position of the blisters and the cracks in the middle of the features are still visible after drying on the 1, 3 and 6h samples. The 12h sample is very different from the other three surfaces. The lack of any features that are similar to the blisters and the position of larger 'bordered' areas suggests that in this case those larger sections of the material might have been washed off during the rinsing procedure.

The first three images in FIGURE 5.8 are strikingly similar to those presented by Vasilev *et al.* as evidence for the formation of pores in ppHepA [32] that has been discussed in the previous section. This strongly suggests that the features reported by these authors were actually blisters while immersed in water, similar to those observed here on ppHex/ppAAm, and that the formation of pores in both instances is the result of an initial swelling step causing cracks in the top layer. This might have been followed by a reduction of the swelling after drying, leaving the cracks to appear as holes in the surface. Unfortunately, no AFM data in liquid has been reported by Vasilev *et al.* that would confirm this and relationships between the two experiments remain speculations. For the present purpose, these results show that for the initial six hours the features on ppHex/ppAAm are still present after drying the sample so that chemical analysis carried out in this time is likely to be comparable to the surface in liquid. However, the change in surface topography on dry ppHex/ppAAm samples before and after treatment makes it likely that the change in WCA is based on a combined effect of surface chemical and topographical changes.
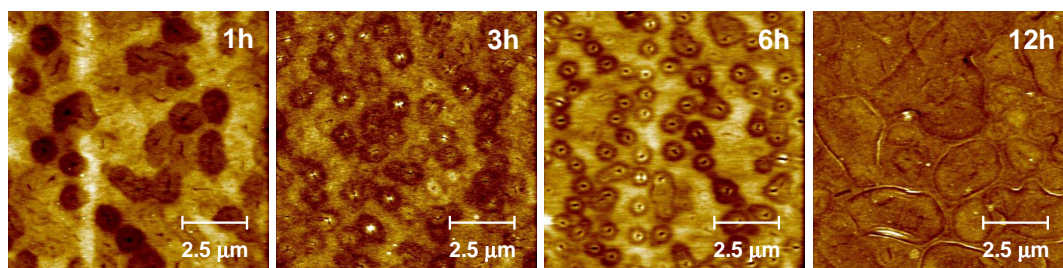
Figure 5.8: AFM micrographs (10 x 10 μm) of ppHex/ppAAm surfaces measured in air after exposure to PBS for 1, 3, 6 and 12 hours at 37℃ and subsequent rinsing.
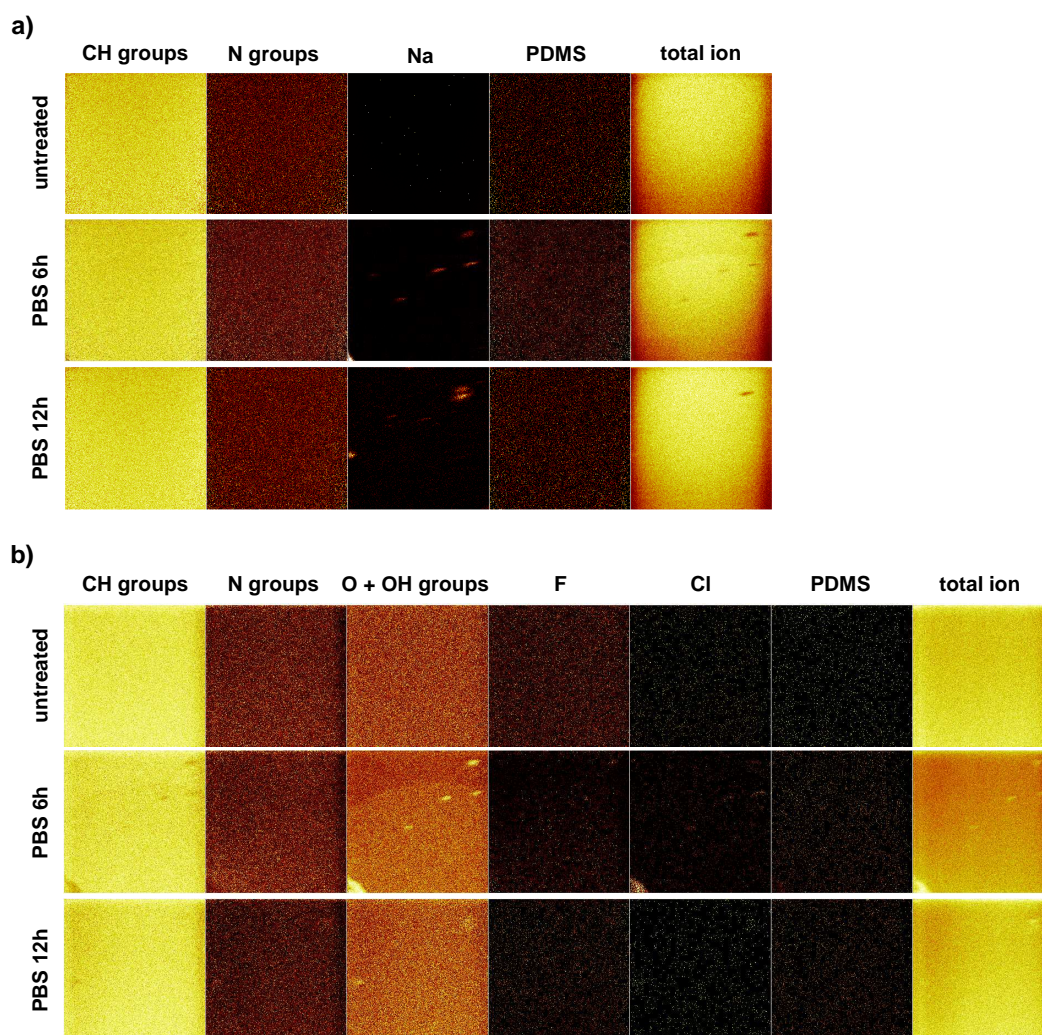
Figure 5.9: Tof-SIMS images of ppHex/ppAAm before and after exposure to PBS at 37°C for 6h and 12h. Signals containing pure hydrocarbon, nitrogen and oxygen functionalities are grouped together. The observed Si containing fragments were typical for PDMS. Images are 500 x 500 μm in size and corrected for the total ion intensity distribution; a) positive ions, b) negative ions.

Because of the more distinct features, the chemistry of the 6h and 12h samples was imaged with time of flight secondary ion mass spectrometry (Tof-SIMS). Images of the positively and negatively charged fragments of the samples and an unexposed ppHex/ppAAm control are shown in FIGURE 5.9 a and b. On all samples, traces of silicon containing fragments were detected that were typical for PDMS contaminations. Furthermore, some F, Cl and Na were observed on the surface, with F being stronger on the unexposed sample. The main components detected were hydrocarbon (CH) groups, followed by oxygen (O + OH) groups and a lesser amount of nitrogen (N) groups. The intensities

on the exposed samples of these main components appear similar that of the unexposed control sample, suggesting that no large scale removal of ppHex or reorientation of polymer chains took place at the top layer of the surface. The images of the CH and N groups show no inhomogeneities on the length scale that can be resolved by the instrument ($\sim 10\ \mu$m). However, this resolution is not good enough to identify chemical differences between the island-features and their surrounding, which are on a smaller length scale of a micrometer or less. The features observed in the images of Na and O groups are likely to be attributed to contaminations of ionic nature, but are not frequent enough to suggest they are part of the plasma polymer surface.

The chemical imaging thus showed that the quantitative analysis carried out in SECTION 5.1.2 is indeed representative for the overall sample and is likely to be relevant for the immersed surface within the first six hours of exposure to an aqueous environment. It further suggests that the chemistry of the top layer of ppHex/ppAAm stays intact during the topographical changes induced upon exposure to PBS. However, an influence of the surface topography on the lower WCA on ppHex/ppAAm compared to ppHex can not be excluded.
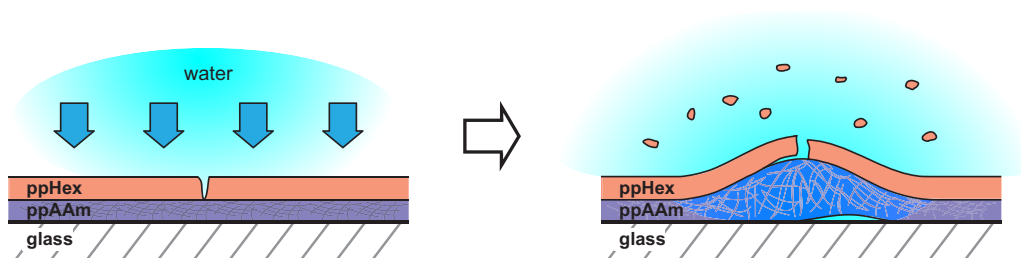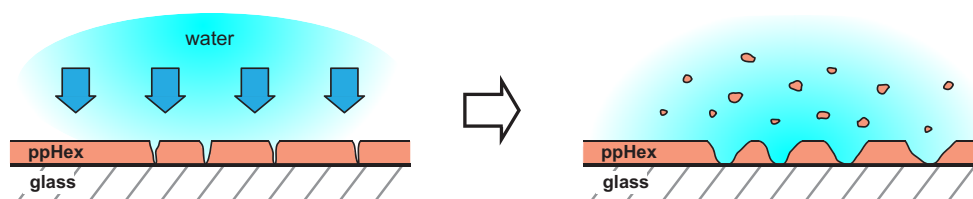
Figure 5.10: Proposed model to describe the formation of blisters and holes in the ppHex/ppAAm and the ppHex deposits on glass. Both processes rely on the presence of defaults in the top ppHex layer through which water penetrates and interacts with the underlying material. On ppHex/ppAAm, blisters are formed due to swelling of the underlying ppAAm film. Partial detachment of ppAAm from glass or ppHex from ppAAm is possible. On ppHex, the tensions in the polymer due to the extraction of low molecular weight material is released by the formation of larger holes.

The reduction of the z-range of the blisters on the AFM images after drying underlines that the blisters are a likely result of a local swelling of ppAAm due to penetration of water rather than a segregation of ppHex. The fact that no blisters were observed on ppHex leads to the assumption that the reason for the swelling could be found in the layered structure of the ppHex/ppAAm.

A model describing the processes that lead to the blistering effect and the formation of holes on ppHex/ppAAm and ppHex, respectively, is proposed in FIGURE 5.10. It is assumed that in both cases water is able to penetrate the ppHex layer through very small defects in the plasma polymer film. These defects could already be present in the film before immersion in water in which case they would have to have dimensions in the submicrometer range because they were not observed with AFM. Alternatively, the defects could be solvent induced effects due to the extraction of low molecular weight fragments from the plasma polymer. A weight loss from plasma polymers attributed to the extraction of material by a solvent was reported before for ppAAm immersed in ethanol [135] and water [32].

The defects in the top plasma polymer layer allowed water to penetrate through the ppHex deposit where they encountered either the ppAAm layer or the glass substrate for the ppHex/ppAAm and ppHex samples, respectively. On ppHex/ppAAm, the presence of water caused the ppAAm to swell locally – swelling of ppAAm upon exposure to solvents is well documented and has been reviewed in SECTION 2.1.3.3 – at the positions with defects in the ppHex coating (FIGURE 5.10). As a result, blisters were formed on ppHex/ppAAm where the ppAAm has been wetted. The loss of low molecular weight fragments and the increased volume of the underlying ppAAm exert stress on the ppHex layer, causing the initial defaults to propagate and form larger cracks.

To explain the pore formation on the ppHex sample, it seems reasonable to assume that the initial steps were similar to the formation of the blisters. The extraction of small molecules from the ppHex layer created tension in the plasma polymer film that could not be released by simple rearrangement of the polymer strands. The stress was instead released by the formation of holes on the surface (FIGURE 5.10). This explanation has also been used by Vasilev *et al.* to explain their own observations on ppHepA [32].

5.2 Effect of an Aqueous Environment on the Gradient

For the biological application of the plasma polymer gradients prepared and characterised in CHAPTER 3, it is important to investigate to which extent the effects of the aqueous environment observed on uniform samples change the surface properties of the gradient. This paragraph presents data on the analysis of the surface chemistry and topography of the shallow diffusion gradient after exposure to PBS for 1h at 37℃ and compares it with data from the unexposed surface that has already been discussed in CHAPTER 3. Exposure parameters were chosen such that they are close to the conditions actually experienced in the biological studies (salt concentration, pH and temperature) while still allowing chemical analysis of the plasma polymer gradients in the absence of any proteins on the surface. The exposure time of 1h corresponds approximately to the time needed until the first cell attachment to the surface can be observed (see SECTION 6.1.2).

5.2.1 Surface Chemistry

5.2.1.1 Wettability

When comparing the WCA profile of the exposed and unexposed samples (FIGURE 5.11), a striking difference in the gradient transition becomes obvious. Based on the results from the uniform samples, a reduction of the WCA on both the ppHex and the ppAAm end of the gradient is expected. The most obvious change, however, is the reduction of the shallow wettability transition from more than 8 mm before exposure to PBS to a steep transition over about 2 mm. Thus, the formerly masked area on which the WCA gradient was prepared (positive x-values) has a constant WCA of 47° which is 9° lower than the WCA of the ppAAm end of the unexposed sample. In comparison, no change in hydrophobicity was observed on the uniform ppAAm sample. Equally, the uniform ppHex and ppHex/ppAAm samples showed no significant change in WCA after 1h of exposure whereas the WCA of the ppHex end of the gradient decreased by 20° (to 74°). Thus, exposure of the gradient to PBS for 1h not only decreased the WCA range between the hydrophilic and the hydrophobic end from 38° to 27° but also reduced the transition area to a step like profile. In the following, XPS analysis and AFM imaging will be used to determine if these are chemical or topographical effects or a combination of both.
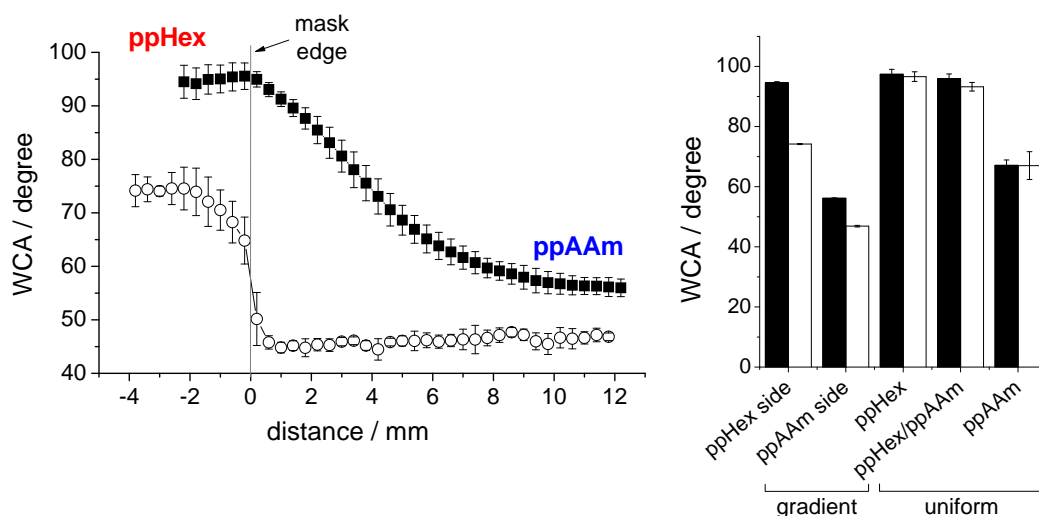
Figure 5.11: Change of the WCA profile on the gradient as deposited (■) and after exposure to PBS for 1h (○). The edge of the mask is set at $x = 0$, with the hydrophobic ppHex side to the left and the more hydrophilic ppAAm side to the right. The histogram compares the WCA of the extreme ends of the gradients with that of uniform plasma polymers (black: unexposed, white: after exposure to PBS). The data is an average of 3 gradients with 5 line-measurements each; error bars represent the standard deviation.

5.2.1.2 Quantification of the Surface Chemistry

The elemental composition of the gradient after exposure to PBS is very similar to that of the unexposed sample. Only carbon, nitrogen and oxygen were detected, suggesting that all traces of salts from the buffer were rinsed off completely after immersion in the liquid. The chemical composition profile obtained from curve fittings of the C 1s signals also showed little differences after the treatment apart from a slightly higher amount of hydrocarbon and a small decrease in C=N/C−O components on the ppAAm end of the gradient. This is also reflected in the N/C ratio of the samples displayed in FIGURE 5.12. However, although the N/C ratio is about 20% lower on the ppAAm side of the exposed gradient, interestingly the N/C ratio profile is the same over the first 2 mm (with respect to the previously masked area) on both samples. This stands in contrast to the WCA profile which has completed its transition after 0.5 mm into the previously masked area after exposure to PBS.

The O/C ratio profile which is also displayed in FIGURE 5.12 is initially higher on the exposed gradient sample but remains constant at approximately the same level as the unexposed sample after 2 mm. Although this could be partly responsible for the decrease in WCA at the beginning of the original gradient, the difference is far too small and does not occur over a distance that is long enough to account for the complete loss of the WCA gradient transition.
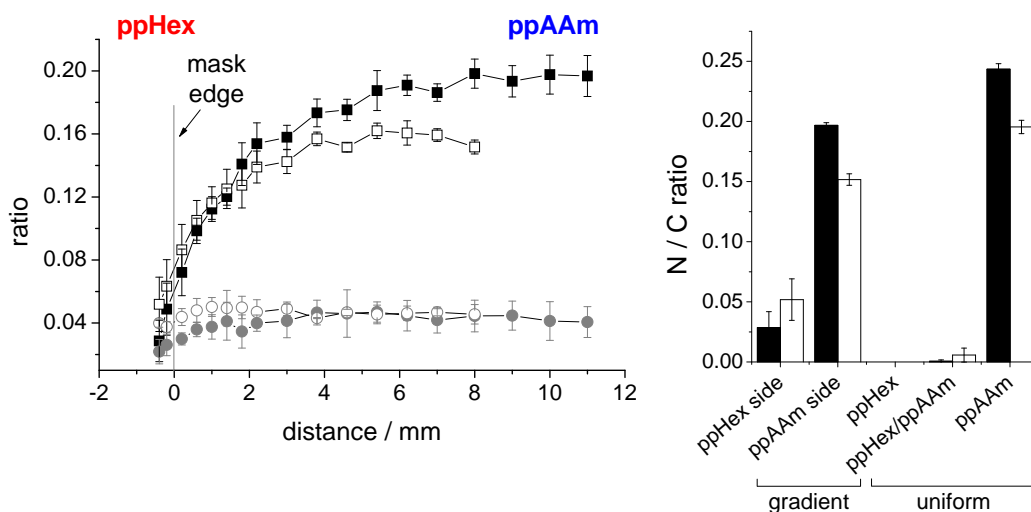
Figure 5.12: Change of the N/C (black) and O/C (grey) ratios determined from XPS analysis along the gradient as deposited (■,●) and after exposure to PBS for 1h (□,○). The edge of the mask is set at $x = 0$, with the hydrophobic ppHex side to the left and the more hydrophilic ppAAm side to the right. The histogram compares the N/C ratio of the extreme ends of the gradients with that of uniform plasma polymers (black: unexposed, white: after exposure to PBS). The data is an average of 3 gradients with 1 line-measurement each; error bars represent the standard deviation.
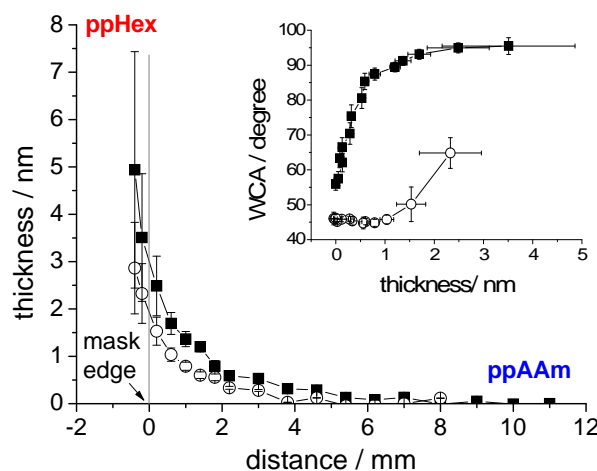
Figure 5.13: Change of the ppHex thickness determined from XPS analysis along the gradient as deposited (■) and after exposure to PBS for 1h (○). The edge of the mask is set at $x = 0$, with the hydrophobic ppHex side to the left and the more hydrophilic ppAAm side to the right. The inset shows the correlation of the thickness to the WCA. The data is an average of 3 gradients with 1 line-measurement each; error bars represent the standard deviation.

To investigate if the thickness of the ppHex top layer has been affected by the aqueous environment, the ppHex thickness of the exposed gradient has been calculated from the XPS data as described previously (see SECTION 3.3.1.3). This data is presented together with the previously calculated ppHex thickness of the unexposed gradient in FIGURE 5.13. Again, the profiles of the two samples are very similar, and only a small decrease in thickness was observed in the gradient area. A plot of the WCA against the ppHex thickness for both the exposed and the unexposed sample (inset in FIGURE 5.13) demonstrates the loss of correlation between the XPS data and the WCA analysis that has previously been established in SECTION 3.3.1.3. The fact that a gradient is still distinctly visible on the thickness profile of the exposed sample underlines that an overall change in surface chemistry in the top 10 nm can not be held responsible for the loss of the WCA gradient. It is, however, possible that small changes in surface chemistry occur in the top layer of the material that might not influence the XPS data but are detected by WCA measurements.

5.2.2 Surface Topography

To study the surface topography of the gradient, AFM micrographs were acquired in 2 mm increments along the sample in PBS at room temperature. Different exposure times of different areas along the gradient can not be avoided; however, imaging was started at the ppHex end of the gradient which is similar in composition to the uniform ppHex/ppAAm sample that was identified in SECTION 5.1.3.1 as the only control sample that showed significant changes in topography over
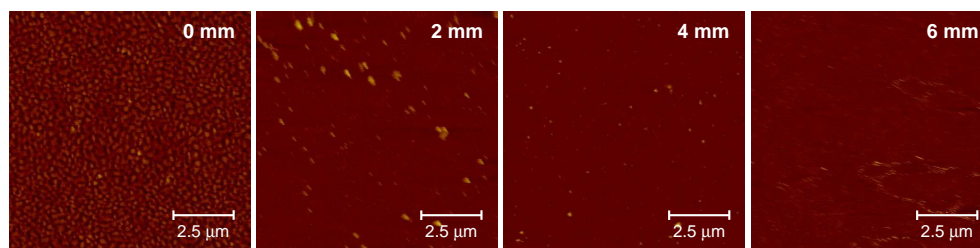
Figure 5.14: AFM micrographs (10 x 10 μm) taken in 2 mm intervals along the gradient in PBS. ppHex side: left; ppAAm side: right.

time. Even so, when control images were taken again on the ppHex end of the gradient after the experiment, the overall appearance of the surface had not changed.

FIGURE 5.14 shows representative AFM images that were acquired on the gradient in liquid. At position $x = 0$ – and in fact on the whole area that was not covered by the mask during the preparation of the gradient – the previously smooth surface now displayed a rough topography. Even though the results from SECTION 5.1.3.1 suggested that topographical changes would take place on those areas of the gradient that consisted of a ppHex/ppAAm like material, the ppHex side of the gradient only showed a roughening of the surface but lacked the blister formation and the appearance of cracks on the surface associated with it. The difference between the ppHex side of the gradient and the uniform ppHex/ppAAm sample can be explained considering the effects described in CHAPTER 4. There, it was demonstrated that the plasma sheath in front of the mask has a considerable influence on the plasma polymerisation in this area, resulting in a coating that is different from that deposited on a completely unobstructed, plain sample. It is therefore likely that the ppHex deposited on the gradient sample in front of the mask has different properties compared to the uniform ppHex/ppAAm sample as has been demonstrated by AFM imaging.

When moving from the beginning of the gradient towards the ppAAm end of the sample, the distinct roughness of the ppHex side disappears. Instead, larger features are observed that decrease in number when moving towards the end of the gradient and disappear completely after $x = 4$ mm (FIGURE 5.14). The route mean square (rms) roughness along the exposed sample is plotted in FIGURE 5.15. Compared to the unexposed sample, which had a low and constant rms roughness (< 0.4 nm), a roughness gradient over 4 mm can be observed after exposure to PBS. The gradient decreases from an rms roughness of 3.9 nm on the ppHex side to 1.5 nm on the ppAAm side, after which the roughness remains constant. On the ppAAm side, the rms roughness does not approach the value of the unexposed gradient and is also 21% higher than on uniform ppAAm.

The exposure of the plasma polymer gradient to PBS thus resulted in the formation of a roughness gradient along the sample which was not present before. This together with the change in the WCA profile are important characteristics that will need to be taken into consideration when a biological response is tested as a function of the surface properties of these gradients. The sharp drop in the WCA profile can now also be explained as the result of a rapidly changing surface topography when moving from the ppHex side of the gradient sample to the beginning of the actual
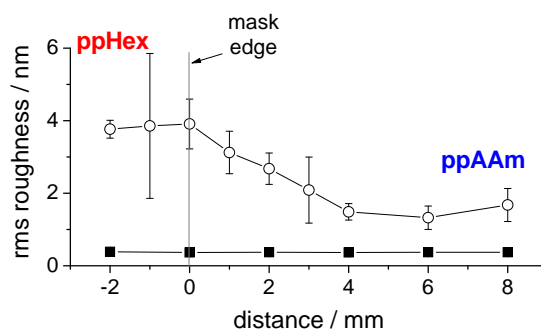
Figure 5.15: Change of the route mean square (rms) roughness along the gradient in air (■) and in PBS (○). The edge of the mask is set at $x = 0$; with the hydrophobic ppHex side to the left and the more hydrophilic ppAAm side to the right. The data is an average of the roughness obtained from at least three AFM micrographs (10 x 10 μm; error bars represent the standard deviation.)

gradient transition. It therefore seems to be mainly a topographical phenomenon, suggesting that in an aqueous environment the surface coverage of the gradient area with ppHex is too thin (though still detectable by XPS on the dried sample) to have a significant influence on the wettability of the gradient.

5.3   Summary

The experiments presented in this chapter showed that the surface properties of plasma polymers can change significantly when exposed to an aqueous environment. To develop a good understanding of the processes involved, the study first focused on time dependent changes on uniform plasma polymers of allylamine (ppAAm), hexane (ppHex) and hexane deposited on top of allylamine (ppHex/ppAAm) upon exposure to phosphate buffered saline (PBS). For all three samples, an initial decrease in the water contact angle that was accompanied by an increase in the amount of oxygen on the surface was noticed. Most changes, however, were completed after 6h and reached an approximate equilibrium. The increase in oxygen was attribute to oxidation of the surface in PBS that yielded carbonyl groups as the main oxidation product. A higher oxygen uptake on ppAAm was explained by the ionic binding of hydroxide anions to amine groups. On ppAAm, some loss of amine functionalities was observed.

The surface roughness of ppAAm and ppHex determined by atomic force microscopy (AFM) increased slightly after exposure to PBS but did not change with exposure time. On ppHex, the formation of small pores was observed when exposed to either water or PBS. These pores were not visible when the sample was placed in protein containing solutions. In these solutions, the roughness of ppAAm did not increase either, suggesting that they have a stabilizing effect on both ppAAm and ppHex.

On ppHex/ppAAm, the formation of blisters was observed in all solutions tested. The surface coverage and the height of the blisters changed slowly over 12h. The blister formation was attributed to the extraction of low molecular weight fragments from the plasma polymer and a local penetration of the liquid under the top layer, resulting in a swelling of the underlying ppAAm. This was supported by the observation of cracks in the middle of the blisters and the fact that although the island features were still present on the dried samples, the height of the features decreased dramatically after drying.

Time of flight secondary ion mass spectrometry was used to image the surface chemistry of the ppHex/ppAAm sample. Although the resolution was not high enough to be able to comment on chemical differences between the islands and the surroundings, it demonstrated that the surface chemistry was uniform on the upper micrometer scale and that no large differences existed between the surface chemistry of the plasma polymer samples before and after exposure to PBS.

A similar study was performed on the shallow plasma polymer gradients. It was shown that the WCA gradient transition was lost after exposure to PBS, giving way to a step like WCA transition from the ppHex to the ppAAm end. In addition, the WCA on both sides of the step-gradient was much reduced compared to the unexposed sample. As demonstrated by XPS analysis, these changes could not be attributed to chemical differences in the top 10 nm. The profile of the N/C and O/C ratios and the thickness profile of the ppHex top layer of the gradients are very similar on the exposed and unexposed sample. In contrast, the topography on the ppHex side of the exposed gradient was found to be very rough and distinctly different from the rest of the sample. However, it was also different from the topography of the ppHex/ppAAm samples because it lacked the typical blisters observed before. The gradient transition area showed larger features that decreased in size and number when moving towards the ppAAm side of the sample. When plotting the roughness of the gradient after exposure to PBS, a gradient profile that stretched over 4 mm was found that was not present on the unexposed sample. The different topography of the ppHex side from the rest of the gradient sample also explains the step-like WCA profile obtained from the plasma polymer gradient after exposure to PBS.

Part II

Biological Response

Chapter 6

Scientific Background

6.1 Cell Adhesion to Surfaces

6.1.1 Relevance of Cell Adhesion to Biomaterials

The development of *biomaterials*, that is, materials used in an biological application, has attracted considerable attention not least because of its promise to bring research a step closer to solve many issues in regenerative medicine such as the repair or replacement of malfunctioning body parts or the targeted delivery of therapeutic agents. A wide variety of materials have been developed to serve as process aids or final products in fields such as tissue engineering [136], biomedical implants [136], drug delivery [137], wound repair [138], biosensors [139, 140], material discovery and basic research of biological processes [141]. As a result, there is a large number of different requirements on the function of biomaterials, ranging from physical properties (stiffness, shape, porosity, topography, *etc.*) to chemical properties (chemical composition, stability or degradability, reactivity, *etc.*) to biological properties (toxicity, affinity to proteins, cells or bacteria, biological activity, *etc.*). Thus, the optimal performance of the biomaterial depends on the combination of various factors. A large number of publications is available on the subject of new biomaterial development and application. A complete review of these is beyond the scope of this chapter and the reader is referred to the literature for a more detailed discussion [136, 142].

Frequently, the requirements on the material can be very demanding, making it difficult if not impossible to combine all the desired properties in a single component. For example, metal implants are often used because of their durability and non-toxic properties. However, especially on pure metals cell attachment to the surface is slow due to a lack of binding sites on the surface. This can be overcome by modifying the metal surface with a cell adhesive layer, as has been demonstrated by coating titanium with a thin allylamine plasma polymer [143].

From the cells point of view, the surface is the most important part of the material. It has been shown that cell growth, spreading and viability are closely linked to the anchorage of the cell to the surface [144–146]. Folkman and Moscona, for example, demonstrated that the spreading of en-

dothelial cells could be controlled by modifying the cell-adhesiveness of a polystyrene substrate with different concentrations of poly(2-hydroxyethyl methacrylate) [144]. It is well established that the properties of the material surface contribute to a successful cell adhesion event and the subsequent cell proliferation. Consequently, the study of the interaction between cells and solid surfaces and the modification of surfaces have developed into a main discipline in the biomaterial area. A promising way to perform chemical surface modifications is plasma polymerisation which has already been used successfully to improve the cell adhesion on various substrates (see SECTION 6.3.1). This chapter will first focus on a general introduction to the processes involved in cell adhesion to solid surfaces. The last part of the chapter will summarize previous work on the application of plasma polymer coatings in the biomaterial sector and their interactions with biological environments.

6.1.2   The Adhesion Process

6.1.2.1   Cell-Surface Interactions

When cells approach a surface, they generally do not interact directly with the substrate material. Upon exposure of the material surface to a physiological environment – either in the body or in *in vitro* cell culture studies – its first interaction (within nanoseconds) takes place with water molecules. The water interacts with the top surface layer to form a water shell immediately above the material surface. The orientation of the water molecules in this shell depends on the chemistry of the surface and therefore varies between different materials [147].

In physiological conditions, the aqueous environment also contains a large number of biologically
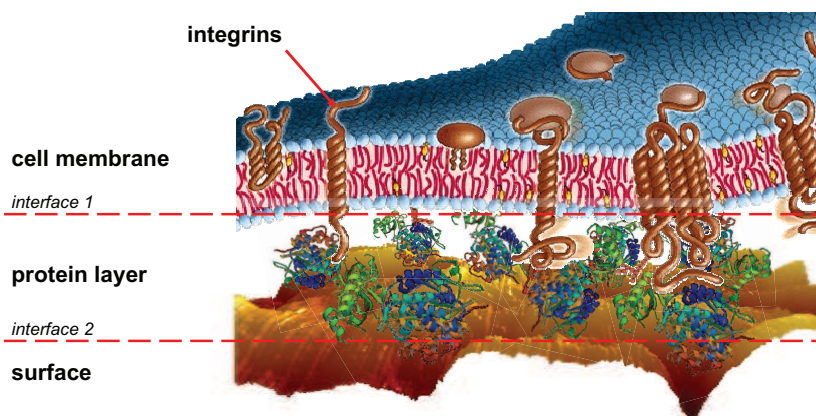
Figure 6.1: Schematic of the cell adhesion process. In protein containing media, proteins adsorb to the sample surface before cell attachment takes place. Cells therefore interact with a protein coated surface. Consequently, two interfaces are created. The cell-protein interaction (*interface 1*) is mediated by integrins situated on the cell membrane and depends on the properties of the protein layer which in turn are governed by the properties of the material surface (*interface 2*). Parts of the images were adapted from [148] and [149].

active molecules, most importantly proteins, that equally have a hydration shell around them [147]. Depending on their concentration, these molecules reach the surface within seconds or minutes, sometimes only limited by diffusion, and thus reach the material surface much faster than cells [150, 151]. The interaction between the hydration shells of the surface and the proteins subsequently influences fundamental kinetic and thermodynamic processes such as protein denaturation or orientation at the interface [147].

Proteins are not only deposited on the surface by adsorption from the surrounding, they can also be expressed by cells and thus change the composition of the protein layer. The general assembly of proteins and other biomolecules that form an insoluble matrix around the cell is called the *extracellular matrix* (ECM). The ECM is important in many normal cell processes such as metabolism, proliferation, differentiation, motility and cytoskeletal organization [150, 152, 153]. Although some cells are able to survive on surfaces without serum proteins or even protein synthesis [154, 155], these are non-physiological conditions that can change the cell activity and contribute to cell death [151].

Cell response therefore takes place between the cell and the protein layer adsorbed to the material (*interface 1* in FIGURE 6.1). A favorable cell response depends on the correct presentation of adhesion promoting structures on the protein layer, which in turn is influenced by the interaction of the protein with the material surface (*interface 2* in FIGURE 6.1) [151]. The processes involved in the adsorption of proteins and their analysis on the surface will be discussed in SECTION 6.2. Here, the focus will lie on the interaction of the cell with the surface bound protein layer.

6.1.2.2 The Formation of Adhesions

The adhesion of cells to a surface is a very complex process in which a multitude of adhesive mechanisms need to be coordinated. The first step for cell adhesion is the recognition of the surface. Only when suitable binding sites – with which proteins in the cell membrane can interact – are presented on the surface will the adhesion process be triggered. Consequently, this leads to the formation of *adhesions* between the cell and the surface. Recent work, however, showed that for some cells (blood, epithelial and chondrocyte cells) an intermediate step exists in the adhesion process between surface recognition and the formation of adhesions and it was suggested that a multistep process (FIGURE 6.2) might have to be considered for other cell types, as well [156].

The large number of chemical groups on the material surface that are presented to the cell – either in an order or in a random manner – can be involved in both strong and weak interactions with the cell. The formation of adhesions requires strong interactions that involve highly specific binding events between epitopes on the surface and receptor molecules from the cell membrane. *Epitopes* are chemically and sterically well defined combinations of chemistries that show a high affinity to the cell receptors [156]. The attractive forces between epitopes and receptors are typically based on hydrogen bonds, hydrophobic and electrostatic interactions that gain their specificity from the well defined structural arrangement relative to each other. The distance over which these attractive force can act is not longer than 0.5 nm in physiological conditions [157, 158]. Consequently, any
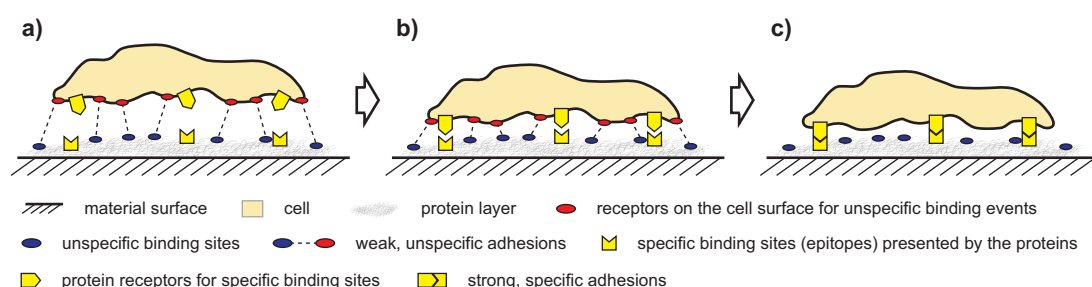
Figure 6.2: Schematic of the multistep cell adhesion model. After recognition of the surface, weak, unspecific interactions are established between the cell and the protein layer (a). This allows enough time for the cell to spread and for adhesion receptors to find specific binding sites (epitopes) on the surface, turn into the right orientation and be activated (b). After strong adhesions are established, the molecules on the cell surface that were involved in the initial interactions are no longer needed and are either degraded or internalized into the cell, allowing the cell to approach even closer to the surface [152].

receptor-epitope interaction requires previous removal of water between the cell receptor and the surface. In addition, a successful binding event relies not only on a collision event between the receptor and the epitope but also requires that the collision occurs in the correct orientation of the epitope and the receptor (FIGURE 6.2 b). The complete formation of a stable adhesion point between the cell and the surface can take several minutes [159].

In the multistep cell adhesion model, the above formation of adhesions is preceded by a faster process based upon unspecific interactions between the cell and the surface (FIGURE 6.2 a). Weak bonds can be established between the cell and random individual points on the surface, causing the cell to change its shape and spread out on the surface. The formation of these interactions can occur in seconds and, if their number is large enough, can provide the necessary strength to hold the cell in place until stable adhesions are created [156]. FIGURE 6.3 provides an overview of the necessary steps involved in the cell adhesion process. The whole process from cell seeding to complete cell attachment to the surface – the approach to the surface from suspension, surface recognition and the adhesion process – generally requires more than an hour [160].

Almost all types of cells that attach to surfaces form connections with the ECM, though the shape, size and distribution of these adhesions can be very different. However, the common feature for all cell surface interactions is the presence of transmembrane cell adhesion receptors that establish a physical link between proteins of the ECM and actin filaments of the cytoskeleton in the cell [161, 162]. The connections of the receptors to the cytoskeleton not only affect intracellular organization but are also presumed to be involved in the formation of receptor clusters that are necessary to provide sufficient strength to the adhesion [153].

There are numerous receptors that contribute to the formation of surface adhesions; two important classes are cadherins and integrins. Cadherins are primarily involved in cell-cell adhesions while integrins predominantly mediate the adhesion of cells to surfaces [153].
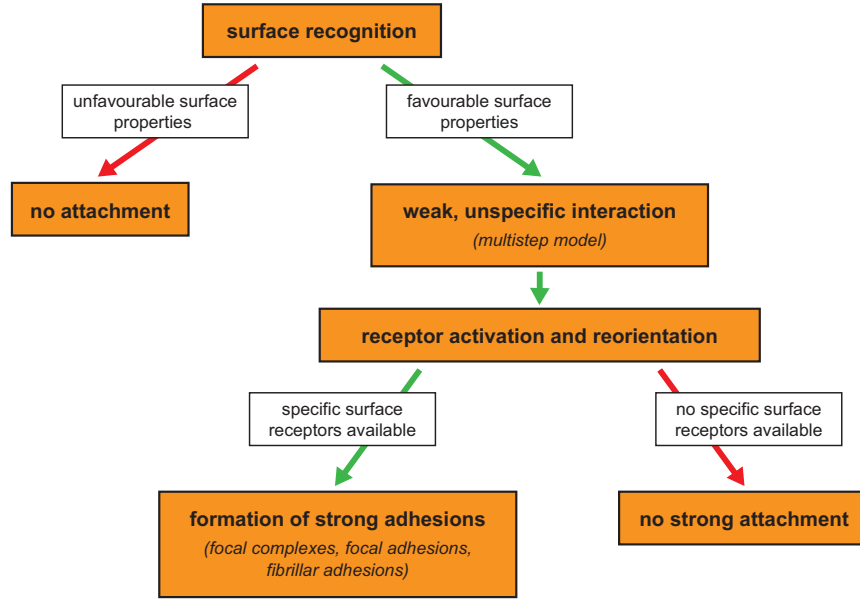
Figure 6.3: Main events between the cell and the surface leading to cell adhesion.

Integrins are heterodimeric proteins with α and β subunits. There are 14 known α and 8 known β subunits that are non-covalently attached to each other in various combinations. So far, more than 20 different types of integrins are known. The most commonly found integrins are $\alpha_5\beta_1$ (for fibronectin) and $\alpha_V\beta_3$ (for vitronectin) that respond to the RGD sequence (see SECTION 6.2) [152, 163]. Even though integrins provide strong bonds with the surface due to their high affinity to certain binding sites, they are not always in an active state and require conformational changes before the formation of adhesions. The stimulus for the activation can be provided either by soluble factors or by the surface [163]. In addition, it has been shown that the connection of integrins to the cytoskeleton is able to contribute to the activation, a process known as *inside-out signalling* [164, 165].

The cell receptors may form different types of adhesions with the ECM. In an initial step to form adhesions, the cell-receptors bind to epitopes presented by the ECM. Subsequently, clustering of the receptors occurs to strengthen the cell-adhesion [152]. The adhesions differ in size, location and morphology (FIGURE 6.4, TABLE 6.1). The most studied types are focal adhesions. *Focal adhesions* – or focal contacts – are elongated, flat structures with a cross section of several micrometer in diameter [166]. They are generally formed at the periphery of the cell [167] and are responsible for strong adhesions between the cell and the surface [152]. The formation of *fibrillar adhesions* takes place in more central locations of the cell; they have elongated or dot-like contact areas [168]. At the edges of the lamellipodium – flat, thin extensions at the cell periphery – *focal complexes* are formed [169]. These adhesions have small dot-like contacts on the surface and are generally associated with cell migration or serve as precursors for focal adhesions [152].
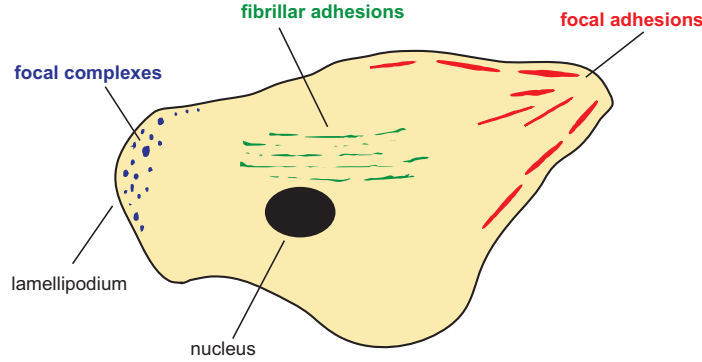
Figure 6.4: Locations of adhesions on the cell [152, 160].

Table 6.1: Properties and classification of cell-surface adhesions [152].

Property	Focal complexes	Focal adhesions	Fibrillar adhesions
Location	Edge of lamellipodium	Cell periphery	Central region of cells
Morphology	Dot-like	Elongated, oval	Fibrillar or beaded
Size (long axis)	1 μm	2 - 5 μm	1 - 10 μm

6.1.2.3 Cell Motility

Cell motility – the ability of cells to move on a surface – is an important process in many applications, including wound healing, tissue engineering and biomedical implants. To enable cellular movement on a substrate, it is necessary that surface adhesions are broken and reformed [170]. Thus, a distinct difference can be observed in the structural organization of adhesions between non-motile and motile cells. While the connections between the integrins and the cytoskeleton are well structured in non-motile cells [171], focal adhesions in motile cells are less organized to allow disassembly and subsequent cell migration [172]. Cell motility therefore requires adhesion forces that are strong enough to keep contact with the surface, but weak enough to allow disassembly of the adhesions [151].

To induce cell movement, the cell first needs to enter into a state of asymmetry. One manifestation of asymmetry are morphological polarities, which are manifested as a clear distinction between a front and a rear site of the cell. These may be induced by temporal or spatial stimuli gradients in the media or on the surface. An important consequence of the polarity is that extensions of active membrane processes such as lamellipodia – where focal complexes are formed – only occur at the front of the cell. The cell stretches out in front to form adhesions, thus creating mechanical stress in the cytoskeleton that is transferred to the rear. This stress together with biochemical regulations leads to the rupture of adhesions at the rear. Hence, cell movement is achieved by an extension of the cell in the front followed by a contraction at the rear. While the cell moves over the newly formed adhesions, more integrins cluster at the binding sites and form larger aggregates to stabilize the adhesion (FIGURE 6.5) [170, 173].
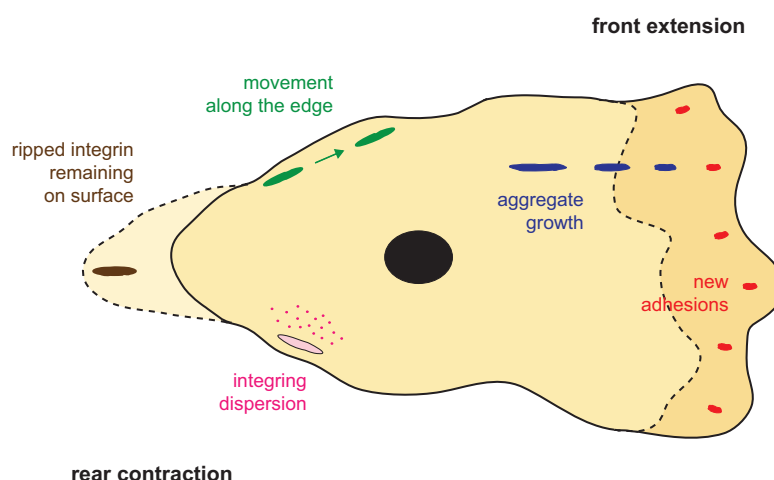
Figure 6.5: Schematic of the dynamics of integrins in migrating fibroblasts. The cell stretches in the front, where new adhesions are formed. The adhesions grow in size as the cell moves across them due to clustering of additional receptors. At the rear the cell contracts, rupturing the adhesions with the ECM. The remaining integrins in the cell membrane either travel as clusters to the front along the cell edge to form new adhesions or are dispersed, using the released integrins in new binding sites [173].

In many cases, the velocity of cell migration was found to be dependent on the rate of adhesion disassembly at the rear [174], whereas the formation of new adhesions generally has little influence on the speed [170]. For fibroblasts (the cell type that will be considered in the experimental work in CHAPTER 7) it has been shown that the bond with the surface is mostly severed by rupture of the adhesions, leaving a large part of the integrins on the surface [170, 175]. The remaining integrins in the cell membrane either disperse to be used for new adhesions in the front or remain aggregated and move forward along the cell edge to form a new connection with the surface (FIGURE 6.5) [170].

6.1.3   Surface Properties Influencing Cell Adhesion

The successful adhesion of a cell depends on the presence of suitable adhesion motifs on the surface. It was established above, that most frequently these adhesion motifs are provided by proteins adsorbed to the material surface [151]. For example, fibronectin contains a sequence of three amino acids (arginine – glycine – aspartic acid) that form the so called *RGD sequence*, a highly specific binding site for many integrins [176]. However, the presence of proteins is not always necessary to stimulate adhesions events. It has been shown, that functionalisation of the material surface with suitable adhesion motifs can promote cell adhesion even in the absence of proteins [150, 177].

Cell attachment to adhesion motifs relies on the correct presentation of these motifs by the protein. Since many essential protein properties (type, amount, denaturation, conformation) depend on the surface properties, the surface indirectly controls the cell response through the protein layer [151]. The protein-surface interactions will be discussed in more detail in SECTION 6.2.

During the manufacturing process, it is the surface of the material and not the protein layer that is modified to achieve a desired cell adhesion. Therefore, most studies have directly correlated cell response to surface properties. It was found early on that for many cell types (fibroblasts, smooth muscle cells, epithelial cells) *wettability* is a major factor that influences cell adhesion, with cell attachment being more favorable on moderately wettable (hydrophilic) surfaces compared to hydrophobic substrates, even if adhesion promoting proteins were pre-adsorbed [3, 178–180]. In addition to the wettability, the *surface charge* has also been shown to have an important influence on cell attachment [3, 179]. However, even though early studies recognized the importance of these factors, the experimental design often did not allow the attribution of cell behavior to one single surface property because of the simultaneous changes of other parameters [3].

Surface properties that are not related to surface chemical effects have also been shown to be of significant importance to cell attachment. Physical properties such as *surface topography*, *surface roughness*, *surface porosity* and *surface texture* may influence cell adhesion to the substrate [181]. The most commonly observed trends indicate that an increase in roughness is accompanied by an increase in cell differentiation and a decrease in cell proliferation [182–186]. However, inverse relationships have been reported, as well [187, 188]. Recently, Biggs *et al.* demonstrated that highly ordered hexagonal nanostructures reduce the adhesion of osteoblasts [189]; cell adhesion increases as the nano-structured surface features were more randomly organized. Later, this effect was also observed for fibroblasts [190]. Similarly, *surface rigidity* has been recognized as an important factor governing cell adhesion [152]. Choquet *et al.* found that fibroblasts respond to a more rigid surface by increasing the bond strength between the integrins and the cytoskeleton to exert more force onto the substrate [191]. Another recent addition to cell-surface interactions was the discovery by Sun *et al.* that cell adhesion can be controlled by *surface chirality*. They found that larger numbers of macrophages and neutrophiles attach to the L-enantiomer of *N*-isobutyryl-cysteine than to its D-form [192].

The fine control of the spatial distribution of the above properties allows an even more elaborate influence on cell adhesion. Patterning of the surface has often been used to obtain defined areas with and without cell adhesion [16, 19, 193]. Surfaces with gradients of the above properties have also been developed for biological applications [6, 7]; the use of chemical (plasma polymer) gradients for cell adhesion studies will be reviewed in more detail in SECTION 6.3.

6.2 Protein Adsorption to Surfaces

6.2.1 Protein Properties

6.2.1.1 Relevant Proteins

Due to the large number of proteins present in serum and their interactions with each other, cell-protein-surface interactions are very complex. Proteins have been identified that either promote cell-adhesion (fibronectin, vitronectin, vinculin, fibrinogen) [194] or inhibit it (albumin). In CHAPTER 8 of this work, the interaction of fibronectin and albumin from bovine serum with the plasma polymer

gradient will be investigated. This paragraph will focus on the introduction of these two example proteins and their properties and discuss protein-surface interactions and the analysis of proteins on the surface.

6.2.1.2 Fibronectin

Bovine fibronectin is a high molecular mass, multidomain glycoprotein that is found in soluble form in blood and in insoluble form in the extracellular matrix [195, 196]. It plays key roles in important cellular processes such as cell adhesion, spreading and motility and wound healing [196, 197]. Bovine fibronectin contains two almost identical subunits that are linked to each other by two disulfide bonds near the C-terminus [197]. The molecular weight has been placed in the region of 450 kDa (about 225 kDa for each subunit) [198]. The concentration of the protein in plasma is about 0.3 mg/ml [199]. Electron microscopy showed that in its extended form on a surface the two subunits of fibronectin are about 60 to 70 nm in length and 2 nm in diameter, joined at an angle of 70° [200]. In solution, the shape can vary from fully extended to a more compact, globular conformation. Near physiological conditions, the globular shape is preferred [201, 202]. Under extreme pH values or when the ionic strength is increased, a partial opening of the structure is observed [203, 204]. The most commonly measured length of fibronectins extended form in solution is 20 to 30 nm [201]. These conformational changes have been found to be reversible, inducing no significant changes in the protein's secondary structure [201, 202].

The cell adhesive property of fibronectin is attributed to a short key sequence of amino acids in the middle of the protein chain. This adhesion motif was initially identified as an RGDS (arginine – glycine – aspartic acid – serine) sequence [205], though later on it has been shown that the *RGD sequence* is sufficient in most cases [176]. Other sequences in the vicinity of the RGD sequence such as PHSRN (proline – histidine – serine – arginine – asparagine) were shown to have synergistic effects that enhance the cell adhesive properties of fibronectin [206]. In solution, the cell binding motif is hidden inside the protein, but becomes exposed upon adsorption of fibronectin to a suitable surface [194]. The right conformation of the protein is essential for the activation of its cell adhesive properties [207].

6.2.1.3 Albumin

Bovine albumin is a highly soluble, multidomain, non-glycosylated and very stable protein that consists of only a single chain [208–210] and has a molecular weight of approximately 67 kDa [211]. Taking up over 50% of the total protein content in serum, albumin is the most abundant protein. It is found in the plasma in concentrations of about 40 mg/ml. Its main functions are the binding of ligands for transport processes, antioxidation and the maintenance of osmotic pressure [210]. The tertiary structure of bovine albumin was subject to some controversy; initially described as an elongated ellipsoid, more recent data indicates that albumin has a heart-shaped structure that was approximated to a triangular prism of 8 x 8 x 8 x 3 nm [209].

6.2.2 Protein-Surface Interactions

6.2.2.1 Driving Forces For Protein Adsorption

The necessary driving force for proteins to adsorb to a solid substrate is largely based on the cumulative effect of a large number of non-covalent interactions [212]. The adhesive forces that hold the protein on the substrate can vary substantially, mainly depending on the chemistry of
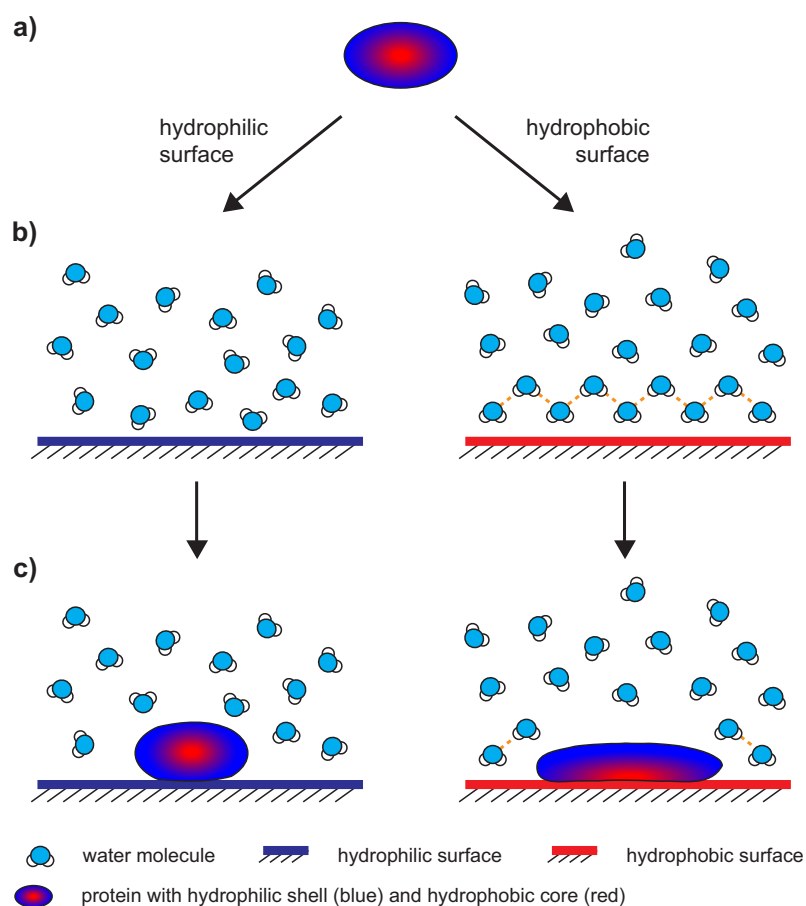
Figure 6.6: Schematic of the adsorption of proteins on hydrophilic and hydrophobic surfaces. a) In solution, the outside of the proteins mainly contains polar groups, while hydrophobic moieties are oriented towards the center of the molecule. b) The water on a hydrophilic material surface has a random orientation, whereas some degree of order is observed in the vicinity of a hydrophobic surface. c) When adsorbing to the hydrophilic surface the protein mostly maintains its shape and the interaction is largely based on hydrogen bonds and electrostatic interactions. Upon adsorption to a hydrophobic surface, the protein's conformation changes significantly, allowing the apolar groups of the molecule to move to the outside to interact with the substrate. A strong driving force for this interaction is the increase in entropy gained by the disassembly of the ordered water layer above the hydrophobic surface.

the surface. Electrostatic interactions rely on the attraction of opposite charges. The degree of ionisation both on the surface and on the protein changes with the ionic strength and the *pH* of the solution; these two parameters therefore have an important effect on the adsorption of proteins, especially on polar surfaces [151, 213]. Hydrogen bonds equally contribute to the ensemble of adhesive forces when polar groups are present on the material surface. In both cases, the adhesion force is created by a *negative enthalpy* released by the approach of the protein to the surface [151].

The interaction of proteins with surfaces of different wettability is a widely studied phenomenon. On both hydrophilic and hydrophobic surfaces, the water layer between the protein and the surface has to be removed before any adhesive forces can have an effect [151]. On hydrophilic surfaces, both the polar groups of the protein and the water interact favorably – over hydrogen bonds – with the substrate. The protein therefore has to compete with the water for interaction with the surface, and it was reported that protein adsorption is significantly hindered on substrates with a strongly bound water layer. On hydrophobic materials, the interaction of water with the surface is unfavorable. As a result, self association between the water molecules is increased (FIGURE 6.6) [214]. When the water molecules are replaced by a protein, their organization near the surface is broken down, increasing the disorder of the system. Thus, the adsorption of proteins to hydrophobic surfaces is accompanied by a considerable *entropy increase* which is the driving force for the adsorption [212]. In addition, even though in aqueous solutions polar groups of the protein preferentially face outwards [212], reducing the interaction of the water with the hydrophobic core, it was estimated that 40 - 50% of the outer regions of smaller proteins are occupied by non-polar groups [151]. Hence, interaction of the protein with the surface may also be more favorable than with water.

The initial adsorption of proteins occurs rapidly and can be as fast as 5 seconds [215]. Although reports about the effect of the surface wettability on the amount of adsorbed proteins are not consistent, in general proteins adsorb in larger quantities on hydrophobic substrates [216, 217]. Factors such as presence/absence of other proteins and their concentrations, surface charge and *pH* can affect these results [150, 151]. In general, the concentration of proteins on the surface is much increased compared to that in solution; the surface concentration of proteins was estimated to be 10^3 times greater [215]. The amount of adsorbed protein is generally the result of an equilibrium between desorption and adsorption [218]. In some cases, however, the adsorption is so strong that the proteins can not be removed in the presence of dilute protein solutions [151].

6.2.2.2 Competitive Adsorption

For practical applications, protein adsorption from a solution containing a mixture of proteins is of significant importance [151]. In this case, the proteins present in solution have to compete for interactions with the material surface. The composition of the adsorbed protein layer depends on the concentration of each protein, its mobility in solution and its affinity towards the surface [219].

A sample immersed in a protein solution will first be covered by the smallest, most mobile proteins such as albumin (FIGURE 6.7). In blood, the fast adsorption of albumin is additionally favored by its abundance in serum [220]. However, if the initially adsorbed proteins are not strongly
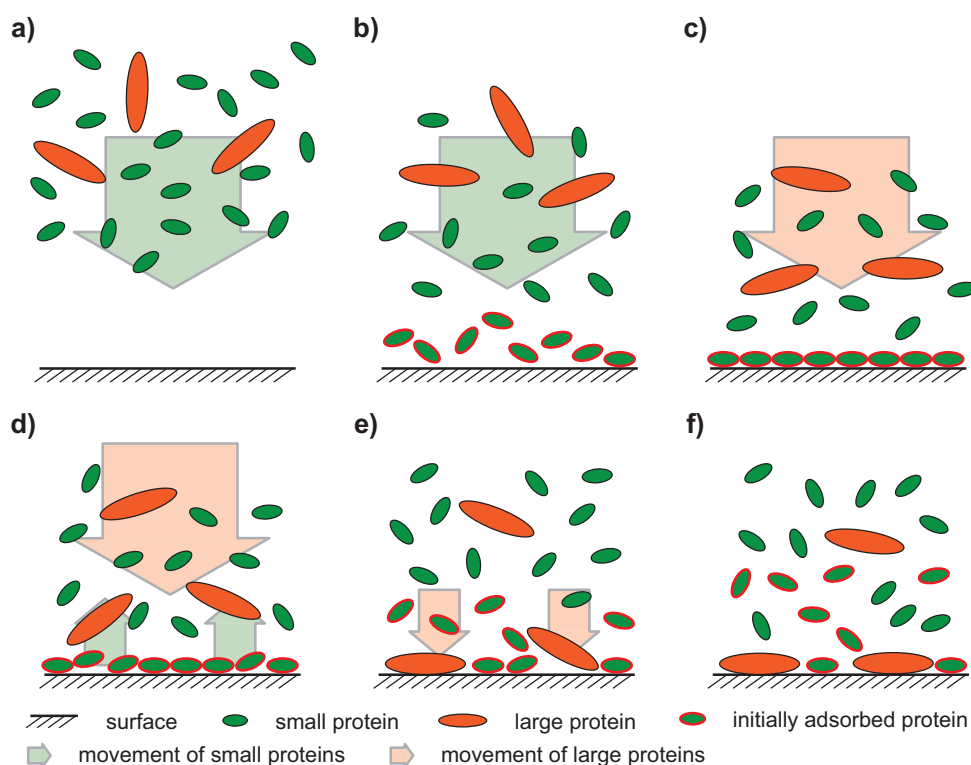
Figure 6.7: Schematic illustration of the Vroman effect. On a surface exposed to a mixture of small (green) and large (orange) proteins (a). Smaller proteins adsorb first because they are more mobile (b). Larger proteins reach the surface later (c). Some of the smaller proteins subsequently desorb from the surface (d), allowing larger proteins with higher affinity to the surface to adsorb (e) and partly replace the initial protein layer (f).

bound to the surface, displacement by larger proteins (such as fibronectin) that travel more slowly to the adsorption site is possible if these have a higher affinity [221]. This phenomenon of displacement of small proteins by larger ones on a surface is known as *Vroman effect*. Consequently, the adsorption of proteins to the surface can be reversible [222, 223].

Protein displacement does generally not occur in a simple two step process where the desorption of one protein is followed by the adsorption of another. Instead, gradual displacement of the first protein takes place. Partial detachment of the adsorbed protein from the surface is followed by partial adsorption of the second protein to the vacated surface area. This then continuous stepwise until the first protein is completely desorbed [220, 224].

Even though the Vroman effect has been observed on many occasions, it is not a general principle that always occurs when surfaces are exposed to protein mixtures. Because the displacement relies proteins having different affinities to the surface, the outcome largely depends on the surface properties [225–227]. The Vroman effect has been reported to be more pronounced on hydrophilic surfaces where the protein-surface interaction is weaker than on hydrophobic surfaces [151].

6.2.2.3   Conformational Changes

Proteins adsorbed to the sample surface are the main adhesive that binds the cell to the surface. The forces ensuring adhesion of the proteins to the surface have been discussed in Section 6.2.2.1. In Section 6.1.2 it was explained that for cell adhesion to the protein layer, specific binding sites (epitopes) need to be present on the protein layer. However, it is not enough to present the right sequence of functional groups, an *active binding site* also needs to be available in the correct sterical arrangement [228, 229]. In many cases, adsorption of the protein to a surface is necessary to achieve a conformation that exposes its cell-binding sites and makes it available to the cell [151, 230, 231]. During protein adsorption, however, additional conformational changes can be triggered in the protein that deactivate the binding sites and may even lead to irreversible denaturation of the protein. Therefore, the adhesion strength of cells to a protein covered surface relies not only on the presence of proteins that carry adhesion motifs, the binding sites also need to be presented in the right conformation [232].

Most proteins are subject to at least small conformational changes when adsorbing to a solid substrate from solution [211, 233, 234]. It has been shown that the chemistry of the surface can induce changes in the conformation and orientation of proteins [207, 235, 236]. Many proteins are subject to significant conformational changes when adsorbing to hydrophobic surfaces [223, 237, 238]. In solution, the hydrophobic moieties of the molecule are oriented towards its center and form a hydrophobic core [151]. On the hydrophobic surface, interaction between the sample and the apolar parts of the protein is preferred. To achieve this, the protein's hydrophobic areas have to be moved outwards, towards the surface, causing its tertiary structure to change. An additional driving force for this process is the additional freedom of movement of the bonds in the protein gained because the hydrophobic parts are no longer forced to the center by an hydrophilic environment. Beside the disassembly of the organization of the water molecules at the surface (see Section 6.2.2.1), the additional degrees of freedom of the chemical bonds also adds to the increase in entropy in the system [151, 211] that can lead to a strengthening of the adhesion over time [227, 239]. In fact, the adsorption of proteins to hydrophobic surfaces can be strong enough to cause denaturation of the protein, preventing desorption of the molecule back into the solution [151].

Studies of the effects of surface topography on the conformation of proteins are scarce and have not yet shown a common trend, not least because the topographies used so far are very different from each other [151]. A more comprehensive study was carried out by Roach *et al.* who investigated the effect of surface curvature on protein conformation by adsorbing albumin and fibrinogen on particles of different diameter [240]. Albumin was found to retain its globular shape on smaller particles (high surface curvature) but took on a flatter structure on larger particles (low surface curvature). In contrast, fibrinogen – which has an elongated shape – was found to be distorted on small particles, presumably adsorbing along its long side and bending around the surface. On larger particles, Roach *et al.* suggested that fibrinogen retains its structure and adsorbs to the surface on its short side.

The protein conformation on a surface can also change due to the presence of other proteins (type and concentration) in the solution [233, 241]. When protein adsorption occurs from dilute solutions of one type of protein, more space is available on the sample surface, making contact between larger areas of the protein and the surface possible. This can consequently lead to a change in conformation compared to adsorption from a concentrated and/or mixed solution, where proteins have to compete for space on the surface and are therefore laterally surrounded by other proteins, forcing them to keep a more compact structure [150, 242]. Co-adsorption of cell adhesion promoting proteins with other proteins has been used to prevent denaturation and maintain the conformation of the active sites that would be lost if adsorption took place from a single protein solution [243].

6.2.3 Analysis of Proteins on Surfaces

6.2.3.1 Challenges in the Analysis of Protein Layers

Identification of the nature, quantity and activity of the protein layer that mediates cell response to solid substrates can provide additional information about the processes involved in cell adhesion. Even though in an application the success of a biomedical material in the body can be simplified to a surface-cell relationship, knowledge about the behavior of the protein layer can aid the development of new materials and help to understand the observed cell response.

SECTION 6.2.2.1 explained that a successful cell response depends on the nature of the protein, the amount of protein adsorbed and the conformation the cell-adhesion mediating protein has on the surface. Since several key proteins that mediate cell adhesion have already been identified [180, 195], the focus of many studies was the analysis of the amount and conformation of adsorbed cell adhesive proteins on the surface [151]. This resulted in the development of numerous analytical tools that have been employed to answer these questions.

Quantification of proteins on surfaces has been achieved with quartz crystal microbalances (QCM) [218, 244, 245], ultraviolet UV spectroscopy [246], radioactive [232, 247–249] and fluorescent labeling [225, 250] and X-ray photoelectron spectroscopy (XPS) [251, 252]. The amount of protein can also be analyzed by measuring the thickness of the protein layer, for example using surface plasmon resonance (SPR) [217, 253], ellipsometry [245, 254–256] or optical waveguide lightmode spectroscopy (OWLS) [253, 257]. To study conformational changes, atomic force microscopy (AFM) [235, 252, 258], fluorescence resonance energy transfer (FRET) [243, 259, 260], time of flight secondary ion mass spectrometry (ToF-SIMS) [251], transmission electron microscopy (TEM) [261], electron spin resonance (ESR) [262], attenuated total internal reflection (ATR) and Fourier transform infrared spectroscopy (FTIR) [218, 232, 263] have all been used. Protein activities were estimated by enzyme linked immuno sorbent essays (ELISA) [254, 264–266] or reaction with labeled antibodies [267, 268].

For the current project, a significant challenge in the analysis is the gradual transition of the surface chemistry; thus, only techniques with small spatial resolution (submillimeter range) are suitable. Imaging of proteins on patterned surfaces has previously been achieved with AFM [235],

TEM [261] and confocal microscopy [250, 260]. These methods, although excellent for the analysis of features on the micrometer and submicrometer scale, are not able to image the whole gradient sample in a single experiment. Moreover, AFM and TEM can not readily distinguish between different types of proteins when co-adsorbed from a heterogeneous solution and are thus not suitable to study displacement effects. Therefore, below only those methods that proved successful in providing supportive information to the present work will be introduced in more detail.

6.2.3.2 Quartz Crystal Microbalance

A quartz crystal microbalance (QCM) detects an increase in mass on the surface of the sensing area. In this technique, the sensing element is based on a quartz crystal disk of typically 10 - 20 mm in diameter with gold electrodes on either side (FIGURE 6.8). A current with a suitable radiofrequency oscillation applied at the electrodes oscillates the quartz crystal at its resonance frequency. Because of the piezoelectric property of the quartz crystal, a mass change on one of the gold electrodes, which acts as the active sensing area, caused a shift in the resonance frequency [269]. The frequency profile is recorded over time and can be converted into a mass change per surface area using the *Sauerbrey equation*:

$$\Delta m = -C \frac{\Delta f}{n_f} \tag{6.1}$$

where Δm is the adsorbed mass, C the mass sensitivity constant (typically 17.7 ng cm^{-2} Hz^{-1} for a 5 MHz crystal), Δf the frequency change and n_f the overtone of the resonance frequency [269].

The active surface can be functionalised or coated to investigate adsorption phenomena on different substrates. However, the Sauerbrey relation only holds true for materials with a low viscoelasticity. When the measurement is carried out in solution, water may couple into the film, producing a hydrogel-like material able to dampen the oscillation. The Sauerbrey equation yields most accurate results in water when applied to data obtained from thin, rigid samples. Höök *et al.* showed that no significant errors will be committed if the film thickness is less than 100 nm [270].
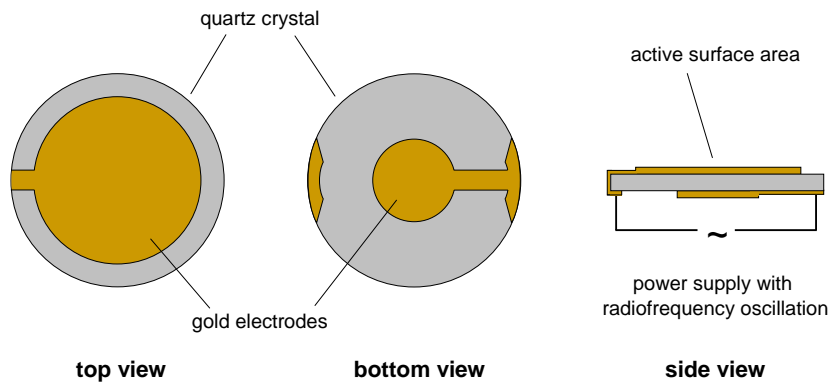
Figure 6.8: Schematic of the quartz crystal in a quartz crystal microbalance.

6.2.3.3 UV Spectroscopy

Ultraviolet (UV) spectroscopy is based on the absorption of UV light when it passes through a solution of molecules containing chromophoric groups (conjugated double bonds). Part of the monochromatic UV light that passes through the sample becomes absorbed, bringing the chromophore to an excited state (FIGURE 6.9). The intensity of the UV light is measured before (I_0) and after (I) passing through the sample to calculate the absorption A [271, 272]:

$$A = -log\frac{I}{I_0} \tag{6.2}$$

The intensity of the absorption strength for a given molecule depends on the concentration c of the solution and can be calculated via the *Lambert-Beer law* [271, 272]:

$$A = \epsilon\, c\, l \tag{6.3}$$

where ϵ is the extinction coefficient of the sample and l the length of the cuvette.

Some amino acids such as tryptophan, tyrosine and phenylalanine are chromophores and retain these properties in the protein [273, 274]. Many proteins therefore absorb UV light between 200 and 300 nm. Measuring the absorption of protein solutions of different concentration at 280 nm is a commonly used way to obtain calibration curves that allow the determination of the concentration of a sample solution [274].
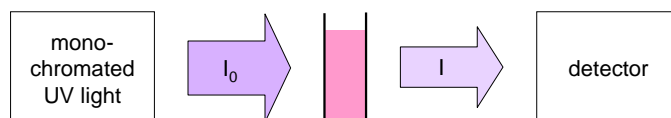
Figure 6.9: Schematic of the experimental setup of a UV spectrophotometer.

6.2.3.4 Fluorescence Spectroscopy

The phenomenon of fluorescence is based on the ability of an atom or molecule to absorb photons which are then reemitted as light at higher wavelengths. Similar to UV active molecules, fluorescently active molecules (or fluorophores) require a conjugated π-bond system; however, instead of releasing the absorbed energy in a non-radiative way (for example thermally or over internal conversion), some of the gained energy is reemitted as light. This process is described in the Jabloński diagram (FIGURE 6.10) [274].

The qualitative detection of a fluorescent signal can be used to prove the presence of a fluorescent compound and/or image the spatial distribution of the fluorophore. When compared to a calibration curve, it can also be used to quantitatively determine the amount of the compound in question on the surface [274].
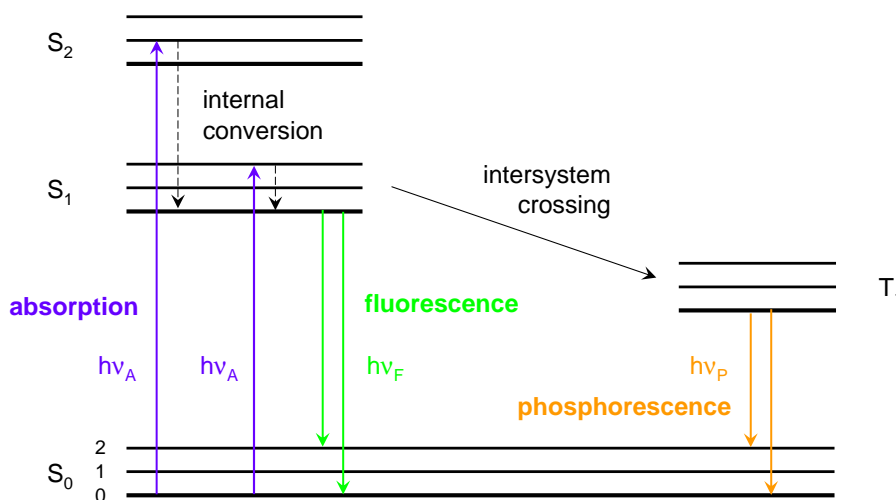
Figure 6.10: Jabloński diagram describing the basic electron transitions in fluorescence and phosphorescence. Upon absorption of light ($h\nu_A$), electrons are excited from the ground state (S_0) to an excited state (S_1 or S_2). From there, energy can be lost in a non-radiative way, for example if the electrons fall down to the lowest level energy level of the excited state or transit to a lower excited state (internal conversion from S_2 to S_1). Electrons then fall back to the ground state, loosing their energy as fluorescence ($h\nu_F$). Phosphorescence is caused when excited electrons undergo a forbidden transition and pass over to the triplet state T_1, where they take longer to relax to the ground state and emit their remaining energy ($h\nu_P$) [274].

Even though most proteins contain intrinsic fluorophores due to the presence of tryptophan, tyrosine and phenylalanine, the fluorescent signal obtained from proteins is generally weak and not very specific. Therefore, the covalent binding of external markers is often used to label the protein. In addition, this allows different proteins to be labeled with different markers that can then be detected simultaneously [274].

6.3 Biological Applications of Surfaces

6.3.1 Plasma Polymers

6.3.1.1 Biomolecule Immobilization

Surface functionalisation is a common way to change the properties of the material surface and introduce not only specific functional groups, but also attach adhesion motifs, DNA segments or biomolecules to the substrate. However, the possible chemical reactions that can be used to functionalise the surface and the success of the method depend on the chemistry of the surface itself and is therefore limited by the functional groups present on the material. Plasma polymerisation provides a convenient intermediate step to introduce the desired functional groups on the surface

because plasma polymers can be deposited on almost any substrate independent of its chemical composition.

NH$_2$ and COOH based plasma polymers are most commonly used to immobilize biomolecules. In both cases, carbodiimide reactions allow the covalent binding of either amines to carboxyl groups or *vice versa* [52]. For example, DNA [275, 276], heparin [34], glucose oxidase [277], RGD [177], RGDS [278] and collagen [279] have been immobilized on amine or carboxyl based plasma polymers. Less popular linkers are alcohols – due to their lower reactivity – and aldehydes; plasma polymers with these groups have been used to bind heparin [280] on hydroxy-groups and collagen and albumin-PEG composites on aldehydes [52].

In addition to biomolecules, polymer chains have been attached to surfaces coated with plasma polymers, as well. For example, Gombotz *et al.* attached poly(ethylene oxide) to an amine containing plasma polymer [281] while Chu *et al.* designed protein repellant surfaces from plasma polymerised di(ethyleneglycol)monovinylether containing streptavidin [282].

6.3.1.2 Surface Chemistry

The chemistry of a surface can readily be modified by depositing a plasma polymer on the substrate material. Thus, functional groups can be created on the surface that enhance or impede protein adsorption and/or cell adhesion to the substrate.

Most commonly, relatively hydrophilic plasma polymer containing amine- and carboxyl-groups have been used to enhance cell adhesion. MacNeil and coworkers showed that human keratinocytes can be cultured on acrylic acid based plasma polymers (ppAAc), forming a tissue that can be transferred to a wound bed [63, 283, 284]. They were also able to show that epithelial cells can be cultured in a serum free media on ppAAc. In addition, other publications demonstrated the suitability of ppAAc to sustain fibroblasts in cell culture [285, 286]. Fibroblasts were also successfully cultured on plasma polymerised allylamine (ppAAm) [112] and isopropylalcohol [17]. Moreover, ppAAm was shown to support growth and proliferation of hepatocytes [116].

Other hydrocarbon based plasma polymers reduced or prevented cell attachment. Mar *et al.* used a tri(ethyleneglycol)dimethylether film deposited from a plasma to prepare a non-fouling surface for an SPR biosensor [287]. Plasma polymerised tri(ethyleneglycol)monoallylether [288], di(ethyleneglycol)monovinylether [253, 289] and ethylene oxide [290] have also been shown to have non-fouling properties towards proteins and cells.

It has been demonstrated by Canavan *et al.* that plasma polymerised poly(*N-iso*propyl acrylamide) (pNiPAM) has similar properties as conventional pNiPAM [291]. Thus, sheets of endothelial cells were obtained from plasma polymerised pNiPAM using its thermosensitivity as demonstrated before on conventional pNiPAM.

6.3.1.3 Spatial Control of a Biological Response

Plasma polymers have been successfully used to create patterned surfaces. Cells cultured in chemically or topographically confined spaces can show significant changes in adhesion and other cell

processes. Patterned surfaces from plasma polymers have previously found applications as cell-based sensors and drug discovery assays [292].

Patterned plasma polymer surfaces are generally realized with the aid of a physical mask such as copper TEM grids. In these cases, a good contact between the mask and the substrate was imperative [15]. Bullett *et al.* prepared patterns of plasma polymerised allylamine (ppAAm) on plasma polymerised 1,7-octadiene and demonstrated that both immunoglobulin G and neuronal cells preferred to attach to the more hydrophilic ppAAm areas [110]. Patterns of plasma polymerised hexane – which prevented the adhesion of ovary cells – were realized by Mitchell *et al.* on tissue culture polystyrene [16]. Cell adhesive tracks of plasma polymerised acrylic acid (ppAAc) were prepared on poly(ethylene oxide) (PEO) based plasma coatings by Sardella and coworkers [293]. They found that fibroblast adhesion is restrained to the ppAAc coated areas, and that cells even migrate from the PEO to the ppAAc surface during the initial phase of cell culture.

Besides metal grids, a poly(D,L-lactide)-film was used to prepare patterned plasma polymer samples. Even though this method can not provide the same intricate patterns that can be achieved with grids, Thissen *et al.* prepared very sharp transitions of acetaldehyde and allylamine plasma polymers to the underlying (PEO) substrate [19]. They also showed that significantly more collagen adsorbed to the plasma polymers than on PEO, which effectively impeded the outgrowth of epithelial tissue to PEO.

Besides plasma polymerisation, several other techniques have been used to prepare patterned surfaces for biological applications. Matsuda and Sukawara obtained patterned surfaces by irradiation through masks and photochemically fixing phenyl-azido derivatised polymers to specific areas of the substrate. They showed that these surfaces can be used to obtain patterned growth of endothelial cells [294, 295]. Okano *et al.* used electron beam irradiation through metal masks to graft polymers onto pNIPAM substrates in a patterned manner. These surfaces were then used to obtain spatially defined cell growth of fibroblasts on the surface that subsequently yielded patterned cell sheets [296]. This technique also allowed the co-culture of rat primary hepatocytes and bovine endothelial cells to obtain cell sheets consisting of two different cell types [297, 298]. Most recently, using these patterned surfaces, the shape of cell sheets has also been controlled, allowing the preparation of cell sheet strips from endothelial cells and fibroblasts [299].

6.3.2 Gradient Surfaces

6.3.2.1 Studying the Biointerface

Knowledge about the interaction of proteins and cells with surfaces of well defined properties is essential for the development of biomaterials. To this end, a fast evaluation of the effect of many different surface properties is desirable. Gradient surfaces have been used extensively to investigate biological interactions and relate them to specific surface properties. This is usually done by changing one property of the surface as a function of distance on the sample while keeping all other attributes constant. In this way, gradients in wettability [4, 179, 300–302], polymer chain density [90, 303–305], charge [306, 307] roughness [308–311] and porosity [312] have been employed

to study the response of cells and proteins. Carboxyl-group density gradients have been shown to guide the outgrowth of neuronal cells [313]. Microscale gradients of RGD containing peptides that show gradual transitions in the same length-scale as cells have been used to study a non-uniform distribution in the microenvironment of melanoma cells [314].

Recently, orthogonal gradients where two different properties are changed in directions perpendicular to each other have attracted the interest of some researchers. On these samples two different surface properties are changed independent of each other so that synergistic and antagonistic relationships between them can be explored. Bhat *et al.* prepared orthogonal gradients in molecular weight and grafting density of poly(2-hydroxyethylmethacrylate) (PHEMA) that where used to evaluate fibronectin adsorption and the adhesion of osteoblasts on the surface [315].

6.3.2.2 Controlling Cell Activity

Gradients can also be used to apply stress to cells, forcing them to provide a directional response. Cell migration can be affected by gradients in chemistry, an effect that has been called *haptotaxis* and was first introduced by Carter [316]. The concept of haptotaxis therefore inherently relies on the presence of a gradient on the sample surface. Brandley and Schnaar showed that a density gradient of surface bound peptides containing the RGD sequence directs redistribution of melanoma cells [317]. Using linear and exponential gradients, they also demonstrated that the observed effects depend on the gradient profile.

6.3.2.3 Plasma Polymer Gradients

Very little work is available on the application of plasma polymer gradients in biological studies. The adsorption of immunoglobulin G on plasma polymer gradients of octadiene and acrylic acid was explored by Parry *et al.* [33]. Robinson *et al.* prepared a *co*-polymer gradient (see SECTION 3.1.3) of plasma polymerised allylamine and octadiene [34]. The resulting density gradient of amine-groups was used to immobilize heparin on the surface. Barry *et al.* achieved deposition of hexane (ppHex) and allylamine (ppAAm) plasma polymers in the interior of porous scaffolds. They thus obtained gradients of ppAAm to ppHex from the outside to the inside of the scaffold and showed that on these samples a more uniform cell density distribution within the scaffold could be achieved [8, 46].

Chapter 7

Cell Response

7.1 Cell Culture on Plasma Polymer Gradients

7.1.1 Experimental Design

To assess the suitability of the gradients prepared in PART I of this work for biological applications, the response of 3T3 fibroblasts to these surfaces was investigated. These cells were previously used on similar surface chemistries created in the interior of 3D scaffolds to achieve an even distribution of cells throughout the whole scaffold [46]. However, in the case of these complex 3D bodies, a relation between the surface properties and the cell response could not be established. SECTION 7.3 in this chapter will address this issue by comparing the results from cell culture with the surface analysis data presented in PART I.

Cell culture was carried out in Dulbeccos Modified Eagle's Media (DMEM) supplemented with 10% foetal calf serum (FCS) under standard cell culture conditions (see APPENDIX E for details). It should be noted that the presence of serum in the media results in the rapid formation of a protein layer on the sample surfaces. The cell response therefore occurs between the cells and the adsorbed proteins as described in CHAPTER 6.

7.1.2 General Characteristics of Adhered Fibroblasts

In an initial assessment of the cell response, 3T3 fibroblasts were cultured on uniform plasma polymer samples. Cell attachment and spreading was observed to start one to two hours after cell seeding. On hydrophobic ppHex deposited on top of ppAAm (ppHex/ppAAm), little to no cells adhered. The few cells found on ppHex/ppAAm were round and did not show any extensions that would indicated the formation of adhesions with the surface (FIGURE 7.1 a). In contrast, the fibroblasts on moderately hydrophilic plasma polymerised allylamine (ppAAm) attached well to the surface and had numerous extensions that suggested the formation of adhesions (FIGURE 7.1 b). This is consistent with previous observations in literature where fibroblasts were cultured on ppHex and ppAAm coated glass and poly(D,L-lactic acid) [8]. Cells cultured on the gradients showed the
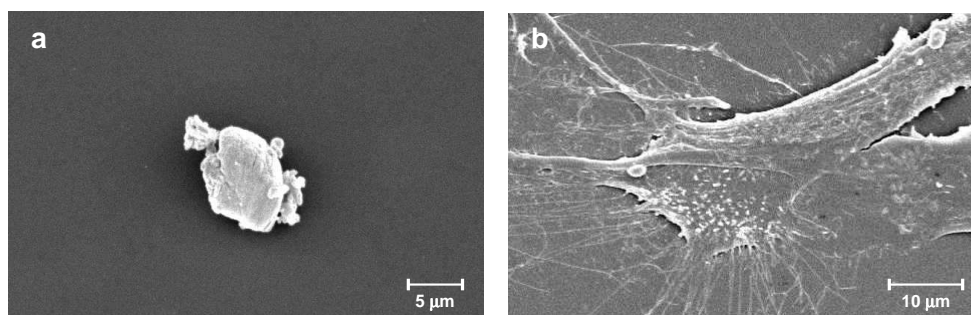
Figure 7.1: Scanning electron microscope images of fibroblasts on uniform ppHex/ppAAm and ppAAm after 1 day of culture. Almost no cells were found on ppHex, but the single cells observed were round and had no extensions (a). Fibroblasts adhered well to ppAAm where they were flat and showed many extensions indicating good cell adhesion (b).

same spreading characteristics that were observed on ppAAm on the transition area. Some round cells were observed both on the ppHex side and the transition area.

To test if fibroblasts are viable on the samples, a live-dead stain was carried out after 1 day of cell culture (FIGURE 7.2). All cells on the surface proved to be alive as indicated by the green fluorescence of Calcein AM. On the gradients, a gradual increase in cell number could be observed. The absence of cells containing the red fluorescent dye (Ethidium homodimer I) shows that there are no dead cells on the surface. Dead cells, however, tend to have weak to no adhesions with the surface and are therefore easily washed away from the substrate during the staining procedure. Therefore, this assay does not prove that there are no dead cells present on the surface in cell culture, but it shows that the surface provides a suitable substrate for fibroblasts and is able to sustain cell adhesion.

In this cell culture experiment, no cells were observed on ppHex/ppAAm or the ppHex side of the gradient. It was also noted that there are more cells on uniform ppAAm than on the ppAAm side of the steep gradient – the ppAAm side of the shallow gradient has not been captured in this experiment. These observations will be discussed in more detail below.

7.1.3 Evolution of the Cell Density on the Gradients

In this paragraph, the cell response of 3T3 fibroblasts on the gradient samples and on uniform ppAAm and ppHex/ppAAm will be investigated. On ppAAm, the cells displayed a characteristic fibroblast-type morphology during all 4 days of cell culture. The cells became confluent on ppAAm after 3 days. Therefore, the number of cells on all samples were only assessed for the first 3 days. On uniform ppHex, no adherent cells and only a very small number of rounded cells were observed. This is consistent with previous studies performed on different substrates that showed that higher cell densities are often obtained on more hydrophilic surfaces [194, 318, 319]. The non-cell adhesive properties of ppHex have been demonstrated before by Mitchell *et al.* with Chinese hamster ovary cells [16]. As has been shown in SECTION 7.1.2, cells with round morphology as those observed on
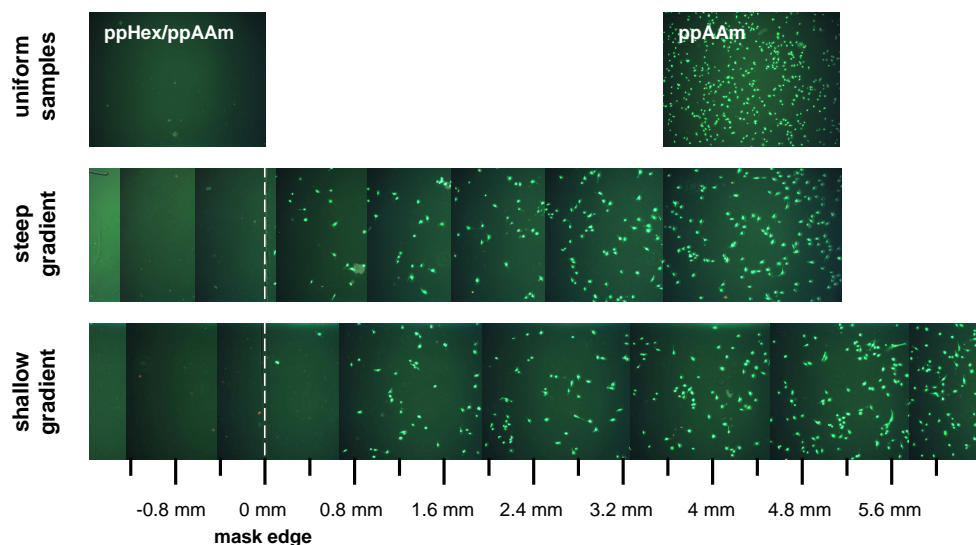
Figure 7.2: Live-dead stain of 3T3 fibroblasts on the plasma polymer gradients and the uniform control samples after 1 day of culture. All cells remaining on the surface are alive (green fluorescence) and no dead cells (red fluorescence) were observed. ppHex side: left; ppAAm side: right; white lines indicate the beginning of the gradients.

ppHex do not have a significant number of extensions and are likely close to apoptosis. These round cells were therefore not included in the assessment of the number of viable cells on the surface.

Qualitatively, a similar behavior to the uniform ppHex and ppAAm samples was observed on the ppHex and ppAAm ends of the gradients. While very few or no cells attached to the unmasked ppHex-coated part, the cell density on the ppAAm end of the gradients was high. For the steep gradient, the zone in which the cell density decreased from the ppAAm to the ppHex surface was less than 1 mm in width, showing a sharp boundary of adherent and proliferating cells at the interface between the unmasked (ppHex side) and masked (gradient) side of the sample (FIGURE 7.3). On the shallow gradient the cell density gradually increased from the mask edge towards the ppAAm part of the sample while only a very small number of cells attached to the ppHex coating (FIGURE 7.4). The increase in cell density was observed over a length of about 7 mm on the shallow gradient after which the cell density became constant. Again, the cells became confluent on most parts of the gradient by the fourth day.

The increase in cell number over time on the gradient samples could have several explanations. Since all suspended cells were removed from culture before the measurements on the first day new cell adhesion from the media can be ruled out. Thus, the increase in cell numbers was attributed to proliferation and/or migration. The overall shape of the trends in FIGURE 7.3 and 7.4 does not change and the increase in cell density approximately stays the same on each of the incremented positions during the 3 days of cell culture. Therefore, it is assumed that cumulative cell migration does not have a significant influence in the cell density distribution and the increase in cell number is attributed to cell proliferation.

When comparing the uniform ppHex samples to the ppHex end of the gradients, the cell numbers were comparable and near zero. However, when compared to the position on the gradient that corresponds in wettability to uniform ppAAm ($x = 1.3$ mm and $x = 6$ mm for the steep and the shallow gradient, respectively), two times as many cells were observed on uniform ppAAm samples at all time intervals (FIGURE 7.3 and 7.4). After attachment, the cell density on both the gradients and the uniform ppAAm samples approximately doubled every 24 h. On the ppAAm side of the gradient samples, the cell number increased approximately 2.3 times on the shallow and 2.7 times on the steep gradient from day 2 to day 3. The close proximity of the carbon, nitrogen and oxygen concentration on the samples shown in TABLE 3.2 in SECTION 3.3.1.3 indicates that this effect is not likely based on differences in the chemical composition. Since non-adhered cells were removed after 24 h of culture, no adhesion of new cells can take place on the surface and this can therefore
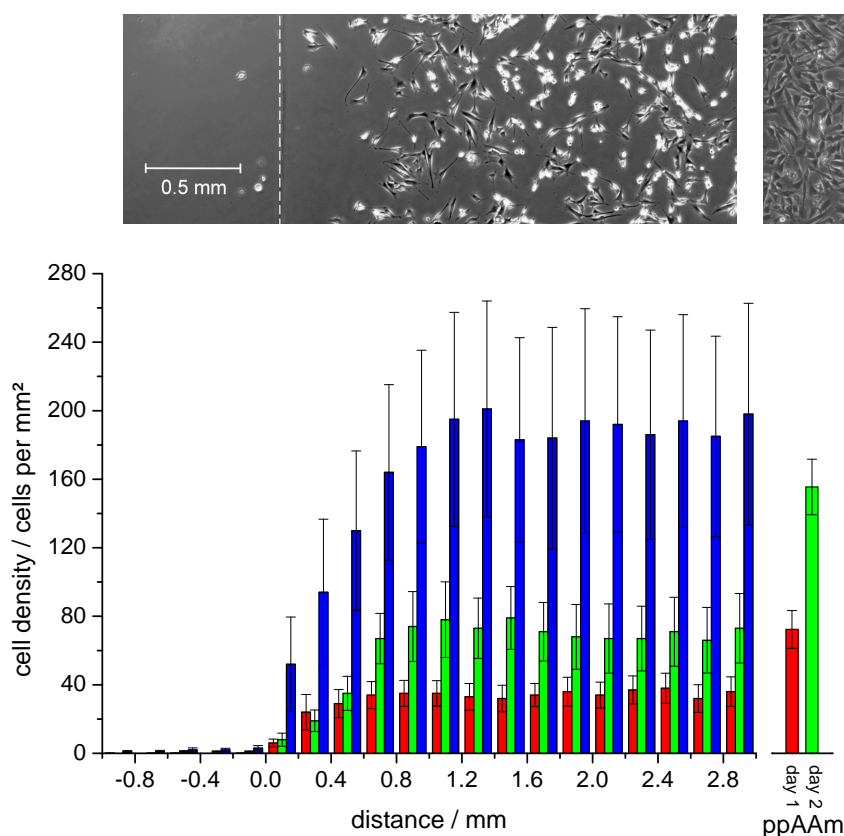
Figure 7.3: Average number of cells in 0.2 mm increments along the steep gradient (left: ppHex; right: ppAAm) after 1 (■), 2 (■) and 3 (■) days of incubation. Error bars represent SEM; $n = 9$. The sample/mask interface was set at the origin of the x-axis. The columns to the right are the average cell numbers on the uniform ppAAm samples after 1 and 2 days ($n = 35$). The top images show the typical cell response after 2 days on the gradient (the vertical line marks the start of the gradient) and the uniform sample.
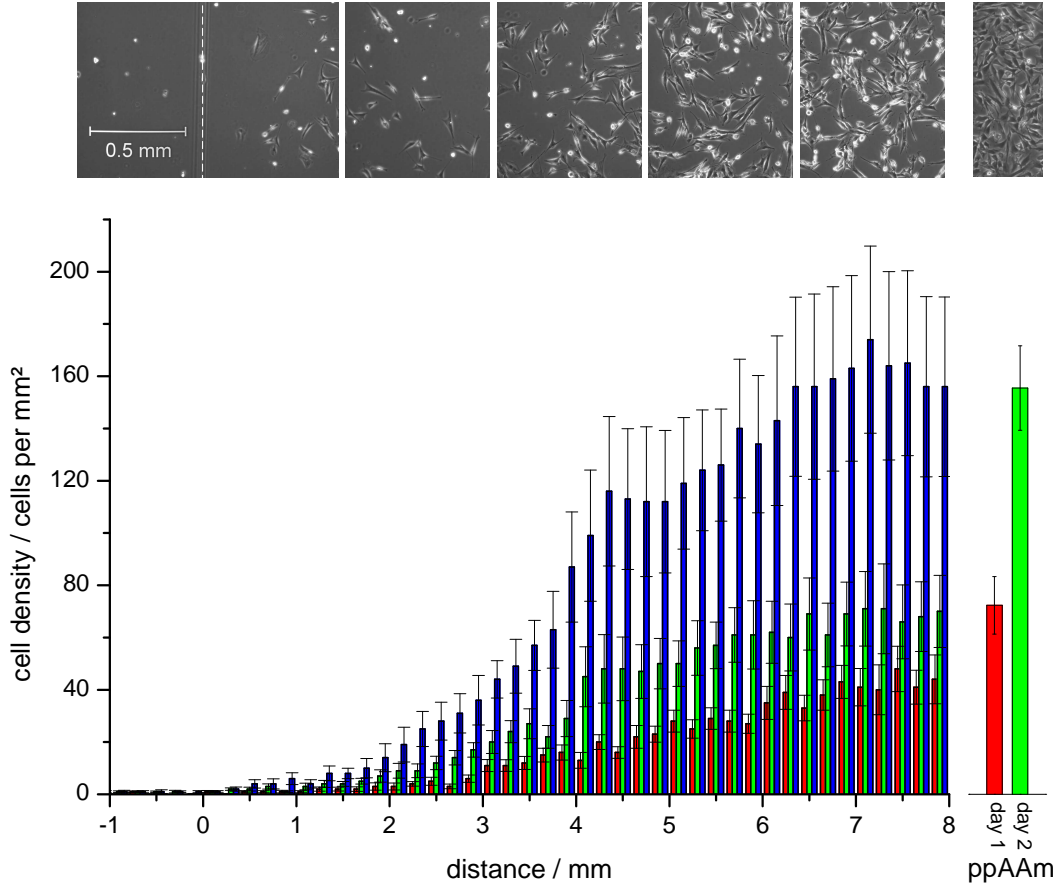
Figure 7.4: Average number of cells in 0.2 mm increments along the shallow gradient (left: ppHex; right: ppAAm) after 1 (■), 2 (■) and 3 (■) days of incubation. The error bars represent SEM; $n = 15$. The sample/mask interface was set at the origin of the x-axis. The columns to the right are the average cell numbers on the uniform ppAAm samples after 1 and 2 days ($n = 35$). The top images show the typical cell response after 2 days on the gradient (the vertical line marks the start of the gradient) and the uniform sample.

not explain the difference between uniform ppAAm and the ppAAm side of the gradient, either. It is also obvious that the proliferation rate on the three samples is the same after day 1; thus, the difference in the cell densities between the uniform sample and the ppAAm end of the gradient samples must be related to events occurring within the first 24 h of cell culture.

7.2 Cell Culture of Non-Proliferating Cells

It has been established in SECTION 7.1.3 that any differences in cell number and therefore any influence the surface has on the cell adhesion must relate to processes occurring within the first day of culture. Consequently, two explanations for are possible: (i) proliferation on the uniform ppAAm

sample was faster than on the gradients and/or (ii) the initial adhesion of cells is higher on the uniform sample so that proliferation on the uniform ppAAm starts earlier than on the gradients.

In order to assess the effect of proliferation on the cell density on the samples, non-proliferating fibroblasts were cultured on the surfaces under the same conditions as before. In this experiment, proliferation does not contribute to the cell density on the surface. Hence it is a good measure of the number of cells that remain adhered to the surface after initial cell seeding. By separating cell proliferation from cell adhesion, it is possible to estimate the number of cells initially adhered on the gradients as compared to the uniform ppAAm sample. Consequently, it can be determined if, within the first 24 h, the untreated cells proliferate faster on the uniform ppAAm surface than on the ppAAm end of the gradient.

Proliferation can be inhibited by treatment of the cells with Mitomycin-C (Mit-C) which cross-links complementary DNA strands [320–323]. Even though contradictory results have been reported on the cytotoxicity of Mit-C [324–326], its cytotoxic effect has been shown to be concentration dependent [327, 328] and Mit-C has been proven to be non-toxic at the concentration used in the present experiment [327, 329].

No Mit-C-treated cells were observed to adhere on ppHex. The average total number of Mit-C-treated cells on the ppAAm samples decreased over 4 days (to 91%, 65% and 49% of day 1 for days 2, 3 and 4, respectively). This was taken as evidence that cell proliferation had been successfully blocked by Mit-C; the decrease in cell number over time was attributed to cell death and hence
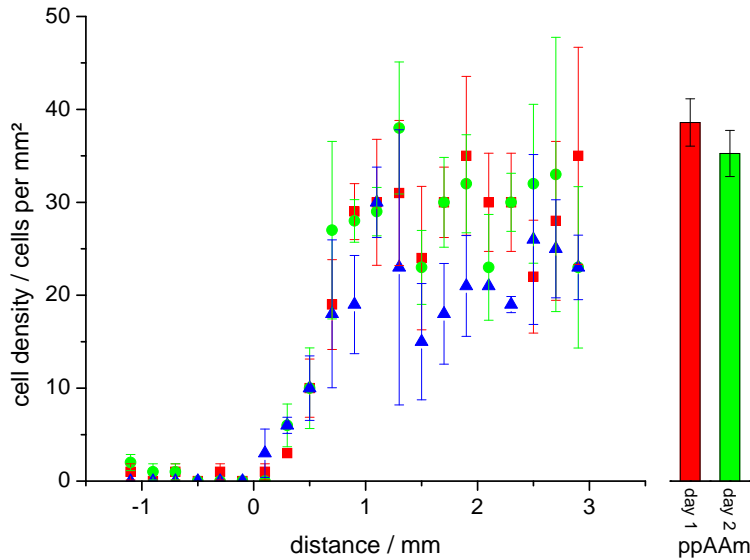
Figure 7.5: Average number of Mitomycin-C treated cells in 0.2 mm increments along the steep gradient (left: ppHex; right: ppAAm) after 1 (■), 2 (●) and 3 (▲) days of incubation. The error bars represent SEM; $n = 3$. The sample/mask interface was set at the origin of the x-axis. The columns to the right are the average cell numbers on the uniform ppAAm samples after 1 and 2 days ($n = 15$).
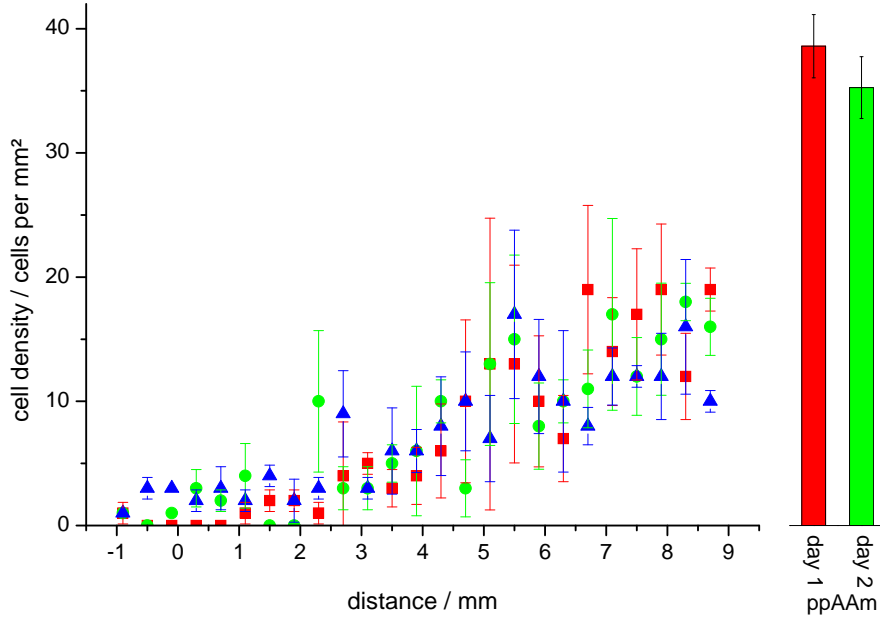
Figure 7.6: Average number of Mitomycin-C treated cells in 0.2 mm increments along the shallow gradient (left: ppHex; right: ppAAm) after 1 (■), 2 (●) and 3 (▲) days of incubation. For clarity, only every second datapoint is shown. The error bars represent SEM; $n = 3$. The sample/mask interface was set at the origin of the x-axis. The columns to the right are the average cell numbers on the uniform ppAAm samples after 1 and 2 days ($n = 15$).

detachment. Thus, to minimize the influence that a decreasing number of Mit-C cells over time has on the data and its interpretation, comparison of the results from experiments with Mit-C-treated cells to those with untreated cells is carried out on the basis of the first day of cell culture.

The cell density of the Mit-C-treated cells on the gradients increased from the ppHex to the ppAAm end (FIGURE 7.5 and 7.6), similar to the experiment with the untreated cells. Since the seeding densities were not exactly the same for the experiments with the Mit-C treated and the untreated cells, the measured cell densities on the gradient samples were normalized to those measured on uniform samples from the same culture batch. Thus, the Mit-C treated and the untreated cell densities can be compared in the same graph (FIGURE 7.7). The untreated cells on the ppAAm end of the gradient reached a density of approximately 50 - 60% of that on the uniform ppAAm sample after 24h of culture. A similar distribution and relative cell number was observed for the Mit-C-treated cells. The fact that the relative cell number of the untreated and the Mit-C-treated cells was approximately the same shows that the proliferation rate of the untreated cells within the first 24h is not faster on the uniform than on the gradient sample. Hence, it can be concluded that the number of cells initially adhered to the uniform samples is approximately twice as high as on the corresponding position on the gradient. Moreover, the overall number of Mit-C-treated cells and their spatial distribution did not change significantly over 3 days, indicating that
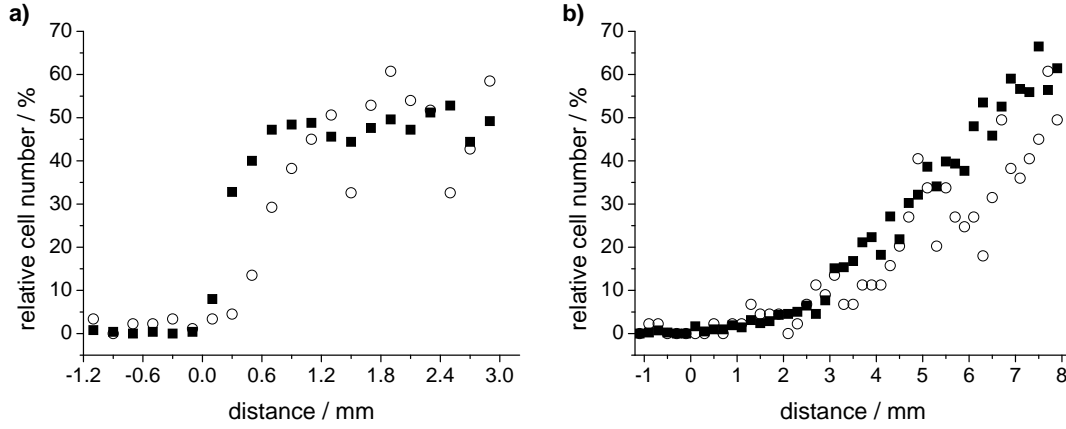
Figure 7.7: Relative number of Mitomycin-C treated (○) and untreated (■) cells on the steep (a) and shallow (b) gradients after 1 day of culture normalised to the uniform ppAAm samples. For the uniform samples $n = 35$ and $n = 15$ for the untreated and the Mit-C treated cells, respectively. For the gradient samples, $n = 3$ and $n = 6$ (steep) and $n = 15$ and $n = 9$ (shallow) for the untreated and Mit-C treated cells, respectively.

migration does not have a major effect on the observed differences between the gradients and the uniform samples. Thus, this experiment supports the second hypothesis, that the initial number of cells attached to the uniform ppAAm samples is higher than that on the gradient samples, resulting in a cell density on the uniform sample that is twice that of the corresponding ppAAm position on the gradient. Therefore, for a similar chemistry and wettability on the ppAAm position of the gradient to the uniform ppAAm sample there is a higher initial cell adhesion on the latter within the first 24h. In addition, it can be concluded that increases in cell number of untreated cells over 2 days (to day 3 of the experiment) are due to proliferation of those cells that adhered to the samples within the first 24 h of the experiment.

The reason for the different initial cell adhesion between uniform ppAAm and its corresponding position on the gradients remains unclear. The influence of surface chemistry on initial cell adhesion has been demonstrated previously by Arima *et al.* on self assembled monolayers, showing distinct differences between hydrophobic and hydrophilic substrates [330]. The present work, however, indicates that besides the mere presence of functional groups, other surface parameters – in particular the properties of the surrounding surface area and cells – are likely to influence the initial cell adhesion. The transferability of findings on a gradient sample to uniform samples with the same surface properties is a key requirement when gradients are used as screening tools. However, this comparison has often been disregarded in literature, either because differences were found but not discussed [310, 313, 317, 331], or because results from control samples were missing altogether [304, 315, 332]. In a study published by Ruardy et al., an increase in the mean spread area of cells was observed on a wettability gradient from the hydrophobic to the hydrophilic end [331]. Though not further discussed in the paper, the comparison of the data on the gradient with

that from uniform samples of corresponding surface chemistry showed a major difference in the mean spread area of the cells. It is possible that the differences between the gradient and the uniform samples are based on differences in the protein expression by the cells. It has been shown before that a counter-gradient of the extra cellular matrix (ECM) proteins laminin and collagen I affects the protein expression of epithelial cells [333]. In the present case, it can be expected that the ECM is different on the uniform and the corresponding area on the gradient sample which could change the cell adhesive properties of the surface. A more detailed investigation of this effect on the plasma polymer gradients was not within the limits of this thesis and has to be explored elsewhere.

7.3 Cell Response and the Relation to Surface Properties

7.3.1 Plasma Polymer Gradients not Exposed to PBS

The following two sections will explore the relationship between the cell density on the gradient shown in SECTION 7.1.3 and the surface properties presented in PART I. If the gradual increase in cell number with distance on the gradient can also be found when the cell density is plotted against a surface property, the origin of the gradual cell response could be explained as a function of this property. Since the transition on the steep gradient is very narrow and therefore more susceptible to errors in the alignment of the sample in the instruments, only the shallow gradient will be considered here.

The cell density of the shallow gradient was plotted against surface analysis data from WCA, XPS and AFM measurements. Here, surface data from freshly deposited, untreated samples will be considered first; relationships with surface data from samples exposed to PBS will be discussed in SECTION 7.3.2. Those surface properties that showed a trend in their relationship with the cell density are shown in FIGURE 7.8. The WCA was the only surface property that displayed a relationship with a linear trend similar to those in SECTION 7.1.3. FIGURE 7.8 a shows that the cell density increased as the WCA decreased on all 3 days of cell culture. For all days, high cell densities were observed on surfaces with low WCA values (ppAAm end). Very few cells attached on the hydrophobic side (ppHex end). The cell density increased as the WCA decreased towards the ppAAm end of the gradient, indicating a close relationship between the WCA and the cell response. When comparing these results to the uniform samples, it was found that the hydrophobic ppHex shows the same cell response as the hydrophobic end of the gradient. On the uniform ppAAm the cell density was always greater than that observed on the corresponding section on the gradients.

When plotted against XPS data, the cell density showed an exponential profile with the N/C ratio that becomes more distinct over the first 3 days of cell culture (FIGURE 7.8 b). Below a threshold value (N/C $\sim$ 0.15) no cell adhesion was observed. Above this value, the cell adhesive properties of the surface increased rapidly. Even though this trend was very different from the linear increase of the cell density observed over distance, it indicates that the presence of nitrogen-functionalities might contribute to the cell adhesive properties of the surface. Uniform ppHex behaved similar to the ppHex end of the gradient, but the cell number on uniform ppAAm was

greater than on the ppAAm end. This was also accompanied by an increased N/C ratio, allowing for the possibility that the increased number of nitrogen on the surface could affect the adhesion of cells on ppAAm. However, the higher N/C ratio on ppAAm only reflects small differences in the elemental composition and does not necessarily indicate the presence of cell adhesion promoting groups.

To explore which chemical groups relate to the cell density in the same way as the N/C ratio, the cell number was also plotted against the relative amount of functional groups on the gradient. Only the hydrocarbon (C−H) and imine/alcohol (C=N/C−O) groups showed the same trend (FIGURE 7.8 c and d). An exponential increase in cell density was observed when the amount C−H groups
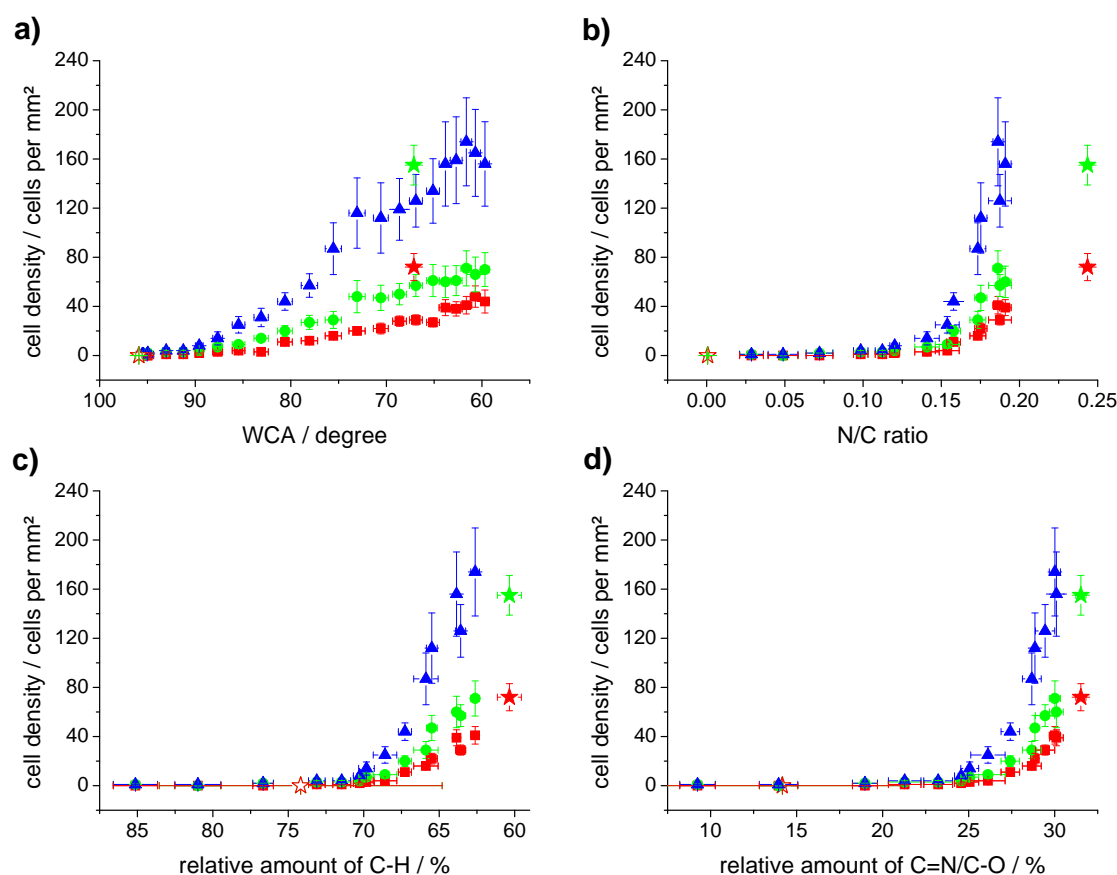
Figure 7.8: Relationship between surface properties of unexposed plasma polymer samples and cell densities on day 1 (■), day 2 (●) and day 3 (▲). The corresponding points for uniform samples on day 1 (red) and day 2 (green) are indicated by ★ and ★, respectively (closed: ppAAm, open: ppHex/ppAAm). Each graph is displayed such that the ppHex side of the gradient is situated at the left and the ppAAm side at the right. Error bars represent standard errors of the mean (cell density: n = 15 and 35; WCA: n = 15 and 22; XPS: n = 3 and 3; for the gradient and uniform samples, respectively).

decreased and when the amount of C=N/C−O groups increased, suggesting that the presence of the latter might have a positive effect on the cell response.

The higher N/C ratio on ppAAm compared to the ppAAm end of the gradient could suggest a link to the increased number of cells observed on uniform ppAAm. However, this difference is not reflected in the percentage of the functional groups identified to be related to the increase in cell number above. This together with the fact that the WCA seems to display a much stronger relation to the cell density on the surface makes it unlikely that the difference in cell number on uniform ppAAm and the ppAAm end of the gradient can be attributed to the difference in the N/C ratio.

7.3.2 Plasma Polymer Gradients Exposed to PBS

To ensure that the comparison between cell response and surface properties is valid, surface analysis data should be used that was acquired from samples in conditions as close to the cell culture environment as possible. The present section will focus on the relation of the cell densities to surface analytical data from plasma polymer samples exposed to PBS (see CHAPTER 5) and explore the differences to the relationships found in SECTION 7.3.1.

As has been shown in SECTION 5.2.1.1, the WCA profile of the gradient changed dramatically; it is therefore not surprising that a plot of the cell density as a function of the WCA did not show a linear relationship. As suggested by the WCA profile on the gradient in FIGURE 5.11, cell adhesion only related to the hydrophilic part of the sample, which was close to 47°.

FIGURE 7.9 shows those surface properties measured on samples exposed to PBS that showed trends when related to cell culture data. The cell density increased as a function of the roughness of the gradient measured when immersed in PBS (FIGURE 7.9 a). As the roughness of the surface decreased from the ppHex to the ppAAm side of the sample, the surface increasingly supported cell adhesion. The relationship between the N/C ratio and the cell number was similar to that observed in SECTION 7.3.1, although the threshold above which cell adhesion occurred slightly decreased due to the loss of polar functional groups during exposure to PBS (FIGURE 7.9 b). This was again related to a decrease in the relative amount of C−H and an increase in the relative amount of C=N/C−O on the surface (FIGURE 7.9 c and d).

From the plots in FIGURE 7.8 and 7.9 it can be concluded that the surface property that shows a trend closest to the cell density distribution along the length of the gradient is the WCA measured on a sample that has not previously been exposed to PBS. The increased roughness observed on the gradient when immersed in PBS also suggests a slight relationship towards the cell number, but does not exactly match the cell adhesion profile in FIGURE 7.4. In addition, it has been argued that the surface roughness is connected to the WCA measured after exposure to PBS (see SECTION 5.2.2). Therefore, even though significant changes in the surface properties of the gradient were identified in CHAPTER 5 when the samples were exposed to PBS, surface analysis of the untreated sample still provided the most suitable description of the cell-surface relationship.

Even though an influence of the surface roughness can not be excluded, it can be assumed that the WCA of the untreated sample largely governs the response of 3T3 cells on the present plasma polymer gradients. This is in agreement with previously published data on the cell response to SAMs of varying chemistries and wettabilities [334]. In the case of a ppHex overlayer on ppAAm, the cell response is therefore determined by the increase in WCA as the thickness of the ppHex layer is increased, obstructing the ppAAm surface chemistry. In SECTION 3.3.1.3 the thickness of the ppHex layer was shown to vary between 0 and 0.4 nm. It is therefore suggested that the cell response of 3T3 fibroblasts mainly relates to the chemistry of the top 0.4 nm of the surface.
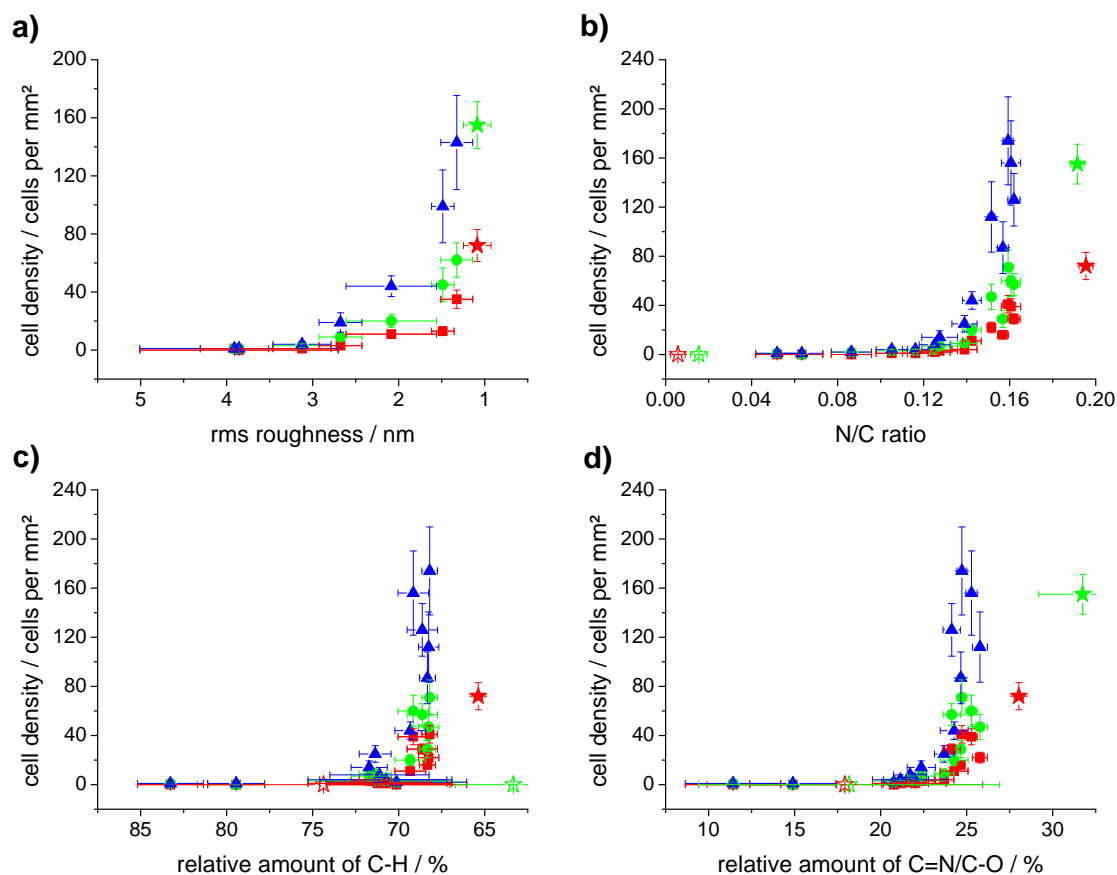
Figure 7.9: Relationship between surface properties of plasma polymer samples exposed to PBS and cell densities on day 1 (■), day 2 (●) and day 3 (▲). The corresponding points on uniform samples on day 1 (red) and day 2 (green) are indicated by ★ and ★, respectively (closed: ppAAm, open: ppHex/ppAAm). Each graph is displayed such that the ppHex side of the gradient is situated at the left and the ppAAm side at the right. Error bars represent standard errors of the mean (cell density: n = 15 and 35; WCA: n = 15 and 22; XPS: n = 3 and 3; for the gradient and uniform samples, respectively).

7.4 Summary

The aim of this chapter was to investigate the cell response of 3T3 fibroblasts to the plasma polymer gradients, to compare the results to the uniform plasma polymer samples and to identify surface properties that control the cell response. The fibroblasts were shown to adhere and grow well on ppAAm but not on ppHex/ppAAm. On the steep gradient, a clear boundary in the cell adhesion was observed between the unmasked (ppHex) and the masked (ppAAm) area of the sample. When fibroblasts were cultured on shallow gradients, the cell number increased from the ppHex to the ppAAm side of the gradients, with little to no cells on the hydrophobic ppHex part of the samples. The cells that adhered showed typical spread fibroblast morphologies and were proven to be viable and proliferate over three days; after the fourth day of cell culture they reached confluency.

The cell number on uniform ppAAm samples did not match the cell density on positions with a corresponding WCA on the gradients but was generally twice as high. By culturing non-proliferating cells on all samples, it was shown that this difference is not related to different proliferation rates of the cells on the samples, but is due to an increased number of cells that adhere to the uniform ppAAm within the first 24 hours of culture. The reason for the increased cell adhesion to uniform ppAAm was not identified, but it was suggested that it could relate to differences in the extra cellular matrix due to protein expression which would change the extracellular matrix and affect cell adhesion.

When plotting the cell density against surface analysis data from PART I of this thesis, only the WCA measured on freshly prepared samples showed the same gradual change in cell number as that observed along the length on the gradient. This indicates a close relationship between the cell response of 3T3 fibroblasts and the wettability of the gradient surface, suggesting that the cells respond to the properties of the top 0.4 nm of the surface.

Chapter 8

Protein Adsorption

8.1 Adsorption and Displacement of Proteins on Plasma Polymers

8.1.1 Relevance of Protein Adsorption and the Vroman Effect

To identify some of the driving forces behind the formation of the cell density gradients on plasma polymer gradient surfaces described in CHAPTER 7, the adsorption of proteins to plasma polymer surfaces was investigated. On the material surface, the presence of cell-adhesive proteins – proteins that present specific binding sites that stimulate cell adhesion – is generally required to promote the attachment of 3T3 fibroblasts. It has been explained in CHAPTER 6 that both the presence of cell adhesive proteins and the correct orientation and conformation of the binding sites are important for the cell adhesion process. In this chapter, the adsorption of two model proteins, albumin and fibronectin, will be investigated. Fibronectin is a serum protein that contains the RGD sequence, a well known cell adhesion motif. It has also been shown that hydrophilic surfaces (OH based SAMs) allow fibronectin to maintain its cell-adhesive function while cell attachment was greatly reduced on hydrophobic CH_3-based SAMs [335]. This was true for the individual adsorption of fibronectin as well as the adsorption of the protein from a mixture of fibronectin and vitronectin. In addition, fibronectin adsorbs in high quantities on nitrogen containing plasma polymers where it was also shown to promote the adhesion of endothelial and fibroblast cells [52].

One hypothesis to explain the gradient in cell density is based on the Vroman effect. Albumin is the most abundant protein in serum and among the first proteins that adsorb to the material surface. A larger, cell adhesion promoting molecule such as fibronectin, which contains the RGD sequence, would need to displace albumin to be able to adhere to the surface. Here, a main focus will be to establish if protein displacement takes place on the gradient. If the Vroman effect is observed on the samples, it is possible that the protein displacement depends on the surface properties and therefore results in larger quantities of cell adhesive proteins on one part of the gradient than on the other. The dependance of fibroblast attachment on the surface concentration of fibronectin has

been demonstrated previously by Plummer *et al.* [336]. This chapter will also investigate if protein displacement changes as a function of distance along the gradient surface.

8.1.2 Uniform Plasma Polymers

8.1.2.1 Measurements on Uniform Plasma Polymers

The adsorption of proteins from solutions containing albumin and/or fibronectin was quantified with quartz crystal microbalance (QCM) measurements. The proteins were adsorbed on uniform ppAAm, ppHex/ppAAm and ppHex *individually* (either albumin or fibronectin), *sequentially* (first albumin, then fibronectin) and *competitively* (albumin and fibronectin at the same time). Typical curves for the mass change on the plasma polymers for each condition are shown in FIGURE 8.1. In TABLE 8.1 the average results for these experiments are listed.

8.1.2.2 Single Protein Adsorption

Both albumin and fibronectin adsorbed on all three uniform plasma polymers (FIGURE 8.1 a and b). The adsorption of albumin was complete after approximately 4 min. For fibronectin the mass change leveled off after 15 min on the hydrophobic surfaces while it was still not completely flat on ppAAm within the timeframe set for the experiment. The amount of both proteins on ppAAm was much higher than on ppHex (BSA: 69%; Fn: 126%) or ppHex/ppAAm (BSA: 78%; Fn: 110%). The mass change on ppHex and ppHex/ppAAm was not significantly different. Protein adsorption therefore takes place on all three uniform plasma polymer samples and none of these surfaces are protein repellant.

These results stand in contrast to data from literature that describe a larger amount of albumin (c = 1 mg/ml) [6, 337] and fibronectin (c = 0.02 mg/ml) [338] being adsorbed on hydrophobic surfaces compared to hydrophilic samples. However, the high affinity of fibronectin to nitrogen-

Table 8.1: Mass change calculated from frequency shifts of the QCM measurements after adsorption of proteins to uniform plasma polymers.

Proteins [a]	Mass change [b] / ng cm^{-2}		
	ppHex	ppHex/ppAAm	ppAAm
Albumin [c]	336 ± 39	319 ± 45	569 ± 49
Fibronectin [c]	65 ± 14	70 ± 23	147 ± 31
Albumin $\rightarrow$ Fibronectin [d]	338 ± 39	321 ± 46	568 ± 40
Albumin + Fibronectin [e]	385 ± 25	368 ± 34	599 ± 52

[a] Protein concentrations were 4 mg/ml and 0.03 mg/ml for albumin and fibronectin, respectively.
[b] The data is an average of 3 measurements; errors represent standard deviations.
[c] Single protein adsorption.
[d] Sequential protein adsorption.
[e] Competitive protein adsorption.
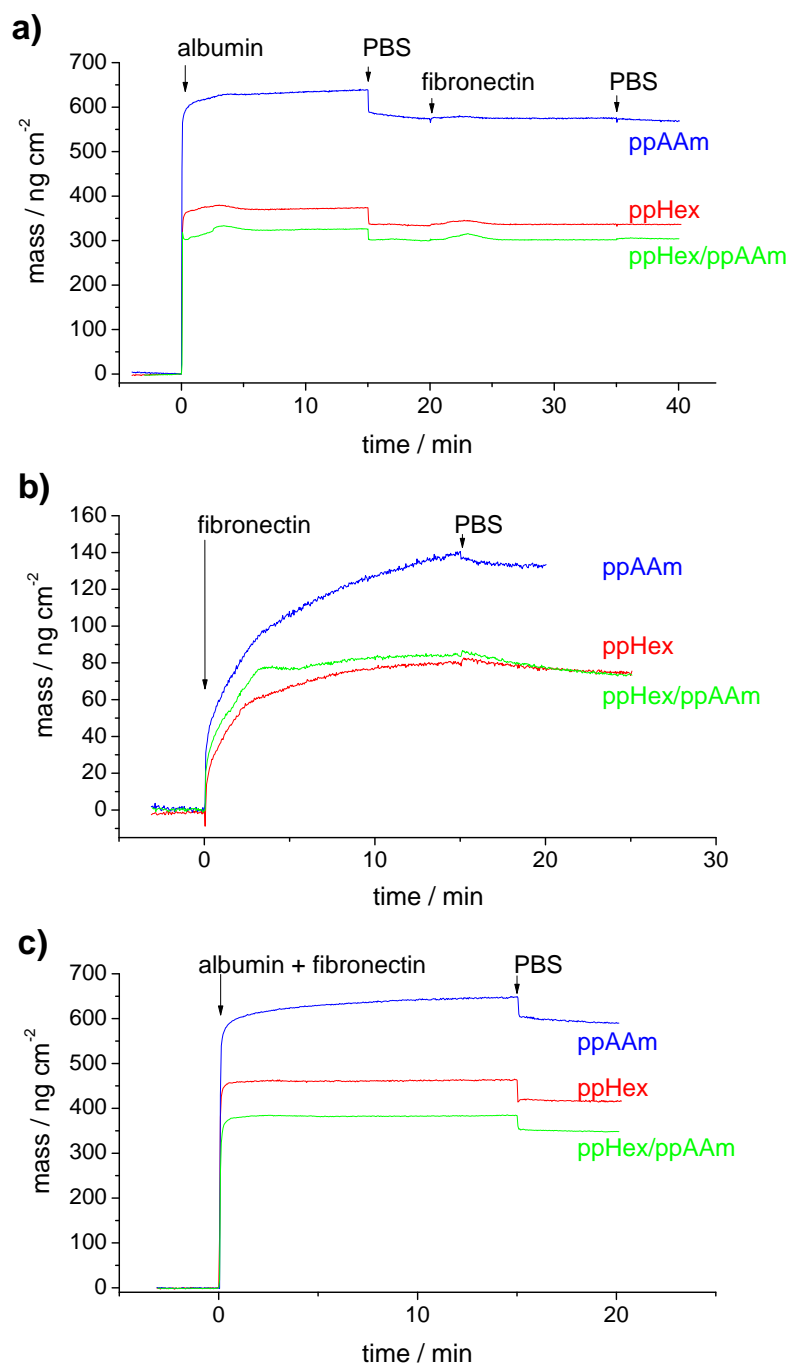
Figure 8.1: Typical mass changes after adsorption of albumin and fibronectin on uniform plasma polymer samples determined by QCM. Protein adsorption was studied from single protein solutions (a and b), from sequential adsorption of albumin before fibronectin (a) and from mixtures containing both proteins (c). The concentration in all solutions was 4 mg/ml and 0.03 mg/ml for albumin and fibronectin, respectively. ppAAm: blue, ppHex: red, ppHex/ppAAm: green.

Table 8.2: Surface concentration and sample surface area available to each protein calculated from QCM data of single albumin and fibronectin solutions.

Surface	Surface concentration / 10^{-12} mol cm^{-2}		Area per molecule / nm^{-2}	
	Albumin	Fibronectin	Albumin	Fibronectin
ppHex	5.01 ± 0.58	0.144 ± 0.031	33 ± 3	1150 ± 250
ppHex/ppAAm	4.76 ± 0.67	0.156 ± 0.051	35 ± 5	1068 ± 350
ppAAm	8.49 ± 0.73	0.327 ± 0.069	20 ± 2	508 ± 110

containing plasma polymers has been reported before [339]. It was suggested that fibronectin can adsorb to certain amine- and amide-containing plasma polymers without any significant denaturation [52] although contrary data was reported that showed that Fn did not promote cell attachment to nitrogen based plasma polymers [339].

The number of proteins on the surface can be calculated from the adsorbed mass using molecular masses of 67000 g/mol and 450000 g/mol for albumin and fibronectin, respectively (see SECTION 6.2.1). The results are displayed in TABLE 8.2 which also shows the average surface area on the sample available to each protein.

The theoretical surface area of albumin – calculated from the protein dimensions given in SECTION 6.2.1.3 – is approximately 24 to 28 nm^2. This quantitatively compares very well to the results obtained here (between 20 and 35 nm^2) and suggests that BSA adsorbed on the surface as a single monolayer with complete surface coverage. The saturation of the surface with protein molecules further indicates that the protein concentration in solution was sufficient to obtain a complete coverage of the surface. The lower surface area of albumin on the hydrophilic surface leads to the conclusion that BSA retains a more globular shape on ppAAm. This is consistent with the globular shape albumin has in water, where the hydrophilic parts of the surface are oriented to the exterior of the molecule [209]. In contrast, albumin occupies a larger surface area on both hydrophobic samples (ppHex and ppHex/ppAAm) where BSA spreads out more on the surface. This is probably related to a restructuring of the protein to move the hydrophobic moieties from the core to the exterior in order to establish hydrophobic interactions with the sample surface. The conformational change also results in an increase of the surface area occupied by the protein.

Fibronectin has an elongated shape composed of two strands (SECTION 6.2.1.2). Its theoretical surface area therefore depends on its orientation on the surface and can be either around 8 nm^2 (end area), 120 nm^2 (side area of one strand) or 240 nm^2 (area of both strands, see FIGURE 8.2). The surface area per protein calculated from the QCM data, however, is significantly higher than any of these values (TABLE 8.2). Therefore, even though the amount of fibronectin in the chamber ($5.3 \cdot 10^{-12}$ mol) was much higher than the total amount of Fn adsorbed on the plasma polymer sample ($<0.07 \cdot 10^{-12}$ mol), it was not sufficient to provide a complete surface coverage. Since protein adsorption is a dynamic process, it can be assumed that the amount of adsorbed protein is limited by adsorption kinetics.
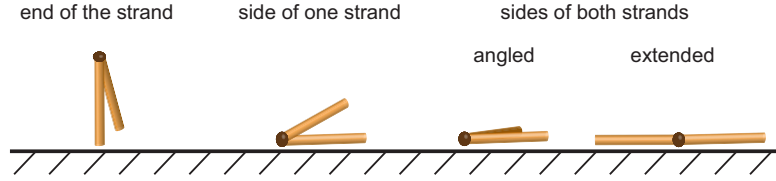
Figure 8.2: Three possible orientations of adsorbed fibronectin. Adsorption can occur either with the end of the strand, the side of one of the two strands or the sides of both strands. For the latter the shape of the protein on the surface can be different (angled or extended).

8.1.2.3   Sequential Protein Adsorption

After the adsorption of albumin, the samples were exposed to a fibronectin containing solution to investigate if any displacement of BSA by Fn takes place upon sequential exposure of the surface to BSA and Fn. (FIGURE 8.1 a). As can be seen from TABLE 8.1, the mass change on all three samples before and after exposure to Fn is negligible. Since fibronectin adsorbed from an individual protein solution on all surfaces, the possibility that displacement does not take place because Fn has a low affinity to the plasma polymers can be excluded. Fibronectin has a much larger molecular weight than albumin; it is therefore thought to be unlikely that exactly the same mass of albumin and fibronectin is exchanged during displacement. Hence, it is concluded that no albumin displacement occurs after sequential exposure of the samples to BSA and Fn.

8.1.2.4   Competitive Protein Adsorption

The mass change during the competitive adsorption of albumin and fibronectin is shown in FIGURE 8.1 c. Similar to the individual protein adsorption experiments, the mass change is largest on ppAAm – 56% and 63% higher than on ppHex and ppHex/ppAAm, respectively (TABLE 8.1). The results for ppHex and ppHex/ppAAm are again in close proximity to each other. When comparing the data to the values obtained from the individual albumin adsorption, an increase in mass of 49, 49 and 30 ng cm^{-2} for ppHex, ppHex/ppAAm and ppAAm, respectively, was observed in the competitive adsorption experiment.

The mass difference between the single albumin and competitive BSA/Fn adsorption experiments can be used to estimate the amount of albumin displaced by fibronectin. For this purpose, a simplified model for the competitive adsorption is adopted in which protein displacement occurs only after albumin has completely saturated the surface and both proteins only adsorb in a single monolayer. Thus, the mass difference ΔM between the single albumin adsorption and the competitive adsorption experiment corresponds to the mass difference between the adsorbed fibronectin (M_{Fn}) and the desorbed albumin (M_{BSA}):

$$\Delta M = M_{Fn} - M_{BSA} \tag{8.1}$$

which can be written as

$$\Delta M = (m_{Fn} \cdot n_{Fn}) - (m_{BSA} \cdot n_{BSA}) \tag{8.2}$$

where m_{Fn} and m_{BSA} are the molecular weight of Fn and BSA and n_{Fn} and n_{BSA} the moles of Fn and BSA that are exchanged.

To obtain n_{Fn} and n_{BSA}, a second equation is needed that was based on the assumption that the surface area covered by the displaced albumin (A_{BSA}) is equal to the surface area occupied by the adsorbed fibronectin (A_{Fn}):

$$A_{BSA} = A_{Fn} \tag{8.3}$$

A_{BSA} and A_{Fn} can be expressed as a function of the average surface area occupied by a single albumin (a_{BSA}) or fibronectin molecule (a_{Fn}):

$$a_{BSA} \cdot n_{BSA} = a_{Fn} \cdot n_{Fn} \tag{8.4}$$

Using EQUATIONS 8.2 and 8.4, n_{BSA} and n_{Fn} can be expressed as

$$n_{BSA} = \Delta M \cdot \left(\frac{a_{BSA} \cdot m_{Fn}}{a_{Fn}} - m_{BSA} \right)^{-1} \tag{8.5}$$

and

$$n_{Fn} = \Delta M \cdot \left(m_{Fn} - \frac{a_{Fn} \cdot m_{BSA}}{a_{BSA}} \right)^{-1} \tag{8.6}$$

ΔM has been reported at the beginning of this section and m_{BSA} and m_{Fn} can be obtained from the literature (see SECTION 6.2.1). For the surface area of albumin, the values calculated from the QCM data (TABLE 8.2) were used for each surface. Since the single adsorption of fibronectin did not provide a complete surface coverage, no experimental data on its surface area was obtained. Therefore, the calculations were done with the theoretical values presented in SECTION 8.1.2.2. Out of the three possible orientations (end, side of one strand, side of both strands as shown in FIGURE 8.2), only the first two yielded physically relevant results. Adsorption of all fibronectin molecules with just the end of one strand would only displace less than 0.5% of the initially adsorbed albumin and it seems unlikely that the binding force necessary for the protein to adsorb and promote cell adhesion is provided in this situation. The most plausible results were obtained with $a_{Fn} = 120$ nm^2 – the adsorption of fibronectin with the side of one strand – and are reported in TABLE 8.3.

The amount of albumin displaced by fibronectin is similar on ppHex and ppHex/ppAAm (17% and 16%). Significantly more albumin was displaced on ppAAm (56%). In all cases, this was accompanied by a considerable increase in the amount of fibronectin adsorbed compared to the adsorption of fibronectin from a single protein solution. The presence of albumin therefore seems to enhance the adsorption of fibronectin on the surface.

Table 8.3: Amount of exchanged albumin and fibronectin and relative change to the adsorption from single protein solutions estimated from the competitive QCM adsorption experiment.

Surface	Exchanged amount of protein / 10^{-12} mol cm^{-2}		BSA displaced [a] / %	Fn increase [a] / %
	Albumin	Fibronectin		
ppHex	0.86 ± 1.22	0.24 ± 0.34	17	64
ppHex/ppAAm	0.77 ± 1.35	0.22 ± 0.39	16	44
ppAAm	4.7 ± 16.4	0.77 ± 2.67	56	137

[a] In comparison to the amount adsorbed from single protein solutions.

The fact that more albumin was displaced on ppAAm could indicate that BSA was not significantly denatured on this sample and retained much of the structure it had in solution. In contrast, on ppHex and ppHex/ppAAm, BSA has likely been subjected to more drastic structural changes, as has already been argued when its surface area was discussed. Consequently, BSA is more tightly bound to the hydrophobic surfaces and desorption back into the aqueous solution is less likely. Thus, the degree of protein displacement is reduced compared to the more hydrophilic ppAAm surface, which is consistent with previously published descriptions of the adsorption of albumin on hydrophilic and hydrophobic surfaces [6].

It is important to emphasize, however, that these results are estimations and the conclusions can therefore only be indications to the processes involved. The main uncertainty lies in the fact that the surface area occupied by a fibronectin molecule could not be obtained experimentally and is likely to be different on the hydrophilic and the hydrophobic surface.

The different data of the sequential (no protein displacement) and competitive (significant protein displacement) adsorption experiments indicates that the residence time of the proteins on the surface is essential in the displacement process. In the sequential experiment, albumin had more time (15 min) for structural rearrangements on the surface, allowing tighter binding and more progressed changes in its secondary structure. It is therefore assumed that fibronectin was not able to displace albumin in the sequential experiment because the degree of denaturation of BSA was too high to allow desorption back into the solution.

8.1.3 Plasma Polymer Gradients

8.1.3.1 Measurements on Gradient Surfaces

The objective of this section is to investigate if a gradual change in the surface concentration of either albumin or fibronectin is present on the gradient surfaces. Only the shallow gradient will be considered because it showed a clear gradual transition in its surface properties and the cell density over several millimeters.

As on uniform samples, protein adsorption on the gradients was carried out from individual protein solutions, sequentially and competitively with fluorescently labeled albumin and fibronectin.

Detailed experimental procedures for this experiment are given in APPENDIX E. Uniform plasma polymer samples were used alongside the gradients for comparison. Quantification of protein adsorption on gradients is difficult with conventional instruments because they generally lack the required spatial resolution. The adsorption of fluorescently labeled proteins allows qualitative conclusions about differences in surface concentrations over the whole sample area. It should be noted that quantification of protein concentrations by this method was not possible and the measured signals only represent relative fluorescence intensities.

8.1.3.2 Intensity Profiles of Labeled Proteins

The fluorescence intensities of labeled albumin and fibronectin on the gradient after single, sequential and competitive exposure are shown in FIGURE 8.3. From this data, it is evident that no gradual transition in the amount of adsorbed protein occurs under any of these conditions. The amount of albumin is low on the unmasked ppHex side of the gradient, but increases rapidly in a step-like profile over 1.5 mm at the beginning of the gradient. The slightly higher intensities at the beginning of the gradient compared to the ppAAm side of the sample are likely the result of drying effects after exposure to the protein solutions. The curves are very similar for individual, sequential and competitive adsorption on the sample which indicates that no significant changes in the albumin concentration occur between these conditions.

For fibronectin, the same step-like profile is observed at the transition from the ppHex side to the gradient part of the sample, with lower intensities on the ppHex side than on the ppAAm side
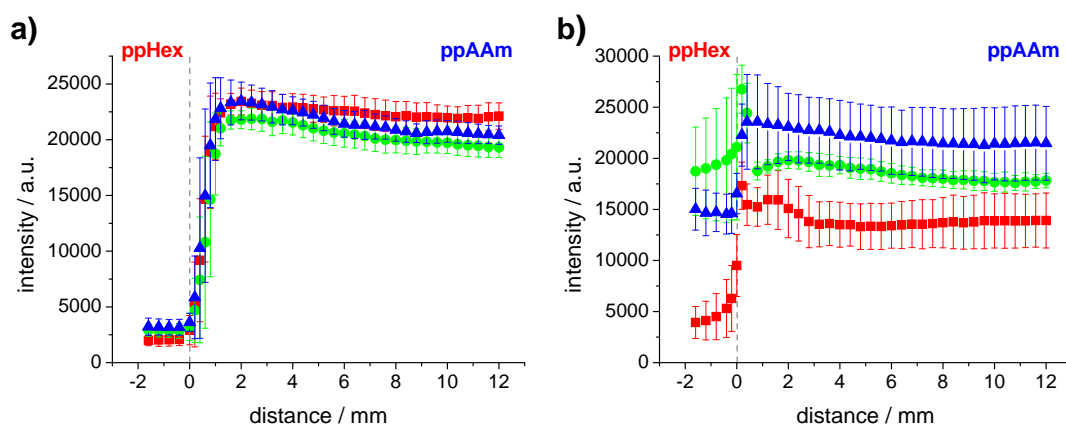
Figure 8.3: Fluorescence intensities from labeled albumin (a) and labeled fibronectin (b) adsorbed on the gradient. The proteins were adsorbed individually (■), sequentially (●) and competitively (▲). The concentrations of albumin and fibronectin were 4 mg/ml and 0.03 mg/ml, respectively. The dashed line indicates the beginning of the gradient. The data is an average from 6 samples with 60 line measurements each. It was taken in 0.2 mm increments along the gradient; only every second measurement is shown. The errors represent standard deviations. ppHex side: left; ppAAm side: right.

(FIGURE 8.3 b). In the sequential adsorption experiment, the fluorescence intensity was very similar across the whole sample, suggesting that there were no differences in the surface concentration of fibronectin in this case. Local increases in the intensity were again observed at the beginning of the gradient on all three curves which – as for albumin – were attributed to drying effects.

The lack of a gradient profile in the protein surface concentration on the samples brings up the question if the experiment is able to visualize protein concentration gradients on plasma polymers. To investigate this further, individual adsorption of albumin and fibronectin was carried out on samples containing five gradients of varying transition length. The preparation of these surfaces was introduced in CHAPTER 4, where hexane was allowed to diffuse on a ppAAm coated surfaces through channels with different cross sections. In consistency with this chapter, the five gradients will be labeled according to the length of the side of the square cross-sections of the channels. The transition lengths of these gradients vary according to the surface analysis techniques employed and can be found in FIGURE 4.2 (WCA) and FIGURE 4.5 (XPS).

The fluorescence intensity on this sample format after adsorption of labeled albumin and fibronectin is shown in FIGURES 8.4 and 8.5 for BSA and Fn, respectively. In both cases, the defined boundaries of the gradients observed on the WCA-map of the surface in FIGURE 4.2 were lost (FIGURE 8.4 a and 8.5 a). This is not surprising considering the changes in the wettability gradient after immersion in PBS shown in FIGURE 5.11 in CHAPTER 5. However, in general higher intensities were observed when moving from the ppHex to the ppAAm side of the surface and when moving towards the smaller channels at the top of the samples.

Line profiles of the fluorescence intensities from the center of each gradient are shown in FIGURES 8.4 b and 8.5 b. For adsorbed fibronectin, the 0.25 mm gradient showed a faster increase than all other gradients while the intensity on 5 mm gradient was significantly lower than the intensity of the other four profiles. The large variations within each profile are most likely due to the low concentration of fibronectin in solution which has already been shown in SECTION 8.1.2 to result in an incomplete surface coverage. Nevertheless, in general gradients in the measured intensity were observed that become steeper as the transition length of the surface gradient decreases.

On the intensity profiles obtained from the adsorption of BSA the concentration dependance on the surface gradient is more distinct. On the 0.25 mm gradient, the surface concentration of albumin increases rapidly after the beginning of the gradient in a step-like manner. The intensity increase is flatter on the 0.5 mm gradient. On the 1, 2 and 5 mm gradients the transition profile is very similar and stretches over a longer distance.

From these results it is evident that gradual changes in the protein surface concentration can be observed with fluorescently labeled proteins. The profile depends on the steepness of the surface gradient and starts turning into a step-like transition when the gradient is formed through an opening with a cross-section smaller than 0.5 x 0.5 mm. The shallow gradient used in CHAPTER 7 and in the present section was prepared through an opening with a height of 0.4 mm and can therefore be expected to show a step-like protein concentration profile as experimentally shown in FIGURE 8.3.
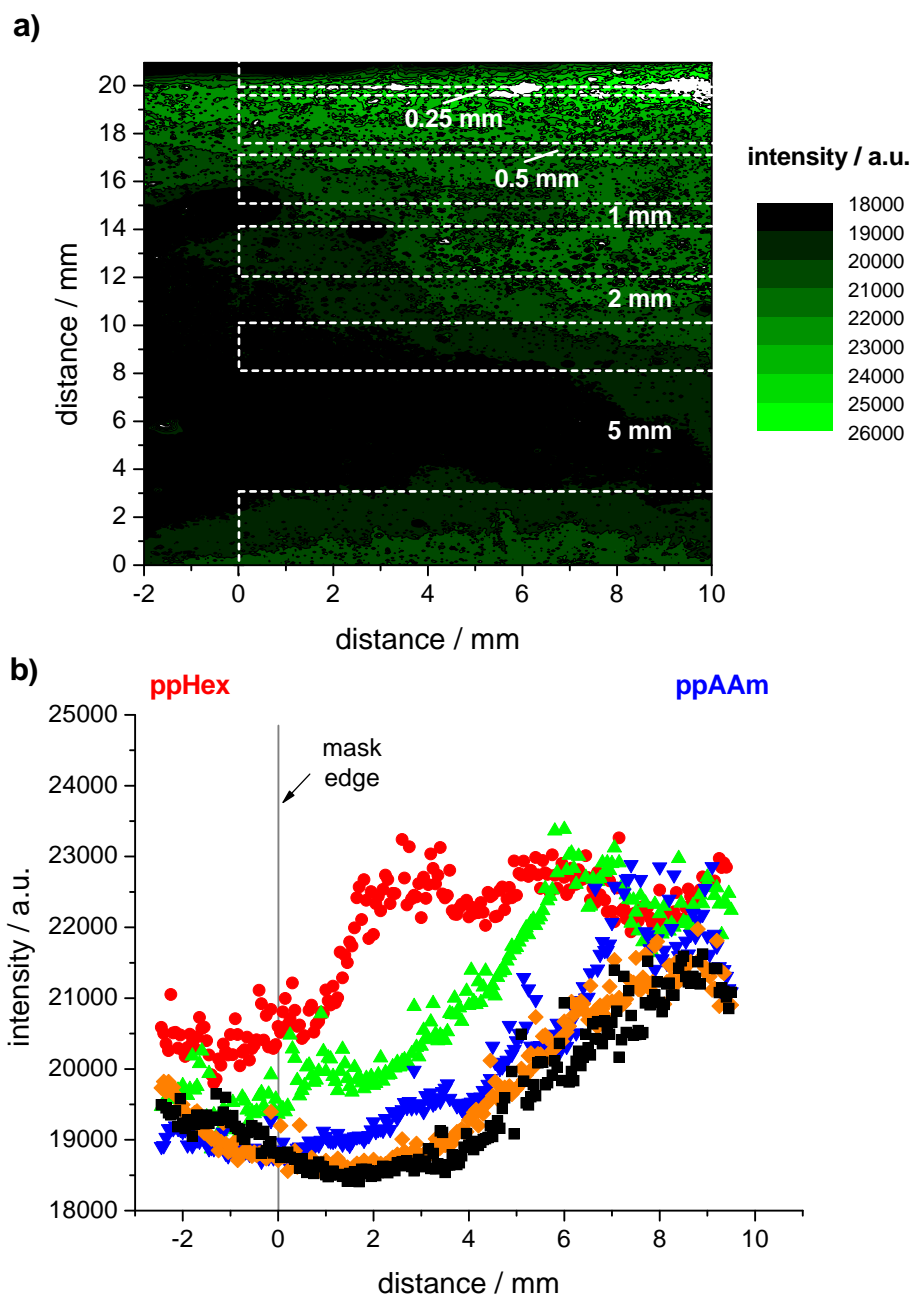
Figure 8.4: Contour plot (a) and line profiles (b) of the signal of fluorescently labeled albumin adsorbed on plasma polymer gradients of different length. The sample contained five gradients with 0.25 (●), 0.5 (▲), 1 (▼), 2 (◆) and 5 mm (■) wide cross sections. The areas covered by the mask during deposition are indicated in (a) by dashed lines. The line profiles shown in (b) were taken from the center of each gradient. The beginning of the gradient was set at $x = 0$. ppHex: left; ppAAm: right.

a)

b)
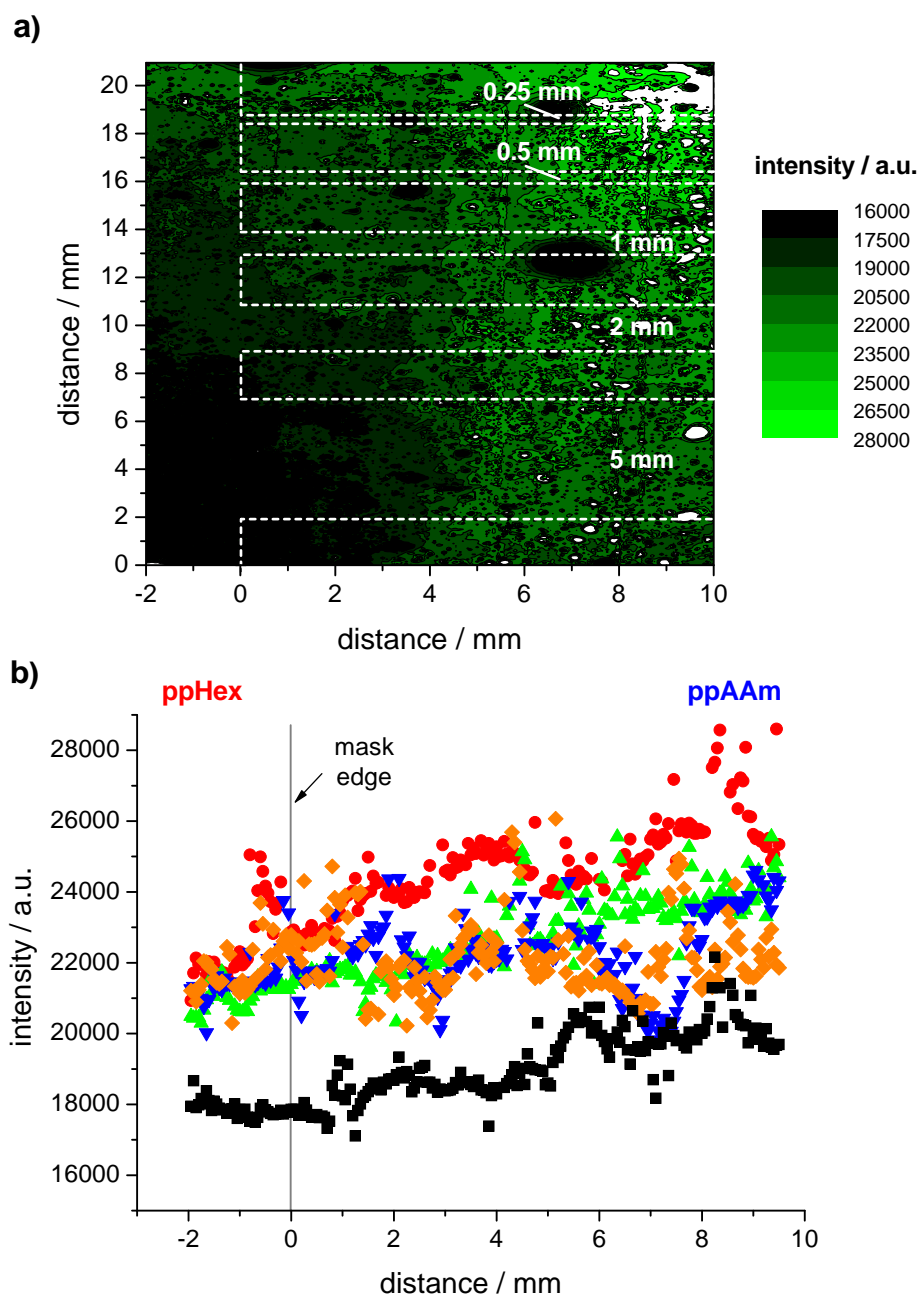
Figure 8.5: Contour plot (a) and line profiles (b) of the signal of fluorescently labeled fibronectin adsorbed on plasma polymer gradients of different length. The sample contained five gradients with 0.25 (●), 0.5 (▲), 1 (▼), 2 (◆) and 5 mm (■) wide cross sections. The areas covered by the mask during deposition are indicated in (a) by dashed lines. The line profiles shown in (b) were taken from the center of each gradient. The beginning of the gradient was set at $x = 0$. ppHex: left; ppAAm: right.

8.1.3.3 Comparison Between Uniform and Gradient Samples

The fluorescence intensity from protein adsorption on the gradients was compared to that on uniform ppAAm and ppHex/ppAAm samples to identify any potential differences between the two sample formats. The uniform samples were analyzed in the same way as the gradient samples. FIGURE 8.6 shows the sample comparison for albumin and fibronectin under all three conditions.

On the scale on which the intensity change occurs on the gradient samples, the fluorescence intensity on all uniform samples is largely constant over distance. This confirms that the step profile on the gradients is related to the surface properties of the sample. For albumin, the concentration on the uniform ppAAm and ppHex/ppAAm samples matches that of the corresponding side of the gradient. In addition, the fluorescence intensity of labeled albumin on the gradients are similar for the sequential and competitive adsorption indicating that there is no significant difference in the amount of albumin adsorbed between these two experimental conditions. Compared to this, the albumin concentration observed after single protein adsorption is slightly higher on the ppAAm side, suggesting that the presence of fibronectin may reduce the amount of albumin on the hydrophilic end of the gradient to a small extent.

The adsorption of fibronectin only on gradients also corresponds to the results from uniform ppAAm and ppHex/ppAAm. However, this is not the case for the sequential and competitive
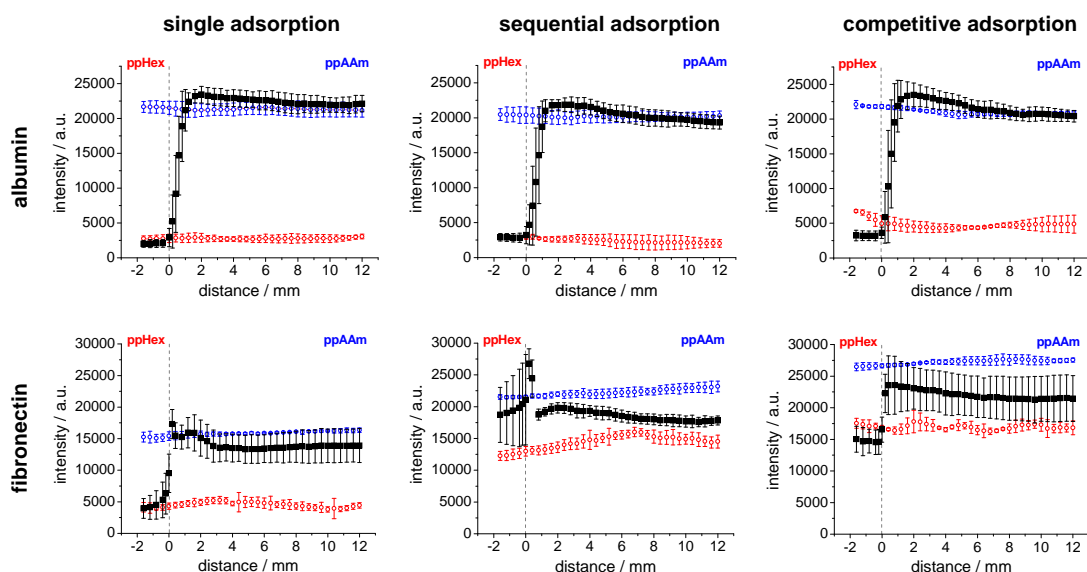
Figure 8.6: Comparison of the fluorescence intensities from labeled albumin and labeled fibronectin adsorbed to gradients (■) and uniform ppAAm (○) and ppHex/ppAAm (○). The concentrations of albumin and fibronectin were 4 mg/ml and 0.03 mg/ml, respectively. The dashed line indicates the beginning of the gradient. The data on the uniform plasma polymers is an average of 3 x 60 line measurements. The errors represent standard deviations. ppHex side: left; ppAAm side: right.

adsorption of fibronectin. As has been noted before, the surface concentration of fibronectin on the gradient is largely uniform over distance after sequential protein adsorption. In this case, the fluorescence intensity on the gradient and uniform samples increased compared to that from the individual adsorption experiment. The surface concentration of fibronectin on the gradient is higher than on ppHex/ppAAm but lower than on ppAAm. Competitive adsorption of albumin and fibronectin gives a step profile of the fibronectin concentration on the gradient but the uniform ppAAm and ppHex/ppAAm samples have slightly higher intensities than the corresponding sides of the gradient. Thus, in both the sequential and the competitive adsorption experiments the presence of albumin increased the amount of fibronectin adsorbed on the samples. This observation is in accordance with the data in SECTION 8.1.2.3 from the QCM experiments.

8.1.3.4 Comparison Between Labeled Albumin and Fibronectin

The fluorescence intensity profiles on the gradient samples shown in FIGURE 8.6 were compared to explore if protein displacement takes place on the plasma polymer gradients. While the intensity increase between the ppHex and the ppAAm side of the gradient is similar for fibronectin and albumin when adsorbed individually, only BSA maintains the step-like profile during sequential protein adsorption. There is no difference in the profile of the fibronectin concentration on the hydrophobic and the hydrophilic side of the gradient.

The fact that no step-transition was visible after sequential protein adsorption indicates that the surface chemical effects did not play a major role in the fibronectin adsorption in this case. It is therefore suggested that under these conditions fibronectin adsorbed on top of a well adhered albumin layer and does not directly interact with the sample surface. This is supported by the observations made in SECTION 8.1.2 where it was concluded that the adhesion of albumin to the surface may strengthen over time and prevent displacement by fibronectin. The fluorescence intensity of fibronectin measured on these samples therefore does not reflect adsorption of fibronectin to the sample surface, but is rather an indicator for the adhesion of Fn to BSA and may therefore vary with the conformation of albumin on the surface. Fn was not detected on the samples after sequential adsorption with the QCM (see SECTION 8.1.2.3). This is attributed to different experimental conditions (adsorption time, temperature etc.) between the QCM and the fluorescence experiments.

The difference in the intensity profile of labeled fibronectin between the ppHex and the ppAAm side of the gradient is smaller than that of albumin in the competitive adsorption experiment. The QCM experiments demonstrated that in this case displacement of albumin by fibronectin occurs on uniform samples. In the competitive fluorescence experiment, this was underlined by an increase in the amount of adsorbed fibronectin on all samples while still maintaining the step-profile on the gradient surface. It is therefore concluded that displacement of albumin by fibronectin occurs on all samples when exposed to a mixture of both proteins under the present conditions. The degree of displacement was different on hydrophilic and hydrophobic surfaces. However, no gradual transition in the extent of protein displacement was observed on the shallow plasma polymer gradient. Instead,

protein adsorption seemed to be independent of the position on the gradient area and correspond to data obtained from uniform ppAAm samples.

8.2   Relation of Protein Adsorption to Surface Properties

8.2.1   Plasma Polymer Gradients not Exposed to PBS

To explore possible relationships between the surface properties and the measured protein adsorption profiles, the intensities obtained from the protein experiments were plotted against surface analysis data. Since adsorption from a protein mixture is most relevant to the processes involved in cell culture media, only the normalised fluorescence intensities of labeled albumin and fibronectin from the competitive adsorption experiments are shown here. The protein adsorption data was plotted against WCA, roughness and XPS data already presented in PART I. SECTION 8.2.2 will focus on the relation with surface data from plasma polymer gradient exposed to PBS while this section
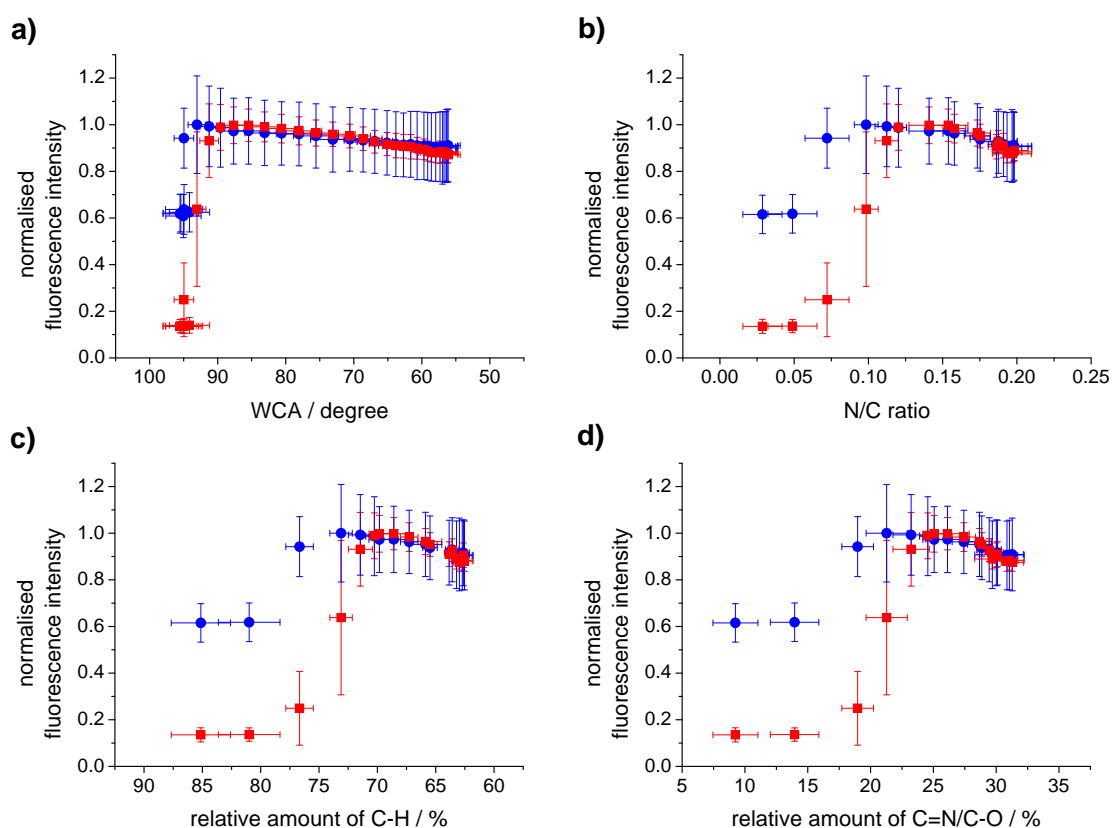
Figure 8.7: Relationship between surface properties of plasma polymer samples and the normalised fluorescence intensity of adsorbed labeled albumin (■) and labeled fibronectin (●). Each graph is displayed such that the ppHex side of the gradient is situated at the left and the ppAAm side at the right. Error bars represent standard deviations.

presents trends between protein adsorption data and results from surface analysis of unexposed samples.

Surface data from unexposed samples that showed trends when plotted against fluorescence intensities from the proteins are summarised in FIGURE 8.7. Most graphs show a rapid transition from high to low intensities for both proteins. The trends are similar for fibronectin and albumin, but more pronounced on the latter because of its higher surface concentration and the larger difference between the ppHex/ppAAm and the ppAAm side of the gradient.

The amount of protein is constant for lower WCAs up to approximately 90° (FIGURE 8.7 a). Above this value, the intensity drops steeply to about 62% and 14% of the original value for fibronectin and albumin, respectively. It is therefore obvious that the proteins do not follow the wettability gradient on the surface.

The intensity transition is less steep when plotted against the N/C ratio of the surface (FIGURE 8.7 b), stretching from an N/C ratio of 0.05 to 0.11. Similar to the cell data in SECTION 7.3.1 this was related to a decrease in the hydrocarbon content (C−H) and an increase in the imine/alcohol groups (C=N/C−O) which are shown in FIGURE 8.7 c and d, respectively. The gradual transition occurred between a relative amount of 70 - 80% C−H and 15 - 25% C=N/C−O. The amount of adsorbed protein therefore relates better to the gradient in chemistry on the sample than to the wettability gradient.

8.2.2 Plasma Polymer Gradients Exposed to PBS

The relationship between surface properties measured in PBS and protein adsorption data is shown in FIGURE 8.8. Compared to the WCA measured on the unexposed sample, the wettability of the exposed samples showed a stronger relation to the fluorescence intensity of the proteins (FIGURE 8.8 a). The protein concentration is constant on the hydrophobic side but increases to its maximum when moving from 65° to 45°. The WCA profile of the plasma polymer gradient exposed to PBS therefore relates better to the amount of adsorbed protein than the wettability of the sample that was not exposed to PBS.

When plotted against the surface roughness, the protein concentration is constant up to an rms roughness of about 3 nm but drops steeply above that value (FIGURE 8.8 b). Thus, the amount of protein does not respond to the gradient in surface roughness observed in PBS.

A more gradual relationship was observed between the measured fluorescence intensity and the N/C ratio (FIGURE 8.8 c). There, the fluorescence signal increased between N/C ratios of 0.06 and 0.13 and thus proceeded over approximately 50% of the measured range on the surface. As in SECTION 8.2.1, this was partly related to the change of imine/alcohol groups (C=N/C−O) on the surface (15 - 21%, FIGURE 8.8 d). The observed profile in the fluorescence intensity of the adsorbed proteins therefore relates better to WCA and XPS data from gradients exposed to PBS than to surface analysis data from unexposed samples.
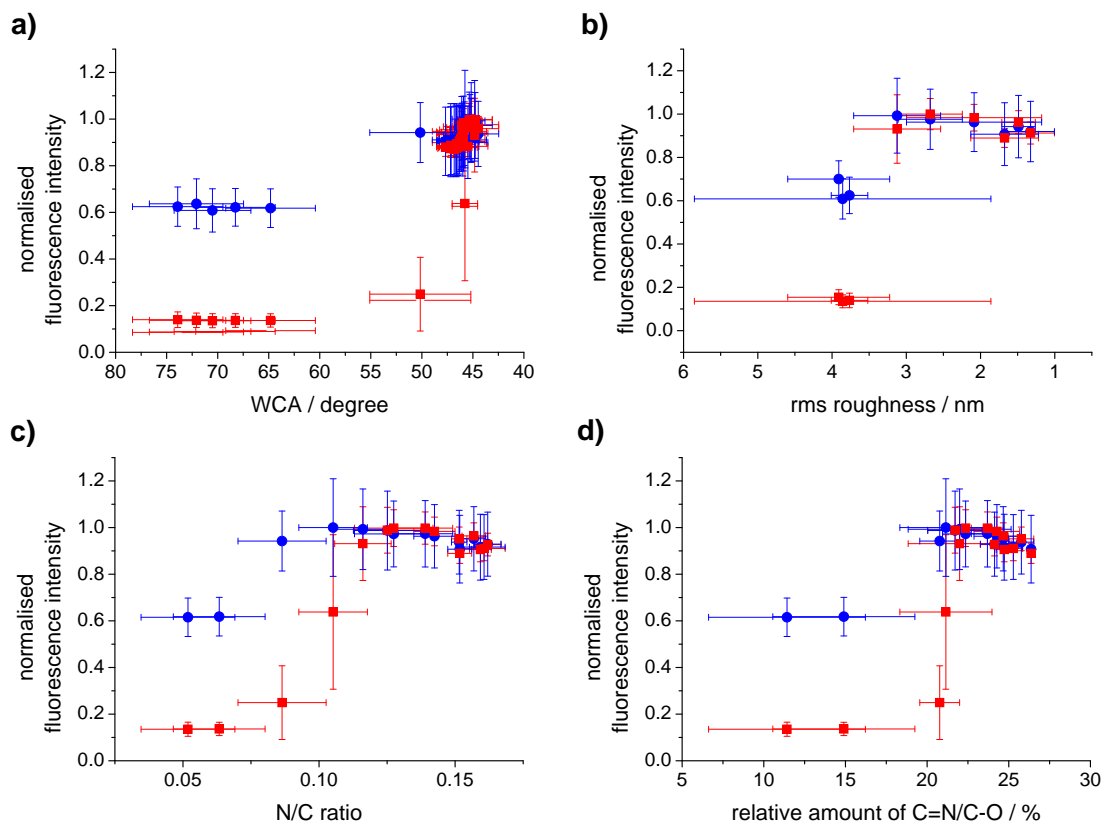
Figure 8.8: Relationship between surface properties of plasma polymer samples exposed to PBS and the normalised fluorescence intensity of adsorbed labeled albumin (■) and labeled fibronectin (●). Each graph is displayed such that the ppHex side of the gradient is situated at the left and the ppAAm side at the right. Error bars represent standard deviations.

8.3   Relevance to the Cell Response

To quantitatively evaluate the relevance of the protein concentration on the gradient sample to the cell density gradient observed in SECTION 7.1.3, the normalised fluorescence intensities of albumin and fibronectin were plotted against the cell number in FIGURE 8.9. These plots showed no gradual relation on any day of cell culture to the amount of protein adsorbed to the surface. It can therefore be concluded that, in contrast to other publications [336], the increase in cell number from the hydrophobic to the hydrophilic end of the gradient can not be explained by a gradually changing surface concentration of fibronectin or by a simple model of the Vroman effect.

Fibronectin has previously been shown to be able to regulate cell adhesion on nitrogen containing plasma polymer surfaces [52]. It is therefore thought unlikely that this would not be the case for the present samples. Nevertheless, it is possible that other important cell adhesive proteins such as vinculin or vitronectin that were not considered in this chapter have an important effect on the adhesion of 3T3 fibroblasts and could be responsible for the gradual response.
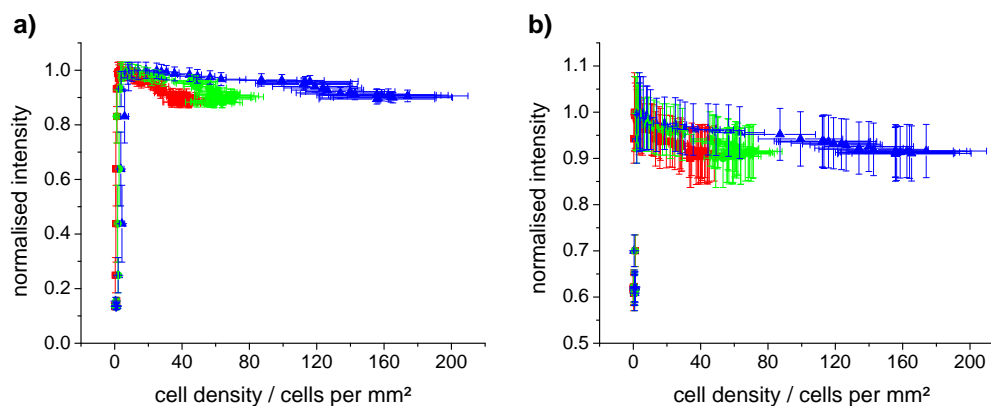
Figure 8.9: Normalised fluorescence intensity of labeled albumin (a) and labeled fibronectin (b) plotted against the cell density along the gradients after 1 (■), 2 (●) and 3 (▲) days of cell culture. Error bars represent SEM; cell density: $n = 15$; fluorescence intensity: $n = 6$

Another likely explanation is that fibroblast adhesion on the gradient is not controlled by protein concentrations on the surface, but by the conformation of cell adhesive proteins after adsorption. SECTION 6.2.2.3 highlighted the importance of the conformation of proteins to trigger and maintain their cell adhesive property. It can be easily imagined that fibronectin increasingly loses its cell binding activity on more hydrophobic surfaces due to progressive denaturation.

8.4 Summary

This chapter investigated the influence of protein adsorption and displacement on the cell density gradient observed on the plasma polymer surfaces. Two model proteins, albumin (non cell adhesive) and fibronectin (cell adhesive), were adsorbed individually (single protein solutions), sequentially (albumin first, then fibronectin) and competitively (from a mixture of albumin and fibronectin). These experiments were used to study the displacement of albumin by fibronectin (Vroman effect) and the relative surface concentration of both proteins on the gradients.

Quartz crystal microbalance (QCM) measurements on uniform ppAAm, ppHex/ppAAm and ppHex were carried out on uniform samples to establish if displacement takes place. The adsorbed protein mass was always higher on the more hydrophilic ppAAm sample than on the hydrophobic ppHex/ppAAm and ppHex samples. It was found that even though both proteins adsorb individually on all three samples, fibronectin was not able to displace albumin in a sequential adsorption experiment. However, displacement took place from a mixture of both proteins. It was calculated that, compared to single albumin adsorption, 16 - 17% of BSA was displaced on the hydrophobic and more than 50% on the hydrophilic sample.

The relative amount of albumin and fibronectin adsorbed on the gradient surfaces was measured with fluorescently labeled proteins. The intensity profile along the gradient showed a steep increase at the beginning but no extended gradient in the protein concentration was observed. Additional

experiments on gradients of different length confirmed that protein concentration gradients can be measured on plasma polymer gradients by this method. It was concluded that the shallow gradient used for the cell culture in the previous chapter is not long enough for proteins to adsorb in a gradual manner. The fluorescence intensities measured on the two sides of the gradient generally matched the intensities of uniform ppAAm and ppHex/ppAAm. The amount of adsorbed fibronectin increased in the sequential and competitive adsorption experiments compared to adsorption from an individual protein solution. It was therefore concluded that the presence of albumin enhances the adsorption of fibronectin to the surface and that displacement takes place on the gradient when it is exposed to a mixture of fibronectin and albumin. However, no distance dependance of the displacement was observed on the gradient.

When plotted against the WCA of the unexposed sample and the roughness of a sample exposed to PBS, the protein concentration showed steep transitions from high to low fluorescence intensities. The fluorescence signal displayed a more gradual change when plotted against the WCA and the N/C ratio of gradients exposed to PBS. For the latter, this was mainly attributed to a decrease in hydrocarbon and an increase imine and alcohol functionalities on the surface.

The results in this chapter showed no distance dependent protein displacement on the gradient. The amount of fibronectin in the transition area was constant and can therefore not explain the cell density gradient. It was suggested that either protein conformation or different cell adhesive proteins may provide an explanation for the observed cell response.

Chapter 9

Conclusions & Outlook

9.1 Conclusions

The first aim of this project was to develop a plasma polymer surface displaying a chemical surface gradient. This was achieved via a new, diffusion based technique which was used to prepare a thickness gradient of plasma polymerised hexane (ppHex) on an allylamine plasma polymer (ppAAm) surface. The steepness of the gradient could be modified by simply changing the distance between the sample and the mask under which the gradient was formed. Here, a shallow gradient with a WCA range of 66° to 93° over 8 mm was prepared. This new method to prepare plasma polymer gradients adds another attractive technique to the repertoire of gradient formation protocols because of its simplicity and the plasma polymers inherent property to adhere to almost any substrate. In addition, it is a valuable model surface to study processes involved in the diffusion of a depositing plasma in porous 3D objects that was reported previously [46].

When characterizing the gradients, it became evident that the gradient profile in surface chemistry varied depending on the analytical technique, with longer transitions being observed when only the top nanometer was sampled. A comparison of the WCA and the thickness of the ppHex overlayer obtained from XPS data allowed an estimation of the depth sensitivity of the WCA measurement to 0.4 nm which was in very good agreement with the values reported by Bain and Whitesides [69].

The penetration of depositing species from a plasma has a much wider relevance than just the use to prepare gradient surfaces. It is important in the deposition of plasma polymers in the inside of porous substrates [8, 46] and can lead to undesired broadening when preparing patterned plasma polymer surfaces through masks. Therefore, the penetration properties of depositing species from a hexane plasma were investigated. Model structures were used to measure the deposition rate of ppHex in pore-like channels of different sizes. It was found that the penetration of plasma species down small channels (square cross sections of 0.25 x 0.25 mm to 5 x 5 mm) is mainly governed by processes occurring in front of the pore opening and seems to relate to the electrical properties of the plasma sheath. It was argued that the plasma sheath – more specifically the sheath thickness

with respect to the size of the opening – is responsible for a decrease in the deposition rate in front of the mask and effectively controls the nature of the plasma species penetrating into the pores. Identification of the nature of the ions penetrating through the opening was accomplished with mass spectrometry and showed that no negative species were able to reach the interior of the channel. The formation of the ppHex deposit inside the channel was shown to have possible contributions from positive ions and neutral species from the gas phase, both of which were found to penetrate at least 4 mm into the pores. This study also revealed that in the channel gas phase polymerisation takes place involving positive ions, whereas no neutral fragments were found with a higher molecular mass than the precursor. It was proposed that this gas phase polymerisation mainly occurs over nucleophilic addition reaction mechanisms, yielding higher molecular mass aliphatic and aromatic products.

For biomaterial applications, the plasma polymer samples will be exposed to aqueous environments. Surface analysis of the plasma polymer surfaces after exposure to PBS revealed some important changes compared to untreated samples. When stored in ambient conditions all samples were always extremely flat and the uniform samples displayed a homogeneous surface chemistry. After exposure to PBS, the uniform samples showed some degree of oxidation which caused a decrease in the wettability and an increase in the oxygen content. These changes mainly occurred within 6 hours after exposure. More dramatic changes were observed in the surface topography of the uniform sample that consisted of a layer of ppHex on top of ppAAm (ppHex/ppAAm). On this sample, exposure to various aqueous environments resulted in the formation of blisters with diameters of less than 1 μm. Fractures in the center of the blisters and a reduction of the height after drying of the sample indicate that the features are a result of water penetrating underneath the top ppHex layer, causing the underlying ppAAm to swell. The height of the blisters in the aqueous solution was reduced when the plasma polymer was exposed to protein containing solutions, suggesting that proteins stabilize the sample to some extent.

The AFM images measured on the dry ppHex/ppAAm samples corresponded to previously published data on ppHepA [32] which demonstrates the reproducibility of this effect and emphasizes the importance of understanding its cause. Since these blisters were only observed on ppHex/ppAAm – the surface of ppAAm largely remained featureless while ppHex showed the formation of small pores – suggests that the sequential deposition of two plasma polymer layers on top of each other might change the overall behavior of the deposit. This is not only important for the present gradient formation, but also affects experiments in which patters are created with two plasma polymer layers [110].

While the exposure of the shallow plasma polymer gradient to PBS had little effect on the XPS data, the wettability gradient was transformed to a step-like transition at the beginning of the gradient. The topography also changes from a previously uniform rms roughness to a rms roughness profile that gradually decreased from the ppHex to the ppAAm side of the gradient. Even though the blisters found on ppHex/ppAAm were not observed on the gradient, the ppHex side up to the beginning of the gradient was significantly different from the rest of the sample. It showed a very ragged topography covered with small circular features. The detection of significant changes on the

surfaces between untreated samples and samples exposed to an aqueous environment showed that even though plasma polymers were generally considered to be smooth materials, in studies involving exposure to an aqueous environment the influence of topographical effects can not *a priori* be excluded. This demonstrates that great care has to be taken in the correlation of surface analysis data and a biological response measured on the surfaces.

3T3 fibroblasts adhered and proliferated well on ppAAm but not on ppHex/ppAAm. On the plasma polymer gradients, the cell number was observed to increase gradually from the hydrophobic (ppHex) to the more hydrophilic (ppAAm) end of the gradient. When comparing the ppAAm side of the gradient samples to uniform ppAAm surfaces, a significant difference in the number of cells was observed. This was related to different initial cell adhesion densities due to the greater number of surrounding cells on the uniform sample. This seems to be the first time that differences were reported between the cell response on uniform and gradient samples.

When plotted against surface analysis data, the cell density displayed a strong relationship with the WCA of the untreated sample. Less pronounced gradient transitions were observed between the cell density and the rms roughness in PBS and the N/C-ratio. The latter was found to be related to a change in the relative amount of hydrocarbon and imide/alcohol functions on the surface. Since the wettability was the only surface property that showed a linear relationship over the whole sample length, it was concluded that the WCA of the untreated sample best describes the gradient in cell adhesion. Relating to the sensitivity of the WCA measurement deduced earlier, this indicates that cell response is mainly governed by the chemistry of the uppermost 0.4 nm of the surface.

Cell response is mediated by proteins and therefore requires a sufficient amount of active cell-adhesion promoting proteins on the surface. The quantification of the amount of albumin and fibronectin gave some indication towards the underlying mechanism in which the proteins translate the properties of the plasma polymers in order to enable cell adhesion. Uniform plasma polymer samples were used to demonstrate that fibronectin (a cell adhesion promoting protein) can displace albumin on ppAAm. However, the relative amount of fluorescently labeled fibronectin that adsorbed on the plasma polymer gradients did not follow a gradient profile but showed a step-like increase at the beginning of the gradient. Therefore, neither protein displacement nor a gradient in the proteins surface concentration can be linearly linked to the observed cell response. Consequently, it is suggested that protein conformation needs to be considered as the main factor that translates the surface properties into a biological response towards cell adhesion.

9.2 Future Work

In the limited time available for a PhD thesis, it will never be possible to explore all leads and some questions will remain unanswered. Below, a brief collection of ideas point out directions for possible future projects.

The method for the preparation of plasma polymer gradients presented in this thesis has not previously been used and therefore opens up the possibilities to explore similar gradient systems

with other precursors. This would demonstrate the broader use of this method. A more challenging continuation of the technique would be the preparation of differently shaped gradients, for example in a radial or orthogonal way. The former approach has already been realized during this work but was not included in the thesis.

Many questions are still open regarding the underlying mechanism of the deposition of plasma polymers in channels or pores. In this work, a beginning was made by studying diffusion from a hexane plasma, but the results are very likely to change when different monomers are used. A better description of these processes could be obtained if the deposition would be carried out under closely monitored plasma conditions that allow an improved estimate of the plasma sheath dimensions. The use of different materials for the mask (conductive and non-conductive) and various geometries of the channel structures may also give more insight in the penetration properties of the depositing species.

Only recently did the behavior of plasma polymers in aqueous environments receive some attention. The formation of blisters on ppHex/ppAAm may indicate that some more attention needs to given to possible differences between layered plasma polymers and single plasma polymer layers. For example, the topography of layers of ppHex/ppHex, ppHex/ppAAm, ppAAm/ppHex and ppAAm/ppAAm in water can be compared to each other. The additional use of other polar and apolar plasma polymers such as plasma polymerised acrylic acid or 1,7-octadiene would complete the picture and allow to decide if this phenomenon is related to the hydrophilic properties of the bottom ppAAm layer.

The differences in the cell number between the ppAAm side of the gradient and the uniform ppAAm is an important conclusion of this work which should be explored in a separate project. It was suggested that protein expression might affect the initial adhesion of cells on the surface and account for these differences. An identification and visualization of the spatial distribution of extracellular matrix proteins and signal transducers from cells could improve the understanding in this area. The cell movement on the gradient could be studied with time lapse microscopy to investigate if any haptotactic effects occur on the surface.

The effect of the protein layer has not been studied in its full extent in this thesis and no knowledge is available on any conformational changes that might affect fibronectin on different position on the gradient. However, the analysis of the protein conformation with a spatial resolution in the sub-millimeter range is challenging. Attenuated total internal reflection (ATR) infrared spectroscopy [218, 232, 263] and fluorescence energy transfer (FRET) [243, 259, 260] have been successfully used to study protein conformation in the past. ATR could be employed as point measurements on the gradient if the absorption is sufficiently strong (or can be amplified). Confocal microscopy might be able to quantitatively measure FRET signals from the protein with a high resolution and thus provide line profiles of conformational changes along the gradient. Labeled antibodies for fibronectins RGD sequence could also help to study the proteins activity on the surface.

Appendices

Appendix A - Constants

C	$=$	17.7 ng cm^{-2} Hz^{-1}	sensitivity constant of a 5 MHz quartz crystal
ϵ_0	$=$	8.854187817 F m^{-1}	permittivity of free space
e	$=$	$1.602176487 \cdot 10^{-19}$ C	electron charge
h	$=$	$6.62606896 \cdot 10^{-34}$ J s	Planck constant
k	$=$	$1.3806504 \cdot 10^{-23}$ J K^{-1}	Boltzmann constant
m_e	$=$	$9.10938215 \cdot 10^{-31}$ kg	electron mass
N_A	$=$	$6.02214179 \cdot 10^{23}$ mol^{-1}	Avogadro constant

Appendix B - Abbreviations

A	absorption
a_{BSA}	surface area occupied by one albumin molecule
A_{BSA}	total surface area occupied by albumin
a_{Fn}	surface area occupied by one fibronectin molecule
A_{Fn}	total surface area occupied by fibronectin
AC	alternating current
AFM	atomic force microscopy
ATR	attenuated total internal reflection
BSA	bovine serum albumin
c	concentration
CF	correction factor
CVD	chemical vapour deposition
CW	continuous wave
Δf	frequency shift
Δm	adsorbed mass on the quartz crystal
ΔM	mass difference
DC	direct current
DMEM	Dulbeccos modified Eagle's media
DOL	degree of labeling
ϵ	extinction coefficient
E_B	binding energy
ECM	extracellular matrix
EDTA	ethylenediaminetetraacetate
E_K	kinetic energy
ESR	electron spin resonance
F	flow rate
FCS	foetal calf serum

Fn	fibronectin
FRET	fluorescence resonance energy transfer
FTIR	fourier transform infrared
γ	surface tension
I	measured intensity
I_0	initial intensity
λ	mean free path *or* wavelength
λ_{De}	Debye length
l	cuvette length
M	molecular mass
m_{BSA}	molecular weight of albumin
M_{BSA}	mass of albumin
m_{Fn}	molecular weight of fibronectin
M_{Fn}	mass of fibronectin
m_i	mean ion mass
Mit-C	Mitomycin-C
MW	molecular weight
ν	frequency
n, n_e, n_i, n_0	particle density (of electrons, e, ions, i, and neutrals, 0)
n_{BSA}	mole of albumin
n_f	overtone of the resonance frequency
n_{Fn}	mole of fibronectin
NR	neutron reflection
$\omega, \omega_e, \omega_{ex}, \omega_i,$	oscillation frequency (of electrons, e, the excitation source, ex, and ions, i)
OWLS	optical waveguide lightmode spectroscopy
ϕ	work function
Φ	electric potential
PBS	phosphate buffered saline
PDMS	poly(dimethylsiloxane)
PEO	poly(ethylene oxide)
PHEMA	poly(2-hydroxyethylmethacrylate)
pK_a	acid constant
PMT	photo multiplier tube
pNiPAM	poly(N-*iso*-propyl acrylamide)
POP	polyolefin plastomer
ppAAc	plasma polymerised acrylic acid
ppAAm	plasma polymerised allylamine
ppHex/ppAAm	ppHex deposited on top of ppAAm
ppHepA	plasma polymerised n-heptylamine
ppHex	plasma polymerised n-hexane

ppHexA	plasma polymerised n-hexylamine
PVD	physical vapour deposition
QCM	quartz crystal microbalance
r	deposition rate
r_0	initial deposition rate
RF	radio frequency
rms	route mean square
σ	cross section of collision
s	sheath thickness
SAM	self assembled monolayer
SEM	scanning electron microscopy
SIMS	secondary ion mass spectrometry
SPR	surface plasmon resonance
θ	water contact angle
t	thickness of the plasma polymer layer
T_e	electron temperature
TEM	transmission electron microscopy
ToF-SIMS	time of flight secondary ion mass spectrometry
u, u_i	velocity (of ions, i)
u_B	Bohm velocity
V_s	sheath potential
VUV	vacuum ultraviolet
W	discharge power input
WCA	water contact angle
XPS	X-ray photoelectron spectroscopy

Appendix C - Chemicals

Chemical	Purity	Catalogue Nr.	Supplier
Albumin, Bovine	$\sim 99\%$	A3059	Sigma-Aldrich
Allylamine	99%	241075	Sigma-Aldrich
BODIPY 650/665-X, SE	-	D10001	Invitrogen
Ethanol	99%	E/0600/17	Fisher Chemicals
Fibronectin, Bovine	-	F4759	Sigma Aldrich
Glutaraldehyde	50%	G006	TAAB
Hexamethyldisilazane	-	H4875	Sigma Aldrich
Hexane	HPLC grade	H/0406/17	Fischer Scientific
Live/Dead Cell Viability Cytotoxicity Kit	-	L3224	Molecular Probes
N,N-Dimethylformamide	$> 99.5\%$, abs.	40228	Fluka
Osmiumtetroxide	2% v/w	O006	TAA
Phosphate Buffered Saline	-	BR0014G	Oxoid
Sodium bicarbonate	$> 99.7\%$	31437	Riedel-de Haën

Appendix D - Materials

Material	Specifications	Catalogue Nr.	Supplier
Cover Slips	22 x 22 mm, No 1.5	MIC3124	SLS
Dialysis Tubing	Cellulose Membrane, 10 x 6 mm, MW retention: > 12000 g/mol	D9277	Sigma-Aldrich
Microscope Slides	76 x 26 mm, h = 1.0 - 1.2 mm	631-0114	VWR
Quartz Crystals	gold coated	QSX301	Q-Sense

Appendix E - Methods

E.1 Plasma Polymer Preparation and Characterisation

E.1.1 Plasma Polymerisation

Plasma polymer deposition was carried out in a T-shaped borosilicate glass chamber with stainless steel endplates that were sealed with Viton O-rings (FIGURE E.1). The plasma discharge was initiated via two external, capacitively coupled copper band ring-electrodes that were connected to a 13.56 MHz radiofrequency power source (Coaxial Power System Ltd.). The impedance was matched manually so that the reflected power was < 1 W. The gas pressure in the chamber was monitored via a pirani gauge (Kurt J. Lesker) and controlled with needle valves (LV10K Leak Valve, BOC Edwards). Samples were placed on a metal tray (18.5 x 12.5 cm) in the center of the chamber. A quartz crystal sensor (STM-100/MF, Sycon Instruments) was positioned in the chamber to monitor the deposition rate and the thickness of the coating. Unless stated otherwise, all plasma polymer depositions were carried out to a thickness of 50 nm on the quartz crystal sensor.

The monomers were subjected to at least one freeze-pump-thaw cycle prior to use, until the base pressure (< 25 mTorr) was established in the vessel holding the frozen monomer. The plasma polymers were deposited on glass substrates; either circular (ø = 12 mm, No 1.5, Scientific Laboratory Supplies Ltd.) or square (22 x 22 mm, No 1.5, Scientific Laboratory Supplies Ltd.) cover slips or microscope slides (26 x 76 mm, VWR International) were used. Prior to the deposition, the
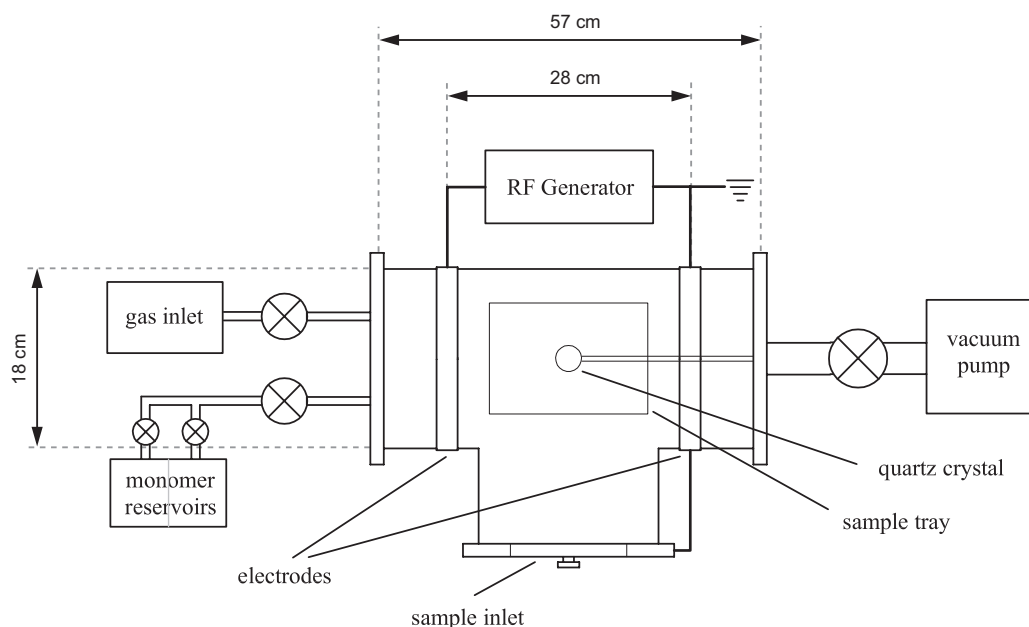
Figure E.1: Schematic of the plasma deposition chamber.

glass substrate was sonicated in water, washed with acetone and cleaned in an oxygen plasma (20 W, 300 mTorr) for 5 minutes. The deposition of the plasma polymers was carried out at a pressure of 300 mTorr with a power of 20 W. To attain a thickness of 50 nm on the quartz crystal sensor, a deposition time of 2 and 5 minutes was typically needed for allylamine and hexane, respectively. After each deposition, the monomer flow was sustained for 3 more minutes to saturate remaining active sites in the polymer.

E.1.2 Preparation of Diffusion Gradients

Shallow gradients were prepared by allowing penetration of depositing species from the plasma under a mask placed at a defined distance on the sample. Gradients with a linear change in surface chemistry were prepared by covering allylamine coated glass substrates with a mask separated from the sample by 0.04 mm by aluminium foil layers. During ppHex deposition, the open part of the assembly faced the monomer feed and allowed a thickness gradient of ppHex to be formed under the mask. These gradients were prepared on both square coverslips and microscope slides. A steep gradient with a sharp transition was obtained on coverslips by placing the mask in direct contact with the sample. Parafilm was wrapped around the assembly to prevent diffusion from the other three sides of the sample.
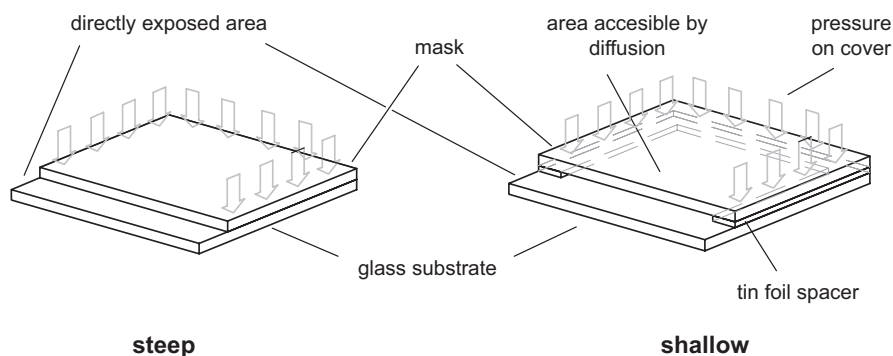
Figure E.2: Sample arrangement for steep and shallow diffusion gradients.

E.2 Plasma Diffusion

E.2.1 POP Mould Fabrication

A polyolefin plastomer (POP) block was prepared from POP granules (Affinity Polyolefin Plastomers, Dow Europe GmbH) by melting the granules at 190 ℃ for 1h under a 25 kg weight. A negative template of the channel structure was machined into a piece of brass. The brass template was sonicated in water and thoroughly washed with hexane three times to eliminate traces of silicon contamination from its surface. The positive structure was then transferred onto the POP block (1 cm in thickness) by hot embossing.

E.2.2 Plasma Polymerisation

Microscope slides (VWR) were sonicated for 15 min in deionised water, washed with acetone and cleaned in an oxygen plasma for 3 min. They were coated with ppAAm for 2:30 min (50 nm on the quartz crystal sensor). The POP mask was placed on the sample and sealed with parafilm at three sides to prevent lateral diffusion of the plasma. The samples were placed in the reactor such that the openings of the channels faced the monomer feed. In contrast to the other experiments, plasma polymerisation of hexane was carried out for 2:13 min (20 nm on the quartz crystal sensor).

For the flow control experiment, a solid block of POP was placed on the ppAAm coated sample. ppHex was deposited for 2:30 min (20 nm on the quartz crystal sensor). During deposition, the sample surface was oriented perpendicular to the direction of the monomer flow with the side of interest (the ppAAm coated side) facing away from the monomer inlet. All analysis was carried out within a week after sample preparation.

E.2.2 Mass Spectrometry of Penetrating Plasma Species

The penetration of plasma species through tubes of varying length was measured in a plasma reactor different from the one described above. The reactor consists of a cruciform vessel closed on each of the four ends with stainless steel end-plates sealed with O-rings. The plasma was excited with a power of 20 W at a frequency of 13.56 MHz (Coaxial Ltd RFG-150) in continuous mode and was applied through a wire wound around one of the axis of the reactor.

A mass spectrometer (Hiden Analytical Ltd EQP 300) was attached to one of the side arms of the plasma reactor. A glass tube holder (FIGURE E.3) onto which several tubes could be mounted was placed in front of the mass spectrometer gate such that only species penetrating through the tubes
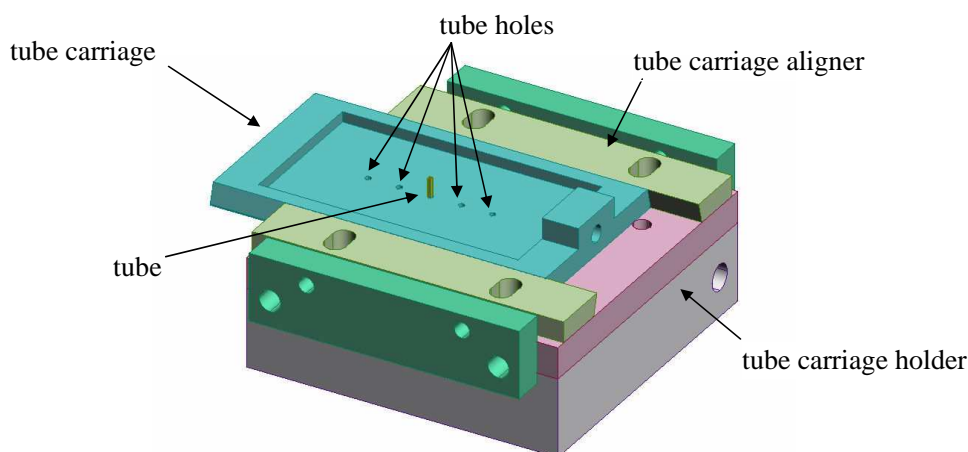
Figure E.3: Schematic design of the glass tube holder used to study the penetration depth of plasma species through tubes. The plasma region is situated above the tube holes while the mass spectrometer is below the tube carriage holder.

would be detected. Glass tubes of different length (0 (no tube), 2, 4, 8 and 12 mm) with a square cross section of 0.5 x 0.5 mm were used. Neutral species were subjected to electron bombardment to ionise and detected them with the spectrometer. This technique has been established before to detect neutral species in a plasma [340].

The pressure was monitored via a Baratron gauge (MKS 627). The reactor had a base pressure of 15 mTorr while the hexane plasma was operated at 100 mTorr. The upper limit of the operating pressure is restricted by the maximum pressure at which conclusive data can be obtained from the mass spectrometer. Even though this pressure is much lower than the one used to prepare the gradients in the channels (300 mTorr), comparison between spectra obtained at two different operating pressures indicate that the differences in the mass spectra are small. It is therefore assumed that the acquired mass spectra can be used to qualitatively explain the processes involved in the plasma polymerisation of hexane inside the channels.

E.3 Plasma Polymer Stability and Degradation

E.3.1 Sample Preparation

Uniform and gradient plasma polymer samples were prepared on glass substrates (approximately 5 x 5 mm) according to the standard procedure described above. The samples were placed in six-well plates (untreated tissue culture polystyrene, Falcon) and 3 ml PBS was added. The well plates were kept in an incubator (37℃, 5% CO_2) for 1h, rinsed twice by immersion in ultrapure water and blow dried with nitrogen gas. WCA, XPS and ToF-SIMS analysis was carried out within four days after sample treatment.

E.4 Cell Culture

E.4.1 General Cell Culture Procedure

NIH 3T3 fibroblasts (obtained from ATCC) were maintained in monolayer culture in a humidified atmosphere at 37℃ and 5% CO_2 for less than five passages in Dulbeccos modified Eagles media (DMEM) supplemented with 10% (v/v) foetal calf serum (FCS), 2 mM L-glutamine, 100 units/ml penicillin, 0.1 mg/ml streptomycin and 0.25 mg/ml amphotericin B (3T3 complete medium). Cell passaging and preparation of single cell suspensions was achieved via enzymatic digestion with 0.25% (v/v) trypsin dissolved in phosphate buffered saline (PBS) at *pH* 7.4 to which 0.02% (w/v) EDTA was added. The cells in single cell suspensions were counted with a haemocytometer and seeded on the samples at a density of 50.000 cells in 3 ml 3T3 complete medium one day after the plasma polymer deposition. The samples were agitated gently for 20 minutes to ensure an even distribution of the cells over the whole sample surface. After static incubation at 37℃ for one day, the media and non adhered cells were removed. The sample was washed with 3 ml PBS for 5 min and after removing the PBS 3 ml of fresh media was added. Images of the cells were taken daily over 4 days at a 5x magnification.

E.4.2   Sample Preparation for SEM

The culture media was removed and the cells were washed 3 times with PBS. The cells were fixed with 2 ml of a solution of 3% glutaraldehyde in PBS over night. The solution was removed and the samples were rinsed 3 times with PBS. The samples were reacted with 2 ml of a 1% OsO_4 solution in PBS for 2 hours, rinsed 3 times with water and successively dehydrated in mixtures of ethanol and water of increasing ethanol content (25%, 50%, 70%, 90%, 95% and 100%) and dried with hexamethyldisilazane (two times for 5 min). After drying over night, the samples were sputter coated with gold (Pelco Sputter Coater 91000) at 20 mA for 5 min.

E.4.3   Life-Dead Stain

For the live-dead stain, the culture media was removed from the well of each sample, the samples were washed three times with PBS and then transferred to new well plates. 1 ml of the staining solution (a mixture of 4 μM Ethidium homodimer I and 2 μM Calcein AM in PBS) was added to each well. The reaction was allowed to proceed for 40 min at room temperature. The reaction solution was removed, the samples were washed 3 times with PBS and imaged in PBS.

E.4.4   Mitomycin-C Treatment

Mitomycin-C (Mit-C) treatment of cells was achieved by incubating $\sim 80\%$ confluent 3T3 fibroblasts in tissue culture flasks with 10 ml Mit-C (100 μg/ml in media) for 2.5h. The cells were washed three times with 10 ml PBS. Fresh media was added and the cells were then incubated for an additional 3 days to confirm that the treatment was effective and proliferation had been suppressed. The rest of the cell culture procedure is the same as described above.

E.5   Image Analysis

E.5.1   Gradient Samples

On gradient samples, images were taken along the length of the gradient over a distance of approximately 12 mm. The images overlapped to at least 1/4. They were overlayed to give a complete image over the whole gradient, which was then divided into 0.2 mm increments along its length. The number of cells in the resulting areas (0.97 x 0.2 mm) was counted manually. The cells were classified either as round or spread. Round cells were considered to be either dead or not strongly adhered to the surface. Thus, only spread cells – cells that showed a typical fibroblast morphology – were used to determine the cell density in these areas. The cell density was then converted into the number of cells per mm^2 to be able to compare the data with the control samples. This process was repeated 3 times on each sample.

E.5.2 Uniform Samples

Images taken of uniform samples were divided into 5 square areas of 0.6 x 0.6 mm. The number of cells in these areas was determined and its average was used as the cell density for the analysed sample. The results reported were averaged over all repeats and converted into cells per mm^2.

E.5.3 Live-Dead Stain

Images on uniform and gradient samples were taken as described above. On each position, images were taken in brightfield and in UV excitation mode, the latter resulting in images showing Ethidium homodimer I labeled (red fluorescence, $\lambda_{Max,Ex} = 495$nm, $\lambda_{Max,Em} = 635$nm) and Calcein AM labeled (green fluorescence, $\lambda_{Max,Ex} = 495$nm, $\lambda_{Max,Em} = 515$nm) cells. The figures presented are a combination of these images that show the fluorescently stained features and the features observed in brightfield mode in the same picture.

E.6 Protein Adsorption

E.6.1 Protein Solutions for QCM Measurements

Bovine serum albumin (BSA) and bovine fibronectin (Fn) were dissolved in PBS that has previously been degassed by sonication for 30 min. The protein concentrations were 4 mg/ml and 0.03 mg/ml for albumin and fibronectin, respectively.

Plasma polymers were deposited on gold coated quartz crystals according to the standard procedures described above. They were conditioned with degassed PBS in the instrument prior to the adsorption experiment until the baseline stabilized. The sample loop was flushed with 1.5 ml protein solution before allowing 0.5 ml of the solution to flow over the sample. The protein adsorption was allowed to proceed under static conditions until the frequency shift stopped changing (less than 15 min). Loosely adsorbed proteins were rinsed off with 0.5 ml PBS. The amount of adsorbed protein was measured following the PBS rinse after the resonance frequency had stabilized again. All measurements were taken at 25℃. The flow rate through the chamber was 12 ml/min.

E.6.2 Protein Labeling

The protein was dissolved in a buffer solution (see Table E.1) and 100 μl of a dye solution of BODIPY 650/665 in DMF (19 mg/ml) were added. The mixture was stirred in the dark at room temperature for approximately 1h 30min. After the reaction, unconjugated dye was separated via dialysis of the protein solution with PBS (exchange volume: 1 l) until the fluorescence signal measured from the dialysis buffer remained constant.

The final concentration of the protein solutions after labeling was determined by UV spectroscopy using spectra obtained from dilutions of unlabeled proteins Figure E.4. The absorption measured at 280 nm and 202 nm was used for albumin and fibronectin, respectively, to obtain the following calibration functions:
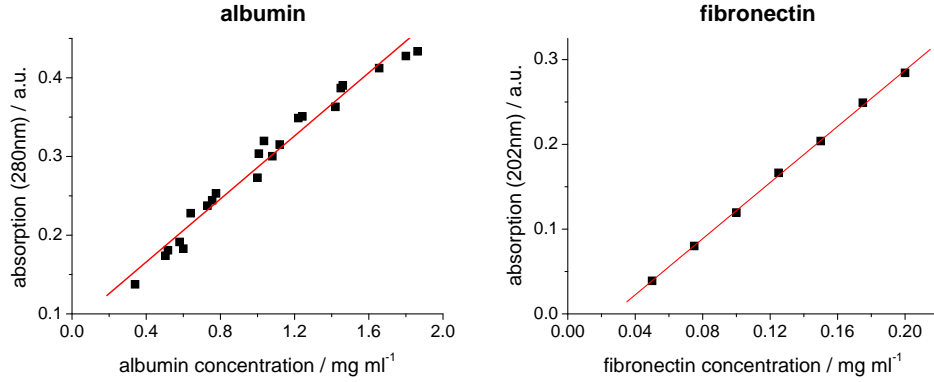
Figure E.4: Calibration curves for the UV absorption of albumin and fibronectin.

Albumin: $\qquad A_{280} = 0.20046 \cdot [albumin] + 0.08567 \qquad R^2 = 0.98599 \qquad$ (E.1)

Fibronectin: $\qquad A_{202} = 1.65532 \cdot [fibronectin] - 0.04371 \qquad R^2 = 0.99964 \qquad$ (E.2)

where A is the absorption at the specified wavelength and $[albumin]$ and $[fibronectin]$ are the concentrations of the proteins in mg/ml.

The experimentally obtained absorption of the labeled protein solution at the respective wavelengths (A_λ with $\lambda_{(A_{protein})} = 280$ or 202 nm) consists of the combined absorption of the protein ($A_{protein}$) and the dye (A_{dye}):

$$A_\lambda = A_{protein} + A_{dye} \qquad (E.3)$$

Therefore, $A_{protein}$ of the labeled protein solutions can be obtained by correcting for the contribution of the absorption of the dye to A_λ. The proteins have no absorption characteristics at the second absorption maximum of the dye (A_{max}), which is found at higher wavelengths ($\lambda_{(A_{max\,dye})}$) than A_λ. Since the ratio between the absorption of the dye at $\lambda_{(A_{protein})}$ and $\lambda_{(A_{max\,dye})}$ stays

Table E.1: Experimental parameters for the protein labeling procedure.

	Albumin	Fibronectin
Quantity	20.5 mg	6.8 mg
Reaction buffer	NaHCO$_3$ (0.1 M)	PBS
Buffer volume for reaction	2 ml	8 ml
Conjugated dye	BODIPY 650/665	BODIPY 650/665
Dye concentration	10 mg/ml	10 mg/ml
Volume of dye solution	100 μl	100 μl
Final buffer volume before dialysis	10 ml	8 ml
Dialysis buffer	PBS	PBS
Exchange volume	1 l	1 l

constant, A_{dye} can be determined if A_{max} of the labeled protein solution is measured and the ratio is known. This ratio, or correction factor CF, was determined by measuring A_λ and A_{max} of the free dye ($A_{\lambda\,free\,dye}$ and $A_{max\,free\,dye}$):

$$CF = \frac{A_{dye}}{A_{max}} = \frac{A_{\lambda\,free\,dye}}{A_{max\,free\,dye}} \tag{E.4}$$

CF and the A_{max} measured in the labeled protein solution can then be used to determine A_{dye}:

$$A_{dye} = A_{max} \cdot CF \tag{E.5}$$

which turns EQUATION E.3 into

$$A_{protein} = A_\lambda - A_{max} \cdot CF \tag{E.6}$$

so that the concentration of the labeled protein solutions can be determined using $A_{protein}$ in the calibration functions in EQUATION E.1 and E.2.

To estimate how many proteins in the solution have been labeled with the dye, it was assumed that all unreacted dye was removed from the solution by dialysis. Hence, the degree of labeling (DOL) was calculated by dividing the concentration of the dye (c_{dye}) in the solution – which was assumed to be equal to the number of labeled proteins – by the total concentration of the protein ($c_{protein}$):

$$DOL = \frac{c_{dye}}{c_{protein}} = \frac{A_{max} \cdot MW}{[protein] \cdot \epsilon_{dye} \cdot l} \tag{E.7}$$

where A_{max} is the absorption at the second absorption maximum of the labeled protein solution (which corresponds to the absorption of the dye), MW the molecular weight of the protein in g/mol, $[protein]$ the concentration of the protein in mg/ml, ϵ_{dye} the extinction coefficient of the dye in l mol^{-1} cm^{-1} and the cuvette length $l = 1$ cm.

For ϵ_{dye}, the data provided by the manufacturer was used, while the molecular weights of the proteins were taken from literature (see SECTION 6.2.1). A_{max} and $[protein]$ were obtained from

Table E.2: Values and results for the calculation of the correction factor (CF) of BODIPY 650/665.[a]

Property	Protein	
	Albumin	Fibronectin
$\lambda_{(A_{protein})}$	280 nm	202 nm
$\lambda_{(A_{max\,free\,dye})}$	651 nm	651 nm
$A_{max\,free\,dye}$	$0.5776 \cdot 10^{-3}$	$20.62 \cdot 10^{-3}$
$A_{\lambda\,free\,dye}$	$0.1458 \cdot 10^{-3}$	$89.07 \cdot 10^{-3}$
CF	**0.252**	**4.320**

[a] Experimental data is written in plain font and calculated values are shown as **bold**.

the UV absorption experiments which were carried out with 1:10 dilutions of the stock solution of labeled proteins. The results for the above calculations are listed in TABLE E.2 and E.3.

E.6.3   Adsorption to Plasma Polymers

The adsorption characteristics of albumin and fibronectin were studied on uniform ppHex and ppAAm as well as on linear gradient surfaces. For these protein experiments, microscope slides were used as substrates for the plasma polymer films.

The adsorption of the individual proteins as well as the displacement of albumin by fibronectin (Vroman effect) was studied on all gradients and uniform samples. For the displacement study, both *sequential* and *competitive* adsorption were used. For the *sequential* adsorption, the surfaces were first exposed to a solution of albumin followed by a solution of fibronectin, while for the *competitive* adsorption a solution containing a mixture of both proteins was used (TABLE E.4). In all solutions, the total concentration of albumin and fibronectin were 4 mg/ml and 0.03 mg/ml, respectively. Solutions of fibronectin were prepared by direct dilution of the stock solution of labeled fibronectin. Labeled albumin was mixed with unlabeled albumin to obtain a 4 mg/ml solution containing 0.2 mass-% labeled protein.

For each set of experiments, 4 microscope slides – one ppAAm and one ppHex/ppAAm coated slide and two microscope slides containing three separate gradients each – were covered with 28 ml protein solution. The samples were stored in the incubator at 37℃ and 5% CO_2 for 1h. Then, the samples were washed 2x with 28 ml PBS for 30 s and dried in air under protection from light. For the sequential exposure to fibronectin, the procedure was repeated with the second protein solution.

The responsiveness of this method to a gradient surface was tested on plasma polymer gradients

Table E.3: Values and results for the calculation of protein concentrations and the degree of labeling (DOL).[a]

Property	Protein	
	Albumin	Fibronectin
$\lambda_{(A_{protein})}$	280 nm	202 nm
A_λ [b]	0.3187	0.5048
A_{max} [b]	0.3040	0.0921
CF	**0.252**	**4.320**
$A_{protein}$ [b]	**0.2420**	**0.1070**
MW	*67000* g/mol	*450000* g/mol
$[protein]$ [c]	**7.80 mg/ml**	**0.91 mg/ml**
ϵ_{dye}	*100000* $\mathrm{l\,mol^{-1}\,cm^{-1}}$	*100000* $\mathrm{l\,mol^{-1}\,cm^{-1}}$
DOL	**0.03**	**0.46**

[a] Experimental data is written in plain font, data from literature in *italic* and calculated values are shown as **bold**.

[b] Values are for a 1:10 dilution of the protein stock solution.

[c] Protein concentration of the stock solution.

Table E.4: Overview of the experimental design of the adsorption experiments with labeled proteins. All sample formats (ppHex/ppAAm, ppAAm, gradients) were exposed to each of these conditions. BSA = albumin, BSA* = labeled albumin, Fn = fibronectin, Fn* = labeled fibronectin.

Type of Adsorption	Protein solution		
	Albumin		Fibronectin
Individual protein adsorption	BSA BSA*		Fn Fn*
Sequential protein adsorption	BSA BSA BSA*	→ → →	Fn Fn* Fn
Competitive protein adsorption	BSA BSA BSA*	+ + +	Fn Fn* Fn

of different transition length. Single protein adsorption from labeled and unlabeled albumin and fibronectin solutions were carried out on surfaces prepared by plasma diffusion through channels as described in CHAPTER 4.

As shown in TABLE E.4, in each set of experiments a control measurement was carried out under the same conditions with unlabeled proteins. These results were used to correct for any unspecific fluorescence detected from the sample that is not related to the dye. The data presented in the results sections show the difference between the intensities of the labeled and the corresponding unlabeled experiments.

Appendix F - Instruments

F.1   X-ray Photoelectron Spectroscopy (XPS)

XPS analysis was carried out on a Kratos AXIS ULTRA. X-rays were produced with a monochromated Al k_{α} source (1486.6 eV) using an emission current of 15 mA and an anode potential of either 10 or 12 kV. The instrument was used in fixed analyser transmission mode (FAT) with a pass energy of 80 eV for widescans and 20 eV for high resolution scans. The analysis area was defined by a magnetic immersion lens system; a hybrid lens was used for uniform samples while a circular aperture ($\varnothing = 110$ μm) was used for the analysis of gradients. The takeoff angle for the photoelectron analyser was 90°. Charge neutralisation was used for all samples. Data Analysis was carried out with CasaXPS using empirical sensitivity factors provided by the manufacturer for quantification of the relative percentage of the detected elements. C 1s curve fits were carried out by restricting the full width half maximum of all components to that of the C−C/C−H component at 284.8 eV. The other components had fixed positions at 285.8 eV (C−N), 286.3 eV (C=N/C−O), 287.9 eV (C(=O)N/C=O) and 288.9 eV (C(=O)O). For samples exposed to PBS, a separate component had to be introduced for C=O at 287.5 eV to ensure a good fit. The assignment of these components was done according to previously published literature [31, 56, 60, 112, 116].

F.2   Water Contact Angle (WCA) Measurement

Uniform Samples

The WCA of uniform samples was measured with a Cam200 instrument (KSV Instruments) using the sessile drop method. Deionised water was used for the measurement. After positioning the droplet onto the surface, 20 images of the drop were taken in 1 second intervals. The baseline was set manually and the contact angle was calculated for each image using a Young-Laplace curve fit. In most cases, the first value was not reflective of an equilibrated state and was therefore generally discarded for all samples. The remaining values were plotted as a function of time (t) and a linear regression was used to determine the actual WCA at $t = 0$.

Gradients

To determine the WCA on gradient samples a DSA100 instrument (Krüss) was used. This instrument allows the deposition of pico-litre sized droplets on the sample surface. The typical drop volume is 110 pl, which corresponds to a base diameter of approximately 75 μm for a WCA of 90°. The sample was moved via an automated stage. WCA measurements were taken in the center of the sample using parallel lines along the length of the gradients. Videos of the evaporating droplets were captured in 18 ms intervals for the duration of 1 second. The WCA was determined for the first stable contact of the water droplet with the surface using a circular curve fit.

F.3   Time of Flight Secondary Ion Mass Spectrometry (ToF-SIMS)

ToF-SIMS analysis was carried out on a SIMS IV time-of-flight instrument (ION-TOF GmbH.) equipped with a gallium liquid metal ion gun and a single-stage reflectron analyser. The instrument was typically operated at a primary ion energy of 15 kV, a pulsed target current of ~ 1.3 pA and a post acceleration of 10 kV. Charges induced on the substrate surface by the positively charged ion beam were compensated with a flux of low energy electrons (20 eV). Large scale images were obtained by rastering the stage under the pulsed primary ion beam. All doses were kept below the static limit with a maximum dose of 1012 ions per cm^2 for both polarities combined. Acquisition of full raw datasets allowed for the retrospective construction of spectra from the imaged areas.

F.4   Atomic Force Microscopy (AFM)

AFM images were taken in tapping mode with a Dimension 3000 (Digital Instruments, Veeco), controlled with *NanoScope* (V5.30, 2005). The images were processed with *The Scanning Probe Image Processor* (SPIP, Version 3.3.6.0, 2005, Image Metrology). The root mean square (rms) surface roughness was determined for 2 x 2 mm^2 images after performing global and linewise plane corrections. Images in liquid were taken in tapping mode at ambient conditions using a glass tip holder on which a contact mode tip was mounted. In protein containing solutions, the force at which the cantilever was driven was set just high enough to remove any absorbed proteins during imaging in order to obtain micrographs of the actual plasma polymer surface.

F.5   Scanning Electron Microscopy (SEM)

SEM images were taken with a JSM-6060LV Scanning Microscope (JEOL Ltd.) The instrument has a tungsten filament as electron source and was operated at 10 kV in high vacuum mode.

F.6   Light and Fluorescence Microscopy

Images of samples used in cell culture experiments were taken with a Leica DM IRB microscope in phase mode. The fluorophores used in the live/dead stain were excited by UV light passed through bandpass filters (N2.1 green BP 515 - 560 nm for Ethidium homodimer I and I3 blue BP 450 - 490 nm for Calcein AM).

F.7   Quartz Crystal Microbalance (QCM)

QCM measurements were carried out with a Q-Sense D300. The instrument has an axial flow chamber with a volume of 80 μl. The active area on the crystal has 0.2 cm^2.

The measured frequency shifts were converted to mass changes according to the Sauerbrey equation:

$$\Delta m = -C \frac{\Delta f}{n_f} \tag{F.1}$$

where Δm is the mass of the adsorbed protein, C the mass sensitivity constant (typically 17.7 ng cm^{-2} Hz^{-1} for a 5 MHz crystal), Δf the change in frequency during adsorption and n_f the overtone of the resonance frequency [269]. For all measurements presented here, the third overtone (14.9 MHz) was used.

F.8 UV Spectroscopy

UV absorption spectra were acquired with a Cary 50 UV-Vis Spectrophotometer (Varian Inc.) using Cary WinUV software and Hellma 104-QG cuvettes with a light path of 10 mm.

F.9 Fluorescence Microscope Slide Scanner

The microscope slide samples prepared for the protein adsorption experiments were scanned with an Axon GenePix 4000b slide scanner. The samples were excited at 635 with a laser that has an illumination area of 10 μm in diameter using 100% power and a PMT gain of 500 V.

For data analysis, circular areas with a diameter of 180 μm were positioned on the scanned image in 0.2 mm intervals to create a rectangular array with 70 x 60 circles for each sample area. Within the circular areas, the measured intensity was averaged to produce a single value for each position on the array. The data was then averaged over all 60 rows to obtain an average intensity that is related to a distance of 14 mm on the samples.

F.10 Deionised Water

Deionised, HPLC grade water (18.2 mΩ) was obtained from an Elga Purelab Maxima instrument. This water was used for all measurements that required purified water and for the preparation of all solutions.

Bibliography

[1] Langer, R.; Vacanti, J. P. *Science* **1993**, *260*, 920 – 926.

[2] Stevens, M. M.; George, J. H. *Science* **2005**, *310*, 1135 – 1138.

[3] Ruardy, T. G.; Moorlag, H. E.; Schakenraad, J. M.; Mei, H. C. V. D.; Busscher, H. J. *Journal of Colloid and Interface Science* **1997**, *188*, 209–217.

[4] Lee, J. H.; Khang, G.; Lee, J. W.; Lee, H. B. *Journal of Colloid and Interface Science* **1998**, *205*, 323–330.

[5] Petronis, S.; Gretzer, C.; Kasemo, B.; Gold, J. *Journal of Biomedical Materials Research A* **2003**, *66A*, 707–721.

[6] Ruardy, T. G.; Schakenraad, J. M.; van der Mei, H. C.; Busscher, H. J. *Surface Science Reports* **1997**, *29*, 3–30.

[7] Kim, M. S.; Khang, G.; Lee, H. B. *Progress in Polymer Science* **2008**, *33*, 138–164.

[8] Barry, J. J.; Howard, D.; Shakesheff, K. M.; Howdle, S. M.; Alexander, M. R. *Advanced Materials* **2006**, *18*, 1406–1410.

[9] Urquhart, A. J.; Anderson, D. G.; Taylor, M.; Alexander, M. R.; Langer, R.; Davies, M. C. *Advanced Materials* **2007**, *19*, 2486–+.

[10] Taylor, M.; Urquhart, A. J.; Anderson, D. G.; Williams, P. M.; Langer, R.; Alexander, M. R.; Davies, M. C. *Macromolecular Rapid Communications* **2008**, *29*, 1298–1302.

[11] Morgenthaler, S.; Zink, C.; Spencer, N. D. *Soft Matter* **2008**, *4*, 419–434.

[12] Genzer, J.; Bhat, R. R. *Langmuir* **2008**, *24*, 2294–2317.

[13] Yasuda, H. *Plasma Polymerization*; Aademi Press: New York, 1985.

[14] Dinelli, F.; Leggett, G. J.; Alexander, M. R. *Journal of Applied Physics* **2002**, *91*, 3841–3846.

[15] Ohl, A.; Schroder, K. *Surface & Coatings Technology* **1999**, *119*, 820–830.

[16] Mitchell, S. A.; Emmison, N.; Shard, A. G. *Surface and Interface Analysis* **2002**, *33*, 742–747.

[17] Mitchell, S. A.; Davidson, M. R.; Emmison, N.; Bradley, R. H. *Surface Science* **2004**, *561*, 110–120.

[18] Bullett, N. A.; Bullett, D. P.; Truica-Marasescu, F. E.; Lerouge, S.; Mwale, F.; Wertheimer, M. R. *Applied Surface Science* **2004**, *235*, 395–405.

[19] Thissen, H.; Johnson, G.; Hartley, P. G.; Kingshott, P.; Griesser, H. J. *Biomaterials* **2006**, *27*, 35 – 43.

[20] Whittle, J. D.; Barton, D.; Alexander, M. R.; Short, R. D. *Chemical Communications* **2003**, 1766–1767.

[21] Gengenbach, T. R.; Vasic, Z. R.; Chatelier, R. C.; Griesser, H. J. *Journal of Polymer Science Part A: Polymer Chemistry* **1994**, *32*, 1399–1414.

[22] Gengenbach, T. R.; Chatelier, R. C.; Griesser, H. J. *Surface and Interface Analysis* **1996**, *24*, 611–619.

[23] Gengenbach, T. R.; Chatelier, R. C.; Griesser, H. J. *Surface and Interface Analysis* **1996**, *24*, 271–281.

[24] Gengenbach, T. R.; Griesser, H. J. *Surface and Interface Analysis* **1998**, *26*, 498–511.

[25] Gengenbach, T. R.; Griesser, H. J. *Journal of Polymer Science Part A: Polymer Chemistry* **1999**, *37*, 2192–2206.

[26] Zhang, Z.; Chen, Q.; Knoll, W.; Förch, R. *Surface & Coatings Technology* **2003**, *174*, 588–590.

[27] Jeon, H. S.; Wyatt, J.; Harper-Nixon, D.; Weinkauf, D. H. *Journal of Polymer Science Part B-Polymer Physics* **2004**, *42*, 2522–2530.

[28] Förch, R.; Zhang, Z. H.; Knoll, W. *Plasma Processes and Polymers* **2005**, *2*, 351–372.

[29] Tamirisa, P. A.; Hess, D. W. *Macromolecules* **2006**, *39*, 7092–7097.

[30] Muir, B. W.; Nelson, A.; Fairbrother, A.; Fong, C.; Hartley, P. G.; James, M.; McLean, K. M. *Plasma Processes and Polymers* **2007**, *4*, 433–444.

[31] Tarasova, A.; Hamilton-Brown, P.; Gengenbach, T.; Griesser, H. J.; Meagher, L. *Plasma Processes and Polymers* **2008**, *5*, 175–185.

[32] Vasilev, K.; Britcher, L.; Casanal, A.; Griesser, H. J. *Journal of Physical Chemistry B* **2008**, *112*, 10915–10921.

[33] Parry, K. L.; Shard, A. G.; Short, R. D.; White, R. G.; Whittle, J. D.; Wright, A. *Surface and Interface Analysis* **2006**, *38*, 1497–1504.

[34] Robinson, D. E.; Marson, A.; Short, R. D.; Buttle, D. J.; Day, A. J.; Parry, K. L.; Wiles, M.; Highfield, P.; Mistry, A.; Whittle, J. D. *Advanced Materials* **2008**, *20*, 1166–1169.

[35] Lieberman, M. A.; Lichtenberg, A. J. *Principles of Plasma Discharges and Materials Processing*; John Wiley & Sons Inc.: New York, 2005.

[36] Denes, F. S.; Manolache, S. *Progress in Polymer Science* **2004**, *29*, 815–885.

[37] Moravej, M.; Hicks, R. F. *Chemical Vapor Deposition* **2005**, *11*, 469–476.

[38] Biederman, H. In *Plasma Polymer Films*; Biederman, H., Ed.; Imperial College Press: London, 2004; Chapter 1, pp 13–24.

[39] Inagaki, N. *Plasma Surface Modification and Plasma Polymerization*; Tenomi Publising AG: Basel, 1996.

[40] Choy, K. L. *Progress in Materials Science* **2003**, *48*, 57–170.

[41] Zeuner, M. In *Plasma Polymer Films*; Biederman, H., Ed.; Imperial College Press: London, 2004; Chapter 4, pp 85–142.

[42] Yasuda, H. *Journal of Macromolecular Science-Chemistry* **1976**, *A 10*, 383–420.

[43] Friedrich, J.; Kuhn, G.; Mix, R.; Unger, W. *Plasma Processes and Polymers* **2004**, *1*, 28–50.

[44] Friedrich, J. F.; Mix, R.; Schulze, R. D.; Meyer-Plath, A.; Joshi, R.; Wettmarshausen, S. *Plasma Processes and Polymers* **2008**, *5*, 407–423.

[45] Holländer, A.; Thome, J. In *Plasma Polymer Films*; Biederman, H., Ed.; Imperial College Press: London, 2004; Chapter 7, pp 247–278.

[46] Barry, J. J. A.; Silva, M. M. C. G.; Shakesheff, K. M.; Howdle, S. M.; Alexander, M. R. *Advanced Functional Materials* **2005**, *15*, 1134–1140.

[47] Denaro, A. R.; Owens, P. A.; Crawshaw, A. *European Polymer Journal* **1969**, *5*, 471–482.

[48] Kobayashi, H.; Bell, A. T.; Shen, M. *Journal of Macromolecular Science-Chemistry* **1976**, *A 10*, 491–500.

[49] Yasuda, H. *Macromolecular Reviews Part D-Journal of Polymer Science* **1981**, *16*, 199–293.

[50] Bieg, K. W. *Thin Solid Films* **1981**, *84*, 411–417.

[51] Wertheimer, M. R.; Fozza, A. C.; Holländer, A. *Nuclear Instruments & Methods in Physics Research Section B-Beam Interactions with Materials and Atoms* **1999**, *151*, 65–75.

[52] Siow, K. S.; Britcher, L.; Kumar, S.; Griesser, H. J. *Plasma Processes and Polymers* **2006**, *3*, 392–418.

[53] Beyer, H.; Walter, W.; Francke, W. *Lehrbuch der Organischen Chemie*, 23rd ed.; Hirzel Verlag: Stuttgart, 1998.

[54] Chatelier, R. C.; Xie, X. M.; Gengenbach, T. R.; Griesser, H. J. *Langmuir* **1995**, *11*, 2576–2584.

[55] Johnston, E. E.; Ratner, B. D. *Journal of Electron Spectroscopy and Related Phenomena* **1996**, *81*, 303–317.

[56] Whittle, J. D.; Short, R. D.; Douglas, C. W. I.; Davies, J. *Chemistry of Materials* **2000**, *12*, 2664–2671.

[57] Gengenbach, T. R.; Griesser, H. J. *Journal of Polymer Science Part A-Polymer Chemistry* **1998**, *36*, 985–1000.

[58] McCurdy, P. R.; Truitt, J. M.; Fisher, E. R. *Journal of the Electrochemical Society* **1998**, *145*, 3271–3277.

[59] Malkov, G. S.; Martin, I. T.; Schwisow, W. B.; Chandler, J. P.; Wickes, B. T.; Gamble, L. J.; Castner, D. G.; Fisher, E. R. *Plasma Processes and Polymers* **2008**, *5*, 129–145.

[60] Fally, F.; Doneux, C.; Riga, J.; Verbist, J. J. *Journal of Applied Polymer Science* **1995**, *56*, 597–614.

[61] Dai, L.; StJohn, H. A. W.; Bi, J.; Zientek, P.; Chatelier, R. C.; Griesser, H. J. *Surface and Interface Analysis* **2000**, *29*, 46–55.

[62] Harsch, A.; Calderon, J.; Timmons, R. B.; Gross, G. W. *Journal of Neuroscience Methods* **2000**, *98*, 135–144.

[63] Haddow, D. B.; Steele, D. A.; Short, R. D.; Dawson, R. A.; MacNeil, S. *Journal of Biomedical Materials Research Part A* **2003**, *64A*, 80–87.

[64] Notara, M.; Bullett, N. A.; Deshpande, P.; Haddow, D. B.; MacNeil, S.; Daniels, J. T. *Journal of Materials Science-Materials in Medicine* **2007**, *18*, 329–338.

[65] Krishnamurthy, V.; Kamel, I. L.; Wei, Y. *Journal of Polymer Science Part A-Polymer Chemistry* **1989**, *27*, 1211–1224.

[66] Schönherr, H.; van Os, M. T.; Förch, R.; Timmons, R. B.; Knoll, W.; Vancso, G. J. *Chemistry of Materials* **2000**, *12*, 3689–3694.

[67] Chang, C.-M. *Polymer Surface Modification and Characterization*; Carl Hanser Verlag: Munich, 1994.

[68] Bubert, H.; Rivière, J. C. *Surface and Thin Film Analysis: A Compendium of Principles, Instrumentation and Applications*; Wiley-VCH: Weinheim, 2002.

[69] Bain, C. D.; Whitesides, G. M. *Journal of the American Chemical Society* **1988**, *110*, 5897–5898.

[70] Wenzel, R. N. *Industrial and Engineering Chemistry* **1936**, *28*, 988–994.

[71] Cassie, A. B. D.; Baxter, S. *Transactions of the Faraday Society* **1944**, *40*, 0546–0550.

[72] Wenzel, R. N. *Journal of Physical and Colloid Chemistry* **1949**, *53*, 1466–1467.

[73] Watts, J. F.; Wolstenholme, J. *An Introduction to Surface Analysis by XPS and AES*; John Wiley & Sons Ltd: Chichester, 2003.

[74] Briggs, D. *Surface analysis of polymers by XPS and static SIMS*; Cambridge Solid State Series; Cambridge University Press: Cambridge, 2005.

[75] Friedbacher, G. *Surface and Thin Film Analysis: A Compendium of Principles, Instrumentation and Applications*; Wiley-VCH: Weinheim, 2002.

[76] Arlinghaus, H. F. *Surface and Thin Film Analysis: A Compendium of Principles, Instrumentation and Applications*; Wiley-VCH: Weinheim, 2002.

[77] de Hoffmann, E.; Stroobant, V. *Mass Spectrometry: Principles and Applications*, 2nd ed.; John Wiley & Sons, Ltd: Paris, 2003.

[78] Genzer, J.; Efimenko, K.; Fischer, D. A. *Langmuir* **2006**, *22*, 8532–8541.

[79] Elwing, H.; Welin, S.; Askendal, A.; Nilsson, U.; Lundstrm, I. *Journal of Colloid and Interface Science* **1987**, *119*, 203–210.

[80] Liedberg, B.; Tengvall, P. *Langmuir* **1995**, *11*, 3821–3827.

[81] Kraus, T.; Stutz, R.; Balmer, T. E.; Schmid, H.; Malaquin, L.; Spencer, N. D.; Wolf, H. *Langmuir* **2005**, *21*, 7796–7804.

[82] Pardo, L.; Wilson, W. C.; Boland, T. J. *Langmuir* **2003**, *19*, 1462–1466.

[83] Gorman, C. B.; Carroll, R. L.; He, Y. F.; Tian, F.; Fuierer, R. *Langmuir* **2000**, *16*, 6312–6316.

[84] Gorman, C. B.; Carroll, R. L.; Fuierer, R. R. *Langmuir* **2001**, *17*, 6923–6930.

[85] Jeon, N. L.; Dertinger, S. K. W.; Chiu, D. T.; Choi, I. S.; Stroock, A. D.; Whitesides, G. M. *Langmuir* **2000**, *16*, 8311–8316.

[86] Tomlinson, M. R.; Genzer, J. *Macromolecules* **2003**, *36*, 3449–3451.

[87] Tomlinson, M. R.; Genzer, J. *Langmuir* **2005**, *21*, 11552–11555.

[88] Caelen, I.; Bernard, A.; Juncker, D.; Michel, B.; Heinzelmann, H.; Delamarche, E. *Langmuir* **2000**, *16*, 9125–9130.

[89] Fosser, K. A.; Nuzzo, R. G. *Analytical Chemistry* **2003**, *75*, 5775–5782.

[90] Lee, J. H.; Jeong, B. J.; Lee, H. B. *Journal of Biomedical Materials Research* **1997**, *34*, 105–114.

[91] Kim, M. S.; Seo, K. S.; Khang, G.; Lee, H. B. *Langmuir* **2005**, *21*, 4066–4070.

[92] Harris, B. P.; Metters, A. T. *Macromolecules* **2006**, *39*, 2764–2772.

[93] Hypolite, C. L.; McLernon, T. L.; Adams, D. N.; Chapman, K. E.; Herbert, C. B.; Huang, C. C.; Distefano, M. D.; Hu, W. S. *Bioconjugate Chemistry* **1997**, *8*, 658–663.

[94] Caelen, I.; Gao, H.; Sigrist, H. *Langmuir* **2002**, *18*, 2463–2467.

[95] Roberson, S. V.; Fahey, A. J.; Sehgal, A.; Karim, A. *Applied Surface Science* **2002**, *200*, 150–164.

[96] Loos, K.; Kennedy, S. B.; Eidelman, N.; Tai, Y.; Zharnikov, M.; Amis, E. J.; Ulman, A.; Gross, R. A. *Langmuir* **2005**, *21*, 5237–5241.

[97] Ionov, L.; Zdyrko, B.; Sidorenko, A.; Minko, S.; Klep, V.; Luzinov, I.; Stamm, M. *Macromolecular Rapid Communications* **2004**, *25*, 360–365.

[98] Ionov, L.; Sidorenko, A.; Stamm, M.; Minko, S.; Zdyrko, B.; Klep, V.; Luzinov, I. *Macromolecules* **2004**, *37*, 7421–7423.

[99] Ionov, L.; Houbenov, N.; Sidorenko, A.; Stamm, M.; Luzinov, I.; Minko, S. *Langmuir* **2004**, *20*, 9916–9919.

[100] Ballav, N.; Shaporenko, A.; Terfort, A.; Zharnikov, M. *Advanced Materials* **2007**, *19*, 998–1000.

[101] Blondiaux, N.; Zurcher, S.; Liley, M.; Spencer, N. D. *Langmuir* **2007**, *23*, 3489–3494.

[102] Wang, X. J.; Bohn, P. W. *Journal of the American Chemical Society* **2004**, *126*, 6825–6832.

[103] Zelzer, M.; Majani, R.; Bradley, J. W.; Rose, F.; Davies, M. C.; Alexander, M. R. *Biomaterials* **2008**, *29*, 172–184.

[104] Bourgès-Monnier, C.; Shanahan, M. E. R. *Langmuir* **1995**, *11*, 2820–2829.

[105] Chaudhury, M. K.; Whitesides, G. M. *Science* **1992**, *256*, 1539–1541.

[106] Good, R. J.; Koo, M. N. *Journal of Colloid and Interface Science* **1979**, *71*, 283–292.

[107] Gaydos, J.; Neumann, A. W. *Journal of Colloid and Interface Science* **1987**, *120*, 76–86.

[108] Yekta-Fard, M.; Ponter, A. B. *Journal of Colloid and Interface Science* **1988**, *126*, 134–140.

[109] Taylor, M.; Urquhart, A. J.; Zelzer, M.; Davies, M. C.; Alexander, M. R. *Langmuir* **2007**, *23*, 6875–6878.

[110] Bullett, N. A.; Short, R. D.; O'Leary, T.; Beck, A. J.; Douglas, C. W. I.; Cambray-Deakin, M.; Fletcher, I. W.; Roberts, A.; Blomfield, C. *Surface and Interface Analysis* **2001**, *31*, 1074–1076.

[111] Steele, J. G.; Johnson, G.; McFarland, C.; Dalton, B. A.; Gengenbach, T. R.; Chatelier, R. C.; Underwood, P. A.; Griesser, H. J. *Journal of Biomaterials Science-Polymer Edition* **1994**, *6*, 511–532.

[112] Hamerli, P.; Weigel, T.; Groth, T.; Paul, D. *Biomaterials* **2003**, *24*, 3989–3999.

[113] Johnson, S. D.; Anderson, J. M.; Marchant, R. E. *Journal of Biomedical Materials Research* **1992**, *26*, 915–935.

[114] Goyal, K. O.; Mahalingam, R.; Pedrow, P. D.; Osman, M. A. *IEEE Transactions on Plasma Science* **2001**, *29*, 42–50.

[115] Kelly, J. M.; Short, R. D.; Alexander, M. R. *Polymer* **2003**, *44*, 3173–3176.

[116] Dehili, C.; Lee, P.; Shakesheff, K. M.; Alexander, M. R. *Plasma Processes and Polymers* **2006**, *3*, 474–484.

[117] Shard, A. G.; Whittle, J. D.; Beck, A. J.; Brookes, P. N.; Bullett, N. A.; Talib, R. A.; Mistry, A.; Barton, D.; McArthur, S. L. *Journal of Physical Chemistry B* **2004**, *108*, 12472–12480.

[118] Cho, W. J.; Saxena, R.; Rodriguez, O.; Ojha, M.; Achanta, R.; Plawsky, J. L.; Gill, W. N. *Journal of the Electrochemical Society* **2005**, *152*, F61–F65.

[119] Mitchell, D. F.; Clark, K. B.; Bardwell, J. A.; Lennard, W. N.; Massoumi, G. R.; Mitchell, I. V. *Surface and Interface Analysis* **1994**, *21*, 44–50.

[120] Tanuma, S.; Powell, C. J.; Penn, D. R. *Surface and Interface Analysis* **1993**, *20*, 77–89.

[121] Alexander, M. R.; Thompson, G. E.; Zhou, X.; Beamson, G.; Fairley, N. *Surface and Interface Analysis* **2002**, *34*, 485–489.

[122] O'Toole, L.; Beck, A. J.; Ameen, A. P.; Jones, F. R.; Short, R. D. *Journal of the Chemical Society-Faraday Transactions* **1995**, *91*, 3907–3912.

[123] Barton, D.; Bradley, J. W.; Steele, D. A.; Short, R. D. *Journal of Physical Chemistry B* **1999**, *103*, 4423–4430.

[124] Gilron, J.; Soffer, A. *Journal of Membrane Science* **2002**, *209*, 339–352.

[125] Yun, J. H.; Rhee, S. W. *Thin Solid Films* **1997**, *292*, 324–329.

[126] Vanooij, W. J.; Brinkhuis, R. H. G. *Surface and Interface Analysis* **1988**, *11*, 430–440.

[127] Briggs, D. *Surface and Interface Analysis* **1990**, *15*, 734–738.

[128] Oran, U.; Swaraj, S.; Friedrich, J. F.; Unger, W. E. S. *Plasma Processes and Polymers* **2004**, *1*, 141–152.

[129] Oran, U.; Swaraj, S.; Friedrich, J. F.; Unger, W. E. S. *Plasma Processes and Polymers* **2005**, *2*, 563–571.

[130] Oran, U.; Swaraj, S.; Lippitz, A.; Unger, W. E. S. *Plasma Processes and Polymers* **2006**, *3*, 288–298.

[131] Swindells, I.; Voronin, S. A.; Fotea, C.; Alexander, M. R.; Bradley, J. W. *Journal of Physical Chemistry B* **2007**, *111*, 8720–8722.

[132] Schwarzenbach, W.; Cunge, G.; Booth, J. P. *Journal of Applied Physics* **1999**, *85*, 7562–7568.

[133] Swindells, I.; Voronin, S. A.; Bryant, P. M.; Alexander, M. R.; Bradley, J. W. *Journal of Physical Chemistry B* **2008**, *112*, 3938–3947.

[134] *CRC Handbook of Chemistry and Physics*, 77th ed.; Lide, D. R., Ed.; CRC Press: London, 1996.

[135] van Os, M. T.; Menges, B.; Foerch, R.; Vancso, G. J.; Knoll, W. *Chemistry of Materials* **1999**, *11*, 3252–3257.

[136] Jagur-Grodzinski, J. *Polymers for Advanced Technologies* **2006**, *17*, 395–418.

[137] Tessmar, J. K.; Gopferich, A. M. *Advanced Drug Delivery Reviews* **2007**, *59*, 274–291.

[138] Ong, S. Y.; Wu, J.; Moochhala, S. M.; Tan, M. H.; Lu, J. *Biomaterials* **2008**, *29*, 4323–4332.

[139] Homola, J.; Yee, S. S.; Gauglitz, G. *Sensors and Actuators B-Chemical* **1999**, *54*, 3–15.

[140] Gerard, M.; Chaubey, A.; Malhotra, B. D. *Biosensors & Bioelectronics* **2002**, *17*, 345–359.

[141] Yliperttula, M.; Chung, B. G.; Navaladi, A.; Manbachi, A.; Urtti, A. *European Journal of Pharmaceutical Sciences* **2008**, *35*, 151–160.

[142] Martina, M.; Hutmacher, D. W. *Polymer International* **2007**, *56*, 145–157.

[143] Finke, B.; Luethen, F.; Schroeder, K.; Mueller, P. D.; Bergeniann, C.; Frant, M.; Ohl, A.; Nebe, B. J. *Biomaterials* **2007**, *28*, 4521–4534.

[144] Folkman, J.; Moscona, A. *Nature* **1978**, *273*, 345–349.

[145] Benzeev, A.; Farmer, S. R.; Penman, S. *Cell* **1980**, *21*, 365–372.

[146] Ruoslahti, E.; Reed, J. C. *Cell* **1994**, *77*, 477–478.

[147] Kasemo, B. *Surface Science* **2002**, *500*, 656–677.

[148] Purves, W. K.; Sadava, D.; Orians, G.; Heller, H. *Life the Science of Biology: The Cell and Heredity*, 6th ed.; Sinauer Associates, Inc. W.H. Freeman and Co.: Sunderland, 2001.

[149] http://www.ionchannels.org/structure.php3, November 2008.

[150] Mrksich, M. *Chemical Society Reviews* **2000**, *29*, 267–273.

[151] Wilson, C. J.; Clegg, R. E.; Leavesley, D. I.; Pearcy, M. J. *Tissue Engineering* **2005**, *11*, 1–18.

[152] Geiger, B.; Bershadsky, A.; Pankov, R.; Yamada, K. M. *Nature Reviews Molecular Cell Biology* **2001**, *2*, 793–805.

[153] Hynes, R. O. *Trends in Cell Biology* **1999**, *9*, M33–M37.

[154] Schneider, G.; Burridge, K. *Experimental Cell Research* **1994**, *214*, 264–269.

[155] Gronowicz, G.; McCarthy, M. B. *Journal of Orthopaedic Research* **1996**, *14*, 878–887.

[156] Cohen, M.; Joester, D.; Geiger, B.; Addadi, L. *Chembiochem* **2004**, *5*, 1393–1399.

[157] Leckband, D. E.; Schmitt, F. J.; Israelachvili, J. N.; Knoll, W. *Biochemistry* **1994**, *33*, 4611–4624.

[158] Leckband, D.; Israelachvili, J. *Quarterly Reviews of Biophysics* **2001**, *34*, 105–267.

[159] Zimmerman, E.; Geiger, B.; Addadi, L. *Biophysical Journal* **2002**, *82*, 1848–1857.

[160] Adams, J. C. *Cellular and Molecular Life Sciences* **2001**, *58*, 371–392.

[161] Jockusch, B. M.; Bubeck, P.; Giehl, K.; Kroemker, M.; Moschner, J.; Rothkegel, M.; Rudiger, M.; Schluter, K.; Stanke, G.; Winkler, J. *Annual Review of Cell and Developmental Biology* **1995**, *11*, 379–416.

[162] Burridge, K.; Chrzanowska-Wodnicka, M. *Annual Review of Cell and Developmental Biology* **1996**, *12*, 463–518.

[163] Hynes, R. O. *Cell* **1992**, *69*, 11–25.

[164] Schwartz, M. A.; Schaller, M. D.; Ginsberg, M. H. *Annual Review of Cell and Developmental Biology* **1995**, *11*, 549–599.

[165] Travis, M. A.; Humphries, J. D.; Humphries, M. J. *Trends in Pharmacological Sciences* **2003**, *24*, 192–197.

[166] Izzard, C. S.; Lochner, L. R. *Journal of Cell Science* **1976**, *21*, 129–159.

[167] Sastry, S. K.; Burridge, K. *Experimental Cell Research* **2000**, *261*, 25–36.

[168] Zamir, E.; Katz, M.; Posen, Y.; Erez, N.; Yamada, K. M.; Katz, B. Z.; Lin, S.; Lin, D. C.; Bershadsky, A.; Kam, Z.; Geiger, B. *Nature Cell Biology* **2000**, *2*, 191–196.

[169] Rottner, K.; Hall, A.; Small, J. V. *Current Biology* **1999**, *9*, 640–648.

[170] Lauffenburger, D. A.; Horwitz, A. F. *Cell* **1996**, *84*, 359–369.

[171] Burridge, K.; Fath, K.; Kelly, T.; Nuckolls, G.; Turner, C. *Annual Review of Cell Biology* **1988**, *4*, 487–525.

[172] Dunlevy, J. R.; Couchman, J. R. *Journal of Cell Science* **1993**, *105*, 489–500.

[173] Palecek, S. P.; Schmidt, C. E.; Lauffenburger, D. A.; Horwitz, A. F. *Journal of Cell Science* **1996**, *109*, 941–952.

[174] Chen, W. T. *Journal of Cell Biology* **1981**, *90*, 187–200.

[175] Regen, C. M.; Horwitz, A. F. *Journal of Cell Biology* **1992**, *119*, 1347–1359.

[176] Ruoslahti, E. *Annual Review of Biochemistry* **1988**, *57*, 375–413.

[177] Lopez, L. C.; Gristina, R.; Ceccone, G.; Rossi, F.; Favia, P.; d'Agostino, R. *Surface & Coatings Technology* **2005**, *200*, 1000–1004.

[178] Van Der Valk, P.; Van Pelt, A. W. J.; Busscher, H. J.; De Jong, H. P.; Wildevuur, C. R. H.; Arends, J. *Journal of Biomedical Materials Research* **1983**, *17*, 808–818.

[179] Schakenraad, J. M.; Busscher, H. J.; Wildevuur, C. R. H.; Arends, J. *Journal of Biomedical Materials Research* **1986**, *20*, 773–784.

[180] Steele, J. G.; Johnson, G.; Underwood, P. A. *Journal of Biomedical Materials Research* **1992**, *26*, 861–884.

[181] von Recum, A. F.; Shannon, C. E.; Cannon, C. E.; Long, K. J.; van Kooten, T. G.; Meyle, J. *Tissue Engineering* **1996**, *2*, 241–253.

[182] Kieswetter, K.; Schwartz, Z.; Hummert, T. W.; Cochran, D. L.; Simpson, J.; Dean, D. D.; Boyan, B. D. *Journal of Biomedical Materials Research* **1996**, *32*, 55–63.

[183] Lincks, J.; Boyan, B. D.; Blanchard, C. R.; Lohmann, C. H.; Liu, Y.; Cochran, D. L.; Dean, D. D.; Schwartz, Z. *Biomaterials* **1998**, *19*, 2219–2232.

[184] Batzer, R.; Liu, Y.; Cochran, D. L.; Szmuckler-Moncler, S.; Dean, D. D.; Boyan, B. D.; Schwartz, Z. *Journal of Biomedical Materials Research* **1998**, *41*, 489–496.

[185] Anselme, K.; Bigerelle, M.; Noel, B.; Dufresne, E.; Judas, D.; Iost, A.; Hardouin, P. *Journal of Biomedical Materials Research* **2000**, *49*, 155–166.

[186] Anselme, K.; Linez, P.; Bigerelle, M.; Le Maguer, D.; Le Maguer, A.; Hardouin, P.; Hildebrand, H. F.; Iost, A.; Leroy, J. M. *Biomaterials* **2000**, *21*, 1567–1577.

[187] Stanford, C. M.; Keller, J. C.; Solursh, M. *Journal of Dental Research* **1994**, *73*, 1061–1071.

[188] Lauer, G.; Wiedmann-Al-Ahmad, M.; Otten, J. E.; Hubner, U.; Schmelzeisen, R.; Schilli, W. *Biomaterials* **2001**, *22*, 2799–2809.

[189] Biggs, M. J. P.; Richards, R. G.; Gadegaard, N.; Wilkinson, C. D. W.; Dalby, M. J. *Journal of Materials Science-Materials in Medicine* **2007**, *18*, 399–404.

[190] Dalby, M. J.; Gadegaard, N.; Wilkinson, C. D. W. *Journal of Biomedical Materials Research Part A* **2008**, *84A*, 973–979.

[191] Choquet, D.; Felsenfeld, D. P.; Sheetz, M. P. *Cell* **1997**, *88*, 39–48.

[192] Sun, T. L.; Han, D.; Rhemann, K.; Chi, L. F.; Fuchs, H. *Journal of the American Chemical Society* **2007**, *129*, 1496–1497.

[193] Chen, G. P.; Imanishi, Y.; Ito, Y. *Journal of Biomedical Materials Research* **1998**, *42*, 38–44.

[194] Koenig, A. L.; Gambillara, V.; Grainger, D. W. *Journal of Biomedical Materials Research Part A* **2003**, *64A*, 20–37.

[195] Hynes, R. O.; Yamada, K. M. *Journal of Cell Biology* **1982**, *95*, 369–377.

[196] Skorstengaard, K.; Jensen, M. S.; Sahl, P.; Petersen, T. E.; Magnusson, S. *European Journal of Biochemistry* **1986**, *161*, 441–453.

[197] Petersen, T. E.; Thogersen, H. C.; Skorstengaard, K.; Vibepedersen, K.; Sahl, P.; Sottrup-jensen, L.; Magnusson, S. *Proceedings of the National Academy of Sciences of the United States of America-Biological Sciences* **1983**, *80*, 137–141.

[198] Khan, M. Y.; Medow, M. S.; Newman, S. A. *Biochemical Journal* **1990**, *270*, 33–38.

[199] Mosher, D. F.; McKeownlongo, P. J. *Biopolymers* **1985**, *24*, 199–210.

[200] Engel, J.; Odermatt, E.; Engel, A.; Madri, J. A.; Furthmayr, H.; Rohde, H.; Timpl, R. *Journal of Molecular Biology* **1981**, *150*, 97–120.

[201] Williams, E. C.; Janmey, P. A.; Ferry, J. D.; Mosher, D. F. *Journal of Biological Chemistry* **1982**, *257*, 4973–4978.

[202] Rocco, M.; Infusini, E.; Daga, M. G.; Gogioso, L.; Cuniberti, C. *Embo Journal* **1987**, *6*, 2343–2349.

[203] Alexander, S. S.; Colonna, G.; Edelhoch, H. *Journal of Biological Chemistry* **1979**, *254*, 1501–1505.

[204] Lai, C. S.; Tooney, N. M.; Ankel, E. G. *Biochemistry* **1984**, *23*, 6393–6397.

[205] Pierschbacher, M. D.; Ruoslahti, E. *Nature* **1984**, *309*, 30–33.

[206] Aota, S.; Nomizu, M.; Yamada, K. M. *Journal of Biological Chemistry* **1994**, *269*, 24756–24761.

[207] Wang, H.; He, Y.; Ratner, B. D.; Jiang, S. Y. *Journal of Biomedical Materials Research Part A* **2006**, *77A*, 672–678.

[208] Rothschild, M. A.; Oratz, M.; Schreiber, S. S. *Hepatology* **1988**, *8*, 385–401.

[209] Ferrer, M. L.; Duchowicz, R.; Carrasco, B.; de la Torre, J. G.; Acuna, A. U. *Biophysical Journal* **2001**, *80*, 2422–2430.

[210] Quinlan, G. J.; Martin, G. S.; Evans, T. W. *Hepatology* **2005**, *41*, 1211–1219.

[211] Norde, W.; Giacomelli, C. E. *Journal of Biotechnology* **2000**, *79*, 259–268.

[212] Norde, W. *Advances in Colloid and Interface Science* **1986**, *25*, 267–340.

[213] Haynes, C. A.; Sliwinsky, E.; Norde, W. *Journal of Colloid and Interface Science* **1994**, *164*, 394–409.

[214] Vogler, E. A. *Advances in Colloid and Interface Science* **1998**, *74*, 69–117.

[215] Nygren, H. *Colloids and Surfaces B-Biointerfaces* **1996**, *6*, 329–333.

[216] Absolom, D. R.; Zingg, W.; Neumann, A. W. *Journal of Biomedical Materials Research* **1987**, *21*, 161–171.

[217] Sigal, G. B.; Mrksich, M.; Whitesides, G. M. *Journal of the American Chemical Society* **1998**, *120*, 3464–3473.

[218] Roach, P.; Farrar, D.; Perry, C. C. *Journal of the American Chemical Society* **2005**, *127*, 8168–8173.

[219] Fabriziushoman, D. J.; Cooper, S. L. *Journal of Biomedical Materials Research* **1991**, *25*, 953–971.

[220] Elwing, H.; Gölander, C. G. *Advances in Colloid and Interface Science* **1990**, *32*, 317–339.

[221] Vroman, L.; Adams, A. L. *Journal of Colloid and Interface Science* **1986**, *111*, 391–402.

[222] Green, R. J.; Davies, M. C.; Roberts, C. J.; Tendler, S. J. B. *Biomaterials* **1999**, *20*, 385–391.

[223] Wertz, C. F.; Santore, M. M. *Langmuir* **1999**, *15*, 8884–8894.

[224] Grinnell, F. *Journal of Cell Biology* **1986**, *103*, 2697–2706.

[225] Renner, L.; Pompe, T.; Salchert, K.; Werner, C. *Langmuir* **2004**, *20*, 2928–2933.

[226] Renner, L.; Pompe, T.; Salchert, K.; Werner, C. *Langmuir* **2005**, *21*, 4571–4577.

[227] Slack, S. M.; Horbett, T. A. *Journal of Colloid and Interface Science* **1989**, *133*, 148–165.

[228] Steele, J. G.; Dalton, B. A.; Johnson, G.; Underwood, P. A. *Journal of Biomedical Materials Research* **1993**, *27*, 927–940.

[229] Steele, J. G.; Dalton, B. A.; Johnson, G.; Underwood, P. A. *Biomaterials* **1995**, *16*, 1057–1067.

[230] Savage, B.; Ruggeri, Z. M. *Journal of Biological Chemistry* **1991**, *266*, 11227–11233.

[231] Seiffert, D.; Smith, J. W. *Journal of Biological Chemistry* **1997**, *272*, 13705–13710.

[232] Burmeister, J. S.; Vrany, J. D.; Reichert, W. M.; Truskey, G. A. *Journal of Biomedical Materials Research* **1996**, *30*, 13–22.

[233] Lewandowska, K.; Balachander, N.; Sukenik, C. N.; Culp, L. A. *Journal of Cellular Physiology* **1989**, *141*, 334–345.

[234] Giacomelli, C. E.; Norde, W. *Journal of Colloid and Interface Science* **2001**, *233*, 234–240.

[235] Bergkvist, M.; Carlsson, J.; Oscarsson, S. *Journal of Biomedical Materials Research Part A* **2003**, *64A*, 349–356.

[236] Cheng, S. S.; Chittur, K. K.; Sukenik, C. N.; Culp, L. A.; Lewandowska, K. *Journal of Colloid and Interface Science* **1994**, *162*, 135–143.

[237] Xia, N.; May, C. J.; McArthur, S. L.; Castner, D. G. *Langmuir* **2002**, *18*, 4090–4097.

[238] Buijs, J.; Norde, W.; Lichtenbelt, J. W. T. *Langmuir* **1996**, *12*, 1605–1613.

[239] Bohnert, J. L.; Horbett, T. A. *Journal of Colloid and Interface Science* **1986**, *111*, 363–378.

[240] Roach, P.; Farrar, D.; Perry, C. C. *Journal of the American Chemical Society* **2006**, *128*, 3939–3945.

[241] Garcia, A. J.; Vega, M. D.; Boettiger, D. *Molecular Biology of the Cell* **1999**, *10*, 785–798.

[242] Seigel, R. R.; Harder, P.; Dahint, R.; Grunze, M.; Josse, F.; Mrksich, M.; Whitesides, G. M. *Analytical Chemistry* **1997**, *69*, 3321–3328.

[243] Baugh, L.; Vogel, V. *Journal of Biomedical Materials Research Part A* **2004**, *69A*, 525–534.

[244] Liu, M. L.; Zhang, Y. Y.; Wang, M. L.; Deng, C. Y.; Xie, Q. J.; Yao, S. Z. *Polymer* **2006**, *47*, 3372–3381.

[245] Rechendorff, K.; Hovgaard, M. B.; Foss, M.; Zhdanov, V. P.; Besenbacher, F. *Langmuir* **2006**, *22*, 10885–10888.

[246] Jones, J. R. *Materials Today* **2006**, *9*, 34–43.

[247] Bremmell, K. E.; Kingshott, P.; Ademovic, Z.; Winther-Jensen, B.; Griesser, H. J. *Langmuir* **2006**, *22*, 313–318.

[248] Jansson, E.; Tengvall, P. *Colloids and Surfaces B-Biointerfaces* **2004**, *35*, 45–51.

[249] Karlsson, L. M.; Tengvall, P.; Lundstrom, I.; Arwin, H. *Physica Status Solidi A-Applications and Materials Science* **2003**, *197*, 326–330.

[250] Benesch, J.; Hungerford, G.; Suhling, K.; Tregidgo, C.; Mano, J. F.; Reis, R. L. *Journal of Colloid and Interface Science* **2007**, *312*, 193–200.

[251] Lhoest, J. B.; Detrait, E.; van den Bosch de Aguilar, P.; Bertrand, P. *Journal of Biomedical Materials Research* **1998**, *41*, 95–103.

[252] Hull, J. R.; Tamura, G. S.; Castner, D. G. *Biophysical Journal* **2007**, *93*, 2852–2860.

[253] Zhang, Z.; Menges, B.; Timmons, R. B.; Knoll, W.; Förch, R. *Langmuir* **2003**, *19*, 4765–4770.

[254] Elwing, H.; Nilsson, B.; Svensson, K. E.; Askendahl, A.; Nilsson, U. R.; Lundström, I. *Journal of Colloid and Interface Science* **1988**, *125*, 139–145.

[255] Tosatti, S.; De Paul, S. M.; Askendal, A.; VandeVondele, S.; Hubbell, J. A.; Tengvall, P.; Textor, M. *Biomaterials* **2003**, *24*, 4949–4958.

[256] Uhlmann, P.; Houbenov, N.; Brenner, N.; Grundke, K.; Burkert, S.; Stamm, M. *Langmuir* **2007**, *23*, 57–64.

[257] Pasche, S.; Vörös, J.; Griesser, H. J.; Spencer, N. D.; Textor, M. *Journal of Physical Chemistry B* **2005**, *109*, 17545–17552.

[258] MacDonald, D. E.; Markovic, B.; Allen, M.; Somasundaran, P.; Boskey, A. L. *Journal of Biomedical Materials Research* **1998**, *41*, 120–130.

[259] Wolff, C.; Lai, C. S. *Biochemistry* **1988**, *27*, 3483–3487.

[260] Baneyx, G.; Baugh, L.; Vogel, V. *Proceedings of the National Academy of Sciences of the United States of America* **2001**, *98*, 14464–14468.

[261] Uyen, H. M. W.; Schakenraad, J. M.; Sjollema, J.; Noordmans, J.; Jongebloed, W. L.; Stokroos, I.; Busscher, H. J. *Journal of Biomedical Materials Research* **1990**, *24*, 1599–1614.

[262] Narasimhan, C.; Lai, C. S. *Biochemistry* **1989**, *28*, 5041–5046.

[263] Chittur, K. K. *Biomaterials* **1998**, *19*, 357–369.

[264] Vermette, P.; Gengenbach, T.; Divisekera, U.; Kambouris, P. A.; Griesser, H. J.; Meagher, L. *Journal of Colloid and Interface Science* **2003**, *259*, 13–26.

[265] Whittle, J. D.; Bullett, N. A.; Short, R. D.; Douglas, C. W. I.; Hollander, A. P.; Davies, J. *Journal of Materials Chemistry* **2002**, *12*, 2726–2732.

[266] Michael, K. E.; Vernekar, V. N.; Keselowsky, B. G.; Meredith, J. C.; Latour, R. A.; Garcia, A. J. *Langmuir* **2003**, *19*, 8033–8040.

[267] Wetterö, J.; Askendal, A.; Tengvall, P.; Bengtsson, T. *Journal of Biomedical Materials Research Part A* **2003**, *66A*, 162–175.

[268] Wetterö, J.; Tengvall, P.; Bengtsson, T. *Biomaterials* **2003**, *24*, 2669–2669.

[269] Höök, F.; Rodahl, M.; Brzezinski, P.; Kasemo, B. *Langmuir* **1998**, *14*, 729–734.

[270] Höök, F.; Kasemo, B.; Nylander, T.; Fant, C.; Sott, K.; Elwing, H. *Analytical Chemistry* **2001**, *73*, 5796–5804.

[271] Atkins, P. W. *Physical Chemistry*, 6th ed.; Oxford University Press: Oxford, 1988.

[272] Wedler, G. *Lehrbuch der Physikalischen Chemie*; Wiley-VCH: Weinheim, 1997.

[273] Lai, C. S.; Homandberg, G.; Miziorko, H.; Wolff, C. *Biopolymers* **1987**, *26*, 1381–1389.

[274] Lakowicz, J. R. *Principles of Fluorescence Spectroscopy*, 2nd ed.; Kluwer Academic: New York, 1999.

[275] Zhang, Z. H.; Chen, Q.; Knoll, W.; Foerch, R.; Holcomb, R.; Roitman, D. *Macromolecules* **2003**, *36*, 7689–7694.

[276] Zhang, Z.; Knoll, W.; Förch, R. *Surface & Coatings Technology* **2005**, *200*, 993–995.

[277] Muguruma, H.; Hiratsuka, A.; Karube, I. *Analytical Chemistry* **2000**, *72*, 2671–2675.

[278] Ito, Y.; Kajihara, M.; Imanishi, Y. *Journal of Biomedical Materials Research* **1991**, *25*, 1325–1337.

[279] Gupta, B.; Plummer, C.; Bisson, I.; Frey, P.; Hilborn, J. *Biomaterials* **2002**, *23*, 863–871.

[280] Yuan, S.; Szakalasgratzl, G.; Ziats, N. P.; Jacobsen, D. W.; Kottkemarchant, K.; Marchant, R. E. *Journal of Biomedical Materials Research* **1993**, *27*, 811–819.

[281] Gombotz, W. R.; Guanghui, W.; Horbett, T. A.; Hoffman, A. S. *Journal of Biomedical Materials Research* **1991**, *25*, 1547–1562.

[282] Chu, L. Q.; Knoll, W.; Förch, R. *Plasma Processes and Polymers* **2006**, *3*, 498–505.

[283] Higham, M. C.; Dawson, R.; Szabo, M.; Short, R.; Haddow, D. B.; MacNeil, S. *Tissue Engineering* **2003**, *9*, 919–930.

[284] Eves, P. C.; Beck, A. J.; Shard, A. G.; Neil, S. M. *Biomaterials* **2005**, *26*, 7068–7081.

[285] Detomaso, L.; Gristina, R.; d'Agostino, R.; Senesi, G.; Favia, P. *Surface & Coatings Technology* **2005**, *200*, 1022–1025.

[286] Detomaso, L.; Gristina, R.; Senesi, G. S.; d'Agostino, R.; Favia, P. *Biomaterials* **2005**, *26*, 3831–3841.

[287] Mar, M. N.; Ratner, B. D.; Yee, S. S. *Sensors and Actuators B-Chemical* **1999**, *54*, 125–131.

[288] Beyer, D.; Knoll, W.; Ringsdorf, H.; Wang, J. H.; Timmons, R. B.; Sluka, P. *Journal of Biomedical Materials Research* **1997**, *36*, 181–189.

[289] Chu, L. Q.; Knoll, W.; Förch, R. *Chemistry of Materials* **2006**, *18*, 4840–4844.

[290] Wu, Y. L. J.; Timmons, R. B.; Jen, J. S.; Molock, F. E. *Colloids and Surfaces B-Biointerfaces* **2000**, *18*, 235–248.

[291] Canavan, H. E.; Cheng, X. H.; Graham, D. J.; Ratner, B. D.; Castner, D. G. *Plasma Processes and Polymers* **2006**, *3*, 516–523.

[292] Sardella, E.; Favia, P.; Gristina, R.; Nardulli, M.; d'Agostino, R. *Plasma Processes and Polymers* **2006**, *3*, 456–469.

[293] Sardella, E.; Gristina, R.; Ceccone, G.; Gilliland, D.; Papadopoulou-Bouraoui, A.; Rossi, F.; Senesi, G. S.; Detomaso, L.; Favia, P.; d'Agostino, R. *Surface & Coatings Technology* **2005**, *200*, 51–57.

[294] Matsuda, T.; Sugawara, T. *Journal of Biomedical Materials Research* **1995**, *29*, 749–756.

[295] Matsuda, T.; Sugawara, T. *Journal of Biomedical Materials Research* **1996**, *32*, 165–173.

[296] Hatakeyama, H.; Kikuchi, A.; Yamato, M.; Okano, T. *Biomaterials* **2007**, *28*, 3632–3643.

[297] Tsuda, Y.; Kikuchi, A.; Yamato, M.; Nakao, A.; Sakurai, Y.; Umezu, M.; Okano, T. *Biomaterials* **2005**, *26*, 1885–1893.

[298] Tsuda, Y.; Kikuchi, A.; Yamato, M.; Chen, G. P.; Okano, T. *Biochemical and Biophysical Research Communications* **2006**, *348*, 937–944.

[299] Idota, N.; Tsukahara, T.; Sato, K.; Okano, T.; Kitamori, T. *Biomaterials* **2009**, *30*, 2095–2101.

[300] Ueda-Yukoshi, T.; Matsuda, T. *Langmuir* **1995**, *11*, 4135–4140.

[301] Choee, J. H.; Lee, S. J.; Lee, Y. M.; Rhee, J. M.; Lee, H. B.; Khang, G. *Journal of Applied Polymer Science* **2004**, *92*, 599–606.

[302] Kennedy, S. B.; Washburn, N. R.; Jr., C. G. S.; Amis, E. J. *Biomaterials* **2006**, *27*, 3817–3824.

[303] Iwasaki, Y.; Sawada, S.; Nakabayashi, N.; Khang, G.; Lee, H. B.; Ishihara, K. *Biomaterials* **1999**, *20*, 2185–2191.

[304] Bhat, R. R.; Chaney, B. N.; Rowley, J.; Liebmann-Vinson, A.; Genzer, J. *Advanced Materials* **2005**, *17*, 2802–2807.

[305] Mei, Y.; Wu, T.; Xu, C.; Langenbach, K. J.; Elliott, J. T.; Vogt, B. D.; Beers, K. L.; Amis, E. J.; Washburn, N. R. *Langmuir* **2005**, *21*, 12309–12314.

[306] Welin-Klintström, S.; Lestelius, M.; Liedberg, B.; Tengvall, P. *Colloids and Surfaces B-Biointerfaces* **1999**, *15*, 81–87.

[307] Riepl, M.; Östblom, M.; Lundström, I.; Svensson, S. C. T.; Gon, A. W. D. v. d.; Schäferling, M.; Liedberg, B. *Langmuir* **2005**, *21*, 1042–1050.

[308] Meredith, J. C.; Sormana, J.-L.; Keselowsky, B. G.; Garcia, A. J.; Tona, A.; Karim, A.; Amis, E. J. *Journal of Biomedical Materials Research* **2003**, 483–490.

[309] Washburn, N. R.; Yamada, K. M.; Simon, C. G.; Kennedy, S. B.; Amis, E. J. *Biomaterials* **2004**, *25*, 1215–1224.

[310] Kunzler, T. P.; Drobek, T.; Schuler, M.; Spencer, N. D. *Biomaterials* **2007**, *28*, 2175–2182.

[311] Kunzler, T. P.; Huwiler, C.; Drobek, T.; Vörös, J.; Spencer, N. D. *Biomaterials* **2007**, *28*, 5000–5006.

[312] Collins, B. E.; Dancil, K. P. S.; Abbi, G.; Sailor, M. J. *Advanced Functional Materials* **2002**, *12*, 187–191.

[313] Li, B.; Ma, Y. X.; Wang, S.; Moran, P. M. *Biomaterials* **2005**, *26*, 4956–4963.

[314] Petty, R. T.; Li, H.-W.; Maduram, J. H.; Ismagilov, R.; Mrksich, M. *Journal of the American Chemical Society* **2007**, *129*, 8966–8967.

[315] Bhat, R. R.; Tomlinson, M. R.; Genzer, J. *Journal of Polymer Science Part B-Polymer Physics* **2005**, *43*, 3384–3394.

[316] Carter, S. B. *Nature* **1967**, *213*, 256–260.

[317] Brandley, B. K.; Schnaar, R. L. *Developmental Biology* **1989**, *135*, 74–86.

[318] Keselowsky, B. G.; Collard, D. M.; Garcia, A. J. *Journal of Biomedical Materials Research Part A* **2003**, *66A*, 247–259.

[319] Keselowsky, B. G.; Collard, D. M.; Garcia, A. J. *Biomaterials* **2004**, *25*, 5947–5954.

[320] Iyer, V. N.; Szybalski, W. *Proceedings of the National Academy of Sciences of the United States of America* **1963**, *50*, 355–362.

[321] Kaplan, D. J.; Tomasz, M. *Biochemistry* **1982**, *21*, 3006–3013.

[322] Tomasz, M.; Das, A.; Tang, K. S.; Ford, M. G. J.; Minnock, A.; Musser, S. M.; Waring, M. J. *Journal of the American Chemical Society* **1998**, *120*, 11581–11593.

[323] Paz, M. M.; Kumar, G. S.; Glover, M.; Waring, M. J.; Tomasz, M. *Journal of Medicinal Chemistry* **2004**, *47*, 3308–3319.

[324] Jampel, H. D. *Ophthalmology* **1992**, *99*, 1471–1476.

[325] Smith, S.; Damore, P. A.; Dreyer, E. B. *American Journal of Ophthalmology* **1994**, *118*, 332–337.

[326] Kim, T. I.; Choi, S. I.; Lee, H. K.; Cho, Y. J.; Kim, E. K. *Molecular Vision* **2008**, *14*, 1222–1228.

[327] Occleston, N. L.; Alexander, R. A.; Mazure, A.; Larkin, G.; Khaw, P. T. *Investigative Ophthalmology & Visual Science* **1994**, *35*, 3681–3690.

[328] Jang, C. H.; Song, C. H.; Pak, S. C. *International Journal of Pediatric Otorhinolaryngology* **2003**, *67*, 173–176.

[329] Nuyts, R.; Pels, E.; Greve, E. L. *Current Eye Research* **1992**, *11*, 565–570.

[330] Arima, Y.; Iwata, H. *Journal of Materials Chemistry* **2007**, *17*, 4079–4087.

[331] Ruardy, T. G.; Schakenraad, J. M.; Vandermei, H. C.; Busscher, H. J. *Journal of Biomedical Materials Research* **1995**, *29*, 1415–1423.

[332] Huwiler, C.; Kunzler, T. P.; Textor, M.; Vörös, J.; Spencer, N. D. *Langmuir* **2007**, *23*, 5929–5935.

[333] Gunawan, R. C.; Choban, E. R.; Conour, J. E.; Silvestre, J.; Schook, L. B.; Gaskins, H. R.; Leckband, D. E.; Kenis, P. J. A. *Langmuir* **2005**, *21*, 3061–3068.

[334] Arima, Y.; Iwata, H. *Biomaterials* **2007**, *28*, 3074–3082.

[335] Barrias, C. C.; Martins, M. C. L.; Almeida-Porada, G.; Barbosa, M. A.; Granja, P. L. *Biomaterials* **2009**, *30*, 307–316.

[336] Plummer, S. T.; Wang, Q.; Bohn, P. W.; Stockton, R.; Schwartz, M. A. *Langmuir* **2003**, *19*, 7528–7536.

[337] Ying, P. Q.; Yu, Y.; Jin, G.; Tao, Z. L. *Colloids and Surfaces B-Biointerfaces* **2003**, *32*, 1–10.

[338] Baujard-Lamotte, L.; Noinville, S.; Goubard, F.; Marque, P.; Pauthe, E. *Colloids and Surfaces B-Biointerfaces* **2008**, *63*, 129–137.

[339] Ertel, S. I.; Ratner, B. D.; Horbett, T. A. *Journal of Biomedical Materials Research* **1990**, *24*, 1637–1659.

[340] Voronin, S. A.; Zelzer, M.; Fotea, C.; Alexander, M. R.; Bradley, J. W. *Journal of Physical Chemistry B* **2007**, *111*, 3419–3429.